UNIVERSITY OF SOUTHAMPTON

FACULTY OF NATURAL AND ENVIRONMENTAL SCIENCES

School of Ocean and Earth Science

Effects of *Posidonia oceanica* seagrass on nearshore waves and wave-induced flows

by

Eleonora Manca

Thesis for the degree of Doctor of Philosophy

October 2010

Graduate School of the
National Oceanography Centre, Southampton

This PhD dissertation by
Eleonora Manca

has been produced under the supervision of the following persons

Supervisors:

Prof. Carl L. Amos, NOC

Prof. Ian Townend , HR Wallingford

Dr. Charlotte Thompson, NOC

Chair of the Advisory panel:
Prof. Peter Statham

UNIVERSITY OF SOUTHAMPTON

ABSTRACT

FACULTY OF NATURAL AND ENVIRONMENTAL SCIENCES
SCHOOL OF OCEAN & EARTH SCIENCE

Doctor of Philosophy

EFFECTS OF SEAGRASS *POSIDONIA OCEANICA* ON NEARSHORE WAVES AND WAVE-INDUCED FLOWS

by Eleonora Manca

This work focuses on the effects of the large Mediterranean seagrass *Posidonia oceanica* on coastal waves and wave-induced flows, which has significant implications for coastal protection. Investigations were made on both a natural shallow *Posidonia oceanica* bed and, in controlled conditions of full-scale *Posidonia* mimics under regular and irregular waves. In the field, waves and currents were monitored during low energy conditions and a Mistral wind event. Data were collected on the distribution of *Posidonia* patches, density and canopy height, as well as bed sediment type and bathymetry. In the flume, measurements were made of water surface elevation along the flume and oscillatory flows at 3 locations and 4 elevations, under several wave conditions, water depths and for 2 canopy densities. The mimics were designed carefully to recreate the hydraulic behaviour of *Posidonia* plants under waves.

Field results indicate that shallow *Posidonia* meadows are effective at reducing wave energy under low wave energy conditions and small wave amplitudes. The flume experiments confirm this trend. Under both regular and irregular waves, drag coefficients decrease with increasing Reynolds vegetation numbers; wave dissipation factors decrease with wave orbital amplitude. Under spectral waves, most wave energy dissipation occurs at the peak spectral frequency and it is largest for the least energetic wave spectra. At high wave Reynolds numbers, the canopy-induced hydraulic roughness (r) appears to be a function of the canopy element density only, and the empirical formula of Nielsen (1992) is successfully applied. However, more work is required in low energy conditions to examine the range of validity of the formula. In natural conditions under small amplitude waves, attenuation of wave-induced flows is negligible in the upper canopy; flume experiments confirm this trend. The typical flow intensification at the canopy top, measured for other seagrasses, occurs only for tests with the largest wave amplitudes, whilst, under smaller waves, flow intensification is located within the upper part of the canopy. In the lower canopy, flows are always reduced and flows decelerate exponentially with increasing orbital amplitude. This is a novel observation in flexible canopies. The artificial canopy, like the natural *Posidonia* bed, enhances flow asymmetries at the canopy top, especially under waves with large wave orbital amplitudes. This is thought to be a mechanism to enhance shoreward drift. Turbulence in the artificial canopy, under regular waves, peaks at the canopy top, as occurs under unidirectional flows and for other seagrass beds exposed to waves. Vertical turbulent exchanges are enhanced at the edge of the seagrass patch and are larger for lower submergence ratios (the ratio of canopy height to water depth). A reduction in submergence ratio in the flume, also causes increased shear stresses at the top of the canopy, lower wave height decay and reduced oscillatory flow attenuation in the lower part of the canopy. The denser canopy, in the conditions tested, increases relative roughness (r/A), wave attenuation, in-canopy oscillatory flow reduction and turbulent kinetic energy at the top of the canopy. Oscillatory flows characterised by small orbital amplitudes can penetrate further into the canopy than larger orbital velocities, inducing a larger drag, thus increasing wave dissipation, as proposed for rigid canopies (corals). This is manifested as a thinner canopy boundary layer under small orbital amplitude waves than the large amplitude waves. A conceptual model is proposed to summarise these findings. Under storm conditions *Posidonia* is believed to be less efficient at reducing wave energy, however it remains effective at reducing sediment transport locally and, by inducing a preferential shoreward drift, at preventing sand dispersal offshor

Contents

Contents i

List of Figures v

List of Tables xv

DECLARATION OF AUTHORSHIP xix

Acknowledgements xxi

Definitions and Abbreviations xxiii

1 Chapter 1: Introduction 1

1.1 General context of the study 1

1.2 Justifications for this study 4

1.3 Objectives 6

1.4 Thesis outline 6

2 Chapter 2: Background information and literature review 9

2.1 Introduction 9

2.2 Wave propagation and dissipation in coastal waters 10

2.2.1 Wave propagation and energy dissipation 10

2.2.2 Wave orbital velocities 12

2.2.3 Wave boundary layers and roughness 13

2.2.4 Friction factors and stresses 16

2.3 Wave-induced forces and drag on submerged bodies 18

2.4 Posidonia oceanica seagrass 19

2.5 Submerged canopies and coastal dynamics 21

2.5.1 Effects of submerged canopies on wave energy 22

2.5.2 Effects of submerged canopies on the flow field 28

2.5.3 Effects of submerged canopies on turbulence 31

2.6 Seagrass, sediments and sediment dynamics 34

3 Chapter 3: Waves and flows in a natural *Posidonia oceanica* bed 37

3.1 Introduction 37

3.2 The field study site 39

3.2.1 Location 39

3.2.2 Hydrodynamics and winds in the Gulf of Oristano....40
3.2.3 Sediment transport and distribution of seagrass in the Gulf of Oristano....42
3.3 Field campaign....44
3.3.1 Boat survey and instrument description....44
3.3.2 Bottom sampling....46
3.3.3 Deployment of the Autonomous Benthic Landers....47
3.4 Data analysis....49
3.4.1 Survey and sampling....49
3.4.2 Hydrodynamic data and turbidity....52
3.5 Results and discussion....56
3.5.1 Survey and sampling....56
3.5.2 Hydrodynamic and turbidity....70
3.6 Concluding remarks....82
4 Chapter 4: Large-scale experiments on wave propagation over artificial *Posidonia oceanica* 87
4.1 Introduction....87
4.1.1 Waves in physical models and the advantages of full scale tests....88
4.2 Description of the experiments....90
4.2.1 The CIEM flume....90
4.2.2 Set-up of the flume....91
4.2.3 Artificial seagrass mimics and patch....92
4.2.4 Instrumentation....96
4.2.5 Sediment characteristics....105
4.2.6 Description and selection of the test conditions....106
4.2.7 Data acquisition....108
5 Chapter 5: The effects of artificial *Posidonia oceanica* on regular waves and flows....115
5.1 Introduction....115
5.2 Data Analysis: Regular wave tests....116
5.2.1 Wave data processing....116
5.2.2 Flow data processing....118
5.3 Results and discussion: Wave dissipation....121
5.3.1 Wave height decay....121
5.3.2 The drag coefficient....126
5.3.3 Wave friction factors and roughness length from wave energy dissipation....128
5.4 Results and discussion: Oscillatory velocities....131
5.4.1 Preliminary observations....131
5.4.2 The oscillatory velocity structure....133

5.4.3 The vertical structure of the oscillatory flow: Effects of submergence ratio, stem density and wave period. 136
5.4.4 The phase shift 139
5.4.5 The flow asymmetry 141
5.4.6 Changes induced by the canopy to the oscillatory flows: horizontal component 142
5.4.7 Changes induced by the canopy to the oscillatory flows: vertical component 148

5.5 Results and discussion: Turbulence 148
5.5.1 Turbulence intensities and turbulent kinetic energy 148
5.5.2 Reynolds stresses and shear coefficient at the canopy top 153

5.6 Concluding remarks 157

6 Chapter 6: Effects of artificial *Posidonia oceanica* on spectral waves and flows 161

6.1 Introduction 161

6.2 Data Analysis: Irregular wave tests 162
6.2.1 Wave data 162
6.2.2 Velocity data 164

6.3 Results and discussion: Waves and spectral wave dissipation 167
6.3.1 Preliminary observations 167
6.3.2 Frequency-dependent wave dissipation 168
6.3.3 Wave Height decay along the patch 171
6.3.4 The drag coefficient 174
6.3.5 Wave dissipation factors and roughness 176

6.4 Results and discussion: Spectral wave-induced velocities 177
6.4.1 Frequency-dependent flow dissipation in the lower canopy 177
6.4.2 Representative wave-induced velocities and attenuation coefficient 181

6.5 Concluding remarks 186

7 Chapter 7: General Discussion and Conclusions 189

7.1 General discussion 189
7.1.1 Effects of *Posidonia oceanica* canopies on flows 189
7.1.2 Effects of *Posidonia oceanica* canopies on wave dissipation and seabed roughness 191
7.1.3 Processes and boundary layer structure in *Posidonia oceanica* canopies 195
7.1.4 The edge effect 200
7.1.5 The effect of stem density on waves and flow changes 201
7.1.6 The effect of submergence ratio on waves and flow changes 201
7.1.7 Limitations of seagrass mimics 202
7.1.8 Implications for sediment transport 203

7.2 Conclusions 205

7.3 Future work 206

APPENDIX A : Field data 209

APPENDIX B: Design of *Posidonia oceanica* mimics 217

B.1 Introduction 217

B.2 Characteristics of Posidonia oceanica meadows 217

B.3 Mimic selection 219

B.3.1 Preliminary tests 219

B.3.2 Mimic options 221

B.3.3 Velocity profile experiments. 222

B.3.4 Final mimic canopy design 226

APPENDIX C: Laboratory data 227

APPENDIX D : Publications and Reports 233

Literature cited 279

List of Figures

Figure 1.1 Posidonia oceanica seagrass beds, (photo courtesy of Ante Zuljevich). _____ *2*

Figure 2.1 Wave orbital motion at different relative depths, and wave orbital amplitude A (adapted from Dean and Dalrymple, 1991). _____ *12*

Figure 2.2 Wave-induced flows under a progressive non-breaking wave A (adapted from Dean and Dalrymple, 1991). _____ *13*

Figure 2.3 Measurements of oscillatory velocity u(z,t) as a function of distance from the bed, at different phases of the wave (modified from Nielsen, 1992). _____ *14*

Figure 2.4 Wave boundary layer thickness definitions A) Jonsson definition (δ_j) and Jensen et al. (δ_{JSF}) from normalised vertical velocity profile. B) Sleath's definition from the velocity defect (δ_S), (modified from Sana and Tanaka [2007]). _____ *16*

Figure 2.5 Posidonia oceanica: A) Morphology of the plants, [modified from Borum et al., 2004] B) Photograph of a Posidonia plant established on 'matte' (Gulf of Oristano, Sardinia, Italy). _____ *20*

Figure 2.6 Distribution of mean horizontal (U), mean vertical velocity (W) , Turbulent kinetic energy (TKE) and Reynolds stresses (τ_{xyz}), with distance inside and above a vegetation canopy, under unidirectional flows. The canopy was made of saltmarsh plants (Spartina sp) with a canopy height 24.5 cm in 42 cm water depth and with an undisturbed U of 6.8 cm/s [from flume studies by Neumeier, 2007] _____ *28*

Figure 2.7 Modelled oscillatory flow reduction parameter (α_w) as a function of the rms wave orbital amplitude (A) divided by the element spacing (S) for different roughness configurations (represented by S/d, where d is the element diameter). The parameter α_w is defined as the ratio between the in-canopy depth averaged rms oscillatory flow and the free stream potential flow. The model was validated with rigid cylinders in-canopy flow [from Lowe et al., 2005b]. _____ *30*

Figure 3.1 Location of the study region in the Gulf of Oristano, Sardinia, Italy. [The background chart was adapted from that of the Istituto-Idrografico-della-Marina, 1985] _____ *39*

Figure 3.2 A) Sectors of fetch from the wave rider buoy of Alghero. B) Annual wave regime for the west coast of Sardinia. Directions of propagation and frequency (%) of significant waves recorded by the RON-Alghero are shown. [Franco et al., 2004]. _____ *41*

Figure 3.3 Swan model output of Mistral waves with a return period of 1 year (10 s peak wave period, 108˚ peak wave direction and 8 m significant wave height) propagating inside the Gulf of Oristano. Arrows indicate wave direction and wave height contours are shown in shaded areas [adapted from De Falco et al., 2008] _____ *42*

Figure 3.4 Distribution of Posidonia meadows in the northern sector of the Gulf of Oristano and in the study region. (De Falco et al., 2006) _____ *43*

Figure 3.5 Location of the survey lines, sampling and instrument deployment sites. Background satellite image from Google Earth-2007. _____ *45*

Figure 3.6 The standard 50 x 50 cm quadrat [Duarte et al., 2001] used for seagrass density measurements. Note: the edges of the quadrat were straight, but are distorted slightly here by the camera lens. _____ *46*

Figure 3.7 Photographs taken at the deployment sites.: (A) Site V1, Posidonia oceanica uprooted plants and debris;(B) Site V2: ABL at meadow edge in the background the edge of the seagrass meadow, with a 20 cm thick matte. Note: the seabed was sandy with some seagrass debris; and (C) Site V3, Posidonia oceanica plants with orange incrusting sponge at its base. 48
Figure 3.8 Diagram of an ABL used during the field campaign [modified from Plomaritis, 2006]. 48
Figure 3.9 Example of the results obtained after filtering of the flow data for the separation of the current and wave component of flow (V1, burst 35). (A) North component of the flow and (B) East component of the flow. 54
Figure 3.10 A graph showing the methods used for the calculation of wave direction, wave orbital velocity (under the trough and under the crest) from the wave-induced components of the flow. 55
Figure 3.11 Bathymetry of the study area. The positions of the ABL deployment sites are shown as triangles. 57
Figure 3.12 Posidonia shoot density plotted against distance from the shoreline, along the instrumented transect. Note: bars of the density measurements are 1 standard deviation. The locations of the ABLs are also indicated. 58
Figure 3.13 Posidonia average leaf length plotted against distance from the shoreline, along the instrumented transect. Note: bars of the length measurements are 1 standard deviation. The locations of the ABLs are also indicated. 58
Figure 3.14 A detail of the canopy height map from the SIS survey: A description of the seabed type, from the observations made by divers, is also shown. 60
Figure 3.15 Canopy height distribution in the study area. 61
Figure 3.16 Frequency distribution of the canopy height obtained from the SIS survey. The vertical blue lines indicate the breaks used for the division in classes of canopy height, used in the canopy distribution maps (Figure 3.14 and Figure 3.15). The division into the 3 classes of Figure 3.17 is also indicated. 62
Figure 3.17 Seabed classification and depth contours of the study area. In the legend CH stands for canopy height. The locations of the ABL stations are indicated. 63
Figure 3.18 Map of the sand grain-size distribution [classified according to the scale of Wentworth, 1922]. A seabed description from the diver surveys is also shown. 66
Figure 3.19 Map of the sand sorting (Folk classification,1974). The seabed description from the diver surveys is also shown. 67
Figure 3.20 Map of the organic content of the seabed sediment. The seabed description from the diver surveys is also shown. 68
Figure 3.21 Map of the mud/sand ratio of the seabed sediment. The seabed description from the diver surveys is also shown. 69
Figure 3.22 Time-series of wind and hydrodynamics. A) Wind speed and direction (model data source: www.windfinder.com, measured data source: Capo Frasca Air Force Base), offshore; B) offshore wave period [at Alghero wave buoy. Source: APAT, 2006] and wave period at the study site; C) offshore wave height and direction [source: APAT, 2006]; D) wave height and direction in the study site; E) currents speed and direction of flow; and F) water depth. 70

Figure 3.23 A) Unidirectional currents (U_m) at sites V3; B) unidirectional currents at sites V2; and C) Unidirectional currents at sites V1. Please note that the range of the vertical axis in the plot A is different than in plots B and C. The vertical yellow bar indicates the start of the SW wind event. The vertical blue bars indicate the start of the mistral event. _____ *73*

Figure 3.24 A)Wave height and direction at the deployment sites; B) orbital velocities under the crest (U_{max}); and C) orbital velocity under the trough (U_{min}). _____ *73*

Figure 3.25 Changes in orbital velocities between Stations V3 and V2 ($U^{V2}_{max}/U^{V3}_{max}$) plotted against the wave orbital amplitude (A). _____ *75*

Figure 3.26 A) Spectral de-shoaled wave heights (H_{m0}) at sites V3, V2 and V1; B) peak wave period (T_p); and C) wave energy flux (P). _____ *77*

Figure 3.27 Wave height variation between the vegetated site (V3) and the site at the edge of the seagrass meadow (V2). Regression lines were plotted with their corresponding correlation coefficients and confidence intervals (95%) for Mistral event and low energy conditions. _____ *78*

Figure 3.28 Wave energy dissipation factors plotted against the wave orbital amplitude. _____ *79*

Figure 3.29 A) Average relative turbidity time-series at V1; B) critical bed shear stress for the sand at V1, compared to the bed shear stress modelled from the measured Umax at V1 Bed shear stress was calculated using Soulsby's (1997) and Nielsen's (1992) methods ; and C) wave-induced velocity (U_{max}) and unidirectional component (U_m) at V1. _____ *81*

Figure 3.30 As Figure 3.29, for all parameters measured or calculated at V2. _____ *82*

Figure 3.31 A) As Figure 3.29, for all parameters measured or calculated at V3. _____ *82*

Figure 4.1 The CIEM wave generator (Photo courtesy LIM/UPC) _____ *91*

Figure 4.2. Cross-section of the profile in the CIEM flume at the start of experiments. _____ *91*

Figure 4.3 Schematic diagram of the artificial seagrass patch used in the experimental set-up [from Stratigaki et al., 2009b]. _____ *92*

Figure 4.4 A) Detail of the canopy during construction of a seagrass patch; and B) A sketch of the geometry of the artificial Posidonia oceanica canopy. _____ *95*

Figure 4.5 Posidonia oceanica mimics seen from the side window of the CIEM flume. The "whip-like" motion of the mimics under waves is apparent. _____ *95*

Figure 4.6 Overview of the patch and the instrument layout within the CIEM flume (looking towards the wave paddle). Wave gauges and velocimeters are secured to the sidewall. _____ *96*

Figure 4.7 The velocimeter array located in front of the leading edge of the patch. _____ *100*

Figure 4.8 Location of an OBS within the mimic canopy. _____ *103*

Figure 4.9 Sketch of the mechanical bed profiler [From LIM/UPC, 2010]. _____ *104*

Figure 4.10 Submerged and emerged beach profile at the start and end of tests with 180 stems/m^2. Z is the depth referred to as Z0 defined in Figure 4.9. X is the horizontal distance from the wave paddle at rest. (adapted from the profile data analysis by LIM/UPC provided during the experiments). The location of the sand bar depended upon water depth is evident, whilst the profile slope was practically constant. _ *105*

Figure 4.11 Grain-size statistical parameters of the sand used in these experiments (provided by LIM/UPC) _____ *105*

Figure 4.12 The Jonswap spectrum and the Pierson-Moskowitz spectrum for fully-developed seas. The peak enhancement factor (γ) is indicated and it is defined as the ratio between a peak spectrum and a peak spectrum of the Pierson-Moskowitz spectrum. _____ *106*
Figure 4.13 Layout of the acoustic and resistance wave gauges and location of the velocity profiles in the wave flume. The beach at the opposite end of the wave paddle had a profile slope of 1:15. _____ *110*
Figure 4.14. Layout of the OBS, ADV and electro-magnetic current-meters. Detail of the leading edge of the patch is shown. _____ *111*
Figure 5.1 A) Example of water surface elevation time series (raw data); and B) Detail from previous plot (A). _____ *117*
Figure 5.2 A) Example of ADV raw data; and B) Detail of A. _____ *119*
Figure 5.3 A) Example of EMCM raw data; and B) Detail of A _____ *119*
Figure 5.4 Example of the method of computation of the wave-induced flow from a measured velocity times series. In green are the de-meaned ensemble horizontal velocity values, corresponding to each wave. The red line is the ensemble averaged <U>. U_{max} corresponding to the peak value of <U>and U_{min}, the minimum value of <U>, are also indicated. _____ *120*
Figure 5.5 Example of wave height decay (Test 33, see Table 5-1). The measured and modelled wave height decay are plotted versus distance. The leading edge of the patch is located at x=0. Red lines and symbols indicate the data measured at the patch, whilst the blue line and symbols represent the data measured in front of the leading edge of the patch (indicated in the legend as pre-patch). _____ *126*
Figure 5.6 Drag coefficients plotted against the Reynolds vegetation number (blue symbols) and the best-fit (blue line, Eq. 5-18). The data are compared with the relationship found in previous studies [Kobayashi et al., 1993; Mendez et al., 1999; Bradley and Houser, 2009]. The data point circled in red was excluded from data analysis as it was considered to be an outlier (the residual was more than 3 times larger than the root mean square error of the fit). _____ *127*
Figure 5.7 Drag coefficients plotted against the Keulegan-Carpenter number (blue symbols) and the best fit (blue line). The data are compared with the relationship found in Mendez and Losada (2004). Two data points were considered to be outliers and excluded from the analysis (indicated by a black circle) because the absolute value of their residuals was more than 3 times greater than the RMSE (root mean square error of the residuals). _____ *128*
Figure 5.8 Friction factors plotted against the wave orbital amplitude for the two stem densities. The red dashed line shows the curve obtained setting r=0.15 m to the Nielsen [1992] formula; whilst the black solid line shows the same curve with r=0.23 m. Data from regular wave test having wave height exponential decay fit R^2>0.60 are shown. _____ *130*
Figure 5.9 Friction factors plotted against the wave orbital amplitude for the two stem densities. The red dashed line shows the curve obtained setting r=0.15 m to Nielsen (1992) formula; whilst the black solid line shows the same curve with r=0.23 m. Data from all regular wave tests. Four data points were considered to be outliers and excluded from the analysis (indicated by a blue circle), because the absolute value of their residuals was more than 3 times greater than the RMSE. _____ *130*
Figure 5.10 U_{max} measured at all elevations at x/L=-0.07 plotted against the predicted value obtained using linear theory (red symbols) and Stoke's second-order theory (black circles). _____ *132*

Figure 5.11 Measured <U> (ωt, z), and <W>(ωt, z) U∞(ωt) for Test 31 (see Table 5-1) at X/L=-0.07 in front of the patch (A); at the patch near the leading edge x/L=0.17 (B) and x/L=0.80, at the patch further shoreward (C). 133

Figure 5.12 The variation of <U> with relative height at different wave phases (x/L=-0.07 in plot A, x/L=0.17 in plot B and x/L=0.80 in plot C). Plot D shows the measured water surface oscillation. The symbols indicate the surface elevation at the wave phase for the velocities profiles in plots A-C: Test 19 (T_p=2 s, H_o=0.36 m, h_s/D=0.37 and 360 stems/m^2). 134

Figure 5.13 The panels correspond to Figure 5.12:Test 24 (T_p=4 s, H_o=0.35 m, h_s/D=0.37 and 360 stems/m^2). 135

Figure 5.14 The panels correspond to Figure 5.12: Test 23 (T_p=3 s, H_o=0.36 m, h_s/D=0.37 and 360 stems/m^2). 135

Figure 5.15 See above: Test 68: (T_p=3 s, H_o=0.35 m, h_s/D=0.37 and 180 stems/m^2). 136

Figure 5.16 Effect of stem density on the vertical structure of U_{max}, (T_p=4s h_s/D=0.42) A) in front of the leading edge of the patch (x/L=-0.07); B) near the edge (x/L=0.17); and C) in the patch (x/L=0.80) (T_p=4 s, H_0=0.41±0.007 m and h_s/D=0.42) 137

Figure 5.17 Effect of stem density on the vertical structure of W_{max}. A) in front of the leading edge of the patch (x/L=-0.07); B) near the edge (x/L=0.17); and C) in the patch (x/L=0.80) (T_p=4 s, H_0=0.41±0.007 m and h_s/D=0.42) 137

Figure 5.18 Effect of submergence ratio (h_s/D) on the vertical structure of $U_{max.}$,: A) in front of the leading edge of the patch (x/L=-0.07); B) near the edge (x/L=0.17); and C) in the patch (x/L=0.80) (T_p=2 s, H_0=0.37±0.017 m and density 180 stems/m^2) 138

Figure 5.19 Effect of submergence ratio (h_s/D) on the vertical structure of W_{max}.: A) in front of the leading edge of the patch (x/L=-0.07); B) near the edge (x/L=0.17); and C) in the patch (x/L=0.80). (T_p=2 s, H_0=0.37±0.017 m and density 180 stems/m^2) 138

Figure 5.20 Effect of period on the vertical structure of U_{max}: A) in front of the leading edge of the patch (x/L=-0.07); B) near the edge (x/L=0.17); and C) in the patch (x/L=0.80) (T_p=4 s h_s/D=0.42) (density 180 stem/m^2, H_0=0.39±0.013 m and h_s/D=0.42) 139

Figure 5.21 Effect of period on the vertical structure of W_{max}: A) in front of the leading edge of the patch (x/L=-0.07); B) near the edge (x/L=0.17); and C) in the patch (x/L=0.80) (density 180 stem/m^2, H0=0.39±0.013 m and h_s/D=0.42) 139

Figure 5.22 Phase lag between the passage of the wave crest and the maximum velocity plotted against A (wave orbital amplitude), for tests having 360 stems/m^2. Plots A-D shown the data measured at various elevations from the bed, at the three x/L locations. 140

Figure 5.23 Phase lag between the passage of the wave crest and the maximum velocity plotted against A (wave orbital amplitude), for tests having 180 stems/m^2. . Plots A-D shown the data measured at various elevations from the bed, at the three x/L locations. 140

Figure 5.24 Stokes asymmetry (R) plotted against Ursell number at different elevation above the bed (plots A-D) (tests having 360 stems/m^2). 142

Figure 5.25 Variation in flow attenuation coefficient (α), with A, at 4 elevations above the bed for the tests with 360 stems/m^2, at x/L=0.17 (plot A) measurements at x/L=0.80 (plot B). 143

Figure 5.26 Variation in the flow attenuation coefficient (α), with A, at 4 elevations above the bed for the tests with 180 stems/m^2 at x/L=0.17 (plot A) measurements at x/L=0.80 (plot B). 144
Figure 5.27 Analysis of fit of the flow attenuation coefficient (α) measured in the lower canopy, to the exponential model (z/h_s=0.36), for tests with 360 stems/m^2 at x/L=0.17 (A) and at x/L=0.80 (B). The 95% confidence bounds are indicated by the dotted lines. 146
Figure 5.28 Analysis of fit of the flow attenuation coefficient (α) measured in the lower canopy, to the exponential model (z/h_s=0.36), for tests with 180 stems/m^2 at x/L=0.17 (A) and at x/L=0.80 (B). The 95% confidence bounds are indicated by the dotted lines. 147
Figure 5.29 Plots of the vertical profiles of horizontal (A) and vertical (B) wave-induced velocities and of horizontal (C) and vertical (D) turbulence. In each plot, the red dots represents measurements at x/L=-0.07; blue stars at x/L=0.17 and green squares at x/L=0.80. Test with T_p=2 s, H_0=0.38 m, density 360 stems/m^2 and h_s/D=0.42. 149
Figure 5.30 Plots of the vertical profiles of horizontal (A) and vertical (B) wave-induced velocities and of horizontal (C) and vertical (D) turbulence. In each plot , the red dots represents measurements at x/L=-0.07; blue stars at x/L=0.17 and green squares at x/L=0.80. Test with T_p=4 s, H_0=0.42 m, density 360 stems/m^2 and h_s/D=0.42. 149
Figure 5.31 Normalised values of turbulent kinetic energy (α_{TKE}) at various elevations (plots A-D) and at two x/L locations (represented by different symbols). Tests with 360 stems/m^2. 151
Figure 5.32 Normalised values of turbulent kinetic energy (α_{TKE}) at various elevations (plots A-D) and at two x/L locations (represented by different symbols). Tests with 180 stems/m^2. 151
Figure 5.33 Normalised values of turbulent kinetic energy (α_{TKE}) at various elevations (plots A-D) plotted for tests with different submergence ratios Different symbols represent the two x/L locations. Tests with 360 stems/m^2, T_p=4 s and H_0=0.45±0.02 m. 152
Figure 5.34 Normalised values of turbulent kinetic energy (α_{TKE}) at various elevations (plots A-D) plotted for tests with different submergence ratios Different symbols represent the two x/L locations. Tests with 360 stems/m^2, T_p=2 s and H_0=0.39±0.03 m. 152
Figure 5.35 Bi-dimensional turbulence stresses <U'W'> (A), <U'U'> (B) and <W'W'> (C), as a function of wave phase at x/L=0.80. Test 31 (T_p=3 s, H_0=0.43 m, h_s/D=0.42 and density =360 stems/m^2). 154
Figure 5.36 Vertical profiles of maximum phase-averaged shear stress, at different locations along the flume (tests with 360 stems/m^2; h_s/D=0.42) at x/L=-0.07 (A); at x/L=0.17 (B); and at x/L=0.80. Note: the different scales on the x axis . 155
Figure 6.1 Power spectra of the raw velocity data at all four relative elevations (h_s/D) from the bed (A-D). The analysis concentrated upon the most energetic component of the velocity spectra (between the vertical lines). 165
Figure 6.2 Spectral densities plotted as a function of wave frequency. The wave spectra (A) compared to the spectra of the wave-induced velocity (B) and the spectra of the turbulent component (C). Note: different scales of the vertical axes) for test 44 at x/L=-0.07 (Tp= 3.7 s, H_0=0.30 m, h_s/D=0.50 and 360 stems/m^2). Different colours represent spectral densities at different elevations above the bed. 166

Figure 6.3 (A) Wave energy density spectra at x/L=-0.07 (in front of the patch), x/L=0.17 (over the patch, near the edge) and x/L=0.80 (over the patch). (B) The difference in the frequency-dependent wave energy dissipation factor ($f_{e,j}$) calculated between sites x/L=-0.07 and x/L=0.17 (blue squares) and between sites x/L=0.17 and x/L=0.80, (green diamonds), plotted at each component of the spectra. Test 42 (T_p=1.98 s, H_0=0.22 m, h_s/D=0.50 and 360 stems/m^2) _____ *169*

Figure 6.4 As for Figure 6.3; Test 43 (T_p= 3.2 s, H_0=0.33 m, h_s/D=0.50 and 360 stems/m^2) _____ *170*

Figure 6.5 As for Figure 6.3; Test 44 (T_p= 3.7 s, H_0=0.30 m, h_s/D=0.50 and 360 stems/m^2) _____ *170*

Figure 6.6: Effect of submergence ratio (h_s/D) on wave height decay along the seagrass patch. Tests 16, 26 and 43 (T_p=3.2 s, density 360 plants/m^2 and H_0=0.33±0.01 m). _____ *171*

Figure 6.7: Effect of stem density on wave height decay along the seagrass patch. Tests 44 (H_0 =0.30 m, T_p=3.7 s and h_s/D=0.5) and test 90 (H_0=0.28 m, T_p=3.7 s and h_s/D=0.5). _____ *172*

Figure 6.8 Effect of submergence ratio (h_s/D) and stem density on the wave height decay coefficient (k_j), for density=360 stems/m^2 (blue symbols) and density=180 stems/m^2 (red symbols). Different symbol types represent different spectral wave conditions. _____ *173*

Figure 6.9 Drag coefficients plotted against the Reynolds vegetation number (Re_v): representative drag coefficient ($C_{d,r}$) from spectral waves (blue squares); and drag coefficient (C_d) from regular waves (blue dots). The data are compared with the relationship found in the present study from regular waves (blue line) and with models, from previous studies [Kobayashi et al., 1993; Mendez et al., 1999; Bradley and Houser, 2009]. Note: the Bradley and Houser curve is an extrapolation for Re_v>800. _____ *175*

Figure 6.10 Representative drag coefficients for spectral waves plotted against the mean Keulegan-Carpenter number (KC) _____ *175*

Figure 6.11 Friction factors for regular and spectral waves plotted against A, for both stem densities. The models obtained by fitting Nielsen formula to regular wave data are also plotted: the dashed line is valid for tests with a stem density 360 stems/m^2 and had "best fit" when the hydraulic roughness (r) was 0.231 m. The solid line was valid for tests with a stem density 180 stems/m^2 with r=0.148 m _____ *176*

Figure 6.12 A) Spectra of the wave-induced flows measured in the lower canopy at the 3 locations along the flume; and B) the spectral attenuation parameter α_j (attenuation of flow at each frequency of the spectral component). The curves represent different locations along the flume. Test 26 (T_p=3.2 s, H_0=0.32 m, h_s/D=0.42 and 360 stems/m^2) _____ *178*

Figure 6.13 The spectral attenuation coefficient α_j in the lower canopy calculated for each wave period (T_j) of the wave-induced velocity spectral component for all 360 stems/m^2 tests (A) and 180 stems/m^2 tests (B). The red asterisks refer to the α_j values obtained at x/L=-0.07; the blue dots refer to the α_j values at x/L=0.17 and the green squares refer to the α_j values at x/L=0.80. _____ *179*

Figure 6.14 Effect of submergence ratio (h_s/D) on the spectral attenuation coefficient (α_j) , calculated for each wave period (T_j) of the wave-induced velocity spectra component. The data at the three locations along the flume are shown in each plot (A-C). Tests 16 (h_s/D=0.37 and H_0 =0.34 m), Test 26 (h_s/D=0.42 and H_0=0.32 m) and Test 43 (h_s/D=0.50 and H_0=0.33 m). All tests were carried out with density of 360 plants/m^2 and T_p=3.2 s. _____ *180*

Figure 6.15 Effect of plant density on the spectral attenuation coefficient (α_j), calculated for each wave period (T_j) of the wave-induced velocity spectral component. The data at the three x/L locations are

shown in each plot (A-C). Tests 44 and 90 with H_0 =0.30 m and H_0 =0.28 m respectively. Both test were carried out with h_s/D=0.50 and T_p=3.7 s. _____ 180

Figure 6.16 Vertical profiles of Ur (representative wave-induced horizontal velocity under spectral waves) for some typical tests with h_s/D=0.50. A) Tests 42 (T_p=1.98 s, H_0=0.22 m and 360 stems/m^2); B) Tests 88 (T_p=1.98 s, H_0=0.21 m and 180 stems/m^2); C) Tests 44 (T_p=3.7 s, H_0=0.30 m and 360 stems/m^2); D) Tests 90 (T_p=3.7 s, H_0=0.28 m and 180 stems/m^2). _____ 181

Figure 6.17 Attenuation parameter of representative velocities (α_r) plotted against the wave orbital amplitude for all tests with stem density 360 stems/m2. A) Data measured at x/L=0.17; and B) data measured at x/L=0.80. _____ 183

Figure 6.18 Attenuation parameter of representative velocities (α_r) plotted against the wave orbital amplitude for all tests with stem density 180 stems/m^2. A) Data measured at x/L=0.17 (inside the canopy near the edge); and B) data measured at x/L=0.80 (further inside the canopy)_____ 184

Figure 6.19 Lower canopy flow attenuation coefficient poltted with wave obital amplitude (A). Tests with 360 stems/m^2 at x/L=0.17 (A) and at x/L=0.80 (B). The fit to an exponential decay function is shown, for both irregular and regular waves (see Chapter 5). _____ 186

Figure 6.20 Lower canopy flow attenuation coefficient poltted with wave obital amplitude (A). Tests with 180 stems/m^2 at x/L=0.17 (A) and at x/L=0.80 (B). The fit to an exponential decay function is shown, for both irregular and regular waves (see Chapter 5). _____ 186

Figure 7.1 Relative bed roughness of an artificial Posidonia canopy compared to sandy beds under various wave conditions. Results from this study under the 2 tested plant densities and wave types (regular and irregular) are shown by the coloured symbols. The letters refer to different studies carried out in flumes with rippled or flat sandy beds (see Nielsen, 1992 and references therein). The range of r/A<0.08 corresponds to flat sandy beds with little sand movement; r/A>0.2 corresponds to rippled sandy beds (Nielsen, 1992). _____ 194

Figure 7.2 Conceptual model of the effect of an artificial Posidonia oceanica canopy on the benthic boundary layer under waves. See description in the text. _____ 197

List of Figures in Appendix

Figure A. 1 Calibration curve of the echosounder for the bathymetry survey (Significance level P=0.05). 209

Figure A. 2 Sand grainsize distribution curves at some representative locations in the field study site. Red curves are the cumulative distribution of grain-size.....211

Figure A. 3 A) Seabed type and grain size distribution in the study area. B) 4 3D maps of the seabed morphology and bathymetry contours in the study region.....213

Figure A. 7 A) Histogram of orbital velocity asymmetries (U_c+U_t) at V1; B) Histogram of orbital velocity asymmetries (U_c+U_t) at V2; C)Histogram of orbital velocity asymmetries (U_c+U_t) at V3. A positive asymmetry indicates a potential net shoreward drift.....215

Figure A. 8 A) Measured turbidity at V1, V2 and V3. B) Measured maximum orbital velocity (U_{max}) and critical orbital velocity for sediment motion at V1 C) Measured maximum orbital velocity (U_{max}) and

critical orbital velocity for sediment motion at V2 D) Measured maximum orbital velocity (U_{max}) and critical orbital velocity for sediment motion at V3. E) Measured mean current and threshold current for sediment motion at V1, V2 and V3. 216

Figure B. 1 A) Posidonia oceanica leaf morphology and classification: Old leaves have a stiff base: Intermediate leaves don't have a base and are longer than 5 cm: juvenile leaves are shorter than 5 cm Rhizome with scales (old sheaths) and leaf shoot (modified from Buia et al., 2003). B) Posidonia oceanica shoots. C) Posidonia oceanica plants. 218

Figure B. 2 Preliminary tests for the selection of the mimic plastic material. Plastic mimics and Posidonia oceanica seagrass shoots in the NOC flume. All mimics were made of 6 leaves and a common structure. The test shown was for a flow depth of 38cm and flow speed of 10 cm s^{-1}. 220

Figure B. 3 LDPE mimics. A: detail of the base, side view. B: Detail of the base, top view. C: Full size mimic..... 221

Figure B. 4 Posidonia oceanica patch in the NOC flume under a 10 cm/s unidirectional flow. 223

Figure B. 5 A) LDPE mimics (Option 1/LDPE), with uniform leaf length patch under a 10cm/s unidirectional flow. B) LDPE Modified mimics (Option 3/LDPE mod), with variable leaf length patch 224

Figure B. 6 Options 1 and 3, "FAST" flow conditions Plots of vertical velocity profiles obtained upstream (A) and downstream (B) of a real Posidonia patch (Seagrass), a mimic patch (LDPE =Option1 and LDPE mod =Option 3) and the board only (Board only). The yellow line refers to the maximum height of the leaf base, the blue line is the top level of the bent canopy and the black line indicates the height of the board that was holding the shoots in place. 224

Figure B. 7 A) PP regular length (Option 2/PP) under a 10 cm/s flow. B) PP variable length (Option 4/PP var) under a 10cm/s flow..... 225

Figure B. 8 Options 2 and Option 4 for "FAST" flow conditions. Plots of vertical velocity profiles obtained upstream (A) and downstream (B) of a real Posidonia patch (Posidonia), a PP mimic patch (PP corresponding to Option 2), a variable length PP patch (PP var, corresponding to Option 4) and the board only (Board only). The yellow line refers to the maximum height of the leaf base, the black line indicates the height of the board, the blue solid line is the top level of the bent canopy and the blue dashed line is the top of the bent PP canopy..... 225

Figure C. 1 Normalised horizontal orbital velocities ($U_{max}/U_{free,}$) in the lower canopy (z/h_S=0.36) plotted with wave orbital amplitude. Tests with 260 stems/m^2. Different colours correspond to different locations: in front of the patch (x/L=-0.07); within the patch near the leading edge (x/L=0.17) and further into the patch (x/L=0.80). The solid lines are the fit to an exponential decay function $\frac{U_{\max}}{U_{free}} = a\exp(bA)$*, with the coefficients a and b reported in Table C. 1 ..... 227*

Figure C. 2 Vertical component of the oscillatory flow. Variation of the vertical flow attenuation coefficient (α_W) with wave orbital amplitude (A) at 4 elevations above the bed for the tests with 360 stems/m^2 at x/L=0.17(plot A) and at x/L=0.80 (plot B)..... 228

Figure C. 3 Vertical component of the oscillatory flow. Variation of the vertical flow attenuation coefficient (α_W) with wave orbital amplitude (A) at 4 elevations above the bed for the tests with 180 stems/m^2 at x/L=0.17(plot A) and at x/L=0.80 (plot B)......229
Figure C. 4 Turbulent kinetic energy (TKE) at different elevations from the bed plotted against wave orbital amplitude (A-D). Symbols in each plot indicate different locations along the flume, (tests with 360 stems/m^2).....230
Figure C. 5 Turbulent kinetic energy (TKE) at different elevations from the bed plotted against wave orbital amplitude (A-D). Symbols in each plot indicate different locations along the flume, (tests with 180 stems/m^2).....230
Figure C. 6Shear stress coefficients (C_f) plotted with wave orbital amplitude (A) for both canopy densities tested. A) near the leading edge of the patch at x/L=0.17 B) and further into the patch at x/L=0.80.....231

List of Tables

Table 2-1 Wave parameters derived from linear and non-linear wave theory. *11*
Table 2-2 Wave height decay parameter (K_i), drag coefficient (C_d), wave dissipation factors (f_e), bed friction factors (f_w), and hydraulic roughness (r) from the literature. *27*
Table 3-1 Settings of the Sediment Imaging Sonar. *46*
Table 3-2 Autonomous Benthic Landers settings and location. *47*
Table 3-3 Sediment characteristics at the deployment sites. *64*
Table 3-4 Minimum, maximum and mean values of the orbital velocities (U_{max} and U_{min}) at V1, V2 and V3. ..... *74*
Table 3-5 Wave orbital velocities asymmetries (S.D. stands for standard deviation) *75*
Table 3-6 Mean and maximum wave Reynolds number calculated at the deployment sites. *76*
Table 3-7 Average and standard deviations of peak wave period (T_p) at three ABL stations, during different sea conditions. *76*
Table 3-8 Mean values and standard deviation of the wave dissipation factors between Stations V3 and V2 (f_e), calculated over low energy conditions; SW winds; the Mistral event and over the whole deployment period. *80*
Table 4-1 Properties of the PVC foam blades used in the construction of the mimics, compared with those of the natural Posidonia oceanica seagrass from the literature. *93*
Table 4-2 Specification of the sensors used in the laboratory experiments [data from LIM/UPC, 2010]. *97*
Table 4-3 Location of the resistive wave gauges: X is the distance along the flume from the wave paddle at rest; x is the distance from the leading edge of the seagrass patch, positive in the direction of wave travel. *98*
Table 4-4 Probe number, status and location of the acoustic wave gauges, where: X is the distance along the flume from the wave paddle at rest and x is the distance from the leading edge of the seagrass patch, positive in the direction of wave travel *99*
Table 4-5 List of ADV measuring devices and their position (X being the distance along the flume from the wave paddle at rest; and x is the distance from the leading edge of the seagrass patch, positive in the direction of wave travel). *101*
Table 4-6 Location and name of the optical backscatter sensors at the start of the experiments. *103*
Table 4-7 Predicted steepness and Ursell number for the programmed tests. Note: REG stands for regular waves and IRR for irregular wave type. *112*
Table 4-8 Predicted threshold of sand motion, friction factors and bed shear stress, using Nielsen [1992] and Soulsby and Clarke [2005] methods for the regular waves tests. A value of 1 for sand motion indicates that sediment motion is predicted. *113*
Table 4-9 List of the performed regular wave tests. Tests that were not analysed because of a corrupted raw file are indicated in red. *114*
Table 4-10 List of the performed irregular wave tests. Tests that were not analysed because of a corrupted raw file are indicated in red *114*

Table 5-1 Key wave parameters measured in front of the leading edge of the seagrass patch (x/L=-0.07) for all tests. L is the total length of the patch; x is the distance along the flume from the leading edge of the patch. All other symbols are listed in the abbreviations section. *123*

Table 5-2 Wave dissipation, drag and wave parameters calculated for all of the regular wave tests: Wave height at x/L=-0.046, R^2 coefficient for the wave decay exponential fit, decay coefficient (k_i). The table contains also values averaged along the patch of: drag coefficient (C_d), Reynolds vegetation number (Re_v), Keulegan-Carpenter number (KC), orbital amplitude above the canopy (A), wave Reynolds number (Re_w) and wave dissipation factor. The results above the bold line (associated with all of the tests having R^2>0.60) are considered to be more reliable. *125*

Table 5-3 Percentage flow reduction (horizontal component) in the lower canopy (z/h_s=0.36). Average values (mean) and standard deviations (S.D.) amongst the tests with two different densities are indicated. *145*

Table 5-4 Flow reduction as a function of A in the lower canopy (z/hs=0.36) for regular waves. The a and b coefficients of the fits to Eq. 5-25 are indicated, as well as their confidence limits (calculated as twice the standard error, with 95% level of confidence) and the correlation coefficient (R^2). *147*

Table 5-5 Percentage flow reduction (vertical component) in the lower canopy (z/h_s=0.36). Average values (Mean) and standard deviations (SD) between the tests with two different densities, are indicated. *148*

Table 5-6 Normalised shear stress and shear stress coefficient at the top of the canopy (z/h_s=1.09), at x/L=0.17 and x/L=0.80 for each test *156*

Table 6-1 Cut-off frequencies (f_{cut}) used in the wave and current data filtering *162*

Table 6-2 Wave parameters and vertically-averaged representative horizontal orbital velocity (Ur) measured at x/l=-0.07 for all spectral wave tests. *168*

Table 6-3 Spectral wave dissipation, drag and wave parameters calculated for all irregular wave tests: wave height at x/L=-0.046; R^2 coefficient for the wave decay exponential fit; decay coefficient (k_i), representative drag coefficient ($C_{d,r}$); Reynolds vegetation number (Re_v); Keulegan-Carpenter number (KC); orbital amplitude above the canopy (A);wave Reynolds number (Re_w); and wave dissipation factor($f_{e,r}$). *173*

Table 6-4 Hydraulic roughness (r) from the Nielsen (1992) formula for spectral wave tests. Mean value and standard deviation (S.D.) for tests with 360 and 180 stems/m^2 are indicated. *177*

Table 6-5 Flow reduction as a function of A in the lower canopy (z/hs=0.36) for both irregular and regular waves. The a and b coefficients of the fits to Eq. 5-25 (exponential decay curve) are indicated, as well as their confidence limits (calculated as twice the standard error, with 95% level of confidence) and the correlation coefficient (R^2). *185*

Table 7-1 A summary of the main parameters obtained from tests with large and small orbital amplitude waves (tests with 360 stems/m^2 , under regular and irregular waves.) The reported parameters related to orbital velocity and turbulence, correspond to measurements made at x/L=0.80 (8 m shoreward of the leading edge of the canopy). A positive value of the phase shift indicates that U_{max} occurs before the passage of the wave crests. A negative value of orbital velocity reduction indicates flow increase *196*

List of Tables in Appendix

Table A. 1 Descriptions of Posidonia oceanica shoots and location of the samples in UTM coordinates (WGS 84 datum) and distance from the shoreline..... 210

Table B. 1 Shallow Posidonia oceanica plants and meadow characteristics. The measured data refer to samples collected during the field campaign in May 2007 described in Chapter 3..... 219
Table B. 2 Plastic materials used in preliminary tests..... 220
Table B. 3 Mimic design options and characteristics of the options further tested..... 222

DECLARATION OF AUTHORSHIP

I, Eleonora Manca

declare that the thesis entitled

Effects of *Posidonia oceanica* seagrass on nearshore waves and wave-induced flows

and the work presented in the thesis are both my own, and have been generated by me as the result of my own original research. I confirm that:

this work was done wholly or mainly while in candidature for a research degree at this University;
where any part of this thesis has previously been submitted for a degree or any other qualification at this University or any other institution, this has been clearly stated;
where I have consulted the published work of others, this is always clearly attributed;
where I have quoted from the work of others, the source is always given. With the exception of such quotations, this thesis is entirely my own work;
I have acknowledged all main sources of help;
where the thesis is based on work done by myself jointly with others, I have made clear exactly what was done by others and what I have contributed myself;
parts of this work have been published as:

Manca, E., V. Stratigaki, and P. Prinos (2010), Large scale experiments on spectral wave propagation over Posidonia oceanica seagrass 6th International Symposium on Environmental Hydraulics 463-468, Taylor & Francis Group, Athens, Greece, 23–25 June 2010.

Stratigaki, V., E. Manca, P. Prinos, I. Losada, J. Lara, M. Sclavo, C. L. Amos, I. Caceres, and A. Sanchez-Arcilla (accepted), Large scale experiments on wave propagation over *Posidonia oceanica*, Journal of Hydraulic Research.

Prinos, P., Stratigaki, V., Manca, E., Losada, I., Lara, J., Sclavo, M., Caceres, I. and Sanchez-Arcilla, A., 2010. Wave propagation over *Posidonia oceanica*: Large scale experiments. In: J. Grune and M.K. Bretler (Eds.), HYDRALAB 3 Joint User Meeting. FZK Coastal Research Centre, University Hannover & Technical University Braunschweig Hannover, Germany, 57-60.

Stratigaki, V., Manca, E. and Prinos, P., 2009. Effects of Posidonia oceanica meadow on wave propagation: Large scale experiments, 4th SCACR International Short Conference on Applied Coastal Research, Barcelona, Spain.

Stratigaki, V., Manca, E., Prinos, P., Losada, I., Lara, J., Sclavo, M., Caceres, I. and Sanchez-Arcilla, A., 2009. Large scale experiments on wave propagation over *Posidonia oceanica*, 33rd IAHR Congress: Water Engineering for a Sustainable Environment. International Association of Hydraulic Engineering & Research Vancouver, Canada, 2878-2885.

Manca, E., V. Stratigaki, I. Caceres, and P. Prinos (2009), Wave Propagation Over Posidonia Oceanica: Report on the experiments, 17 pp, Universitat politecnica de Catalunya, Barcelona (Spain).

Signed: ……..

Date:…….

Acknowledgements

The author was sponsored by the Master And Back Program of the Regione Autonoma della Sardegna. Experiments in the CIEM Flume were funded by the European project Hydralab III (022441-RII3), within the 6th Framework Program. The author is grateful for this support.

Special thanks go to my supervisors Prof. Carl L. Amos, Prof. Ian Townend and Dr. Charlotte Thompson, for their precious comments and support throughout my PhD (and the much needed Turkish coffees). I am truly grateful to Prof. Mike Collins and Prof. Tom Spencer for the time they dedicated to reading and examining this thesis. I take this chance to thank also Prof. Vincenzo Pascucci from Universita' degli Studi di Sassari, for his patience and understanding during the last months of writing. I am grateful to Dr Simone Simeone, Dr Gianni De Falco, Dr Angelo Perilli and Dr Andrea Cucco from IAMC Oristano for their technical support during the field campaign in Sardinia. I would also like to thank Prof. Georg Umgiesser and Maike Paul for their contribution to the data collection in the field. I am grateful to Prof. Panayotis Prinos and the HYDRALAB program organisers, for giving me the opportunity of participating and contributing to the CIEM flume experiments. This, probably, would not have happened if my friends Monique and Dimitris did not mentioned my name at a conference! For this reason (and also for the fun) I wish to thank them. Also thanks to Vicky Stratigaki for sharing the flume-fun and the (less fun) experiment aftermath! I treasure the suggestions of Prof. Peter Nielsen and Prof. Peter Frigaard and I'm truly grateful to them. I am really thankful to Prof. Agustín Sánchez-Arcilla, Dr Daniel Gonzales, and to Prof. Xavier Gironella for the support offered during my stay at the Department of Hydraulic Engineering of Universitat Politecnica De Catalunya. I wish to thank, in particular, the staff of LIM and the PhD students, that contributed to the experimental set-up in the CIEM flume; for their patience and the hard work in building the 7200 much detested *Posidonia* mimics (and the 7200 holes). Without this assistance a crucial part of this research would be missing. Moltes gracies to Joaquim Sospedra for the fine waves and to Oscar and Ricardo for the fine music. I am particularly grateful to Dr. Ivan Cáceres and Dr Jose Alsina, not only for the massive help and the great tips on data-processing, but also for their hospitality, the networking chances and our interesting lunch discussions. A big thanks to the friends/family that assisted me (also) in the field

work (Stefano, Nadia, Rita, Mimmo, zio Franco, Piero, Teresa e Alex) and to the little muse Cleo, for inspiring me smiles and laughter.

A “bery bery” special thank indeed to my friends in Southampton, who shared with me the fun, the cakes, the parties, the difficulties, the bad food, the stress, the disappointments, the weather, the anger, the desperation, the final pain, and also the moments of hope, happiness, soberness, and glory (?) of these PhD years…A very wise woman and nobel prize scientist once say “Above all don’t fear difficulties, the best comes from them” (Rita Levi Montalcini, 1909-). We should make sure that we will share some of the best also in the future.

Grazie also to Ari, Ire, Alessia, Flower and Ve’, which also were close to me on this PhD rollercoaster, comforting me/laughing at me (remotely). I will always be grateful to my family because they never stopped supporting, stimulating and encouraging me,

And finally a particular massive thanks to Alex, my inspiration and strength, for your constant support, for putting up with me even during these outrageous end-of-PhD days, for the British comedies, the adventures in the wild and under the Sea, and above all for your love and for believing (and persuading me) that the “acknowledgements moment” will certainly arrive one day.

Definitions and Abbreviations

a Wave amplitude (1/2 wave height)

b Average width of seagrass leaf

d Diameter of canopy element

d_m Mean grain size

d_{50} Median grain size

f_e Wave dissipation factor

$f_{e,r}$ Representative wave dissipation factor for random waves (at the peak frequency)

$f_{e,j}$ Spectral wave dissipation factor for random waves (at the each wave frequency)

f_w Wave friction factor at the bed

g Constant of gravity

h_s Seagrass canopy height

j Frequency component

k Wave number

l Thickness of the leaves or mimic blades.

r Hydraulic roughness, as defined in [Nielsen, 1992]

t Time

x Horizontal coordinate measured from the leading edge of the artificial seagrass patch

y Lateral coordinate

z Vertical elevation from the bed

z_1 Roughness length under waves

w_s Settling velocity of sand

A Wave orbital amplitude

ABL Autonomous benthic lander

ADV Acoustic Doppler velocimeter

AWG Acoustic wave gauge

C Wave celerity

Cg Wave group celerity

CBL Canopy boundary layer

CIEM Large wave flume facility at Universitat Politecnica de Catalunya

D(z,t) Velocity defect function

D Water depth

D^* Dimensionless grain size

E Wave energy density

E Modulus of elasticity

EMCM Electro -Magnetic Current Meter

F_d Drag force

F_i Inertia force

H Wave height

H_0 Wave height in front of the leading edge of the seagrass patch

H_T Target wave height

IRR Irregular wave test

K_i Exponential wave height decay coefficient over artificial seagrass

K_b Exponential wave height decay coefficient over sand

KC Keulegan-Carpenter number

L Total length of the artificial seagrass patch

N Number of stems/m^2

NOC National Oceanography Centre

OBS Optical backscatter sensor

P Wave energy flux

R Stokes flow asymmetry parameter

REG Regular wave test

SIS Sediment Imaging Sonar

S_j Wave spectra

SU_j Wave-induced velocity spectra

T Wave period

TKE Turbulent kinetic energy (in the xz plane)

TKE_t Total turbulent energy

T_p Peak wave period

T_j Period of the j^{th} component of the wave spectra

<U > Ensemble averaged velocity (horizontal component)

<U'> Ensemble averaged turbulence (horizontal component)

<U'W'>; <W'W'>;<U'U'>; Bi-dimensional component of the Reynolds stresses

U De-meaned orbital velocity (U_{inst}-U_m)

U_c Characteristic orbital velocity, at the top of the canopy (as defined in Mendez et al., 1999)

U_{free} Free-stream orbital velocity (Stokes theory)

U_{inst} Instantaneous flow velocity (horizontal component)

U_m Mean horizontal component of flow

U_{max} Maximum orbital velocity

U_{mcr} Critical mean velocity for initiation of sediment motion

U_{min} Minimum orbital velocity

U_r Representative value of the horizontal orbital velocity at the peak frequency (irregular waves)

U_{rms} Root mean square value of the horizontal orbital velocity

U_{wcr} Critical wave orbital velocity for initiation of sediment motion

U_∞ Free-stream horizontal wave orbital velocity (linear theory)

UR Ursell number

W De-meaned vertical component of flow

<W >Ensemble averaged velocity (vertical component)

<W'> Ensemble averaged turbulence (vertical component)

WBL Wave boundary layer

WG Resistive wave gauge

W_m Mean vertical component of flow

W_{max} Maximum vertical orbital velocity

W_{min} Minimum vertical orbital velocity

W_{rms} Root mean square value of vertical orbital velocity

W_{free} Free stream vertical wave orbital velocity (Stoke's theory)

X Horizontal coordinate. Origin at the wave paddle at rest

Z_0 Roughness length under unidirectional flows

α Attenuation coefficient of the horizontal orbital velocities (regular waves)

α_j Spectral attenuation coefficient of horizontal orbital velocities (irregular waves)

α_r Representative attenuation coefficient of the horizontal orbital velocities at the peak wave frequency (irregular waves)

α^W Attenuation coefficient of the vertical orbital velocities (regular waves)

γ Jonswap spectra peak enhancement factor

δ Thickness of the wave boundary layer

δ_s Stokes's length-Thickness of the wave boundary layer in laminar flow

δ_x Horizontal distance

ε_f Wave dissipation rate

ε_j Spectral wave dissipation rate (irregular waves)

λ Wave length

λ_1, λ_2 Scaling parameter for vegetation mimics as defined in [Ghisalberti and Nepf, 2002]

ν Kinematic viscosity of water

ξ Water surface elevation

ρ Fluid density

ρ_s Solid material density or sediment density

τ_{cr} Critical bed shear stress for initiation of sediment motion

τ_{max} Maximum wave bed shear stress

τ_w Wave bed shear stress

φ Phase shift (between the phase of the wave and the phase of U_{max})

ω Wave radian frequency ($2\pi/T$)

Δf_b Discrete frequency bandwith

ΔS Canopy element spacing

"Recognizing that healthy and productive coastal ecosystems, already increasingly stressed by land-based sources of pollution, coastal development, and habitat destruction, have a growing role in mitigating the effects of climate change on coastal communities and economies in the near term…

We stress the need for sustainable management of coastal and marine ecosystems, including mangrove, wetland, seagrass, and coral reefs, as protective and productive buffer zones that deliver valuable ecosystem goods and services that have significant potential for addressing the adverse effects of climate change."

The Manado Ocean Declaration [*WOC*, 2009].

1 Chapter 1: Introduction

1.1 General context of the study

Coastal zones are characterised by fragile and complex equilibria and subjected to strong human pressure. Seagrass beds are a key coastal ecosystem and are considered some of the Earth's most valuable habitats, with an estimated value of about $ 19000 USD ha/annum, [*Costanza et al.*, 1997, based on services and goods provided].

Seagrasses are marine/estuarine flowering plants that sustain a rich and bio-diverse ecosystem providing food, spawning grounds, nursery areas, and protection to fish species of commercial interest [*Boudouresque et al.*, 2006] as well as to protected and endangered species [*Hughes et al.*, 2009]. Seagrass beds have been compared to forests, in terms of primary production, they supply 1% of the net primary production to the global ocean [*Duarte and Cebrian*, 1996] and are estimated to be responsible for 15% of the total net CO_2 uptake by ocean biota [*Duarte and Chiscano*, 1999]. Thus, seagrasses play a significant role in the regulation of the global carbon cycle. In addition, seagrass meadows have a widely-recognised role in stabilising sediments and reducing hydrodynamic energy, thereby protecting coasts from erosion [*Boudouresque and Jeudi de Grissac*, 1983; *Madsen et al.*, 2001; *Borum et al.*, 2004; *Koch et al.*, 2006b; *Le Hir et al.*, 2007].

Recent European legislation (Water Framework Directive, 2000; Marine Strategy Framework Directive, 2008) has adopted seagrass ecosystems as indicators of the status of coastal waters; they are used widely in management strategies of the environmental quality in coastal areas. However, seagrass beds world-wide are declining [*Duarte*, 2002; *Orth et al.*, 2006], at a rate of 7% per annum and the rate of loss is accelerating [*Waycott et al.*, 2009].

Posidonia oceanica is a perennial large seagrass species (Figure 1.1), endemic to the Mediterranean Sea, where it covers about 25% of the sea bed at water depths between 0 and 45 m [*Pasqualini et al.*, 1998]. Seagrass meadows are extremely important components of coastal European waters because of their abundance and their

essential ecosystem functions [*Borum et al.*, 2004]. *Posidonia* beds are protected under the Barcelona Convention and by national legislation. Despite the conservation effort, *Posidonia* meadows are threatened seriously in some areas.

Figure 1.1 *Posidonia* oceanica seagrass beds, (photo courtesy of Ante Zuljevich).

Some Mediterranean seagrass beds are declining because of natural causes, but most disturbances are anthropogenic [*Borum et al.*, 2004; *Boudouresque et al.*, 2006; *De Falco et al.*, 2006; *Tigny et al.*, 2007]. The main anthropogenic threats are water pollution (23%), the construction of coastal infrastructure (21%) and fishing (18%) [*ETC/BD*, 2009]. Changes to hydrodynamic regimes can cause also the loss of *Posidonia* beds (18%) which can be both natural or induced by the construction of new coastal defences or other infrastructure [*ETC/BD*, 2009]. It is ironic that the infrastructure built for coastal protection is often damaging to the recognised natural buffers (such as seagrass meadows), against coastal erosion.

Coastal erosion is a major issue throughout Europe, where the area lost or critically-impacted by erosion is estimated to be 15 km^2 /annum, with larger areas subjected to the risk of coastal flooding [*Eurosion*, 2004]. Erosion becomes a serious problem when coastal developments do not leave space for the natural system to adapt to the new conditions [*Marchand*, 2008] or when natural buffers are degraded. Mediterranean coasts are densely-populated and a large percentage of the coastline is urbanised [60-70% of the European Mediterranean coast; *Mangos et al.*, 2010]. Coastal erosion and flooding will be an even greater problem given the UN-IPCC prediction for climate change and sea level rise [*Vermaat et al.*, 2005; *IPCC*, 2007], and evidence of an increase in storm wave height in the Mediterranean [*Franco et al.*, 2004]. Furthermore, the European coastal population is growing rapidly [having doubled in the past 50 years; *Eurosion*, 2004]. Costs for coastal defences, which are already very large [an estimated 160,000 €/km of coast in the Mediterranean, *Mangos et al.*, 2010], are due to increase in the future. It has been estimated that coastal Mediterranean countries would have to spend an extra 527 million €/annum on coastal defences (considering both investment and maintenance costs) if the protection offered by the existing *Posidonia* meadows was lost [*Mangos et al.*, 2010].

Recent trends in coastal management and engineering are towards alternative, "soft" and more sustainable approaches to coastal protection, with greater attention being placed upon the protection provided by coastal ecosystems. However, detailed understanding of the physical processes in coastal ecosystems is still lacking even though this knowledge gap has been long recognised. In 1999, Massel wrote:

"*The understanding of physical processes at vegetated coasts is not adequate enough to develop effective management plans or engineering design of coastal developments which are today subjected to very stringent requirements to minimise their impact on the environment… Hydrodynamics of vegetated coastal-zones, and especially the processes associated with wave-motion, are still very poorly understood.*"

More than a decade after Massel's statement, wave-induced hydrodynamic processes in submerged vegetation are still not clearly understood and quantified [*Backhaus and Verduin*, 2008; *Koch et al.*, 2009]. This statement is especially true for storm waves [*Fonseca et al.*, 2006; *Koch et al.*, 2006b], which have the largest impact on coastal erosion.

1.2 Justifications for this study

The economic evaluation of the services and goods provided to humans by ecosystems is becoming an increasingly important tool in the decision-making process for environmental policy [*NRC*, 2005; *Mangos et al.*, 2010]. To improve the valuation of benefits provided by *Posidonia* meadows, more information is required regarding the characteristics of the coastal meadows and their effectiveness in defending the coastline against erosion. The benefits derived from ecosystem services, such as wave attenuation and coastal protection, have a specific value which is often variable in space and time [*Koch et al.*, 2009]. Wave energy dissipation by seagrass beds is very variable and depends upon several factors such as the seagrass species and the wave conditions [*Möller et al.*, 2002; *Koch et al.*, 2009]. *Posidonia oceanica* is believed to reduce wave energy but, despite its abundance and importance for Mediterranean coasts, its role remains unquantified. For these reasons, it is particularly important to determine how effective *Posidonia* is at reducing wave energy under varying wave conditions and water levels, especially under storm conditions. The dependence between wave reduction and wave period in seagrass canopies is poorly understood whilst storm waves-seagrass interactions need defining [*Koch et al*., 2006].

Detailed studies of wave-vegetation interactions, under controlled conditions, have been performed mainly with scaled models [*Asano et al.*, 1988; *Dubi and Tørum*, 1994; *Løvås and Tørum*, 2001], with their associated scaling effects. More specifically, studies on *Posidonia oceanica* have only been carried out in small flumes, under unidirectional flows [*Folkard*, 2005; *Maltese et al.*, 2007].

The effects of marine/estuarine submerged vegetation on unidirectional flows have been studied at a variety of scales in the field [*Leonard and Luther*, 1995; *Neumeier and Ciavola*, 2004; *Thompson et al.*, 2004] and in laboratory flumes [*Fonseca et al.*, 1982; *Gambi et al.*, 1990; *Baptist*, 2003; *Nepf and Ghisalberti*, 2008]. The interaction between aquatic vegetation and oscillatory flows is less well studied and has been identified as an important area for research, especially with respect to seagrass species [*Fonseca et al.*, 2006; *Koch et al.*, 2006b; *Bouma et al.*, 2007]. The response of a seagrass meadow under waves is more complex than that under steady currents; the rapid oscillation of the canopy (of the order of seconds) results in greater mixing of water between the region above and within the plants [*Koch and Gust*, 1999]. Data on

the effect of canopies on oscillatory flows are lacking, particularly for *Posidonia oceanica*.

The reduction of wave-induced velocities over rigid canopies depends upon the wave period (and A, wave orbital amplitude). The relationship between orbital velocity reduction and A has not yet been established for flexible vegetation. Studies on coral reefs have revealed that dissipation of oscillatory flows is a key element in the wave energy dissipation processes [*Lowe et al.*, 2007]. This link has not yet been explored for seagrass canopies.

Direct observations of the effect of seagrass canopies on sediment motion are limited [*Bouma et al.*, 2007] or show contrasting results. Field experiments indicate an enhanced sediment deposition [*Gacia and Duarte*, 2001] or reduced resuspension [*Gacia et al.*, 1999; *Terrados and Duarte*, 2000; *Granata et al.*, 2001] in a *Posidonia oceanica* canopy at a water depth of 15 m. In contrast, an increase in sediment transport, in the form of suspended load, was determined by the increase in water turbulence due to vegetation [*Baptist*, 2003]. According to some authors, flexible canopies do not directly induce sediment deposition, but rather prevent sediment resuspension [*Neumeier and Ciavola*, 2004; *Le Hir et al.*, 2007]. Furthermore, shear stress at the bed is expected to be larger in seagrass exposed to waves than currents [*Koch and Gust*, 1999]. Little work has been undertaken on wave-induced turbulence over a vegetated bed which, together with oscillatory flows, ultimately control shear stress at the beds (and hence sediment stability). Data revealing the effect of canopies on bed shear stress are lacking, and therefore sediment models with vegetation are likely to be inaccurate.

Despite their widely recognized importance in coastal protection, few coastal models take into account the effects of vegetation over the seabed. A requirement for more detailed field measurements and laboratory studies has been identified to improve hydrodynamic models and models of sediment resuspension/transport in seagrass meadows [*Madsen et al.*, 2001; *Teeter et al.*, 2001; *Dean and Bender*, 2006; *Koch et al.*, 2006a]. In order to incorporate the effects of submerged vegetation in coastal models, processes involved in wave propagation over vegetated beds need to be better understood, whilst quantitative results on wave or flow transformation over submerged vegetation need to be transformed into useful parameters [*Mendez and Losada*, 2004; *Le Hir et al.*, 2007]. Friction factors and wave boundary layers are largely affected by the wave regime but, in many studies, an indication of the regime (i.e. wave Reynolds number) is not given explicitly. A clear understanding of how seagrasses modify their

physical environment under waves will also benefit ecological research within the *Posidonia* ecosystem, such as transport of nutrients, larvae, and oxygenation. Improvements of ecosystem and coastal dynamics models are necessary, as these are essential tools for coastal management and the protection of these delicate ecosystems.

1.3 Objectives

The present work focuses upon the effects of seagrasses on coastal waves and wave-induced flows, which has significant implications for coastal protection. In order to achieve these objectives, both field measurements and flume observations,at full-scale, of wave height and flows in a shallow *Posidonia oceanica* patch were collected.

The specific scientific aims of the study are:summarised below.

- To evaluate the effects of a natural shallow *Posidonia oceanica* meadow on wave heights and wave-induced flows.
- To estimate the importance of shoot density and submergence ratios (h_s/D h_s=height of seagrass, D=water depth) on wave dissipation and on oscillatory flows under waves.
- To determine drag coefficients, friction factors and roughness caused by an artificial full-scale *Posidonia oceanica* bed under a range of wave conditions, submergence ratios and seagrass densities.
- To observe changes in oscillatory flows and turbulence, in a *Posidonia oceanica* canopy.
- To determine how orbital amplitude and flow regime affect bed friction and oscillatory flows in *Posidonia oceanica* beds.
- To observe sediment motion in the field, over a *Posidonia* canopy, by monitoring of the turbidity levels.

1.4 Thesis outline

This thesis is divided into 7 Chapters. Details on their contents are provided in the opening section of each Chapter.

- Chapter 1 and 2 provide an introduction to the topics of research undertaken together with a review of the relevant published literature.

- Chapter 3 describes the field campaign in a shallow *Posidonia oceanica* site in the Gulf of Oristano, Sardinia, Italy, presenting and discussing the results. Information on bathymetry, sediment characteristics, seagrass distribution and canopy height were collected. Changes in wave height and on the flow field in the *Posidonia* bed were related to prevailing hydrodynamic conditions. Furthermore, the field campaign provided information on the characteristics of *Posidonia oceanica* meadow for the design of the laboratory experiments.
- In Chapter 4, the full-scale experiments in the CIEM flume (on wave propagation over artificial *Posidonia oceanica* patch) are described. This Chapter contains also a brief introduction to waves in physical models and a description of the regular and random wave test conditions.
- Chapters 5 and 6 present the methods of data analysis, as well as the results and discussion on the experiments in the CIEM flume, for regular and random wave data-sets, respectively. In both Chapters, the effect of submergence ratio, seagrass density and wave amplitude, on wave height decay and oscillatory flows structure, are investigated. Wave dissipation is evaluated in terms of wave height decay, friction factors, and drag coefficients. Estimates of roughness are also given. Canopy effects on turbulence and above-canopy shear stresses under regular waves are reported in Chapter 5. The nature of regular waves (Chapter 5) was exploited, to investigate in detail the structure of oscillatory flows within the canopy boundary layer, both in terms of magnitude and phase. Irregular wave tests (Chapter 6) were used to assess how wave energy and oscillatory flows were attenuated, at the different components of the wave spectra.
- Chapter 7 brings together the findings from the previous Chapters, focusing upon the importance of *Posidonia oceanica* for coastal protection under different wave conditions. A conceptual model on the structure of the canopy boundary layer and on the mechanisms behind wave energy dissipation by a *Posidonia* canopy is proposed.
- Appendix A contains data relevant to *Posidonia oceanica* in the field (Chapter 3).
- Appendix B provides a brief description of the preliminary experiments and results used, in the selection of *Posidonia* mimics design.
- Data relevant to Chapters 5 and 6 are reported in Appendix C.
- Publications and reports derived from this work are presented in Appendix D.

2 Chapter 2: Background information and literature review

2.1 Introduction

This Chapter contains a brief introduction to the topics relevant to this thesis. Section 2.2 introduces wave propagation and dissipation in the nearshore zone, according to classical theories. Oscillatory flows produced by waves are also described whilst particular attention is given to the modification of these flows near the seabed (the wave boundary layer). Friction exerted by a submerged body is often quantified as a friction factor (f_w) or a drag coefficient (C_d); these are covered separately in Section 2.2.4 and Section 2.3, respectively. The derivation of these factors, from classical studies, is described.

In Section 2.4, the Mediterranean seagrass species, the subject of this study, *Posidonia oceanica,* is described in detail. Key aspects of its biology and ecology are summarised because understanding them is important in interpreting its effects on nearshore dynamics. This Section describes also the typical morphological characteristics of *Posidonia* and the structure of the meadows that it forms. This is important information that was used in the setup of the flume experiments, as described in chapters 4 to 6.

Section 2.5 summarises previous studies undertaken on the relationship between submerged canopies and coastal waves, flows and turbulence. This review incorporates several types of canopy (e.g. seagrass, saltmarsh and corals), partly because there have been very few investigations undertaken into the hydrodynamics within *Posidonia oceanica* beds, also because the general processes occurring within other submerged canopies might be analogous.

Finally, in Section 2.6, the effects of seagrass beds on the dynamics and composition of sediments are described; this is because one of the final objectives of

this thesis is to interpret the results, in terms of the implications to sediment transport and stability of the littoral zone.

2.2 Wave propagation and dissipation in coastal waters

2.2.1 Wave propagation and energy dissipation

As waves travel towards the coast they undergo significant transformation; they can be refracted/diffracted by bottom/shore topography and partly reflected back to sea, but, ultimately, their energy is dissipated. Energy dissipation occurs mainly through friction at the seabed and by wave breaking.

As waves approach the shore their height increases; they become steeper and they may reach a height that causes wave breaking, thus dissipating a large amount of energy (energy losses through breaking will not be treated here). Assuming constant water depth, the breaking wave height is predicted by the Miche breaking criteria, as reported in *Soulsby* [1997]:

$$H = 0.142\lambda \tanh\left(\frac{5.5D}{\lambda}\right) \qquad \textbf{Eq. 2-1}$$

The increase in wave height towards the shore can be predicted from the conservation of energy flux ($ECg=E_0Cg_0$, for definitions see Table 2-1)

$$H = H_0\sqrt{\frac{Cg_0}{Cg}} \qquad \textbf{Eq. 2-2}$$

where the subscript $_0$ refers to the most seaward location. The equation is obtained assuming no energy losses through breaking and bottom friction, that waves propagate parallel to the bottom contours and that the bed slope is gentle [i.e. smaller than 1/10; *Massel*, 1999]. Wave parameters derived from linear wave theory and Stokes' second order theory are summarised in Table 2-1. Generally, Stokes' theory is more appropriate to describe waves in intermediate to shallow waters.

Over a horizontal bed, wave energy loss by non-breaking waves is manifested by decay in wave height, because wave height is proportional to the square of wave energy. The wave energy dissipation rate (ε_f) (the rate of energy dissipation per unit area due to friction at the bed) is obtained from the loss of wave energy flux (δP) and is expressed as:

$$\varepsilon f = -\frac{\delta P}{\delta x} = -\frac{\delta E C_g}{\delta x} \qquad \textbf{Eq. 2-3}$$

where δx is the distance between the two locations considered (see coordinate definition in Figure 2.2). From $\varepsilon_{f,}$ a dissipation factor *fe* due to friction can be calculated. Many formulas exist, but one of the most used is the one proposed by *Jonsson* [1966]:

$$fe = \frac{3\varepsilon_f}{2\pi\rho u_\infty^3} \qquad \textbf{Eq. 2-4}$$

where U_∞ is the free stream horizontal orbital velocity. Energy dissipation factors (f_e) for sands under oscillatory flows range from $0.06<f_e<0.5$ [*Nielsen*, 1992]. The largest value (>0.1) are associated with sandy seabeds with bedforms [*Sleath*, 1984].

Table 2-1 Wave parameters derived from linear and non-linear wave theory.

Parameter	Linear wave theory	Stoke's second order wave theory
Sea surface oscillation, ξ (m)	$\frac{H}{2}\cos(kx-\omega t)$	$\frac{H}{2}\cos(kx-\omega t)+\frac{H^2k}{16}\frac{\cosh kD}{\sinh^3 kD}(2+\cos 2kD)\cos 2(kx-\omega t)$
Wave celerity, C (m/s)	$\sqrt{\frac{g\lambda}{2\pi}\tanh kD}$	$\sqrt{\frac{g\lambda}{2\pi}\tanh kD}$
Horizontal oscillatory velocity, U (m/s)	$\frac{\pi H}{T}\frac{\cosh kz}{\sinh kD}\cos(kx-\omega t)$	$\frac{\pi H}{T}\frac{\cosh kz}{\sinh kD}\cos(kx-\omega t)+\frac{3}{16}\frac{H^2\omega k\cosh 2kz}{\sinh^4 kD}\cos 2(kx-\omega t)$
Vertical oscillatory velocity, W (m/s)	$\frac{\pi H}{T}\frac{\sinh kz}{\sinh kD}\sin(kx-\omega t)$	$\frac{\pi H}{T}\frac{\cosh kz}{\sinh kD}\sin(kx-\omega t)+\frac{3}{16}\frac{H^2\omega k\sinh 2kz}{\sinh^4 kD}\sin 2(kx-\omega t)$
Wave group velocity, Cg (m/s)	$\frac{1}{2}C\left[1+\frac{2kD}{\sinh 2kD}\right]$	$\frac{1}{2}C\left[1+\frac{2kD}{\sinh 2kD}\right]$
Wave Energy Density, E (j/m^2)	$\frac{1}{8}\rho g H^2$	$\frac{1}{8}\rho g H^2$

Waves at sea are not simple monochromatic waves, but are composed of a spectrum of wave heights, frequencies and directions. Wave spectra are often approximated by semi-empirical spectral forms. Measured wind waves over continental shelf waters are best simulated by JONSWAP spectrum [*Soulsby*, 1997]. The JONSWAP spectrum is characterised by a sharp peak and a spectral width (defined by the γ parameter) of 3.3.

2.2.2 Wave orbital velocities

Neutrally-buoyant particles follow a circular trajectory in waves characterised by a small wavelength compared to the water depth ($D/\lambda>1/2$), their orbital velocity at the bed is very small, or null (Figure 2.1). In relatively shallow conditions ($D/\lambda<1/20$) or in intermediate conditions ($1/20<D/\lambda<1/2$), particle trajectories are elliptical in the water column and follow a back and forth motion at the bed (Figure 2.1).

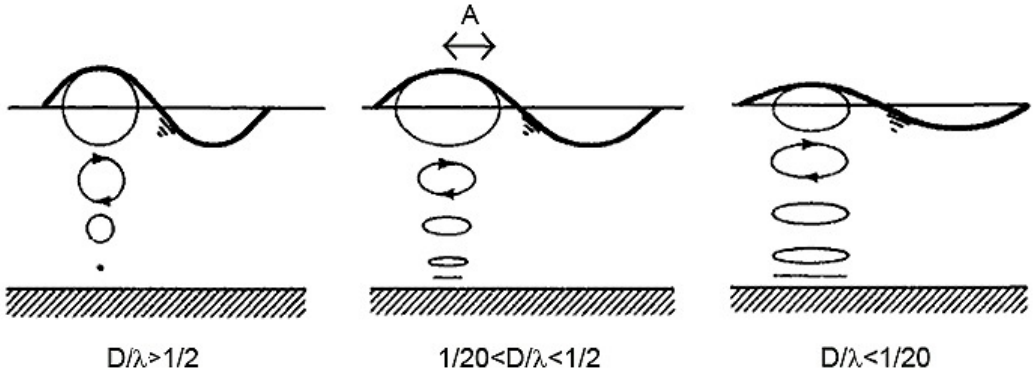

Figure 2.1 Wave orbital motion at different relative depths, and wave orbital amplitude A (adapted from *Dean and Dalrymple,* 1991).

Under idealised sinusoidal waves the horizontal component of the velocity (U) is at a maximum beneath the wave crest and is directed shoreward, whilst under the trough, U is negative and directed to seaward (Figure 2.2). The vertical component of the velocity (W) is zero at the crest and trough of the wave. At the zero surface displacement phase, ($x=\lambda/4$ and $x=3\lambda/4$) U=0 and W is maximum (Figure 2.2).

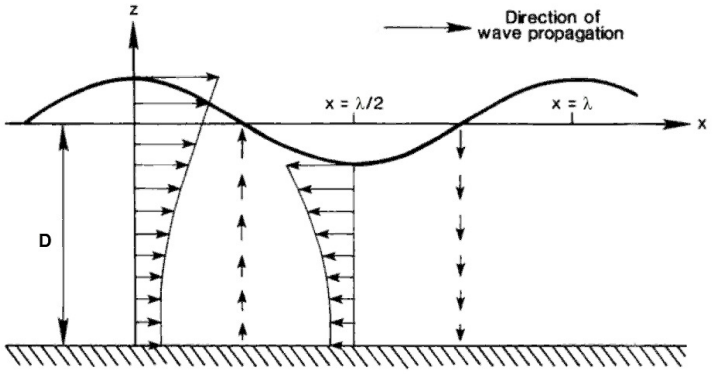

Figure 2.2 Wave-induced flows under a progressive non-breaking wave A (adapted from *Dean and Dalrymple*, 1991).

Above the wave benthic boundary layer, the magnitude of the maximum orbital velocity increases with elevation (z) and can be predicted with standard wave theories (Table 2-1). As waves become non-linear, the velocity at the crest becomes larger than the velocity at the trough (as a result of wave steepening), there are better predicted by non-linear theories (such as Stokes's wave theory).

2.2.3 Wave boundary layers and roughness

The Wave Boundary Layer (WBL) is defined as the area where the wave-induced water motion is significantly affected by the boundary [*Nielsen*, 1992]. The characterisation of the WBL is an essential precursor to studies of sediment transport, sediment-water fluxes, transport of chemical particles or benthic biological processes. The drag force exerted by the bed (in the direction opposite to the flow) produces a loss of momentum to the bed, which is manifested by a deceleration of flow, evident as a vertical velocity gradient within this layer. The wave-induced velocity, just above the WBL, is unaffected by the bed and defined as the free stream velocity U_∞. In a pure oscillatory motion it can be expressed as a function of time as:

$$U_\infty(t) = \mathrm{U}_\infty \cos\omega t = A\omega\cos\omega t \qquad \textbf{Eq. 2-5}$$

where ω is the wave radian frequency:

$$\omega = \frac{2\pi}{T} \qquad \textbf{Eq. 2-6}$$

and A is the particle orbital amplitude above the wave boundary layer.

The characteristics of the WBL depend upon the flow regime, characterised by the wave Reynolds Number

$$\mathrm{Re}_w = \frac{AU_\infty}{\nu} \qquad \textbf{Eq. 2-7}$$

and on the relative bed roughness (r/A), defined as the ratio of the hydraulic roughness length (r) to the wave orbital amplitude at the top of the WBL. The hydraulic roughness is associated with the vertical length scale of the boundary layer and the physical size of the roughness elements (such as the sediment grain size diameter).

Generally, in the WBL, the horizontal velocities near the bed (and bed shear stress) are ahead (in terms of phase) of the free stream velocity (Figure 2.3). Also, the peak of U(z,t) ("overshoot") does not occur at z=∞, as in logarithmic boundary layers, but at a certain elevation above the bed (between 5 and 10 cm in the example shown in Figure 2.3, *Nielsen*, 1992). This feature is clear in laminar wave boundary layers [*Dean and Dalrymple*, 1991], but experimental data shows that it is also valid for rough turbulent layers [*Nielsen*, 1992; *Massel*, 1999], however their quantitative prediction is more complicated [*Massel*, 1999]. The WBL is defined as rough turbulent when $\mathrm{Re}_w > 5\times10^4$ [*Dean and Dalrymple*, 1991] i.e. for large waves and/or rough bottoms.

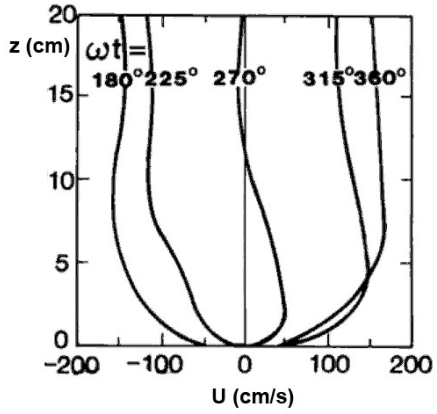

Figure 2.3 Measurements of oscillatory velocity u(z,t) as a function of distance from the bed, at different phases of the wave (modified from *Nielsen*, 1992).

In a uniform turbulent boundary layer created by unidirectional currents, the vertical length scale of the boundary layer is generally expressed as Z_0, the elevation from the bed at which the velocity is zero. The zero velocity is generally obtained from the downward extrapolation of the vertical velocity profile using the classic Karman-

Prandtl Law of the Wall which assumes that only the bed shear stress, fluid density and elevation define the velocity gradient.

In rough turbulent regime Z_0 only depends upon the hydraulic roughness (r) and, in fully rough conditions, Z_0 is assumed to be equal to:

$Z_0=r/30$ **Eq. 2-8**

Often, Z_0 is expressed in terms of the median grain diameter (d_{50}) for sandy beds [*Soulsby*, 1997]

$Z_0=d_{50}/12$ **Eq. 2-9**

In oscillatory flows, the vertical scale of the wave boundary layer is also influenced by the horizontal free-stream wave orbital amplitude, A [*Nielsen*, 1992]. The normalised defect function D(z,t) can be used to determine the vertical length scale of the wave boundary layer (z_1) [*Nielsen*, 1992].

$$D(z,t)=\frac{U\infty-U(z,t)}{A\omega} \quad \textbf{Eq. 2-10}$$

The defect function has a complex solution for laminar oscillatory flows. The defect function, has been used also successfully for turbulent boundaries; from experimental evidence, in fully rough regimes, has the form:

$$z_1=0.09\sqrt{rA} \quad \textbf{Eq. 2-11}$$

[*Nielsen*, 1985]

Experimental results show that the rough turbulent boundary layer structure becomes increasingly analogous to the smooth laminar solution, as the relative roughness r/A increases [*Nielsen and Guard*, 2010]. Assuming a constant hydraulic roughness, as A increases, so does z_1 and the thickness of the wave boundary layer.

In a pure harmonic oscillatory boundary layer the boundary layer thickness (δ_L) is related to the Stoke's length:

$$\delta_L=\sqrt{\frac{T\nu}{\pi}} \quad \textbf{Eq. 2-12}$$

Therefore it increases with wave period (T) for a given kinematic viscosity (υ). The thickness of a rough turbulent boundary layer (δ) is not as easy to quantify and has been defined in different ways: *Jonsson* [1966] defined δ to be the minimum distance from the bottom to a point where the horizontal component of the ensemble-averaged velocity $<U_w>$ equals the free-stream wave velocity amplitude (δ_J in Figure 2.4). According to *Jensen et al*.,[1989] (δ_{JSF} in Figure 2.4), δ is the distance from the bottom,

to the point of maximum velocity. Whilst *Sleath* [1987] expressed δ in terms of the velocity defect (U_d=U∞-U(z,t)) as the distance from the bottom to a point where defect velocity amplitude $\hat{u}_d$ is 5% of the free-stream velocity amplitude (δ_S in Figure 2.4).

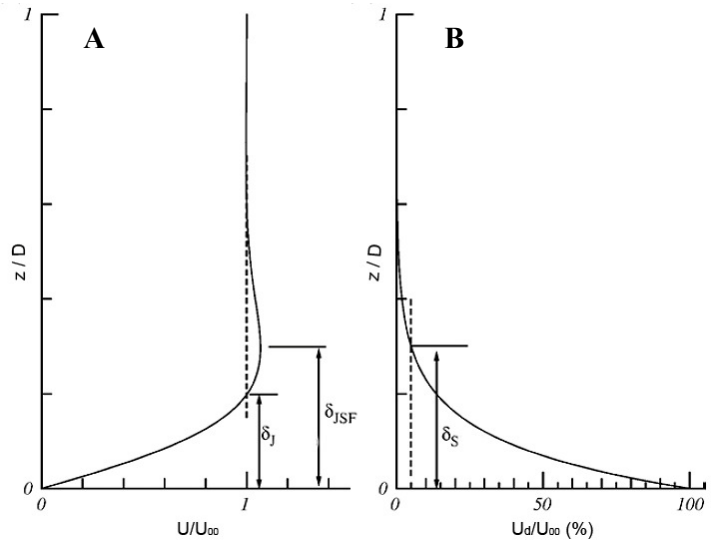

Figure 2.4 Wave boundary layer thickness definitions A) Jonsson definition (δ_j) and Jensen et al. (δ_{JSF}) from normalised vertical velocity profile. B) Sleath's definition from the velocity defect (δ_S), (modified from *Sana and Tanaka* [2007]).

In oscillatory boundary layers, the water motion caused by waves is not only oscillatory: a non-zero wave-averaged drift exists that is produced by the presence of a small vertical component of the orbital velocity [*Longuet-Higgins*, 1953]. This component is present in both symmetric and asymmetric waves, operating in the direction of wave propagation. In turbulent regimes, wave asymmetry can give rise also to a steady streaming within the wave boundary layer [*Ribberink and Al-Salem*, 1995; *Scandura*, 2007] in the opposite direction to Longuet-Higgins' drift. According to numerical simulations underataken by *Holmedal and Myrhaug* [2009], as the wave length increases in Stokes waves, the Longuet-Higgins' drift decreases and the seaward drift (determined by wave asymmetry) tends to dominate the steady component of flow within the WBL.

2.2.4 Friction factors and stresses

Friction factors (f_w) for rough beds under oscillatory flows are an order of magnitude larger than under unidirectional flows, depending upon relative roughness (r/A) and the flow regime [*Nielsen*, 1992]. Consequently, bed shear stresses under

waves with a certain oscillatory velocity $<U_w>$ are much larger than under currents of the corresponding U_m velocity [*Nielsen*, 1992; *Soulsby*, 1997]. Often, friction parameters are obtained as a wave dissipation factor f_e, from the loss of wave energy as waves travel along the bed (defined in Eq. 2.4).

Generally, the wave dissipation factor f_e is smaller than the friction factor f_w at the bed. However as pointed out by *Nielsen* [1992], the scatter is larger than the difference between the parameters f_e and f_w; therefore f_e can be assumed to be equal to f_w.

For fully-rough turbulent flows, f_w can be obtained using Swart's formula [as reported in *Sleath*, 1984] as

$$f_w = \exp\left[5.213\left(\frac{r}{A}\right)^{0.194} - 5.977\right] \qquad \textbf{Eq. 2-13}$$

This has been modified by *Nielsen* [1992] to:

$$f_w = \exp\left[5.2\left(\frac{r}{A}\right)^{0.2} - 6.3\right] \qquad \textbf{Eq. 2-14}$$

The *Soulsby* equation may also be used [1997]

$$f_w = 0.237\left(\frac{r}{A}\right)^{0.52} \qquad \textbf{Eq. 2-15}$$

Friction factors are also defined in terms of the shear stress at the bed

$$\tau_0 = 0.5 f_w \rho (A\omega)^2 \qquad \textbf{Eq. 2-16}$$

The shear stress experienced at the bed represents the transfer across the xz plane of horizontal momentum of the flow (where coordinates are defined as in Figure 2.2). Above a flat impermeable bed the distribution of the oscillatory component of the shear stress in the fluid depends upon time and elevation only whilst, if the bed is porous, the shear is also not horizontally uniform [*Nielsen and Guard*, 2010].

Shear stresses across a plane (Reynolds stresses) are equivalent to momentum transfer by turbulent motions. Reynolds stresses at a particular elevation in turbulent flows can be obtained from components of turbulence [*Sleath*, 1987], as:

$$\langle \tau_{xz} \rangle = -\rho \langle U'W' \rangle \quad \textbf{Eq. 2-17}$$

In most turbulent conditions, the shear stress at any elevation z is proportional to the turbulent kinetic energy (TKE), which can be obtained from near-bed turbulence measurements:

$$\tau_{xz} = \rho \beta TKE \quad \textbf{Eq. 2-18}$$

$$TKE = \sqrt{u'^2 + w'^2 + v'^2} \quad \textbf{Eq. 2-19}$$

where β is a constant that *Stapleton and Huntley* [1995] found to be equal to 0.19 in a wave/current environment. The method was also used to obtain the shear stress at the bed on sandy/rippled beds and was successful in several turbulent regimes [*Thompson et al.*, 2003; *Pope et al.*, 2006].

2.3 Wave-induced forces and drag on submerged bodies

Submerged bodies exposed to flows are subjected to mainly 3 types of forces: drag forces, inertial forces, and lift forces, which are assumed to be proportional to empirical coefficients [Cd, Cm and Cl, respectively, *Massel*, 1999]. Experimentally-determined drag coefficients incorporate both the contribution of the pressure drag (difference in pressure between the stagnation region upstream of the object and the downstream separation region) and frictional drag (shear stress in the boundary layer). Under waves, these parameters were found to be proportional to the Reynolds number (as for unidirectional flows) and also dependent upon the Keulegan-Carpenter (KC) number [*Sharpkaya and Isaacson*, 1981].

$$KC = \frac{U_{\max} T}{b} \quad \textbf{Eq. 2-20}$$

where b is the characteristic length of the submerged body projected in the direction of the flow, T is the wave period and U_{max} is the maximum horizontal orbital velocity. This parameter allows the comparison of two length scales: that of the object and the distance travelled in the flow direction (roughly equal to U_{max}*T).

Total wave-induced force is often represented by the Morison's equation, which includes two components: the drag force and the inertial force. The drag force adjusted for oscillatory flows can be expressed as

$$F_d = 0.5\rho C_d S U_{\max}^2 \cos(\omega t)\left|\cos(\omega t)\right| \quad \textbf{Eq. 2-21}$$

in which S is the projected area of the elements in the direction of the flow, ω is the radian frequency and ρ the water density. The inertial force is:

$$F_i = \rho\ C_m V U_{\max} \omega \sin(\omega t) \quad \textbf{Eq. 2-22}$$

where V is the volume of the submerged body. In general inertial forces are dominant for very small values of KC, for KC>100 drag forces dominate [*Massel*, 1999].

2.4 *Posidonia oceanica* seagrass

Posidonia oceanica is a large perennial phanerogam (flowering plant) endemic to the Mediterranean Sea, where it colonises between 1 and 2% of the total seabed and about 25% at depths shallower than 45 m [*Pasqualini et al.*, 1998].

A further 8 species are part of the genus *Posidonia* and they are all found in Australia. *Posidonia oceanica* is included in the Barcelona Convention's list of protected species [*Cavazza et al.*, 2000].

Posidonia oceanica seagrass meadows are distributed in shallow areas from the surface to a depth of 30-40 m in clear conditions, and plants have been found to depths of 48m [*Gobert et al.*, 2006]. *Posidonia* colonises sandy seabeds with a wide range of grain-sizes: from fine and medium [*De Falco et al.*, 2000; *De Falco et al.*, 2006], to coarse sands [*Cavazza et al.*, 2000]. *Posidonia* also develops on consolidated beds, such as old *matte* reefs [*Ballesta et al.*, 2000; *De Falco et al.*, 2003], subtidal rocky shores [*Cancemi et al.*, 2000], and even artificial substrata such as rubble mounds [*Di Carlo et al.*, 2005].

The plant (Figure 2.5) has ribbon-like leaves, 1 cm wide and up to 75 cm long, attached to a system of rhizomes, a type of modified stalk. The rhizomes can grow horizontally and vertically to adapt to the rate of sediment deposition. The roots grow from the base of the rhizome and anchor the plant firmly to the ground. The network of root systems, rhizomes of the old plants, and sediment form a compact structure called a *matte*. The matte, on average, accretes vertically 1 m every century [*De Falco and Piergallini*, 2003], and can be thousands of years old. The colonization of *Posidonia oceanica* is a very slow process. The vertical growth rate of the rhizomes has been estimated to be in the range of 1-4 mm year^{-1} [*Mateo et al.*, 2003; *Kendrick et al.*, 2005],

one of the slowest growth rates amongst seagrasses. The horizontal growth of each shoot has been measured at 10-60 mm year^{-1} [*Kendrick et al.*, 2005].

The density of the shoots is variable ranging from 150 to over 700 shoot/m^2 depending upon depth and health status of the meadow [*Buia et al.*, 2004; *Gobert et al.*, 2006]. Generally, meadows are denser in shallow waters [*Gobert et al.*, 2006] and the shoot density does not significantly change throughout the year [*Pergentmartini and Pergent*, 1994; *Gacia and Duarte*, 2001]. The length and number of the leaves is largest in late summer [*Gacia and Duarte*, 2001; *Gobert et al.*, 2006]. For example, adult leaf length in a meadow in Calvi (Corsica, France) was 25.04±12.0 cm in January and 40.09±10.4 in August [*Gobert et al.*, 2006]. The old leaves senesce and detach from the rhizome during the first autumn storms [*Mateo et al.*, 2003]. However, some leaves remain present and the leaf-sheaths (Figure 2.5A) are persistent on the rhizomes after the leaf-blade has been shed [*Gobert et al.*, 2006].

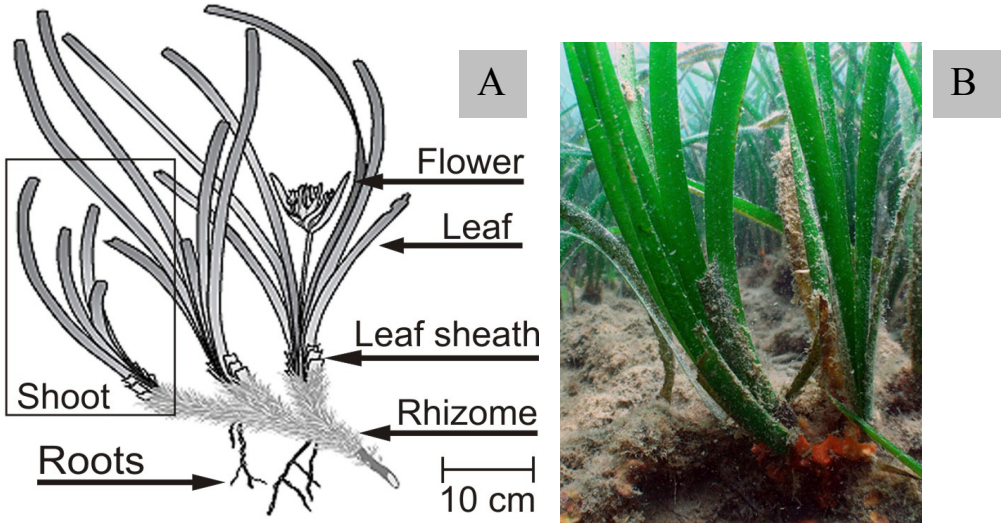

Figure 2.5 *Posidonia oceanica*: A) Morphology of the plants, [modified from *Borum et al.*, 2004] B) Photograph of a *Posidonia* plant established on 'matte' (Gulf of Oristano, Sardinia, Italy).

The main physical factors controlling the growth of *Posidonia* are: light availability, sedimentation rates, salinity, hydrodynamic energy and temperature [*Koch et al.*, 2006b]. The depth of colonisation of a *Posidonia* meadow is determined by turbidity [*Koch*, 2001; *Duarte et al.*, 2007] and the hydrodynamic conditions [*Koch*, 2001]. Dense uniform *Posidonia* meadows extend up to the surface in sheltered bays, whilst in more exposed areas the meadow edge is deeper and often plant distribution is patchy [*Buia et al.*, 2004]. Intense wave action can also help to reduce the load of

epiphytes on the leaves [*Koch*, 2001] and it might be important in the colonisation process: after storms up-rooted plants are able to disperse and colonise other areas [*Almela et al.*, 2008]. The use of wave exposure indexes (indexes of wave energy reaching a site, based upon fetch and wave characteristics), works well to predict the presence of meadows in lakes, but does not function properly in marine coastal areas, where complicated processes (such as complex bathymetry, wave reflection and refraction) affect wave propagation [*Koch*, 2001]. In wave-dominated environments, seagrasses are generally found where waves are of the intermediate type ($1/20<D/\lambda<1/2$) [*Koch et al.*, 2006b]. In a site exposed to large waves and swell (Maimoni beach, Sardinia, Italy, for example) *Manca* [2006] related the distribution of the *Posidonia* plants to the mobility of sand. Large patches of *Posidonia* meadow were not present in the nearshore on mobile sand, unless anchored by a hard substratum. *Posidonia oceanica* plants are more resistant to sediment burial than other smaller species of seagrass, but significant mortality has been reported when the burial level was over 10 cm [*Cabaco et al.*, 2008]. Seagrasses are able to adapt to new sedimentation rates/erosion when they are the result of a natural event and recover from damage caused by extreme (storms) or regular (dune migration) natural events [*Cabaco et al.*, 2008]. Feedback processes and interactions with the hydrodynamics and coastal sediment transport are induced by the growth of the meadow itself [*Kendrick et al.*, 2005]. *Posidonia oceanica* is believed to be able to affect hydrodynamics and sediment dynamics, as are other species of seagrasses. More details on this subject can be found in Sections 2.5 and 2.6.

2.5 Submerged canopies and coastal dynamics

This Section describes experimental results on the relationship between flows from several types of submerged canopies (seagrass, saltmarsh, seaweeds and rigid canopies, such as corals). A wide range of canopies are discussed because very few investigations have been performed on the hydrodynamics within *Posidonia oceanica* beds. The general processes occurring within submerged canopies may be analogous; as such, it is useful to interpret these, in relation to *Posidonia* canopies. However, it is important to recognise throughout that, quantitatively, other studies might not be comparable because the structure and the morphology of the canopies differ

significantly and the studies have been carried out under a wide range of hydrodynamic conditions. Furthermore, most knowledge of the hydrodynamics in submerged canopies is derived from studies under steady unidirectional flows. The behaviour of a canopy could be expected to be different under waves, than steady unidirectional flows, but the results and theories derived from these are also reported here, for comparison.

2.5.1 Effects of submerged canopies on wave energy

The measured wave height attenuation through natural seagrass beds varies between 1.6-80% [*Koch et al.*, 2006; *Prager and Halley,* 1999] . *Bradley and Houser* [2009] found mixed seagrass bed dominated by *Thalassia testudinum* caused a reduction in wave height by 30 %, over a distance of 39 m. Wave height reduction has been documented also for other vegetation types: for example a reduction of wave height of 60% by a Norwegian kelp forest (*Laminaria hyperarborea*) was recorded by *Mork* [1996]; *Möller et al.* [1999] found a wave height reduction of 60-96% over salt-marsh (on average, approximately four times greater than over the adjacent sand flat). However, other types of vegetation, such as the Californian kelp *Macrocystis*, had a negligible effect on waves, as they tend to move passively with the flow [*Elwany et al.*, 1995; *Prager and Halley*, 1999]. The large divergence of *in-situ* results can be attributed not only to the different vegetation characteristics, but also to tidal, weather and general hydrodynamic conditions, as well as bathymetry and sediment characteristics prevalent in the studies [*Möller et al.*, 2002].

In pioneering small-scale laboratory experiments wave energy attenuation by seagrass was found to be quite similar amongst different species of natural seagrass (*Zostera* sp*, Syringodium* sp*, Halodule* sp*, Thalassia* sp): a 44% reduction of wave energy over a 1 m test section was found when canopy height was almost equivalent to the water depth (h_s/D=1) [*Fonseca and Cahalan*, 1992]. A wave height attenuation by polypropylene mimics of *Posidonia australis* of about 5% per m was found when h_s/D=1 [*Wallace and Cox*, 2000]. Both studies involved the use of plants (or mimics) at full-scale in a relatively small flume and when scaling effects were ignored.

Vegetation-induced drag under waves is related to shoot stiffness [*Bouma et al.*, 2005] and plant morphology [*Koch et al.*, 2006b]. The effect of plant density is still controversial, some authors state that increased density enhances wave height reduction [*Bouma et al.*, 2005; *Penning et al.*, 2009], whilst no effect of plant density was observed by others [*Fonseca and Cahalan*, 1992; *Augustin et al.*, 2009]. Wave height

reduction is larger when the canopy occupies the whole of the water column and consequently is greatest at low tide [*Fonseca and Cahalan, 1992; Meijer, 2005; Mork, 1996]*.

Wave energy over canopies might not be dissipated at the same rate amongst the different frequency components of the waves, according to some studies. Canopies made of rigid elements and coral reefs are more efficient at attenuating short period components of the wave energy spectrum [*Lowe et al.*, 2005a; *Lowe et al.*, 2007]. In a Dutch salt-marsh, the percentage energy dissipation was largest for waves having the shortest period [*Meijer*, 2005]. Similarly *Thalassia* seagrasses acted as low pass filters in a very low energy conditions (T_p=1.3 s), as wave energy at secondary peaks of the spectra (2.6 s, the longer waves recorded) was not attenuated [*Bradley and Houser*, 2009]. However most energy reduction took place at the peak frequency. On the contrary, results from a study on English salt-marshes indicate that wave energy attenuation by those plants was not frequency-dependent [*Möller et al.*, 1999].

The variability in wave dissipation by submerged vegetation is very large and it is unlikely to find a common behaviour for all types of vegetation and conditions [*Mendez and Losada*, 2004]. However, the calculation of a parameter, such as a friction factor or a drag coefficient, that could be used for modelling vegetation effects on coastal environment, is desirable. Vegetation resistance has often been represented as a drag force and obtained from the decay in wave height across the vegetation. In several studies, it was found that most of the wave height reduction occurred in the first few metres of a vegetation field: wave energy reduction was found to be maximum at the front of salt-marshes [*Möller et al.*, 1999] and beds of *Laminaria hyperarborea* kelp [*Dubi and Tørum*, 1994]. Wave height decay over submerged vegetation has generally been expressed by an exponential function of the type:

$$\frac{H(x)}{H_0} = \exp^{-ki\Delta x} \qquad \textbf{Eq. 2-23}$$

where H(x) is the wave height measured along the field, Ho is the wave height in front of the leading edge and separated by a distance Δx. The exponent K_i is the wave decay coefficient. K_i values ranged between 0.015 to 0.1 in the experiments conducted in a flume by *Asano* [1988], using kelp mimics. In the field [*Möller et al.*, 1999] reported K_i to be 0.01 in a British salt-marsh, whilst in mixed seagrass beds K_i ranged between 0.004 and 0.02 [*Bradley and Houser*, 2009] (for more details see Table 2-2).

Wave height decay can be expressed in terms of drag coefficient acting on the canopy elements. The following equation was derived for rigid canopies [*Dalrymple et al.*, 1984], using the conservation of energy equation and assuming linear wave theory to be valid:

$$\frac{H(x)}{H_0} = \frac{1}{\left\{\left[\frac{g^2 C_d N b H_0 (\cosh^3 kh_s + 2)\sinh kh_s}{9\pi C_g C^3 \cosh^3 kD}\right]x + 1\right\}} \qquad \textbf{Eq. 2-24}$$

where C_d is the drag coefficient acting on each canopy element; h_s is the plant stem height, N is the number of stems/m^2, b is the cylinder diameter (or the width of the seagrass blades), k is the wave-number, C is the wave phase speed and C_g is the wave group speed. Eq. 2-24 has been extensively used to obtain C_d in vegetated beds [*Kobayashi et al.*, 1993; *Mendez et al.*, 1999; *Augustin et al.*, 2009], under the assumption that inertial forces are negligible and that the horizontal velocity of the vegetation is significantly smaller that the orbital velocity of the waves. *Mendez and Losada* [2004] state that for flexible vegetation the value of C_d obtained from Eq.2-24 is valid for flexible canopies if the relative velocity of the flow relative to the vegetation elements is used, instead of the flow velocity (therefore taking into account the motion of the vegetation). Also, the formula does not take into account the reflection induced by the canopy; however, this has a negligible effect on wave energy losses [*Mendez and Losada*, 2004; *Meijer*, 2005]. The rigid model of *Dalrymple et al.,* (Eq.2-24), used in the estimate of C_d, has been proven to be valid for natural seagrass [*Bradley and Houser*, 2009]. The value of C_d calculated using the relative velocity did not differ significantly from the C_d obtained from the measured flow velocity [*Bradley and Houser*, 2009]. Moreover, laboratory experiments undertaken on vegetation of different stiffness show that the difference in C_d between flexible and rigid plants is negligible [*Augustin et al.*, 2009].

Kobayashi et al. [1993] presented an analytical solution for predicting wave propagation over vegetation (kelp) assuming an exponential wave decay and that the vegetation can be approximated as rigid cylinders. The calculated C_d ranged between 0.075 and 2.93 which was related to a modified Reynolds number by:

$$C_d = 0.08 + \left(\frac{2002}{\mathrm{Re}}\right)^{2.4} \qquad \text{(for } 2200 < \mathrm{Re_v} > 18000\text{)} \qquad \textbf{Eq. 2-25}$$

with Re_v (Reynold's vegetation number) being the Reynold's number acting on the kelp and defined as:

$$\mathrm{Re}_v = \frac{bU_c}{\upsilon} \qquad \textbf{Eq. 2-26}$$

Where: υ is the kinematic viscosity of water; b the width of the leaf; and U_c the characteristic velocity (the U_{max} at the top of the canopy). *Mendez et al*. [1999] extended Kobayashi's model for random waves and found the same relationship with an improved fit to the experimental data by *Asano et al.* [1988]. When taking into consideration the oscillation of flexible mimics, *Mendez et al.* [1999] found the following function between C_d and Reynold's vegetation numbers:

$$C_d = 0.4 + \left(\frac{4600}{\mathrm{Re}_v}\right)^{2.9} \qquad \text{(for } \mathrm{Re_v} > 1000\text{)} \qquad \textbf{Eq. 2-27}$$

As pointed out by *Dalrymple et al* [1984], the value of C_d is greater for swaying vegetation than for rigid canopy elements for the same value of wave energy attenuation. In a later study, *Mendez and Losada* [2004] found that C_d for kelp was better correlated to the Keuglan-Carpenter number (KC) than to Re_v .

$$C_d = 0.47\exp(-0.052KC) \qquad \text{(for3<KC<59>)} \qquad \textbf{Eq. 2-28}$$

the KC number is defined as:

$$KC = \frac{T_p U_c}{b} \qquad \textbf{Eq. 2-29}$$

with T_p being the peak wave period.

Under oscillatory flows, in fact, C_d for cylinders not only depends on the Re number but also on the KC number (see section 2.3) particularly for low KC values [KC<30, *Massel*, 1999].

All the estimates for C_d presented above were obtained from models calibrated on *Asano*'s [1988], *Dubi'*s [1995] and *Lovas*' [2000] datasets on wave energy attenuation obtained in the flume over artificial kelp *L. hyperaborea*. Literature results for C_d are summarised in Table 2-2. *Posidonia* and other seagrass canopies have a completely different morphology from the more studied kelp beds.

Wave dissipation over a seagrass bed dominated by *Thalassia testudinum* in low-energy environments (with Re_v numbers much lower than in the previous studies, cited above) was found to be more accurately described by the vegetation Reynolds number than the Keulegan-Carpenter (KC) number [*Bradley and Houser*, 2009]. In that

study, the representative drag coefficient was found to range between 2 and 0.15 and to be highly correlated to the Re_v

$$C_d = 0.1 + \left(\frac{925}{\mathrm{Re}_v} \right)^{3.16} \quad \text{(for } 200<\mathrm{Re}>800\text{)} \quad \textbf{Eq. 2-30}$$

Augustin et al. [2009] in contrast, did not find a significant relationship between C_d and Re_v from flume experiments of wave reduction over near-emergent *Spartina* plants. Furthermore, the parameter C_d was poorly correlated with KC. Interestingly, Augustin et al.'s [2009] test conditions were weakly non-linear (with a H/D ratio of 0.2-0.4) and (numerically computed) friction factors were well correlated to the Ursell number (which is a measure of wave non-linearity). For near-emergent plants, the friction factor increased with the Ursell number, with a steeper gradient for the denser *Spartina* field. *Gaylord et al.* [2003] also concluded that the drag induced by kelp plants increases if exposed to waves and currents or non-linear waves that are able to create a net mass transport (Stokes drift). The drift would interfere with the motion of the leaves increasing the relative velocity of the leaves and the drag. Instead kelp fronds tend to move passively with the flow if exposed to fully linear waves with no current.

Wave energy dissipation over a roughness patch can be quantified also by a wave dissipation factor (f_e) or a wave friction factor at the bed (f_w). Published values for friction over canopies are reported in Table 2-2. For coral reefs f_w varied between 0.15 and 0.28 [*Lowe et al.*, 2005a and references therein] and under spectral waves f_w was found to increase with wave frequency [*Lowe et al.*, 2005a]. Numerically-derived friction factors, for low density salt-marsh vegetation under short waves, ranged between 0.05 and 0.19 and were significantly dependent on the submergence ratio [*Augustin et al.*, 2009]. Modelled friction factors in a natural salt-marsh exposed to waves varied between 0.07 and 0.38 and were, on average, 0.24 [*Möller et al.*, 1999]. Hydraulic roughness obtained from wave energy dissipation, (r defined from Eq.2-14) varied between 0.03 and 0.38 and was largest for the smallest Reynolds Number [*Bradley and Houser*, 2009].

The complex relationship between storm waves and seagrass-induced wave attenuation still needs to be verified. Although storm waves result in increased water levels along the coast and, by bending the plants, decrease the percentage of water column occupied by seagrass, they also usually have longer wave periods which are

capable of producing stronger near-bottom motion at greater depths [*Koch et al.*, 2006b].

Table 2-2 Wave height decay parameter (K_i), drag coefficient (C_d), wave dissipation factors (f_e), bed friction factors (f_w), and hydraulic roughness (r) from the literature.

Para-meter	Values	Type of vegetation	Conditions	Reference
K_i	0.015-0.1	*Laminaria hyperarborea* (kelp) mimics	Laboratory 1:10 scale $h_s/D=0.56$ and $h_s/D=0.48$	[*Asano et al.*, 1988]
C_d	0.075-2.93	*Laminaria hyperarborea* (kelp) mimics	Modelled based on Asano 1988 experiments $2200<Re_v>18000$	[*Kobayashi et al.*, 1993]
C_d	0.09-1.55 0.33-6.9 (considering mimics oscillation)	*Laminaria hyperarborea* (kelp) mimics	Modelled based on Asano 1988 experiments, valid also for random waves. $200<Re_v>15500$ and $2300<Re_v>20000$ (considering mimics oscillation)	[*Mendez et al.*, 1999]
C_d	0.01-0.52	*Laminaria hyperarborea* (kelp) mimics	Modelled based on Dubi 1995 experiments; non-breaking random waves $3<KC>59$	[*Mendez and Losada*, 2004]
K_i	0.01	Salt-marsh	UK coast; meso-macro tidal	[*Brampton*, 1992 as reported in Moller et al., 1999]
C_d	0.5-3	Salt-marsh	Dutch estuary; tidal conditions	[*Meijer*, 2005]
K_i	0.004-0.02	Mixed seagrass dominated by *Thalassia testudinum*	Microtidal shallow (1- 1.5 m depth) Average $0.25<h_s<0.30$ m ($0.16<h_s/D<0.3$); Density 1100 stems/m^2 $200<Re_v>800$	[*Bradley and Houser*, 2009]
C_d	2-0.15			
r (m)	0.03-0.38			
f_w	0.07-0.38	Salt-marsh	UK coast; meso-macro tidal	(Möller et al., 1999)
f_w	0.05-0.19	Salt-marsh	Laboratory ; $h_s/D=0.75$; Density: 94 and 104 stems/m^2; $3500<Re_v>9500$	(Augustin, 2009)
f_e	0.24±0.03	Coral reef flat	Meso tidal; $7<T_p<10$ s; $0.7<H_0<2.2$ m; $1.1<D<3$ m	(Lowe et al., 2005)
r	0.16±0.03			

2.5.2 Effects of submerged canopies on the flow field

Under unidirectional flows, submerged vegetation is known to reduce current speed inside the canopy and to intensify it above the canopy [*Gambi et al.*, 1990; *Nepf and Vivoni*, 2000; *Neumeier and Ciavola*, 2004; *Neumeier*, 2007] the leaves bend in the direction of the current creating a surface over which the current flows (skimming flows, see an example in Figure 2.6). This type of flow has also been observed above some seagrass beds [*Fonseca et al.*, 1982; *Koch and Gust*, 1999; *Thompson et al.*, 2004]. In flume experiments with *Posidonia oceanica* mimics, unidirectional currents decelerated progressively with distance inside the canopy and accelerated above it [*Folkard*, 2005; *Maltese et al.*, 2007]. However, in the field, on a wave-sheltered *Posidonia oceanica* meadow, *Gacia et al.* [1999] observed a reduction in currents inside the canopy and an increase very close to the bed. A steeper velocity gradient was observed above the canopy, but there was not an intensification of flows compared to non-vegetated areas.

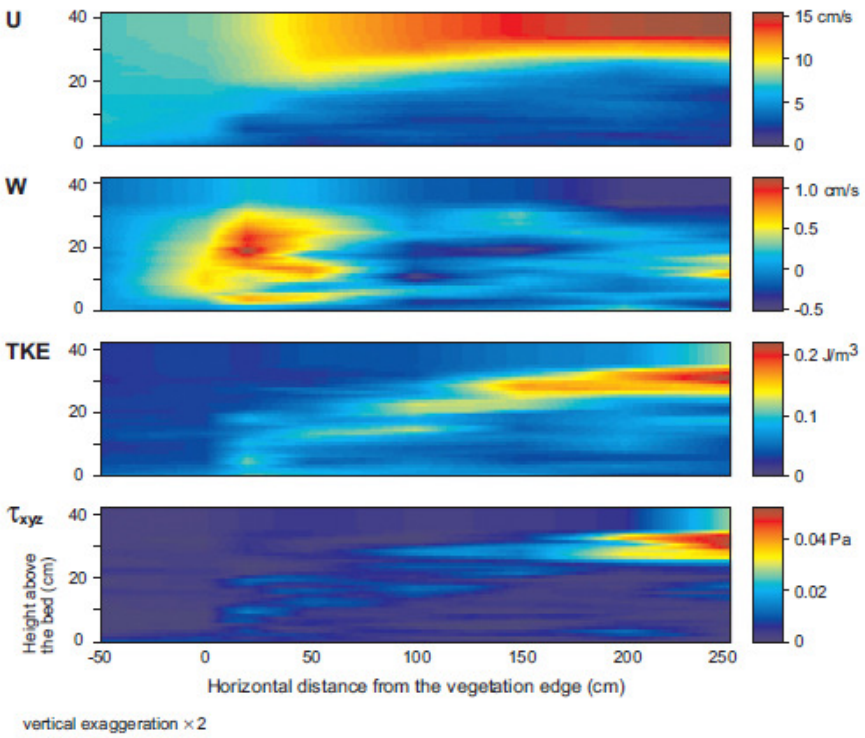

Figure 2.6 Distribution of mean horizontal (U), mean vertical velocity (W) , Turbulent kinetic energy (TKE) and Reynolds stresses (τ_{xyz}), with distance inside and above a vegetation canopy, under unidirectional flows. The canopy was made of saltmarsh plants (*Spartina sp*) with a canopy height 24.5 cm in 42 cm water depth and with an undisturbed U of 6.8 cm/s [from flume studies by *Neumeier*, 2007]

Energy reduction reaches its maximum at some distance inside a vegetation patch [*Leonard and Luther*, 1995; *Fonseca and Koehl*, 2006; *Maltese et al.*, 2007] and the vertical velocity profile requires a certain adjustment length, a distance downstream from the leading edge of the canopy, before being fully developed [*Peterson et al.*, 2004; *Lowe et al.*, 2005b].

Some studies report that vertical velocity profiles over a canopy fit the Karman-Prandtl relationship [*Gambi et al.*, 1990; *Neumeier and Amos*, 2006b; *Neumeier*, 2007], and the vegetation is seen as a macro-roughness. According to other authors, the region of the canopy top is characterized by a shear layer which is more similar to a mixing layer rather than a boundary layer and the logarithmic boundary layer might develop above this mixing layer [*Ghisalberti and Nepf*, 2002; *Maltese et al.*, 2007]

Plant canopies with high shoot density have a larger capacity to attenuate unidirectional flows [*Gambi et al.*, 1990; *Neumeier and Ciavola*, 2004; *Peralta et al.*, 2008]. Also, the lesser the part of the water column that the canopy occupies, the more effective it is at reducing unidirectional flows [*Fonseca and Fisher*, 1986; *Thompson et al.*, 2004]. *Peterson et al.* [2004] found also that the width of the "seagrass–edge zone" (area of transition between the upstream free flow and the transformed flow within the canopy) increases with decreasing shoot density.

The interactions between submerged canopies and wave-induced flows and the resulting vertical flow structure are not clearly defined, especially for flexible canopies. Early studies on artificial canopies exposed to waves show that the local flow field is affected by the vegetation, even when wave damping is small [*Kobayashi et al.*, 1993]. Also, wave orbital velocities can be modified by artificial seagrass meadows [*Price et al.*, 1968] and kelp beds [*Lovas and Torum*, 2001], promoting a net drift in the direction of wave propagation. In canopies made of rigid cylinders, regular short-period waves are capable of driving more flow though the canopy, than unidirectional flows, whilst flow reduction under monochromatic waves increases with increasing wave orbital amplitude [*Lowe et al.*, 2005b], (Figure 2.7). Similarly flow attenuation within coral canopies increases with increasing wave periods [*Lowe et al.*, 2007].

In mangrove forests, wave-induced flows attenuate rapidly with distance from the vegetation front. However the profile of the U and W components of flow are basically uniform with depth (for $L/h_s=16$) [*Massel et al.*, 1999]. A model study by *Li and Yan* [2007] showed that the magnitude of the horizontal component of the wave-induced (U) velocity decreases within a vegetated bed, but that the shape of the vertical profiles

remains unchanged; this is in contrast with results from flume experiments on the interactions between wave-induced flows and coral canopies [*Reidenbach et al.*, 2007] and canopies made of rigid cylinders [*Lowe et al.*, 2005b] where, an intensification of flow was observed just above the canopy, as in open channel experiments. The same structure of the vertical velocity profile was observed in 1:10 scale experiments, with artificial kelp beds [*Lovas and Torum*, 2001] exposed to very energetic waves (equivalent to wave periods of 7.9-11.1 s and wave heights of 4.4 and 6.6 m at full scale). However, all the observations in the *Lovas and Torum* study were made on the total velocity data (i.e the contribution of mean, wave-induced flows and turbulence to the measured flow were not separated) measured on a sloping bed. Seagrass beds appear to affect the magnitude and structure of the oscillatory flows when exposed to long period waves, creating a reduction of flow within the canopy and flow intensification above. In particular, flow intensification above the canopy was observed in the field under long waves in mixed *Posidonia australis* and *Posidonia sinuosa* beds [*Wallace and Cox*, 2000] (10s period waves) and above *Amphibolis antartica* seagrass (15 s) by *Verduin and Backhaus* [2000].

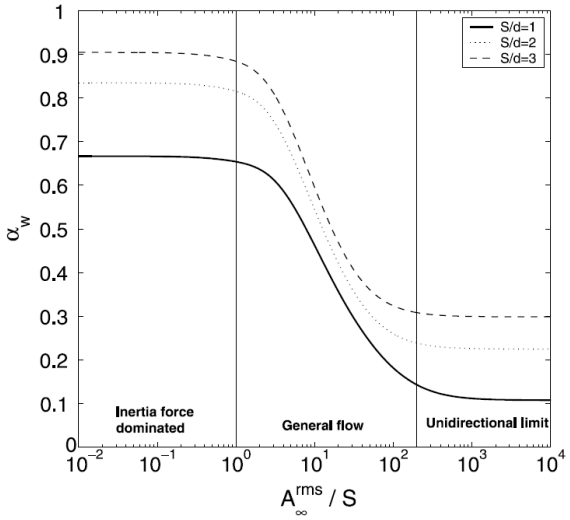

Figure 2.7 Modelled oscillatory flow reduction parameter (α_w) as a function of the rms wave orbital amplitude (A) divided by the element spacing (S) for different roughness configurations (represented by S/d, where d is the element diameter). The parameter α_w is defined as the ratio between the in-canopy depth averaged rms oscillatory flow and the free stream potential flow. The model was validated with rigid cylinders in-canopy flow [from *Lowe et al.*, 2005b].

In an attempt to explain flow intensification above the seagrass canopy observed in the field [*Verduin and Backhaus*, 2000], *Backhaus and Verduin* [2008] developed a

Lagrangian plant model. Comparing model observations on flexible canopies with those on rigid plants, the authors concluded that the intensification is not due to the motion of the leaves. The model, which was not verified, produces an increasingly impermeable canopy with increasing flow velocities. This process is thought to be responsible for the deflection and intensification of the flow, above the canopy.

Seagrass canopies of different morphology, size, and structure under oscillatory flows, produced remarkably different flow structures in the *Backhaus and Verduin* model [2008]. Therefore, observed flows in kelp canopies, or differing seagrass species, might not be the same as for full-scale *Posidonia* canopies.

The distribution of the vertical component of the oscillatory flows, in vegetated beds under waves, is less well known than horizontal flows. The total vertical velocity (waves+currents) over artificial kelp beds has been shown to decrease near the water surface and increase within the canopy and above the canopy, [*Lovas and Torum*, 2001]. The vertical component of the flow spectrum, under long waves at 15 cm from the seabed (roughly $z/h_s=0.3$) increased over the entire frequency range inside a *Amphibolis* meadow, it decreased at the transition zone between the meadow and bare sand [*Verduin and Backhaus*, 2000].

2.5.3 Effects of submerged canopies on turbulence

Turbulence intensities within a submerged canopy exposed to unidirectional currents have been found to increase [*Gambi et al.*, 1990; *Fonseca and Koehl*, 2006] and decrease [*Leonard and Croft*, 2006] relative to the surrounding unvegetated areas. Turbulence increases with increasing current speed until the canopy starts bending and then skimming flow develops, which reduces the turbulence levels [*Nepf*, 1999]. Turbulence inside a canopy is complicated as it is created, dissipated, advected and re-scaled as a function of elevation [*Koch*, 2001; *Neumeier and Amos*, 2006a]. A turbulence maximum is generally found at the canopy-water interface in uniform unidirectional flows [*Gambi et al.*, 1990; *Ghisalberti and Nepf*, 2002; *Leonard and Croft*, 2006; *Neumeier and Amos*, 2006b; *Neumeier*, 2007](Figure 2.6), and above patches of *Posidonia* mimics [*Folkard*, 2005]. In the lower canopy, a low-turbulence zone was found in tidal marshes and a positive relationship was found between turbulence intensity and shoot density [*Neumeier and Amos*, 2006a]: The edge of the meadow is found to be an area of high turbulence [*Neumeier*, 2007]. Furthermore,

turbulent flow energy usually decreases exponentially with distance into the canopy [*Leonard and Luther*, 1995].

If the submerged vegetation produces sufficient drag under unidirectional unconfined flows (low submergence ratio, h_s/D) a shear layer is created above the canopy [*Nepf and Vivoni*, 2000]: this phenomenon is seen in terrestrial canopies [*Raupach et al.*, 1991]. Two zones can be differentiated inside the canopy [*Nepf and Vivoni*, 2000; *Neumeier and Amos*, 2006a; *Nepf and Ghisalberti*, 2008] (see below).

- The lower canopy, where turbulence is generated within stem wakes (small-scale) and turbulent exchanges occur predominantly through longitudinal advection. The lower layer is an area of low momentum transport due to low turbulence and reduced flows. The density and morphology of the canopy greatly influences the turbulence in this region.
- The upper canopy, where both mean and turbulent profiles are influenced by the shear layer above. The transfer of momentum from the shear vortices above the canopy is a fundamental driver of the flows inside the canopy; it opposes the form drag exerted by the canopy elements [*Nepf and Ghisalberti*, 2008]. In these regions, the details of the structure (diameter, density) of the canopy elements are less important than in the lower canopy.

A similar turbulence structure to the above was observed in *Posidonia oceanica* canopies under unidirectional flows [*Hendriks et al.*, 2008]. According to *Nepf and Ghisalberti* [2008] in the upper canopy the turbulence scale is close to the width of the shear layer and approximately equal to the canopy height (h_s) (for rigid roughness elements). The roughness length was equal to the elevation corresponding to 85-90% of the canopy biomass [*Neumeier and Amos*, 2006b; *Neumeier*, 2007] in marsh canopies. The roughness length increased with plant density and was dependent only upon canopy characteristics and not on flow velocity or depth [*Neumeier*, 2007]. However some authors [*Shi and Hughes*, 2002; *Lefebvre*, 2009] found the roughness to be much smaller (the order of mm). *Gacia et al* [1999], using the time-averaged vertical velocity profile (and assuming that a logarithmic profile existed above and inside the canopy), estimated the roughness length (Z_0) to be 10±2.2 cm in a *Posidonia oceanica* meadow sheltered from waves (when canopy height was 68±11.5 cm and stem density was 291±133 stems/m^2). Moreover the roughness length Z_0 was found to decrease with decreasing canopy height.

The importance of the above-canopy shear stress decreases when the flow is confined (high submergence ratio) [*Nepf and Vivoni*, 2000]. Also under waves, the role of the shear at the top of rigid canopies is minor [*Lowe et al.*, 2008], especially for the shorter waves (smaller A) [*Lowe et al.*, 2005b].

Information on turbulence and on boundary layer structure induced by seagrass canopies in wave-dominated environments is scarce. Near-bed turbulence levels were 3 times smaller in a *Posidonia* meadow than in an adjacent sandy bed. Reynolds stresses were higher at the edge of the meadow [*Granata et al.*, 2001]. The same study showed a reduction in the total kinetic energy of a flow, from 100 cm to ≈10 cm above the bottom; this was larger in the meadow (up to 95%) than over the sand (35 to 75%). Under long-period waves, a bed of *Amphibilis antartica* seagrass presented a peak of mean kinetic energy at the canopy top and small vertical turbulent motions [*Verduin and Backhaus*, 2000]. In tidal environments, a small species of seagrass, *Zostera mulleri*, was found to extend the boundary layer upwards and to enhance bed roughness especially when waves were present [*Bryan et al.*, 2007].

In flume experiments with coral canopies exposed to waves, large and periodic wall shear stresses, just above the coral, were attributed to sharp velocity gradients at the canopy top. In these experiments, the canopy shear stress under oscillatory flows was determined from the peak in the vertical profile of the phase-averaged term (<U'W'>) of the Reynolds stresses [*Reidenbach et al.*, 2007; *Lowe et al.*, 2008]

$$\left\langle \tau_{xz} \right\rangle \cong \rho \left| \left\langle U'W' \right\rangle_{\max} \right| \qquad \textbf{Eq. 2-31}$$

The shear stresses, obtained by *Reidenbach et al.* [2007], from the normalised value of the wave-induced peak shear stress ($<U'W'>/<U_{rms}>^2$), ranged between 0.008 and 0.004; they were on average 0.007 according to *Lowe et al.* [2008]. The term $\left\langle \tau_{xz} \right\rangle$ of Eq. 2-31 represents the canopy shear stress (analogous formula to the bed shear stress) and it can be also expressed as [*Sleath*, 1987; *Lowe et al.*, 2008]:

$$\langle \tau_{xz} \rangle = 0.5 \rho C_f U_{\inf}{}^2 \qquad \textbf{Eq. 2-32}$$

Average values of C_f (the shear stress coefficient at the top of the canopy) of 0.014±0.002 were found for coral canopies with a mean submergence ratio (h_s/D) of 0.27, exposed to waves; these were very similar values to those calculated for the same canopy under unidirectional flows, [*Lowe et al.*, 2008].

2.6 Seagrass, sediments and sediment dynamics

According to *Koch* [1999] and *Koch and Gust* [1999], unidirectional flows over seagrass beds of *Thalassia testudinum* deflect the water over the meadow resulting in lower mixing between the water column and the water within the canopy (unless wind is present). The low mixing is believed to enhance sediment deposition. In contrast, waves produce a back-and-forth movement of the leaves, thus increasing the mixing between the water above, and within, the plants. The authors state that "higher shear stress could be observed near the bottom of wave-dominated sites and more particles could be maintained in suspension".

The modified bottom boundary layer, induced by meadows, might promote sediment deposition by reducing re-suspension rates in a 15m deep *Posidonia oceanica* meadow [*Granata et al.*, 2001] and in shallower meadows protected from wave action [*Gacia et al.*, 1999]. Although reduced, vertical mixing and sediment resuspension are important processes in seagrass habitats; reduced hydrodynamic energy is not the only mechanism for trapping sediments in seagrass and protecting shorelines from erosion [*Koch*, 1999; *Koch*, 2001]. The *matte* structure of *Posidonia oceanica* traps great quantities of sediment and stabilises the seabed [*Gacia et al.*, 1999]. According to early studies [*Jeudi de Grissac and Boudouresque*, 1985], the development of a *matte* structure has a "reef effect" and reduces the seabed slope, therefore limiting sediment erosion. Sediment accumulation amongst seagrass, in the long-term reduces water depth; this in turn, helps reducing wave energy and protecting the coast [*Koch et al.*, 2009]. *Price at al*. [1968] tested an artificial seagrass bed under waves and concluded that the meadow might promote onshore sediment transport, by increasing the net drift towards the shore. Recently, it was observed that the collision of particles with the leaves, leading to loss of momentum, is another mechanism for particle retention in *Posidonia oceanica* beds [*Hendriks et al.*, 2008]. However, some studies indicate that

sediment trapping in low density or low biomass seagrass meadows is largely insignificant [*Mellors et al.*, 2002; *van Katwijk et al.*, 2010].

Sediments in the *Posidonia oceanica* meadows have usually a different composition to those in adjacent areas [*Jeudi de Grissac and Boudouresque*, 1985]. In general, the meadows are characterised by finer sediments richer in organic matter [*Gacia et al.*, 1999; *De Falco et al.*, 2000]. However, a detailed study on the distribution of sediments within a *Posidonia sinuosa* meadow, in a high energy environment in Western Australia showed high variability within the meadow; the distribution depended upon seasonality and to the degree of exposure to waves [*Van Keulen and Borowitzka*, 2003]. *Manca* [2006] studied the wave climate, sediment grain-size distributions, and sediment transport patterns at a site exposed to some of the largest waves in the Mediterranean (Maimoni Beach, Sardinia). This study found bimodal sediments and relict deposits of coarse sand only within the *Posidonia* meadows. The bimodality of sediments within the *Posidonia* meadow has been attributed to the presence of carbonate sand and the abundance of carbonate-producing organisms supported by the ecosystem. An increase in carbonate and bioclast content was also found in other studies [*Jeudi de Grissac and Boudouresque*, 1985; *De Falco et al.*, 2000; 2003]. The sediment is coarser, but still mainly composed of biogenic materials, in the inter-matte channels and the high energy areas at the edges of the meadows. This characteristic has been attributed to the erosion of the matte and the depletion of fine sediments, resulting in a relative enrichment of coarse grains [*De Falco et al.*, 2000].

3 Chapter 3: Waves and flows in a natural *Posidonia oceanica* bed

3.1 Introduction

Posidonia oceanica, the most abundant seagrass species in the Mediterranean, has a fundamental role in the coastal sand budget and in protecting the shoreline from erosion [*Jeudi de Grissac and Boudouresque*, 1985; *Gacia and Duarte*, 2001; *De Falco et al.*, 2006]. *Posidonia* meadows are known to act like a shallow reef inducing wave breaking and reducing the wave energy reaching the coast [*Jeudi de Grissac and Boudouresque*, 1985], but seagrass also dissipates energy by enhancing friction at the bed [*Fonseca*, 1983; *Koch et al.*, 2006b; *Bradley and Houser*, 2009; *Koch et al.*, 2009]. *Posidonia oceanica* has a different morphology to the aquatic vegetation previously in the field [*Koch and Gust*, 1999; *Möller*, 2006; *Augustin et al.*, 2009; *Bradley and Houser*, 2009] or in wave tanks [*Asano et al.*, 1992; *Fonseca and Cahalan*, 1992; *Wallace and Cox*, 2000; *Bouma et al.*, 2005]. Hence wave energy reduction rates can be expected to be different.

Previous *in-situ* studies of *Posidonia oceanica*, carried out on a 15 m deep meadow off the Catalan coast, established that a meadow reduces the currents [*Gacia et al.*, 1999] and wave orbital velocities in the canopy [*Granata et al.*, 2001]; hence, prevents sediment resuspension [*Gacia et al.*, 1999; *Gacia and Duarte*, 2001]. *Posidonia* is thought to increase bed roughness (Z_o), when wave effects are neglected [*Gacia et al.*, 1999]. Little work has been done in terms of wave-induced flows in seagrass beds, particularly for *Posidonia* meadows. Moreover, wave dissipation by bottom friction has not been quantified over *Posidonia oceanica* beds, despite their widely-accepted importance for Mediterranean coasts. In addition, seagrass is known to affect sediment composition [*De Falco et al.*, 2000; *De Falco et al.*, 2008], but direct observations of the effect of seagrass canopies on sediment motion are limited [*Bouma et al.*, 2007], or show contrasting results (Baptist, 2003).

This chapter describes a field study of a shallow *Posidonia oceanica* meadow, and its interactions with waves and wave-induced flows. The study site, located within the Gulf of Oristano (West coast of Sardinia, Italy), is characterised by a very shallow *Posidonia oceanica* bed, exposed to the prevailing NW (Mistral) waves, which dominate the littoral dynamics. The *Posidonia oceanica* meadow distribution and its canopy height were mapped using a high resolution sonar. Bathymetric maps and sediment charts were also produced, to characterise the area; these were used to examine the distribution of *Posidonia oceanica*.

The effect of a *Posidonia* patch on the hydrodynamics was evaluated from data collected by 3 autonomous multiprobe instruments that recorded water level, flow velocity and turbidity, at 3 locations. The instruments recorded over 1 week, covering both low energy conditions and a typical Mistral event. Wave height reduction over the *Posidonia oceanica* bed was quantified in terms of wave height decrease and wave dissipation factors (f_e). Wave-induced flows were separated from the unidirectional component and compared at the 3 locations. Wave-induced flow asymmetry was evaluated to verify laboratory evidence that seagrass might induce a net drift of water towards the shore [*Price et al.*, 1968]. Turbidity records were also analysed. However, the study conditions prevented any conclusions been drawn on sediment suspension within and outside the seagrass bed.

The next section of the Chapter (Section 3.2) introduces the study region, in particular the typical hydrodynamic conditions, the seagrass distribution and the sediment dynamics. The field campaign consisted of three parts (survey undertaken from a small vessel, bottom sampling by divers and instrument deployment); it is described in Section 3.3. The methods used for the data analysis are reported in Section 3.4. The results are presented and discussed in Section 3.5. This section is subdivided into two major parts: the description of the seabed and the *Posidonia* meadow and the interaction of *Posidonia* with waves, unidirectional flows and wave-induced flows. The findings are summarised in Section 3.6.

Results from this sonar survey have been compared with results from other studies of canopy height distribution, for different species of seagrass (*Paul et al.*, in preparation).

3.2 The field study site

3.2.1 Location

The study site is located in the Gulf of Oristano (west coast of Sardinia, Italy), near the small fishing harbour at the inlet of the Santa Giusta lagoon (Figure 3.1). The site is located in the central part of an asymmetrical 20 km long sandy beach, interrupted only by the mouths of several coastal lagoons and the Tirso River.

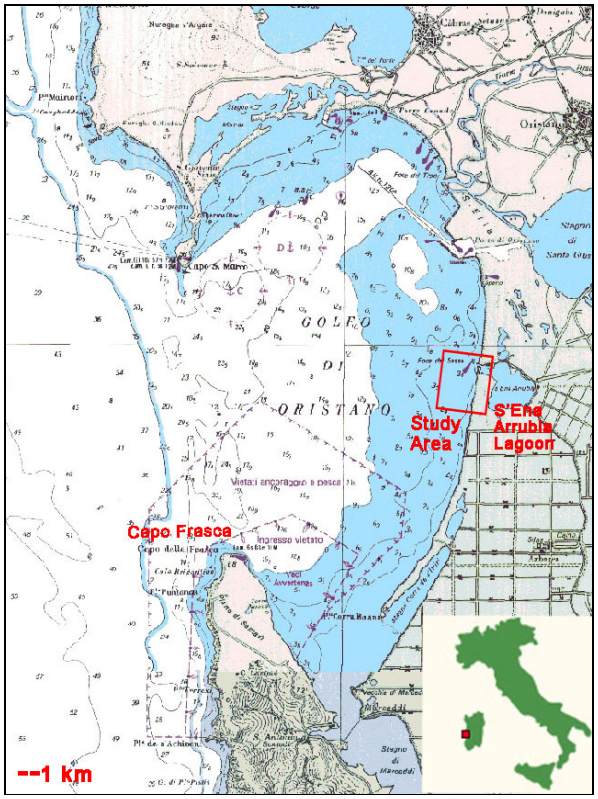

Figure 3.1 Location of the study region in the Gulf of Oristano, Sardinia, Italy. [The background chart was adapted from that of the *Istituto-Idrografico-della-Marina*, 1985]

In the shallow, microtidal Gulf of Oristano, wind-driven circulation and waves play a very important role in the coastal dynamics at intermediate time-scales [*Cucco et al.*, 2006; *Tigny et al.*, 2007]. The site is exposed to swell from the SW and to the prevailing NW winds; it is characterised by a *Posidonia oceanica* meadow that extends almost to the shore. These characteristics were the main factors in the selection of this study site. The study region (Figure 3.1) extends to a maximum depth of about 8.5 m.

3.2.2 Hydrodynamics and winds in the Gulf of Oristano

The general circulation off the Gulf of Oristano is driven by a branch of the main surface flow entering the Mediterranean, at Gibraltar, which is directed northwards along the west coast of Sardinia. Sardinian shorelines are classified as microtidal, and the mean tidal range in the Gulf is 0.2 m [*Ferrarin and Umgiesser*, 2005]. Meteorological surges and wind-induced surges have often a more significant effect on sea level than tidal oscillations; wave and wind action dominate the hydrodynamics in the Gulf of Oristano [*Cucco et al.*, 2006]. A clockwise water circulation inside the Gulf is generated by the dominant Mistral winds blowing from the NW sector [*Cucco et al.*, 2006]. Libeccio (SW) and Scirocco (SE) winds both produce an anti-clockwise circulation, with currents directed northward in the central part of the Gulf.

At Capo Frasca, (southern cape of the Gulf of Oristano, south of the study area, see Figure 3.1), the wind, which is predominantly from a NW direction, is stronger than 13.5 m/s once every 4 days (i.e. 25 % of the records) [*ARPA-Sardegna*, 2005]. For more than half of the year, the wind reaches a speed greater than 8 m/s. Winds from the NW and W occur during 50% of the observations, whilst winds from the southern sectors (E, SW, and S) occur 26% of the time. Mistral winds are linked to the general Mediterranean atmospheric conditions; they develop in the Gulf of Lions and thus have a long fetch before reaching the west coast of Sardinia (Figure 3.2). As a consequence, the highest waves in the Alghero-provenzal basin are recorded along the west coast of Sardinia [*SDGM and ECMWF*, 1993].

The weak winds are influenced by the local topography and are often related to local breeze regimes, which can be significant during the summer. In the study region the prevalent land breeze is from the S, whilst the sea breeze is from the W (*IAMC Oristano*, oral communication).

The closest wave rider buoy to the study area is that of Alghero (around 100 kmto the north of the Gulf). It is a directional wave rider belonging to the RON (Rete Ondametrica Nazionale, National wave-riders network) buoy network, moored at a depth of 85 m [*RON*, 2010]. In Alghero, the average gross annual wave energy flux (recorded between 1990 and 2003) is 54.02 Kw/m [*APAT*, 2006]. A significant wave height increase of 1.5 cm/yr has been found from measurements by the Alghero wave buoy [*Franco et al.*, 2004]. From the data it emerges that the typical direction of wave propagation on the western coast of Sardinia is 300° N, (range 295°-330° N, 75% of waves propagate from this sector) and frequently waves have a significant height of 2 m

[*APAT*, 2006] (Figure 3.2). Waves with heights greater than 2 m propagate from the same sector, with no seasonal variation. Most of the storm waves have a mean direction of propagation of between 300° N and 315° N (Figure 3.2). Smaller waves from the southern sectors, S (190° N) and SW (225° N) are also observed. SW waves occurred only in 5% of the cases and the maximum wave height recorded for this sector was 5.5 m.

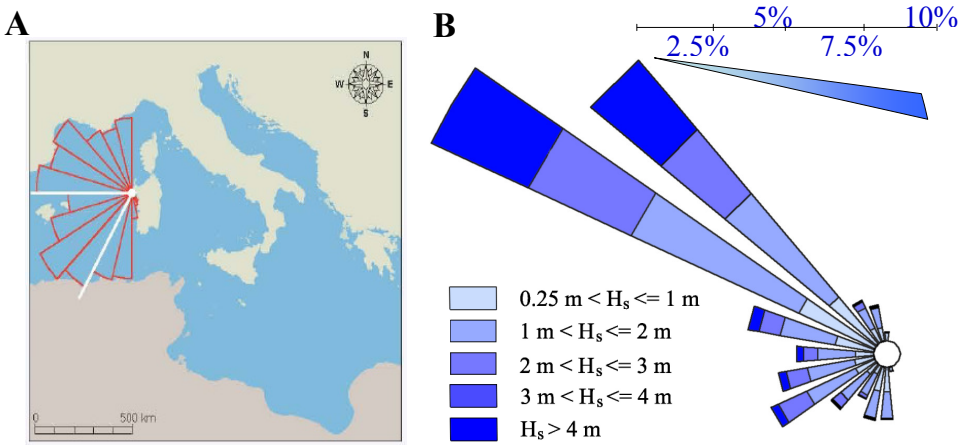

Figure 3.2 A) Sectors of fetch from the wave rider buoy of Alghero. B) Annual wave regime for the west coast of Sardinia. Directions of propagation and frequency (%) of significant waves recorded by the RON-Alghero are shown. [*Franco et al.*, 2004].

The mean wave periods recorded were within the range of 2-13 s. The longest wave periods were related to the largest waves from the NW sector (270-330°N). The most common waves (2 m height) [*APAT*, 2006] had a mean period of between 3.5 and 6.5 s. These patterns are confirmed by model studies of wave propagation inside the Gulf of Oristano (reported in Figure 3.1, adapted from De Falco et al. [2008]), which show that waves entering this shallow Gulf are reduced significantly by bottom friction. Wave height reduction is significant in the northern and southern sector of the Gulf. Mistral waves enter the central part of the Gulf, where they are perpendicular to the shoreline. *Atzeni* [2003] also reports that the mean annual longitudinal net energy flux in the southern part of the Gulf of Oristano is zero as the net wave energy flux is normal to the shoreline.

Vertically-averaged current velocities are largest in the northern part of the Gulf, where they reach 0.4 m/s under a 15 m/s Mistral forcing; these are reduced to 0.1 m/s in the sheltered coastal areas [model results of *Cucco et al.*, 2006].

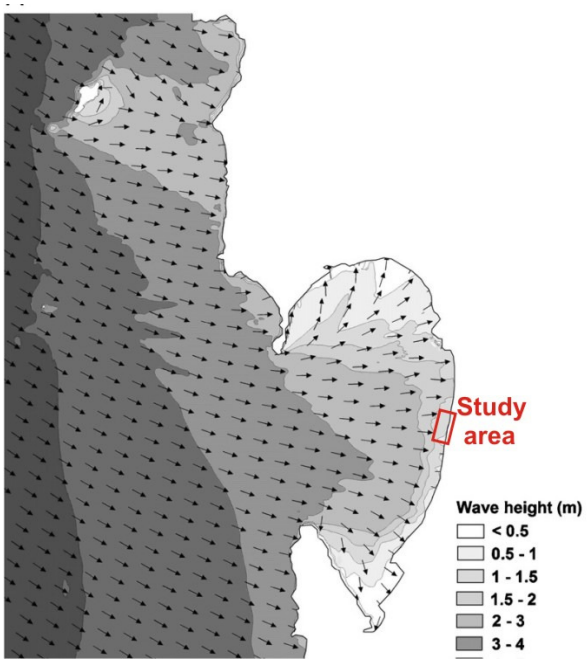

Figure 3.3 Swan model output of Mistral waves with a return period of 1 year (10 s peak wave period, 108° peak wave direction and 8 m significant wave height) propagating inside the Gulf of Oristano. Arrows indicate wave direction and wave height contours are shown in shaded areas [adapted from *De Falco et al.*, 2008]

3.2.3 Sediment transport and distribution of seagrass in the Gulf of Oristano

The sediment input from the sea is low and even the major river entering the Gulf, the Tirso River (Figure 3.1), carries only a limited amount of solids [Atzeni, 2003]. The river has a large dam that retains water coming from 64% percent of the basin and has an average run-off lower than 5 m^3/s [*De Falco et al.*, 2008]. The majority of the fine sediments from the Tirso river are deposited to the north of the mouth and towards the deepest part of the Gulf [*De Falco et al.*, 2006]. Sediments from the central sector of the Gulf were deposited by a paleo-river and are mainly siliciclastic and poorly sorted [*De Falco et al.*, 2008]. The more sheltered northern and southern sector of the Gulf are characterised by sediments rich in carbonates and coarse biogenic particles, derived from the epiphytes and vagile fauna associated with *Posidonia oceanica* beds. Sediment winnowing, in a NW to SE direction and induced by dominant Mistral waves, is believed to have occurred in the central areas of the Gulf, [*De Falco et al.*, 2008]. Assuming that coarse sediment cannot be transported within the meadow, the winnowing had to take place prior to the establishment of the *Posidonia* meadow [which can take up to 600 years, *Kendrick et al.*, 2005]. Previous studies [*Carboni et al.*,

1990] also found possible longshore sediment transport of the sandy fraction to the south at the study area. In addition, the shape of the littoral barrier of Corru s'Ittiri, to the south of the study area, indicates a net long-shore southward transport. The sandy shores of the northern sector of the Gulf have undergone significant variations, due to littoral drift, human activities and natural erosion [*Tigny et al.*, 2007]. The area is characterised by a highly degraded and retreating *Posidonia oceanica* meadow. The shoreline evolution is partially related to changes in the position of the upper limit of the *Posidonia oceanica* meadow [*Tigny et al.*, 2007].

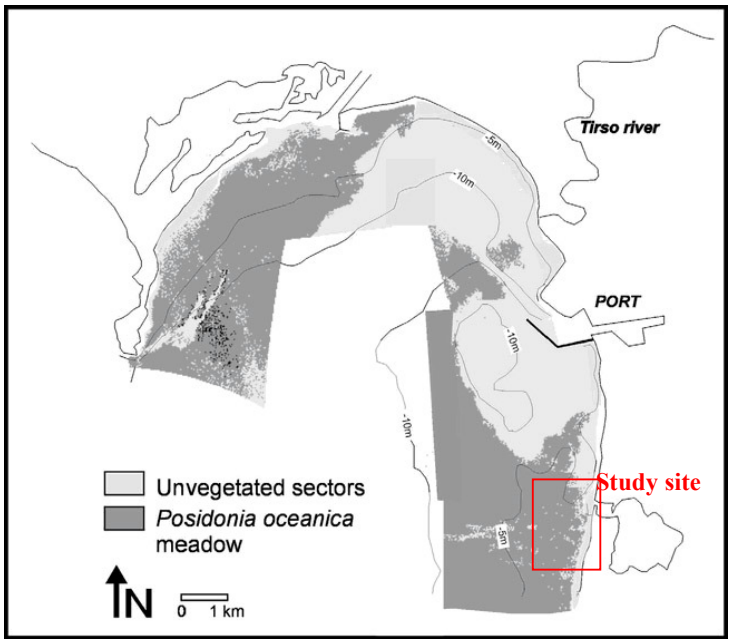

Figure 3.4 Distribution of *Posidonia* meadows in the northern sector of the Gulf of Oristano and in the study region. (De Falco et al., 2006)

About 70% of the Gulf is colonised by *Posidonia oceanica* [*Baroli et al.*, 2003]. Siltation resulting from increased sedimentation following dredging of the large Oristano harbour (north of the study site, Figure 3.4), has caused a deterioration of the *Posidonia oceanica* beds to the south of the breakwater [*De Falco et al.*, 2006]. Another large un-vegetated area is located near to the Tirso River embankment. *Posidonia oceanica* density is not related to water depth [*De Falco et al.*, 2008] and is, on average, 287 shoots/m^2 in the Gulf [*Baroli et al.*, 2003]; in particular, it averages 314±76 shoots/m^2 in the central sector [*De Falco et al.*, 2008]. The upper limit of the meadow is progressively closer to the shore to the south of the small S'Ena Arrubia harbour, in the northern part of the study area [*Baroli et al.*, 2003] (see Figure 3.4).

Near to the study site, the rhizome growth rate is similar to the physiological growth rate of *Posidonia oceanica* (0.7cm/year), indicating that vertical rhizome growth is not stimulated by sediment accumulation, as it is in the northern, more sheltered, sectors of the Gulf [*De Falco et al.*, 2008]. Research into the morpho-dynamics the Gulf of Oristano [*De Falco et al.*, 2000; *De Falco et al.*, 2003; *Tigny et al.*, 2007; *De Falco et al.*, 2008] indicate some connection between the seagrass beds, sediment composition, sediment dynamics and waves in the Gulf.

3.3 Field campaign

3.3.1 Boat survey and instrument description

A survey of the study area was undertaken on the 13th and 14th May 2007 during low energy conditions (wave heights less than 0.1 m). The vessel was equipped with a GPS, an echosounder, and an SIS (Sediment Imaging Sonar, Marine Electronics Ltd.). The SIS and the echosounder were deployed on a downrigger and positions were recorded with the GPS (resolution ± 10 m). A total of 17 lines were surveyed, at an average speed of 3 knots, with an average line spacing of about 100 m (Figure 3.5). On the 14th May, clear water conditions permitted visual observation of the seabed from the vessel and direct comparison with SIS real-time data visualisation. It was concluded that the data accurately reproduced the bottom types.

The SIS is a high-frequency (1.1 MHz), single beam sonar with a rotating head, derived from the Image profiling Sonar 1640/2640 by Marine Electronics Ltd. A detailed description of the instrument characteristics can be found in Lefebvre et al. [2009]. The device records echograms (backscatter information along a beam) of the water column and the seabed as image files (*.img) for each sweep [*Lefebvre et al.*, 2009]. The beam angle was fixed at 90˚, and the SIS recorded every 0.9˚; thus, each sweep was composed of 100 beams. The SIS swept over the bed perpendicularly to the direction of boat travel; therefore a zig-zag shaped track was produced. The transmit pulse duration was set to 62 μs, providing a vertical resolution of 3.9 cm and the range (distance along a beam) was set to 10 m. In order to obtain accurate depth values, the speed of sound was set before starting the data acquisition.

The speed of sound was calculated from measurements of water salinity and temperature (Table 3-1). Temperature and velocity profiles showed a well-mixed water

column, therefore, no correction was needed for a change in speed of sound with depth. The horizontal distance over which the sweep was recorded depended upon the water depth (between 2.5 and 8.5 m) and the boat speed, since the sweep angle was fixed. Therefore horizontal resolution was greatest in shallow waters.

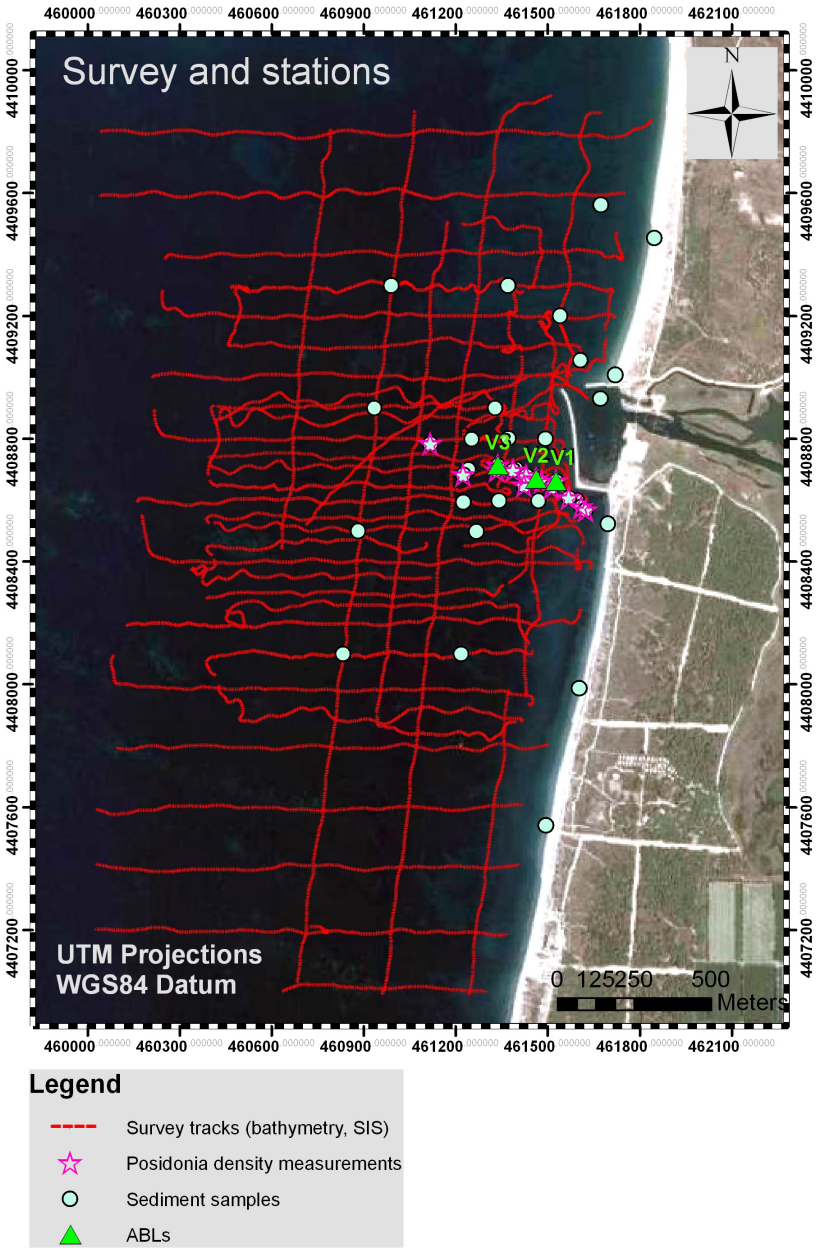

Figure 3.5 Location of the survey lines, sampling and instrument deployment sites. Background satellite image from Google Earth-2007.

Before the field survey, the SIS was used typically on a fixed frame, to obtain high-resolution images of the bed and bed roughness. This was the first time that the SIS has been used in a survey mode and, hence, was considered experimental. Since this work, the device has been used successfully in other field surveys [*Lefebvre et al.*, 2009].

Table 3-1 Settings of the Sediment Imaging Sonar.

Transmit pulse (μs)	62
Vertical resolution (cm)	3.9
Depth of transducer head (m)	0.8
Water temperature (ºC)	19.3
Salinity	37.6
Velocity of sound (m/s)	1522

3.3.2 Bottom sampling

During the acoustic survey of the study site, divers collected *Posidonia* and sediment samples, measured *Posidonia* shoot density and took underwater pictures at the ABL deployment sites. Fourteen *Posidonia* sampling stations were selected randomly chosen along a cross-shore survey transect, orientated in a NW-SE direction and passing through the ABL deployment sites (Figure 3.5). At least 5 *Posidonia* shoots were collected at each site from several plants. *Posidonia* shoot density was measured *in-situ*, by counting the number of shoots inside a 50 x 50 cm standard sampling quadrat, following a standard protocol [*Duarte et al.*, 2001] (Figure 3.6).

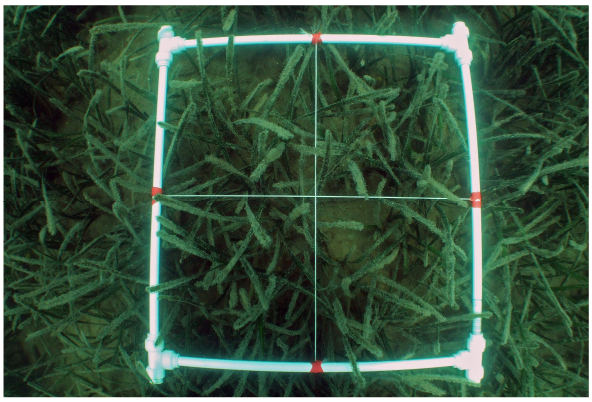

Figure 3.6 The standard 50 x 50 cm quadrat [*Duarte et al.*, 2001] used for seagrass density measurements. Note: the edges of the quadrat were straight, but are distorted slightly here by the camera lens.

In addition, a total of 36 sediment samples (Figure 3.5) were collected by divers from the upper 5 cm layer of the seabed, both at the *Posidonia* sampling sites and in a grid over a wider area. Also 5 sediment samples were collected from the swash zone of beaches lying to the north and south of the harbour, with a 500 m spacing.

3.3.3 Deployment of the Autonomous Benthic Landers

On the 10th May, three ABLs (Autonomous Benthic Landers constructed by Valeport Ltd) multiparametric instruments were deployed along a north-westerly oriented transect (Figure 3.5). The ABLs consist of: i) a capacitance-type pressure sensor; ii) an electromagnetic current meter (EMCM); and iii) an optical backscatter sensor measuring water turbidity. A diagram of one of the ABLs is shown in Figure 3.8 and a photograph of an ABLs mounted on its frame is shown in Figure 3.7. The elevation of each sensor above the sea bed is reported in Table 3-1, as well as other relevant instruments settings and details on the deployment station.

Table 3-2 Autonomous Benthic Landers settings and location.

Site	V1	V2	V3
Site description	Sand	Sand, 0.5 m from the shoreward edge of *Posidonia* meadow	*Posidonia* meadow
Average depth (m)	4.3	4.9	*5*
Distance from shore (m)	218	275	404
OBS and Pressure Sensor height above bed (m)	0.5	0.5	0.5
EMCM height above bed (m)	0.27	0.27	0.27
Total duration of the deployment (hours)	146	187	187
Sampling rate (Hz)	4	4	4

The distance between sites V1 and V2 and sites V2 and V3 were 65 m and 132 m, respectively. Pressure signals were recorded every hour, for 15 minutes, at a frequency of 4 Hz. Current and turbidity data were recorded every 20 minutes for 4 minutes at 4 Hz. Details of the functioning of each sensor of each ABL are given below.

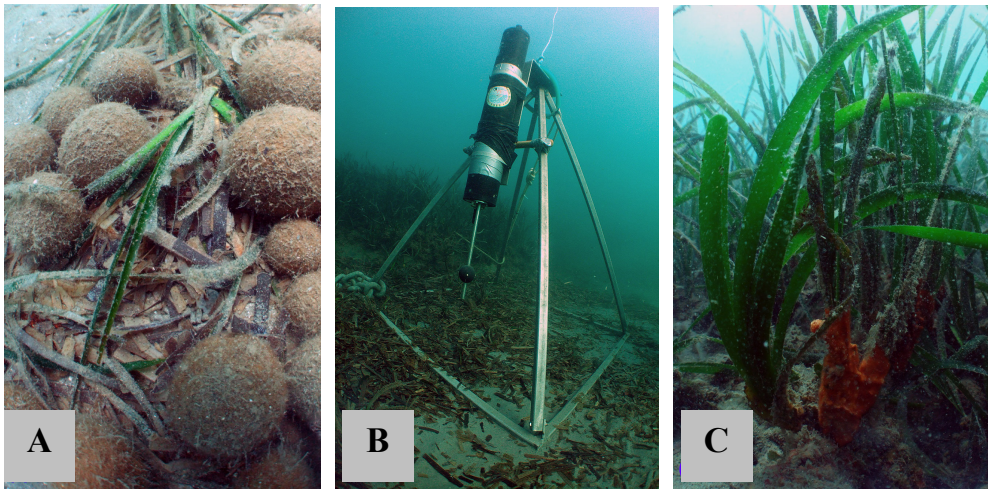

Figure 3.7 Photographs taken at the deployment sites.: (A) Site V1, *Posidonia oceanica* uprooted plants and debris;(B) Site V2: ABL at meadow edge in the background the edge of the seagrass meadow, with a 20 cm thick matte. Note: the seabed was sandy with some seagrass debris; and (C) Site V3, *Posidonia oceanica* plants with orange incrusting sponge at its base.

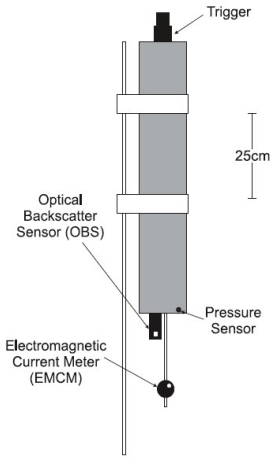

Figure 3.8 Diagram of an ABL used during the field campaign [modified from *Plomaritis*, 2006].

The pressure sensor consisted of a thin silicon diaphragm which deflects with changes in water pressure. This deflection is translated into changes in capacitance and converted into a voltage signal which is in phase with waves.

The Electro-Magnetic Current Meter (EMCM), utilises the Faraday principle of electromagnetic induction, which states that the water moving in a magnetic field will produce a voltage that is proportional to the velocity of the water. It has a sampling volume that is typically two to three times the diameter of the probe (40 mm) [*LIM/UPC*, 2010]. The voltage difference is measured between two electrodes once every cycle of an AC electro-magnet that generates the magnetic field. The

manufacturer's calibration curve was used to convert from voltage to velocity signal. These instruments are able to detect very slow flows and are not affected by the presence of obstacles in the sampling volume [*Collar and Griffiths*, 2001] (such as seagrass leaves).

Optical Backscatter Sensors (D&A Instrument) work by detecting infra-red light scattered from suspended matter and their response, which is almost linear, depends upon the composition, size and shape of the particles in suspension [*Van Rijn*, 2007]. For this reason, a good empirical calibration with local sediment is required, in order to transform voltage output into suspended sediment concentration.

3.4 Data analysis

3.4.1 Survey and sampling

3.4.1.1 Bathymetric data processing

The data collected with the echosounder were calibrated (see calibration regression in Figure A. 1, Appendix A) and corrected for tides. The water level for the tidal correction was obtained from the ABL records, obtained during the survey. GPS positions were converted to UTM coordinates (WGS84). The correct depth measurements were coupled with the GPS positions, then interpolated using the Kriging method and transformed into raster format in ARCMAP 9.1 (TM) (5 m cells).

3.4.1.2 SIS data processing

The SIS data were processed, to obtain canopy height and water depth. The manufacturer's software (Sediment Imager converter 1.0) was used to convert the raw data from the SIS, into backscatter intensity, beam angle, and distance from the transducer head. The algorithm for processing the SIS data in survey mode was developed originally by *Lefebvre* (2009) for *Zostera marina* canopies; it was modified in the present work for *Posidonia oceanica*. Moreover the algorithm for the canopy height measurement was improved recently. The seabed represents the sharpest contrast in acoustical impedence and is the strongest acoustic signal [*Warren and Peterson*, 2007]. However, the submerged vegetation produces also a strong backscatter signal from immediately above the bottom, to the height of the canopy [*Sabol et al.*, 2002]. Therefore, the SIS was able to differentiate the seabed from the *Posidonia* canopy

(where present). The canopy was detected as a secondary backscatter peak, because of the relatively high reflection, caused by the air bubbles within the leaves [*Lefebvre et al.*, 2009].

The vertical position of the seabed was obtained as the depth corresponding to the maximum backscatter. Only the 5 central beams (±1.8 degrees; on average 0° corresponds to the nadir) of each sweep were averaged reducing the need for a correction for the beam angle [*Lefebvre*, 2009]. Values of the depth of the seabed (D) were then corrected for tide variations that were recorded during the survey.

The canopy height (CH) was detected as the maximum difference in backscatter between two measurements along a beam, using a method similar to that developed by *Warren and Peterson* [2007]. Only backscatter data between the bed and 0.80 m above the bed were used in this analysis. This upper depth limit was greater than the expected maximum canopy height, obtained from the typical maximum leaf length of *Posidonia oceanica* [0.75 m, *Buia et al.*, 2004]. More details on the method used to detect canopy height are presented in a manuscript prepared in collaboration with *Paul et al.* (in preparation).

3.4.1.3 Sediment analysis

Sediment samples were split into sub-samples (about 50g each), one of which was wet-sieved at 63 μm with de-ionised water to separate the sand fraction from the fines and to wash out any salts. Both the sand fraction and the fraction smaller than 63 μm were oven-dried for 12 hours at 60°C, then weighted. The sand/mud ratio was obtained as the ratio, by weight, of the sand and the < 63 μm fraction.

The grain size spectra of the sand fraction were determined using a 2 m tall settling tower. A detailed description of the settling tower of the NOC sediment dynamics laboratory can be found in *Plomaritis* [2006]. Grain-size distribution of each sediment sample was determined from the settling velocity (w_s) of each grain, which is determined by the size, shape and the density of the particle. There are two main advantages in using a settling tower for grain-size analysis instead of a more conventional mechanical procedure (such as dry sieving): i) the grain size distribution is not divided into large discrete categories and it is more accurate (compared to sieving); and ii) the method is more suited for sediment dynamics studies [*Rigler et al.*, 1981;

Plomaritis et al., 2008] as the effect of the grain density and shape (which affect incipient motion) are taken into account.

In order to avoid turbulence in the waters in the settling tower, which might affect negatively the results, the gravel fraction (> 2000 μm) was discarded. Gravel was present in a few samples, but it constituted a negligible percentage. The measurement was repeated at least 3 times for each sample (using 1g sub-samples, divided randomly with a sediment splitter). During the analysis, the resulting grain size distribution curves were checked; as such curves were discarded when obvious instrumental errors were observed, before obtaining average grain-size parameters. The settling velocities (w_s) of each grain were converted to grain diameter (d_{50}), corresponding to a spherical grain of quartz, using Soulsby's formula [*Soulsby*, 1997] with the support of a Matlab routine *Cal_settling* [*Neumeier and Ciavola*, 2004]. The equation for this transformation is:

$$w_s \equiv \frac{\nu}{d_{50}}\left[(10.36^2 + 1.049D_*^3)^{0.5} - 10.36\right] \qquad \textbf{Eq. 3-1}$$

where: d_{50} is the median diameter of grains (m); s is the ratio of density of quartz grain (2650 kg m^{-3}) and density of water (ρ); υ is the kinematic viscosity of water (assumed to be equal to 1.0 X 10^{-6} m^2 s^{-1}); and D_* is the dimensionless grain size defined as:

$$D_* = \left[\frac{g(s-1)}{\nu^2}\right]^{1/3} d_{50} \qquad \textbf{Eq. 3-2}$$

The temperature of the water was regularly monitored during the analysis and a maximum variation of 2°C occurred. For each station at least six replicas of grain-size distribution curves were obtained; they were averaged, to obtain a final grain size distribution. The variation due to the temperature difference was quantified as smaller than the variation between replicas (which migh represent the accuracy of the procedure). For example, a temperature variation of 2ºC would produce a difference of 0.032 φ in the mean grain size (d_m), while the standard deviation of d_m between replicas was 0.17 φ, at Station V2. The statistical parameters of the grain-size distributions (mean, sorting, skeweness and kurtosis) were also calculated according to the graphical method defined by *Folk and Ward* [1957]. The percentage of organic matter in the sediment was obtained by incineration in a furnace at 450°C for 6 hours. Maps of the distribution of grain size, sand sorting, mud/sand ratio and organic fractions were produced in ARCMAP, using a nearest neighbour interpolation; they were transformed into a raster file with a 5 m size cell.

3.4.1.4 Seagrass plants and meadow characteristics

Density measurements were converted to number of shoots per m^2 , whilst the measurements from several samples from the same site were averaged. The leaves were distinguished by class (young, intermediate, or adult) following the standard method proposed by *Buia et al*. (2003) (illustrated in Appendix B). The number, length and width of the leaves in each shoot were measured when fresh. The base height (part of the leaf inserted in the rhizome, below the ligule, Appendix B for definitions) of intermediate and adult leaves was also measured.

3.4.2 Hydrodynamic data and turbidity

The ABLs are equipped with software that transforms the raw data into high frequency calibrated PUV files (pressure, U and V component of velocity) and calculates the statistical parameters for waves and currents, during the entire deployment. The statistical files are easy to obtain. However an unspecified filtering technique is applied and more importantly wave-induced currents are not separated from the total current signal. Each burst file contains 2048 samples. The PUV files were used in this study to obtain a time-series of depth, wave characteristics, currents and orbital velocities at the 3 stations: V1, V2 and V3.

3.4.2.1 Water levels and waves

The data were corrected for atmospheric pressure and for pressure attenuation with depth, based upon the method described by *Tucker and Pitt* [2001]. The pressure data were converted into sea surface elevations, using the UNESCO pressure/depth relationship [*Kamphuis*, 2002]. Time-series of depth were obtained then by adding the mean water depth and the instrument height above the seabed. The sea surface elevations were de-trended to filter out any tidal signal. Calibrated sea level data were used to calculate wave characteristics, using both a zero-crossing analysis [*Kamphuis*, 2002] and a spectral analysis method. Wave spectra were calculated by applying a Fast Fourier Transform, as is common practice [*Tucker and Pitt*, 2001]. The Power Spectral Density was estimated using the Welch's modified average periodogram method [*Welch*, 1967], with a 8 segment Hamming window and 50% overlap. The characteristic wave height (H_{m0}) was estimated from the wave spectra (up to 1Hz):

$$H_{m0} = 4(\sum_{j=1}^{n} S_j \Delta f_b)^{0.5} \quad \textbf{Eq. 3-1}$$

where n is the number of frequency components and Δf_b is the frequency bandwidth (0.039 Hz). The wave period (T_p) was obtained from the inverse of the frequency, corresponding to the maximum spectral energy [*Kamphuis*, 2002]. The wave energy per unit area (E) was obtained as

$$E = \frac{1}{8}\rho g H_{m0}^2 \quad \textbf{Eq. 3-3}$$

From the product of the wave energy density (E) and the wave group velocity (C_g), the wave energy flux (P) was obtained using:

$$P = EC_g \quad \textbf{Eq. 3-4}$$

With C_g obtained from wave theories (see Table 2.1, Chapter 2)

$$C_g = \frac{1}{2} C \left[1 + \frac{2kD}{\sinh 2kD} \right] \quad \textbf{Eq. 3-5}$$

where D is the water depth; C is the wave celerity and k is the wavenumber. The wavenumber was obtained by using a polynomial approximation, to solve the wave dispersion relationship [*Hunt*, 1979].

Wave height variation as a response to changes in water depth was taken into account (see Chapter 2) by calculating a de-shoaled wave height (H'_{mo}, the wave height without the shoaling effect). The following formula was applied to the measured H_{mo} at V1 and V2:

$$H'_{m0} = \frac{H_{m0}}{\sqrt{\frac{C'_g}{C_g}}} \quad \textbf{Eq. 3-6}$$

where the prime is relative to the most seaward location.

3.4.2.2 Currents and wave orbital velocities

The U and V data from the PUV files represent the current components measured by the EMCMs at 27 cm above the bed, in the X and Y planes respectively. The current meter was fitted with a compass to convert the X and Y components to north/south and east/west components of the flow. Bursts from each instrument were filtered using an elliptical filter, a method applied successfully with this type of instrument [*Plomaritis et al.*, 2008]. The filter, with a cut-off frequency of 0.067Hz (15 s), permitted the wave-

induced component of the total current signal to be separated from the current component (i.e. unidirectional currents from other sources, such as wind-induced circulation, tides etc.). An example of the results obtained using the filter is shown in Figure 3.9. The unidirectional current components (U_m) for each burst were analysed as vectors, obtaining average unidirectional current direction and magnitude. Wave orbital velocity under the wave crest (maximum wave-induced current intensity in the direction of wave propagation) and under the trough (minimum wave-induced current in the opposite direction of wave propagation) were calculated as shown in Figure 3.10. The direction of wave propagation was calculated by applying a linear regression to the data in each burst (see Figure 3.10).

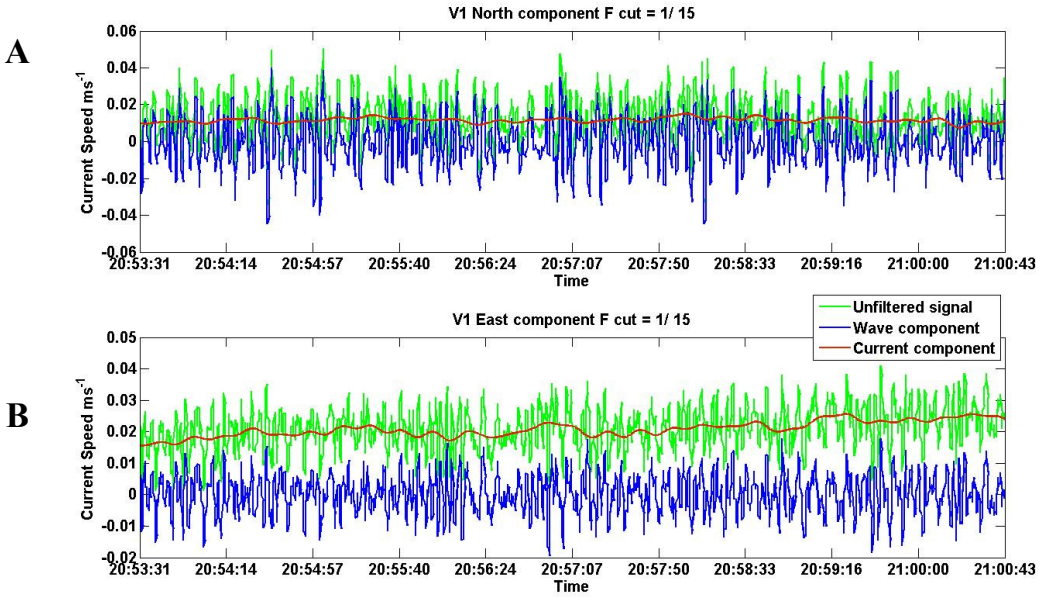

Figure 3.9 Example of the results obtained after filtering of the flow data for the separation of the current and wave component of flow (V1, burst 35). (A) North component of the flow and (B) East component of the flow.

The measured unidirectional velocities were compared to a theoretical critical current speed able to initiate sediment motion. This theoretical value was obtained using Soulsby's method [1997]:

$$U_{mcr} = 7\left(\frac{D}{d_{50}}\right)^{1/7}\left[g(\frac{\rho_s}{\rho}-1)d_{50}f(D_*)\right] \quad \textbf{Eq. 3-7}$$

where D is the water depth, d_{50} is the median grain-size obtained from grain-size analysis of the sand at the deployment sites; D_* is calculated using Eq. 3.2 and $f(D_*)$ is defined as

$$f(D_*) = \frac{0.30}{1+1.2D_*} + 0.055[1-\exp(-0.020D_*)] \quad \textbf{Eq. 3-8}$$

The threshold orbital velocity, for the sand at the deployment sites, was calculated using the *Komar and Miller* [1974] approach,

$$U_{wcr} = \left[0.118g(\frac{\rho_s}{\rho}-1)\right]^{2/3} d^{1/3}T^{1/3} \quad \textbf{Eq. 3-9}$$

where T is the peak wave period and d (grain size diameter) is taken as the measured median grain size (d_{50}). The formula is valid only for sand with d<0.5mm.

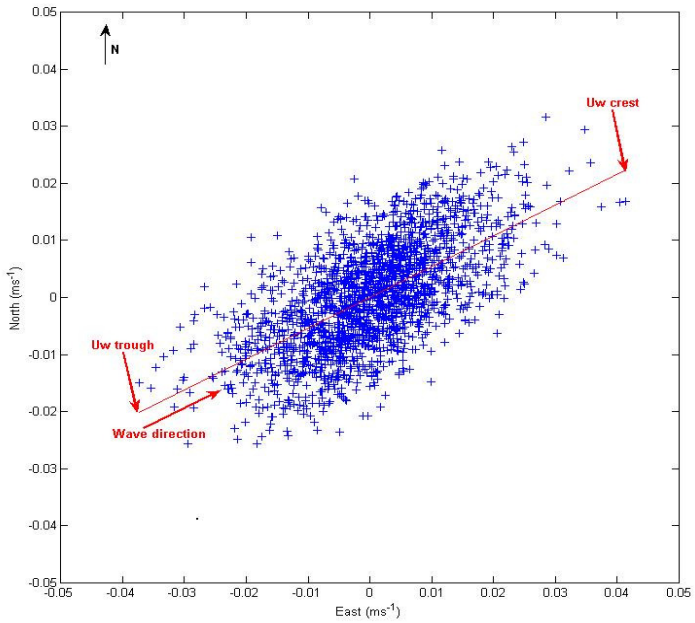

Figure 3.10 A graph showing the methods used for the calculation of wave direction, wave orbital velocity (under the trough and under the crest) from the wave-induced components of the flow.

3.4.2.3 Turbidity

Turbidity at the three stations (V1, V2 and V3) was measured by an Optical Backscatter Sensor mounted 50 cm above the seabed on the ABL frame. Since the

response of the OBS sensors depends strongly upon the size, composition and shape of the suspended particles, a reliable calibration is essential to convert the sensor output from volts to suspended sediment concentration (SSC) in mg/l. Several attempts were made to calibrated the OBS, using the technique proposed by the manufacturer [*D&A-Instruments-and-engineering*, 1988]. However a reliable calibration curve was not obtained. For these reasons, the results are presented and analysed in terms of relative turbidity. An "ambient" level was defined as the average of the values measured by each OBS, over a period of 6 hours in low energy conditions (during the night of day 2 of deployment). Each OBS output (averaged over a burst) was then normalised against the "ambient" level.

3.5 Results and discussion

3.5.1 Survey and sampling

3.5.1.1 Bathymetric map

The area, from the 3 m contour to a maximum depth of 8.5 m, is characterised by a complex irregular bathymetry, particularly tothe south of the S'ena Arrubia harbour (Figure 3.11). The deepest areas are located north of the harbour and along NW-SE oriented channels. A distinctive deep channel, about 150 m in width, starts just offshore from the instrumented transect, about 400 m NW of Station V1. The presence of this channel was observed in aerial photographs and it was confirmed during diver survey, which noticed in the area a deep-cut trough in the seagrass "matte", with sides of about 1m in height. Other smaller channels were evident lying about 1000 m to the south of the harbour, with a similar orientation. A 3D map, enhancing the morphology of the seabed is shown in Appendix A (Figure A. 3B).

3.5.1.2 Canopy characteristics and distribution.

Large variability in *Posidonia* shoot density and leaf length (at a small scale) emerged from the divers' measurements taken along the deployment transect (see Figure 3.5 for location of the stations). *Posidonia* shoot density along the transect varied between 187±40 and 356± 73 shoots/m^2 (Figure 3.12 and Table A. 1, in Appendix A). Shoot density was, on average, 251 shoots/m^2, with an average standard deviation of 51. This value is comparable to densities derived from previous studies in the central areas

of the Gulf of Oristano, performed at a larger scale [314±76 shoots/m^2, from *De Falco et al.*, 2008]. Therefore, the *Posidonia* bed is classified as "very sparse", according to *Giraud's* [1977] classification.

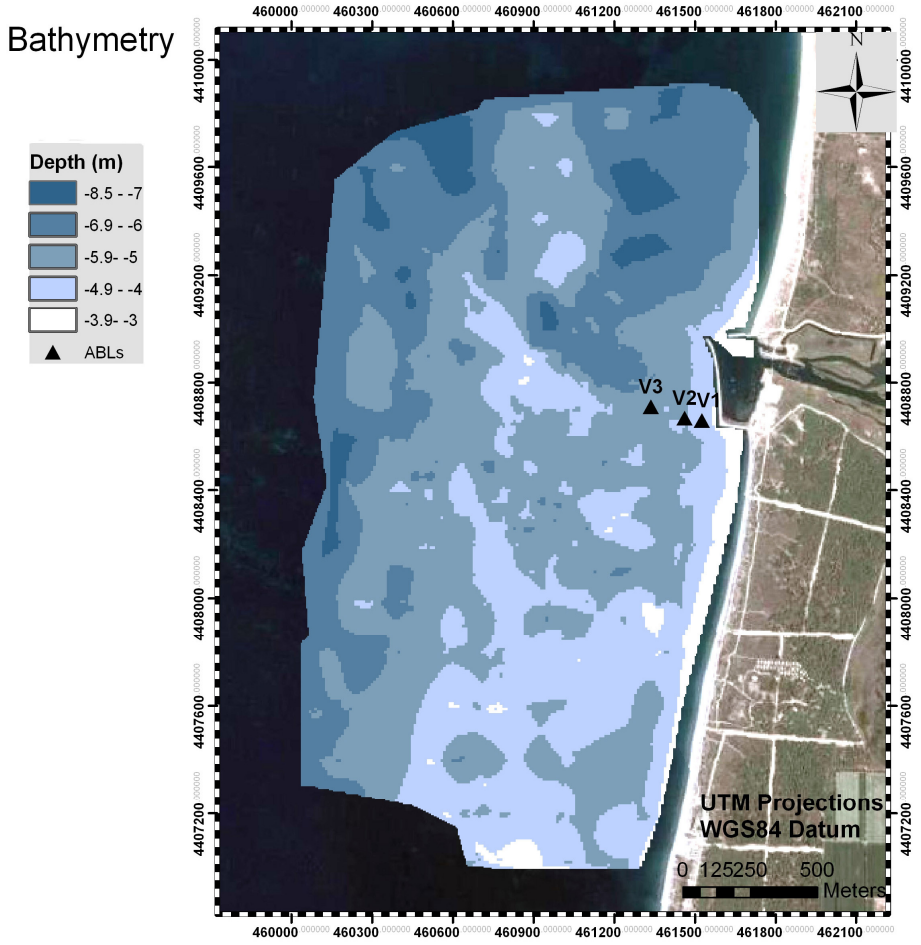

Figure 3.11 Bathymetry of the study area. The positions of the ABL deployment sites are shown as triangles.

The shallowest *Posidonia* plants along the transect were located at a depth of about 4.7 m, near Station V2 located about 280 m from the coast; there were characterised by the lowest plant density. According to the published literature *Posidonia* density is highest in shallow waters [*Buia et al.*, 2004; *Gobert et al.*, 2006]. However this was not the case in the study area, where no trend between density and depth (or distance from the shore) was found. This conclusion is in agreement with previous evidence in the Gulf of Oristano [*De Falco et al.*, 2008].

On average, the shoots had 5 leaves, 0.9 cm in width (see Table A. 1). Leaf length was, on average, 27.3 cm and reached up to 37.2 cm (Figure 3.13 and Table A. 1,

in Appendix) along the transect. The mean leaf length was 31.6 cm at the most seaward deployment site (V3). Likewise, no trend was found between leaf length and depth or distance from the shoreline.

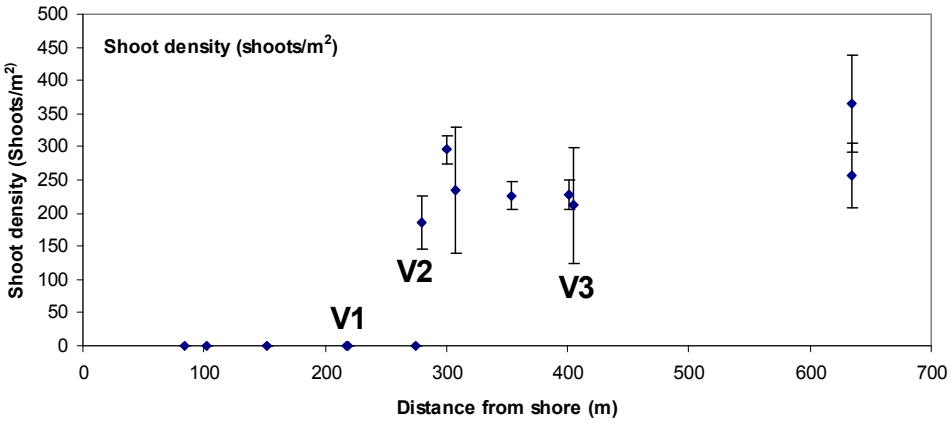

Figure 3.12 *Posidonia* shoot density plotted against distance from the shoreline, along the instrumented transect. Note: bars of the density measurements are 1 standard deviation. The locations of the ABLs are also indicated.

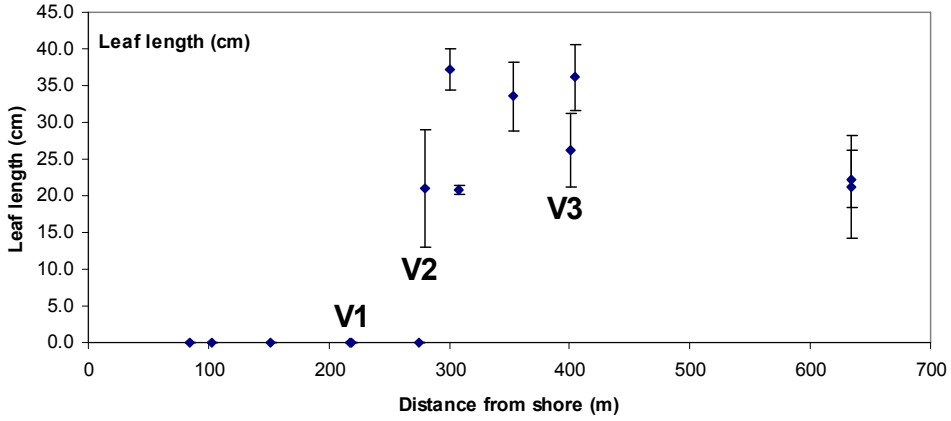

Figure 3.13 *Posidonia* average leaf length plotted against distance from the shoreline, along the instrumented transect. Note: bars of the length measurements are 1 standard deviation. The locations of the ABLs are also indicated.

In general, the diver surveys revealed that the smallest seagrass patches and meadow edges were associated with the smallest and least dense plants. The *Posidonia* meadow at V3 was established on old matte (see"Observations" in Figure 3.14). The site V2 was located some 50 cm inshore of a meadow edge, with a matte 'step' of approximately 20 cm, whilst the most shoreward site (V1) was characterised by a sandy substrate. At shallow depths, the *Posidonia* bed appeared to be disturbed, with a large

amount of dead shoots and areas of very sparse plants. Shallow areas were often characterised by a layer of seagrass debris (as near to the Station V1, Figure 3.7A), which, south of the harbour, could be up to 40 cm thick and made of detached old leaves, roots and "balls" of *Posidonia* fibres (see purple dots, Figure 3.14). Patches of a different and smaller seagrass (*Cymodocea nodosa*) were observed off the southern breakwater and to the north west of the harbour entrance (cyan dots,Figure 3.14). *Cymodocea nodosa* is a pioneering seagrass species, smaller than *Posidonia,* with thin and more flexible leaves; these may vary in length between 10 and 40 cm [*Duarte and Sandjensen*, 1990]. *Cymodocea* leaf length in the study site was estimated to be about 20 cm, but the leaves bend very easily and the canopy lies close to the seabed. Patches of *Cymodocea nodosa* have been observed elsewhere in the Gulf, mainly in shallow areas where the *Posidonia* beds appear disturbed [*Baroli et al.*, 2003].

The visual observations of the seabed type were compared to the information obtained on canopy height distribution resulting from the SIS survey (Figure 3.14). A map of the canopy height of the whole study is shown in Figure 3.15. Generally, there was good correspondence between the SIS survey results near the transect together with the diver observations in the same area. In the area surveyed the maximum canopy height detected by the SIS was 48 cm (Figure 3.16). Most of the canopy height was between 22 and 25 cm. The average canopy height (24±4.8 cm) was slightly smaller than the average *Posidonia* leaf length measured by divers (27±4.3 cm). This difference can be attributed partially to the vertical resolution of the SIS which, for this first experimental survey, was 3.9 cm (Section 3.3.1). In addition, the seagrass canopy height results are lower than the seagrass leaf length; this is because, when the leaf length was measured they were held completely straight whilst, in a natural canopy, leaves might be slightly inclined. As observed from the measurements taken along the transect, the canopy height was not related to water depth, nor to distance from the coast; this is probably a result of the patchy nature of the meadow.

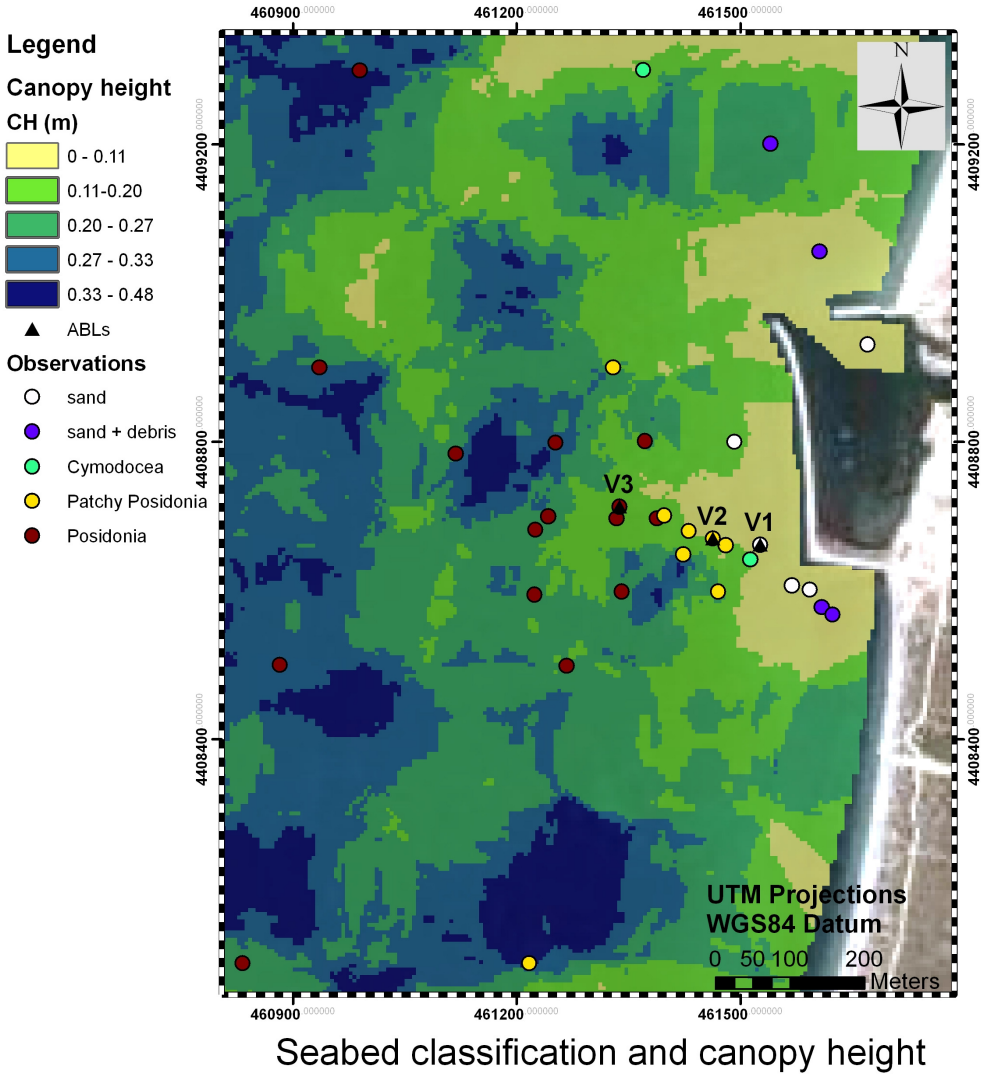

Figure 3.14 A detail of the canopy height map from the SIS survey: A description of the seabed type, from the observations made by divers, is also shown.

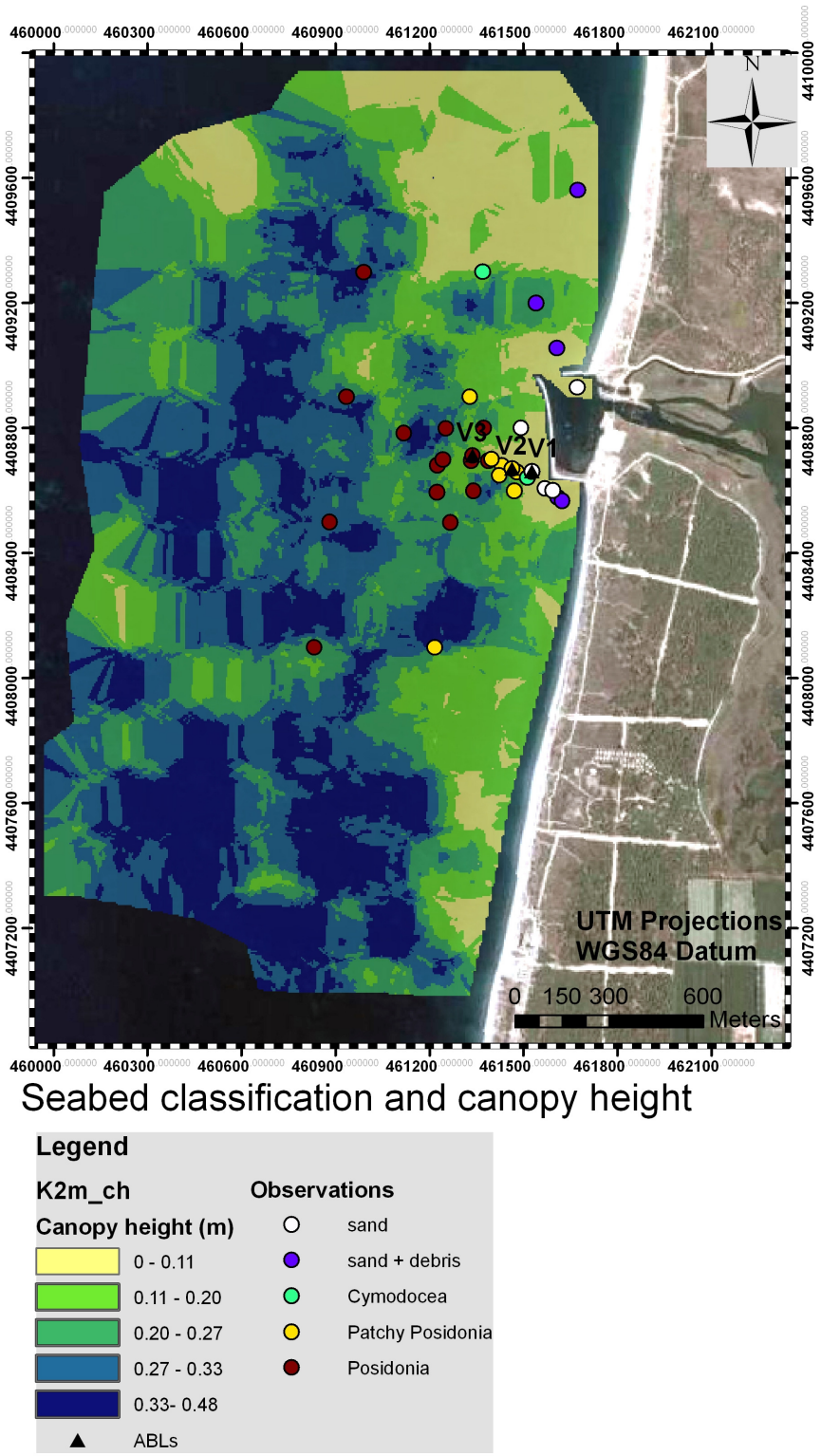

Figure 3.15 Canopy height distribution in the study area.

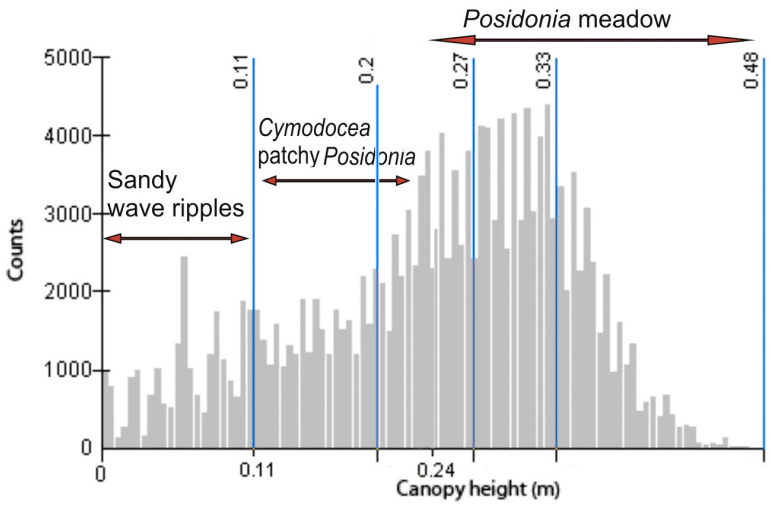

Figure 3.16 Frequency distribution of the canopy height obtained from the SIS survey. The vertical blue lines indicate the breaks used for the division in classes of canopy height, used in the canopy distribution maps (Figure 3.14 and Figure 3.15). The division into the 3 classes of Figure 3.17 is also indicated.

Based upon the SIS dataset and the information collected by divers, a map of the seabed type was produced (Figure 3.17). The seabed classification has been based upon the following considerations:

- a canopy height of less than 0.10 m was interpreted as being a sandy area, with little *Posidonia* debris or wave ripples;
- areas with canopies shorter than average (with heights of between 0.10 and 0.24 m) were interpreted as being patches of *Cymodocea nodosa*, an edge of a *Posidonia* meadow or a small *Posidonia* patch; and
- areas with a tall canopy (> 24 cm) were interpreted as being a thick *Posidonia* canopy.

Areas of bare sediment were located to the north of the harbour, as evident in previous work [*De Falco et al.*, 2006], at depths of less than 4 m and around the breakwaters. The thickest canopy was located mostly at depths greater than 5 m. The meadow was predominantly patchy, with the smallest patches lying in the shallowest waters (between 5 and 3 m depth). The meadow was more uniform in the southern part of the survey area. The NW-SE orientated wide channel, which is evident in the bathymetric map, corresponded to an area of bare seabed (NW corner of the map), or with canopy thickness less than the average (Figure 3.17). A survey undertaken at a

higher spatial resolution would have defined more clearly this channel and other smaller "intermatte" channels.

Figure 3.17 Seabed classification and depth contours of the study area. In the legend CH stands for canopy height. The locations of the ABL stations are indicated.

3.5.1.3 Sediment characteristics: grain size and sorting

Maps of sediment characteristics were produced from the analysis of the sediment samples from the shore and the seabed; they are presented in Figures 3.18 to Figure 3.20. Sediment characteristics measured at the ABL deployment sites are summarized in Table 3-3. The full sand grain size distribution at the sites and from some representative stations, are shown in the plots reported in Appendix A (Figure A. 2).

The sand fraction at Stations V3 and V2 (within the *Posidonia* meadow and at its edge, respectively) had very similar grain-size distributions but the latter was richer in mud and organic matter. Sand at Station V2 can be classified as fine (Wentworth's classification, as in *Soulsby,* 1997), moderately-well sorted [Folk's classification, 1974], whilst sand at Station V3 was slightly richer in fines and well sorted. Sand at Station V1 (an un-vegetated site) was coarser (medium to coarse sand) and less well-sorted (moderately-sorted) than at V2 or V3.

Table 3-3 Sediment characteristics at the deployment sites.

Site	Description	Mz (phi)	Mz (µm)	Sorting	mud/sand (%)	Organics (%)
V1	non-vegetated, closest to shore, 4.3 m depth	1.27	5	0.82	1.41	5.17
V2	non-vegetated , 50 cm off the edge of a *Posidonia* meadow, 4.9 m depth	2.53	172.6	0.62	2.52	3.34
V3	*Posidonia* meadow, 5 m depth	2.30	202.8	0.45	6.10	7.19

The Sations V2 and V3 were located within a belt parallel to the shoreline of fine/medium-fine sands better sorted than the surrounding sands (Figure 3.18 and Figure 3.19). Sands at V2 and V3 lack the coarse component that characterised the harbour sand, the sand at V1 and on beach swash zone (see grain-size distribution curves in appendix and Figure 3.18). However farther offshore, where *Posidonia* was abundant, the coarse sand was generally poorly sorted (Figure 3.18). Often the sand samples from the *Posidonia* beds were characterized by coarse biogenic particles such as gastropods shell or echinoderm spine fragments they were derived clearly from organisms living amongst the *Posidonia* plants. This coarse, poorly sorted, sand was also found in a previous study [*De Falco et al.*, 2008] and has been interpreted as a relict sand deposited by the paleo river and later colonized by *Posidonia.* According to these authors, the coarse sand grains and the biogenic fragments could not be mobilized after colonisation, because seagrass meadows are known to reduce sediment transport and resuspension [*Gacia and Duarte*, 2001; *Granata et al.*, 2001; *De Falco et al.*, 2008]. Sand grain sorting to the north of the harbour, in the mostly un-vegetated area, improved towards the beach; to the south of the harbour, its distribution was more

complicated. Highly mobile, fine sand was located in a narrow strip alongshore between the thick *Posidonia* beds and the 4 m contour (see map in Figure A. 3, Appendix A). On the beach and in the shallows the fine sand might not be stable due to wave action; its distribution might indicate that the mobile sand does not significantly penetrate the established *Posidonia* beds, suggesting that offshore sediment transport is inhibited by the presence of the canopy. Organic content was highest to the southwest of the harbour, [as found by *De Falco et al.*, 2008]; it tended to decrease towards the shore (Figure 3.20). In particular, areas with thick seagrass canopies were characterised by very high values of organic matter (up to 15%). The sand from the region near the lagoon (inside the harbour) had a large amount of organic matter (up to 18%). Both seagrass meadows and the lagoon could be a source of organic matter, which would account for the high content in the sediments. Seagrass meadows are known to produce and trap organic particles, as they are a sheltered environment [*Gacia and Duarte*, 2001] and are able to collect material through loss of momentum of particles on collision with the leaves [*Hendriks et al.*, 2008].

The highest mud content was at the entrance of the S'Ena Arrubia harbour and to the south (with a mud/sand ratio up to 15, see Figure 3.21), whilst inside the harbour the content of mud was low (with mud/sand ratio of 3). The shallowest areas located near the beach, and the areas\a\ close to the breakwaters were poor in organic matter and mud, most probably as a result of the more intense wave action and absence of *Posidonia* plants.

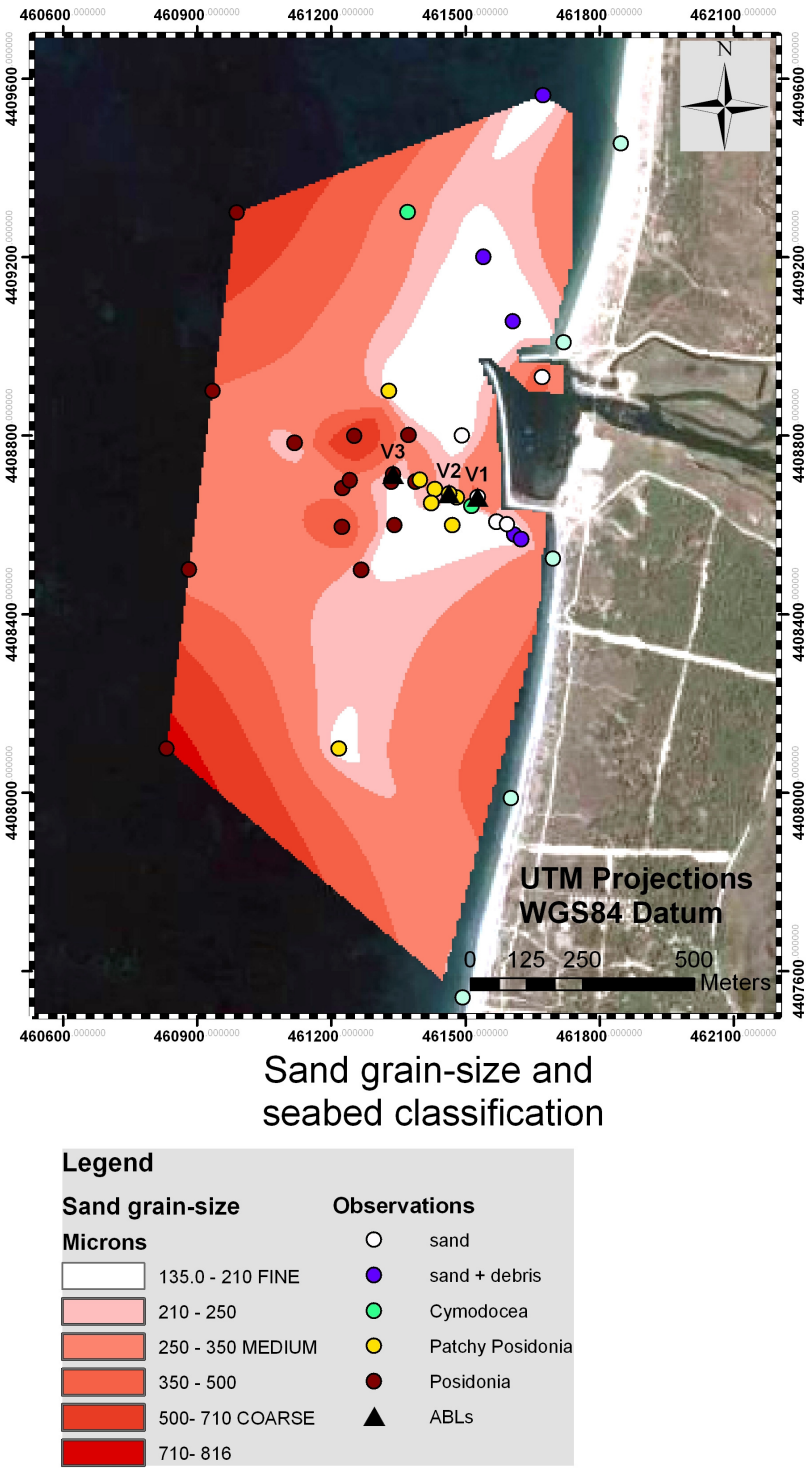

Figure 3.18 Map of the sand grain-size distribution [classified according to the scale of *Wentworth*, 1922]. A seabed description from the diver surveys is also shown.

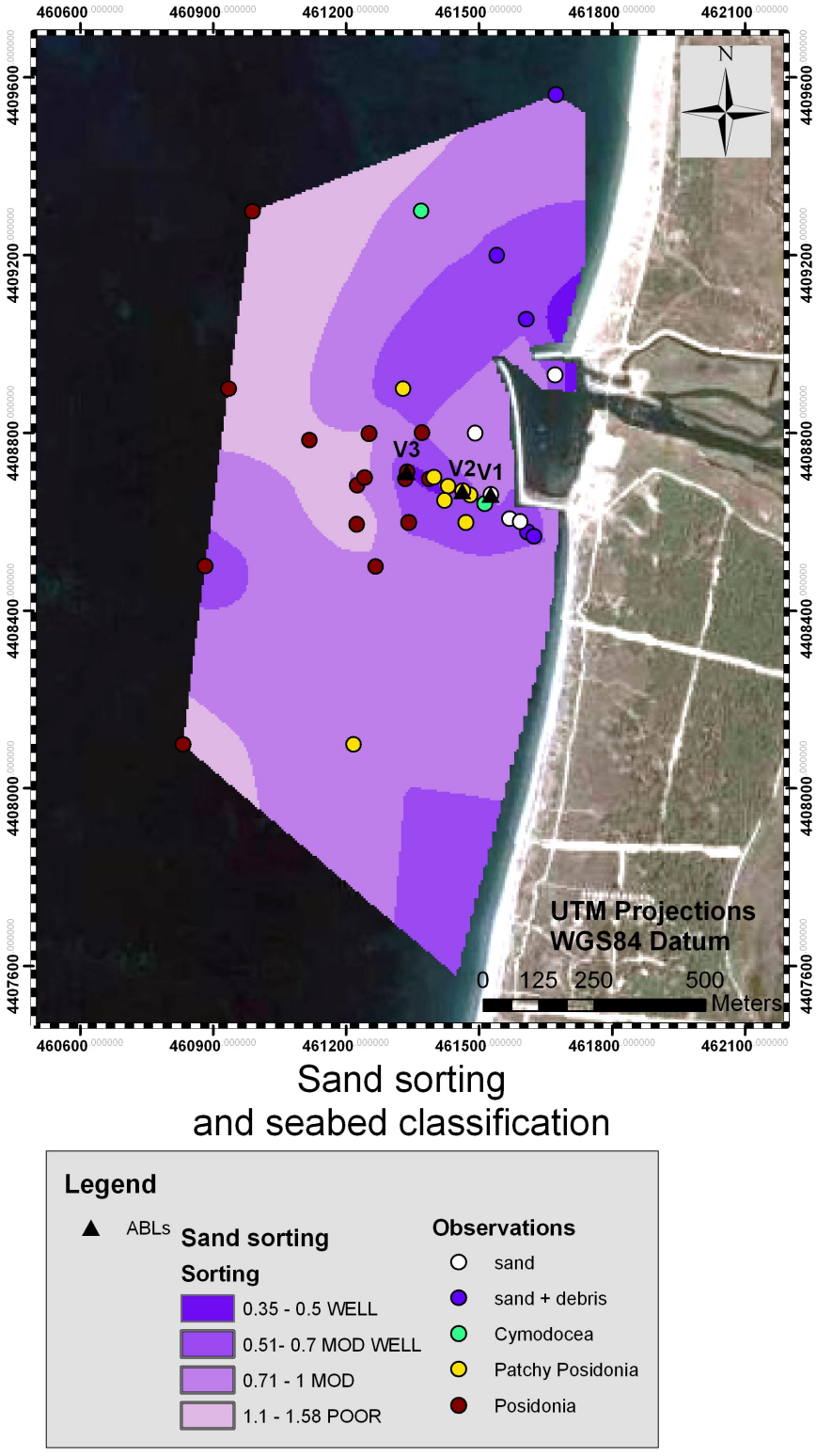

Figure 3.19 Map of the sand sorting (Folk classification,1974). The seabed description from the diver surveys is also shown.

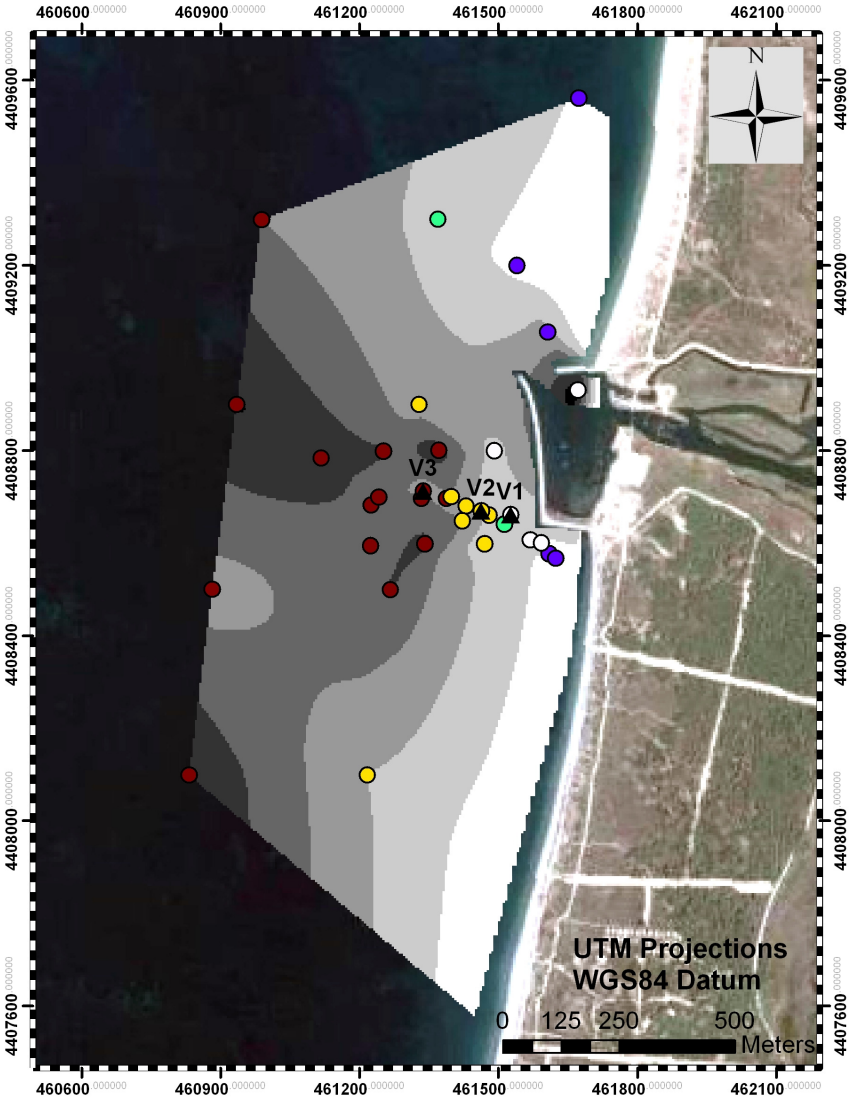

Figure 3.20 Map of the organic content of the seabed sediment. The seabed description from the diver surveys is also shown.

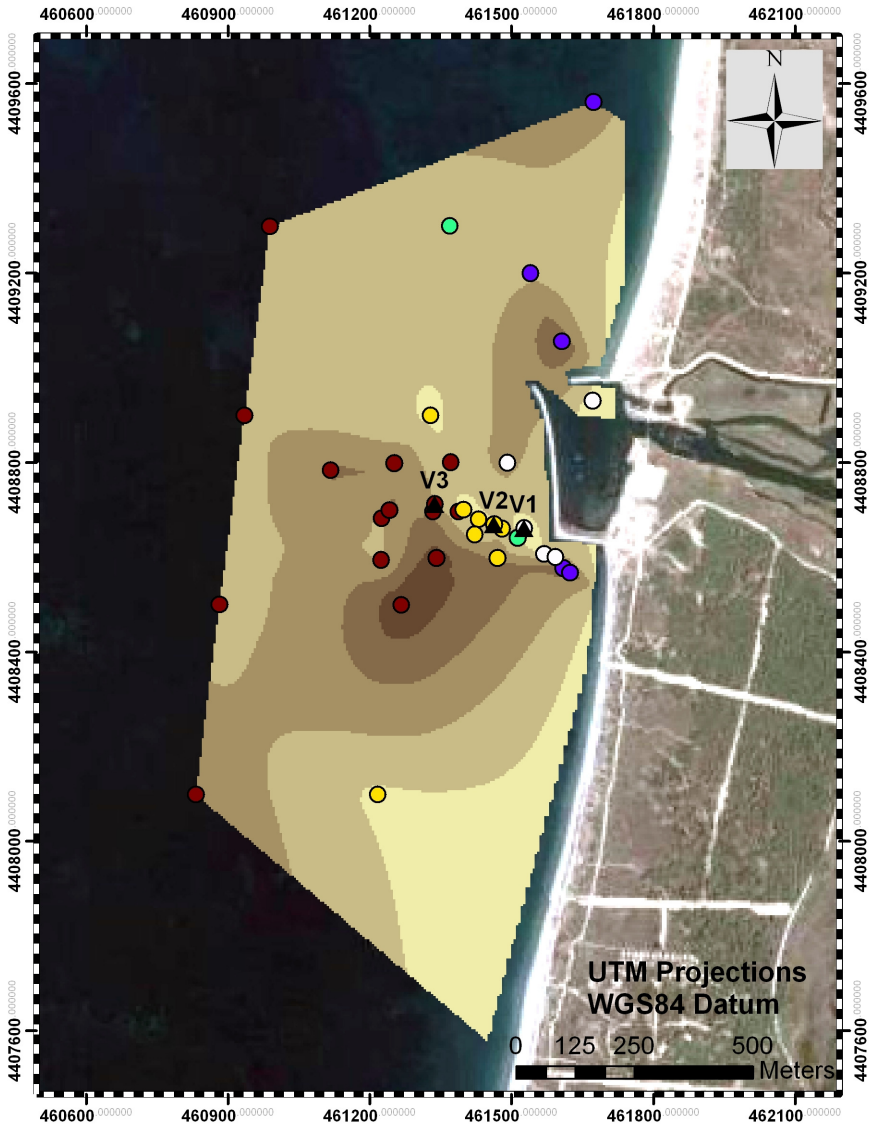

Figure 3.21 Map of the mud/sand ratio of the seabed sediment. The seabed description from the diver surveys is also shown.

3.5.2 Hydrodynamic and turbidity

3.5.2.1 General wind and hydrodynamic conditions

The first four days of the deployment were characterized by low energy conditions, with a light westerly breeze that reached 10-13 knots (5.2-6.7 m/s) during the day and a weaker breeze in late evening from the S/SE (Figure 3.22A). Significant wave heights were less than 0.20 m in the Gulf of Oristano, at site V2 (Figure 3.22D) and less than 1 m outside the Gulf (Figure 3.22C).

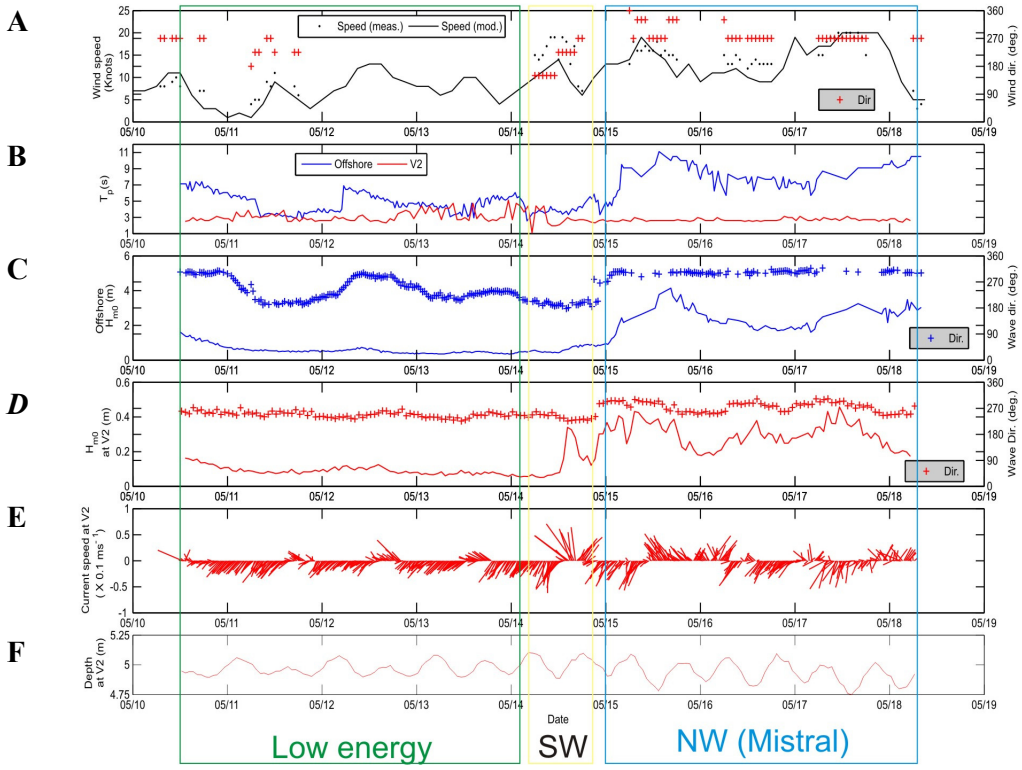

Figure 3.22 Time-series of wind and hydrodynamics. A) Wind speed and direction (model data source: www.windfinder.com, measured data source: Capo Frasca Air Force Base), offshore; B) offshore wave period [at Alghero wave buoy. Source: *APAT*, 2006] and wave period at the study site; C) offshore wave height and direction [source: *APAT*, 2006]; D) wave height and direction in the study site; E) currents speed and direction of flow; and F) water depth.

During the low energy period, unidirectional currents were weak (less than 3 cm/s) and followed a similar pattern each day: they were directed to the southwest during the day, whilst, during the night, their speed decreased slightly and they flowed to the NW (Figure 3.22E).

On the afternoon of the 14th May, a moderately strong (15 knots) southwesterly wind blew, creating (offshore the Gulf) waves of 1.5 m propagating from the SW. At

V2, waves of up to 35 cm high were recorded. This wind (the Libeccio) lasted only a few hours, but created strong currents at V2 directed towards the north; these were the strongest currents recorded during the deployment.

A strong northwesterly wind (the Mistral) started to blow during the night of the 14th May and reached over 20 knots the following day. The Mistral wind dropped during the night and strengthened during the day. Outside the Gulf, the significant wave height reached a 4 m significant height whilst, in the study area, the maximum significant wave was 0.45 m. Currents were strong, but their direction was very variable during the Mistral period.

Offshore waves generally had a longer period than in the Gulf. In particular, the longest waves (with a 10 s period) originated from a northwesterly direction, during the Mistral, between 15th and 18th May. In the Gulf, the peak wave period varied between 1.5 and 5 s, before the Mistral event. More constant short-period waves (2.5-3s) were recorded during the Mistral event and SW winds. The small and short waves (with a constant period) indicate that waves were created mainly locally in the Gulf area. The tidal range during the deployment was on average 15 cm and the mean water level dropped slightly during the Mistral event (Figure 3.22F). Peak Mistral winds between 16 and 26 knots, are quite common in the area and occur 9.76% of the time [from the entire wind records from Capo Frasca air base, *ARPA-Sardegna*, 2005]. Mistral winds stronger than those measured in May, occur slightly less often (7.54% of the time) and are less strong 10.36% of the time. The Mistral event, creating the conditions observed during the deployment was, therefore, a quite common, moderate Mistral perturbation. Offshore waves with a 1-year return period have a significant wave height of 8 m [*Franco et al.*, 2004]; this is double the height measured during the survey, confirming that the Mistral during the deployment was a rather common moderate event.

SW winds occur generally less commonly and are less strong than the Mistral winds [*ARPA-Sardegna*, 2005]. SW winds with a speed of 15 knots occur in the area about 3.14% of the time; and 6.22% of the time they are stronger, indicating that this was a quite weak SW perturbation.

3.5.2.2 Unidirectional currents at the three sites

The night/day current pattern described for site V2 (at the meadow edge), typical of low energy conditions, was also observed farther inshore, at V1. The currents shifted from a south-easterly direction during the day to a northerly direction in the late evening

(Figure 3.23 B and C). During SW winds, the current speeds reached 12.5 cm/s at site V1 and 7.2 cm/s at site V2. Both at V1 and V2 SW winds produced a nearshore current directed to the north, in agreement with published model results for the Gulf of Oristano [*Cucco et al.*, 2006]. During the Mistral period currents were strong, particularly during the peak wind speed, however the current direction was highly variable. During windy conditions, the same night/day regular pattern of current speed and direction (observed during the low energy conditions) was not recorded. The flow reversal did not seem to be linked to the tidal phase (see Figure 3.22 E and F). It is likely that the breeze regime was responsible for the flow reversal and that the pattern was broken during wind perturbations.

At the *Posidonia* site (V3), conditions were very different. Average current values during the deployment were 3 cm/s at site V1, 2 cm/s at site V2 and 0.9 cm/s at the *Posidonia* site V3 (Figure 3.23). At V3 the current speed was directed alongshore and was on average more than a third smaller than on bare sand (V1) and less than half that at V2. The regular flow reversal typical of low energy conditions at V1 and V2 was not observed at the *Posidonia* site, and currents were constantly orientated southwards (with only one exception on the 12th May). During SW winds currents were smaller than at V1 and V2, where the current speed reached the highest values recorded. Also, during the Mistral event, currents had a constant southerly direction and they were not stronger than during the low energy conditions.

From these results it emerges that the unidirectional current conditions within the *Posidonia* canopy were somewhat constant direction compared to the other sites, and practically independent of the wind regime and sea conditions. At the meadow edge and on sand, by contrast, the wind regime had a large influence on the unidirectional currents close to the seabed and probably even sea breezes were able to influence currents in such water depths (4 to 5 m). The EMCM current meter at V3, was located at 27 cm above the seabed, hence within the *Posidonia* canopy (at V3 leaf length was 36.1±4.5 cm). Since the depth at V3 and V2 was practically the same, it is likely that the current reduction was caused by the presence of the *Posidonia*, as has been observed in deeper meadows [*Gacia and Duarte*, 2001; *Granata et al.*, 2001].

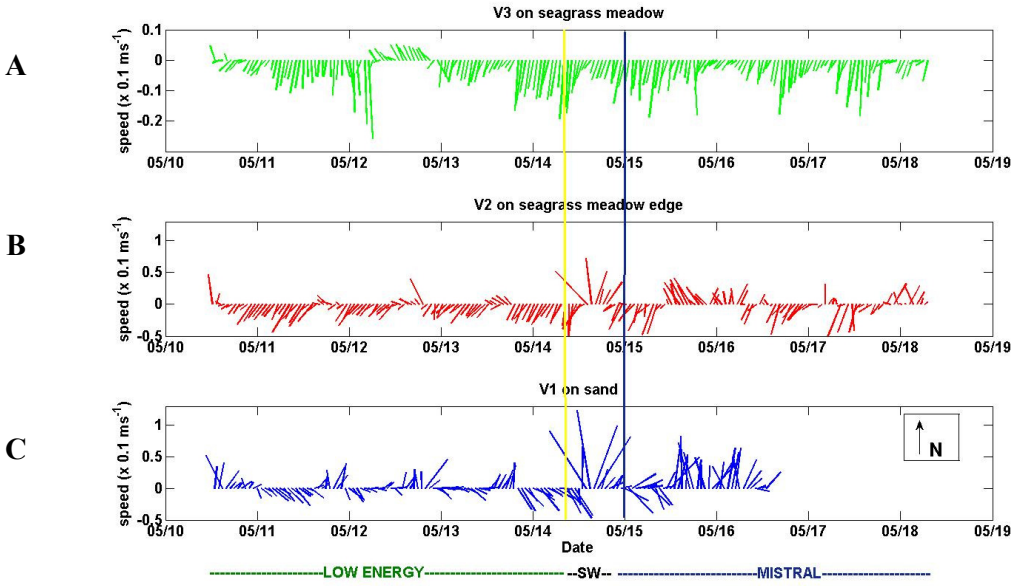

Figure 3.23 A) Unidirectional currents (U_m) at sites V3; B) unidirectional currents at sites V2; and C) Unidirectional currents at sites V1. Please note that the range of the vertical axis in the plot A is different than in plots B and C. The vertical yellow bar indicates the start of the SW wind event. The vertical blue bars indicate the start of the mistral event.

3.5.2.3 Wave orbital velocities

The oscillatory component of the velocity signal was separated successfully from the unidirectional component. Mean values of maximum wave orbital velocities (U_{max}) in the low energy conditions were around 3 cm/s at V2 and V3 and 3.5cm/s at V1; during the storm period they were approximately 8 cm/s at V2 and V3, and over 11 cm/s at V1 (Figure 3.24 and Table 3-4).

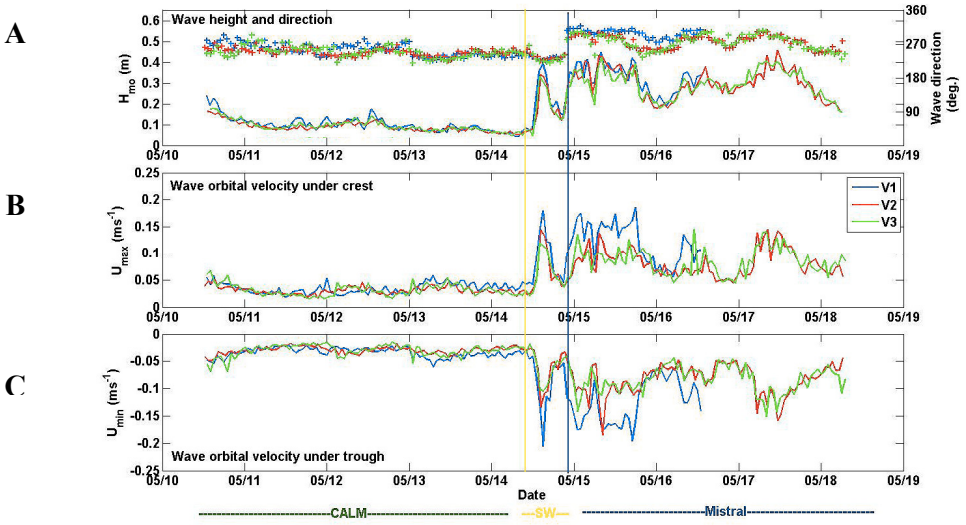

Figure 3.24 A)Wave height and direction at the deployment sites; B) orbital velocities under the crest (U_{max}); and C) orbital velocity under the trough (U_{min}).

Table 3-4 Minimum, maximum and mean values of the orbital velocities (U_{max} and U_{min}) at V1, V2 and V3.

Site	V1		V2		V3	
Velocity (cm/s)	U_{max}	U_{min}	U_{max}	U_{min}	U_{max}	U_{min}
Min	1.76	-2.04	1.59	-1.74	1.55	-1.48
Max	18.63	-20.55	14.43	-18.54	14.45	-15.12
Mean (low energy)	3.49	-3.44	3.06	-2.97	3.10	-3.03
Mean (windy)	11.47	-11.89	8.06	-8.24	8.15	-8.02

The larger orbital velocities at V1 were probably a result of the larger waves and shallower depths at this station. On average, over the deployment period, wave orbital velocities were constant as waves travelled over the seagrass bed between V3 and V2. The changes in wave-induced velocity at the two sites were investigated for different wave conditions (represented by the wave orbital amplitude) (Figure 3.12). Orbital velocity changes were expressed as the ratio:

$$\alpha_{\max} = \frac{U_{\max}^{V2}}{U_{\max}^{V3}} \qquad \textbf{Eq. 3-10}$$

Oscillatory velocities were reduced shoreward of the seagrass meadow when the ratio was less than 1. The wave orbital amplitude was calculated from linear theory as:

$$A = \frac{U_{\max} T_p}{2\pi} \qquad \textbf{Eq. 3-11}$$

A large scatter amongst the data was found, the range in A was small and the trend was not significant (R^2=0.21, for an exponential fit). However, there is some evidence that wave-induced velocities under shorter waves (small A) were not reduced (or only very little), as waves travelled between V3 and V2 over the seagrass. Some wave-induced flow reduction occurred for the largest A. The large scatter might be due to the small distance between measurement sites, or to the variations in wave direction.

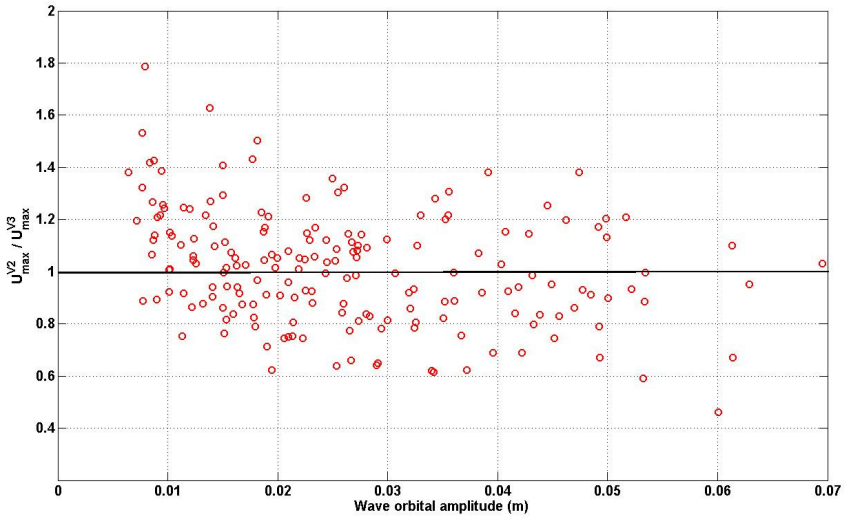

Figure 3.25 Changes in orbital velocities between Stations V3 and V2 ($U^{V2}_{max}/U^{V3}_{max}$) plotted against the wave orbital amplitude (A).

Wave-induced flow asymmetries ($U_{max}+ U_{min}$) were evaluated to verify laboratory evidence that oscillatory flows over seagrass have a positive asymmetry, hence that seagrass induces a net shoreward drift of water (and sediment) [*Price et al.*, 1968]. The asymmetry was largely positive (directed shoreward), at V3 and its mean value was positive (see Appendix A, Figure A. 7). This pattern occurred more often than at V1 and V2, where the mean value was in fact negative This observation might confirm previous work, which found a potential shoreward drift over an artificial seagrass canopy [*Price et al.*, 1968].

Table 3-5 Wave orbital velocities asymmetries (S.D. stands for standard deviation)

Orbital velocity asymmetry ($U_{max}+U_{min}$ (cm/s)	**V1**	**V2**	**V3**
Mean	-0.11	-0.04	0.08
S.D.	0.10	0.89	0.10

Finally, the wave orbital velocities were used to compare the present field conditions with those in previous studies and to the laboratory conditions described in Chapter 4, 5 and 6. The wave Reynolds number (Re_w) was calculated for all stations using:

$$\mathrm{Re}_w = \frac{AU_{\max}}{\upsilon} \qquad \textbf{Eq. 3-12}$$

Mean and maximum values of Re_w are reported in Table 3-6.

Table 3-6 Mean and maximum wave Reynolds number calculated at the deployment sites.

Wave Reynolds number (Re_w)	V1	V2	V3
Mean	1.9×10^3	1.3×10^3	1.4×10^3
Max	1.2×10^4	7.2×10^3	7.1×10^3

The Reynolds vegetation number (Re_v) has been used in studies on wave propagation over vegetation, [*Kobayashi et al.*, 1993; *Mendez et al.*, 1999; *Bradley and Houser*, 2009] instead of the more general wave Reynolds number (see Chapter 2).The Re_v number was calculated forV3 from,

$$\mathrm{Re}_v = \frac{bU_{\max}}{\upsilon} \qquad \textbf{Eq. 3-13}$$

with b=0.01 m (the measured leaf width), and the kinematic viscosity of water was 1.36×10^6. Re_v was on average 414 during the deployment, although it reached 1006 under storm conditions.

3.5.2.4 Wave characteristics and wave height variations

Spectral wave height (H_{m0}) ranged between 0.05 and 0.21 m at the edge of the *Posidonia* patch (V2) and at the *Posidonia* site (V3) during low energy conditions; it reached 0.46 m during the Mistral event (Figure 3.26 A).

Peak periods were more variable at all sites during the low energy period than during the Mistral event and the SW winds (Figure 3.26 B). Waves at V1 during the Mistral event were shorter than at both other sites. Average wave periods at all sites are reported in Table 3-7.

Table 3-7 Average and standard deviations of peak wave period (T_p) at three ABL stations, during different sea conditions.

Conditions	T_p at V1 (s)	T_p at V2 (s)	T_p at V3 (s)
Low energy	3.2±1.0	3.1±0.7	3.3±0.9
SW	2.7±0.3	2.7±0.2	2.7±0.1
Mistral	2.5±0.2	2.7±0.2	2.7±0.1

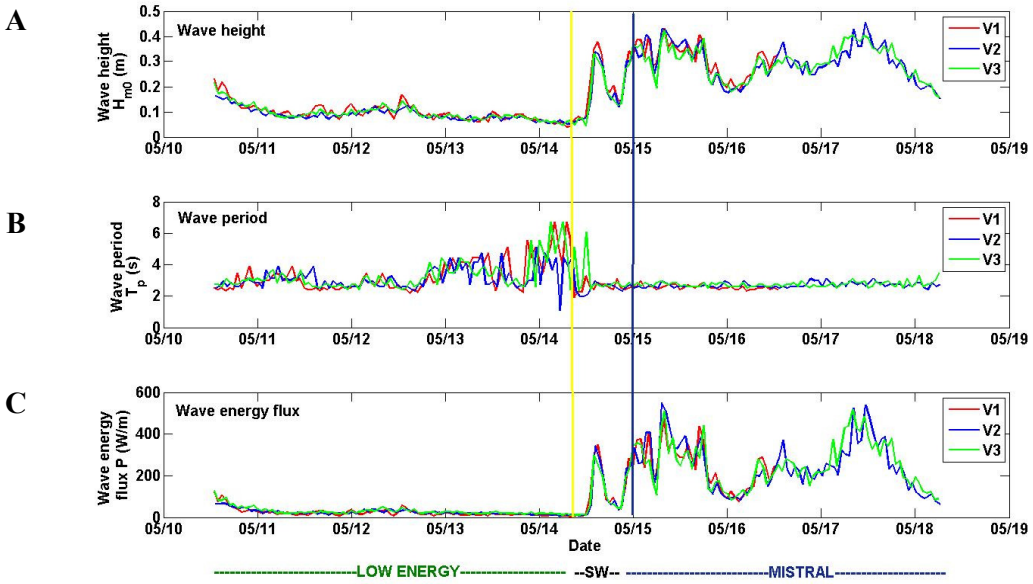

Figure 3.26 A) Spectral de-shoaled wave heights (H_{m0}) at sites V3, V2 and V1; B) peak wave period (T_p); and C) wave energy flux (P).

Difference in significant wave height, as waves travelled between V3 and V2 were negligible during the Mistral event. However, wave height reduction over the *Posidonia* bed took place during low energy conditions, as waves at V2 were 5% smaller than at V3 (Figure 3.27). Despite taking shoaling into account in these estimates of wave height, the greatest wave heights were measured at the most shoreward site (V1). On average, the waves at V1 were 8.5% larger than at V2 during the Mistral event and 8% larger under low energy conditions. Also waves at V1 propagated from a more northerly direction, than at any of the other stations, both during the low energy period and the Mistral event (Figure 3.24). Waves at V1 were not always incident to the instrumented transect. This fact, and the shorter periods, might indicate that processes other than shoaling (such as wind stress acting on the water surface, wave diffraction and reflection induced probably by the presence of the breakwater) might have played an important role on waves at V1. Station V2 was located farther from the breakwater; however it cannot be ignored that such processes might have affected waves there (indeed, the wind effect was present).

A study undertakn by *Bradley and Houser* [2009] found wave height reduction to be much larger than found here (30%, over a 39 m distance), for a similar vegetation Reynolds numbers ($200<Re_v<800$) and similar tidal range. This latter study was undertaken over a mixed seagrass bed, with comparable canopy height, dominated by *Thalassia testudinum,* a seagrass with ribbon-like leaves similar to *Posidonia*. However,

that site was located within much shallower depths (1.5m), whilst wave height decay depends upon canopy submergence ratio [*Fonseca and Cahalan*, 1992]. Moreover, winds were much weaker causing only little interaction on sea surface elevation.

It is very difficult to compare field data on wave height decay over vegetation with previous work on natural seabeds, due to the large variability in conditions and plant characteristics [*Möller et al.*, 2002; *Koch et al.*, 2009]. Because many processes occur synoptically in the field, it is difficult to evaluate the real capacity of *Posidonia* beds to reduce wave energy; likewise to understand the mechanisms involved.

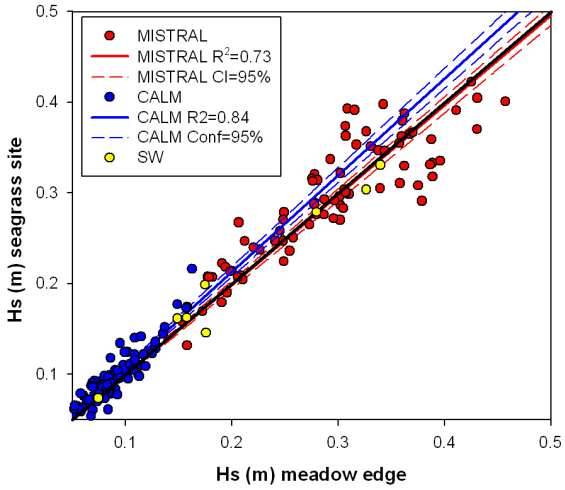

Figure 3.27 Wave height variation between the vegetated site (V3) and the site at the edge of the seagrass meadow (V2). Regression lines were plotted with their corresponding correlation coefficients and confidence intervals (95%) for Mistral event and low energy conditions.

3.5.2.5 Wave energy dissipation and friction factors

Wave energy dissipation rates (ε_f) were calculated from the loss of wave energy, as waves travelled between V3 (within the seagrass) and V2, at the shoreward edge of the patch. The formula (Eq. 2.3) used was:

$$\varepsilon f = -\frac{P3 - P2}{\Delta x} \qquad \textbf{Eq. 3-14}$$

with P3 and P2 being the wave energy flux at V3 and V2 respectively, and Δx 132 m is the distance between V3 and V2. Jonsson's equation (Eq. 2-4) was then used to derive the wave dissipation factor:

$$f_e = \frac{3\varepsilon_f}{2\pi\rho u_{\max}^3} \qquad \textbf{Eq. 3-15}$$

The wave orbital velocity (U_{max}) measured at V2, was used, assuming that it was equal to the free-stream orbital velocity (U_∞) i.e. assuming that the current meter

was located above the boundary layer. This assumption is valid for the un-vegetated site, as in wave-dominated conditions the thickness of the wave boundary layer is, for medium sand, of the order of mm or few cm [*Soulsby*, 1997]. However, it might not be strictly valid at V3 over *Posidonia*, since wave boundary layers are affected by seagrasses [*Koch et al.*, 2006a; *Bryan et al.*, 2007].

Mean values and standard deviations of f_e are listed in Table 3-8 , for low energy conditions, SW winds, and the Mistral event as well as for the mean conditions over the whole deployment period. On average *fe* was 0.263, which is comparable to friction factors found for coral reefs [*Lowe et al.*, 2005a and reference therein] and saltmarshes [*Möller et al.*, 1999], i.e. assuming $f_e=f_w$ as for sandy beds [*Nielsen*, 1992]. Wave dissipation factors were, on average, larger in low energy conditions than during high energy periods; this is consistent with observations on wave height decay (in the previous Section).

Friction exerted by rough beds under waves varies with Reynolds wave number (Re_w) and the wave orbital length (A) [*Nielsen*, 1992]. For this reason, the dissipation factor was plotted against the wave orbital amplitude (A, defined in Section 3.5.2.3).

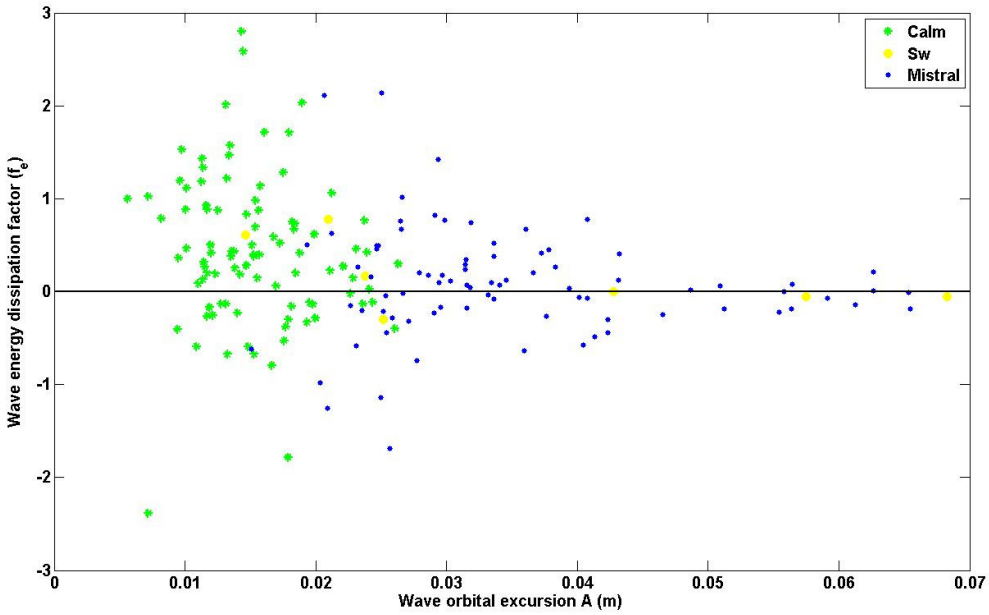

Figure 3.28 Wave energy dissipation factors plotted against the wave orbital amplitude.

Generally the largest friction factors were found for waves with the smallest orbital amplitude (A), as observed for waves travelling over sandy and rippled beds [*Nielsen*, 1992] or coral reefs [*Lowe et al.*, 2005a]. However, the trend between A and *fe*

was not significant, probably due to the scatter in the data. The variation in the data was quite large (Table 3-8), with periods where f_e was negative, ie. wave energy increased as waves passed over the seagrass patch. These negative values could well be associated with an increase in wave height (at the station located closer to shore) induced by wind stress (during windy periods) or wave reflection from the nearby breakwater.

Friction factors are small and notoriously difficult to measure [*Madsen et al.*, 1988], especially in the field. Moreover the presence of a breakwater near the deployment site made the task of measuring friction induced by the seagrass even more difficult. Surface buoys could not be used to locate the ABL's and the GPS malfunctioning during the deployment; this meant that it was necessary to use the breakwater as a reference point to locate the instruments.

In the folowing calculations, wave energy loss has been calculated at the peak frequency; however, it might have differed between the various components of the wave spectra [*Madsen et al.*, 1988]; this will be examined in the laboratory experiments undertaken with random waves (Chapter 6).

Table 3-8 Mean values and standard deviation of the wave dissipation factors between Stations V3 and V2 (f_e), calculated over low energy conditions; SW winds; the Mistral event and over the whole deployment period.

Wave dissipation factor (f_e)	Low energy	SW	Mistral	All
Mean	0.431	0.165	0.09	0.263
Standard deviation	0.804	0.390	0.693	0.722

3.5.2.6 Turbidity and sediment concentration

A steady increase in water turbidity was detected from the 14th May at all stations (Figure 3.29, 3.30 and 3.31), before the start of the strong wind events. Peak turbidity was reached on the 16th May, during strong Mistral winds; it started to decrease before the maximum Mistral speed (and the peak wave height) which were reached one day later. On the 15th and 16th May a large superficial sediment plume was observed coming out of S'Ena Arrubia harbour, and directed towards the south. This plume might have been caused by a sudden increase in discharge from the lagoon that was transported southwards by surface currents. The steady increase in turbidity was probably caused by suspended matter advected to the deployments sites from the lagoon. However smaller peaks in turbidity were observed (Figure 3.29). Unidirectional currents measured near

the bed were much lower than the threshold current value necessary to induce sediment motion and local resuspension (the threshold values were 0.36 m/s, 0.37 m/s and 0.38 m/s at V1, V2 and V3 respectively, see Appendix A1, Figure A. 8E).

In order to investigate the possible correlation between wave energy and relative turbidity, wave-induced bed shear stresses were calculated; these were compared to the threshold values for sediment suspension. The bed shear stress was calculated from the measured U_{max} at each site using both Soulsby's and Nielsen's formulae (details on the methods are reported in Chapter 4, Section 4.2.6). Peak bed shear stress induced by waves often corresponded to peaks in relative turbidity. In some cases shear stress exceeded the threshold value for sediment motion, calculated from the D_{50} of the sand sampled at each site (more details are given in Section 4.2.6 of Chapter 4). This observation suggests that, even at the seagrass site, fine sediment resuspension was possible during the high energy events, at least for the finest fraction of the sediment.

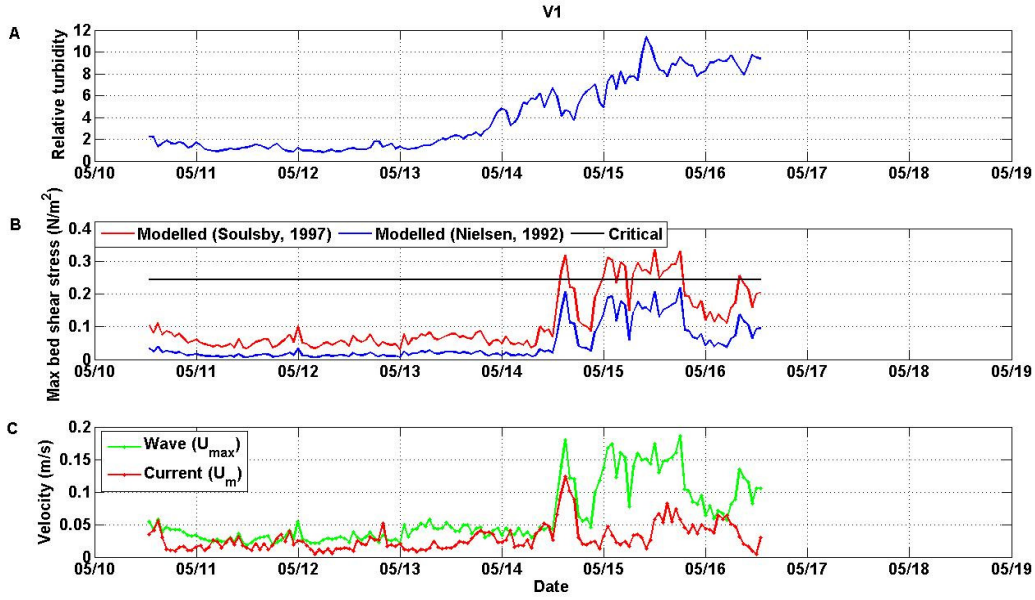

Figure 3.29 A) Average relative turbidity time-series at V1; B) critical bed shear stress for the sand at V1, compared to the bed shear stress modelled from the measured Umax at V1 Bed shear stress was calculated using Soulsby's (1997) and Nielsen's (1992) methods ; and C) wave-induced velocity (U_{max}) and unidirectional component (U_m) at V1.

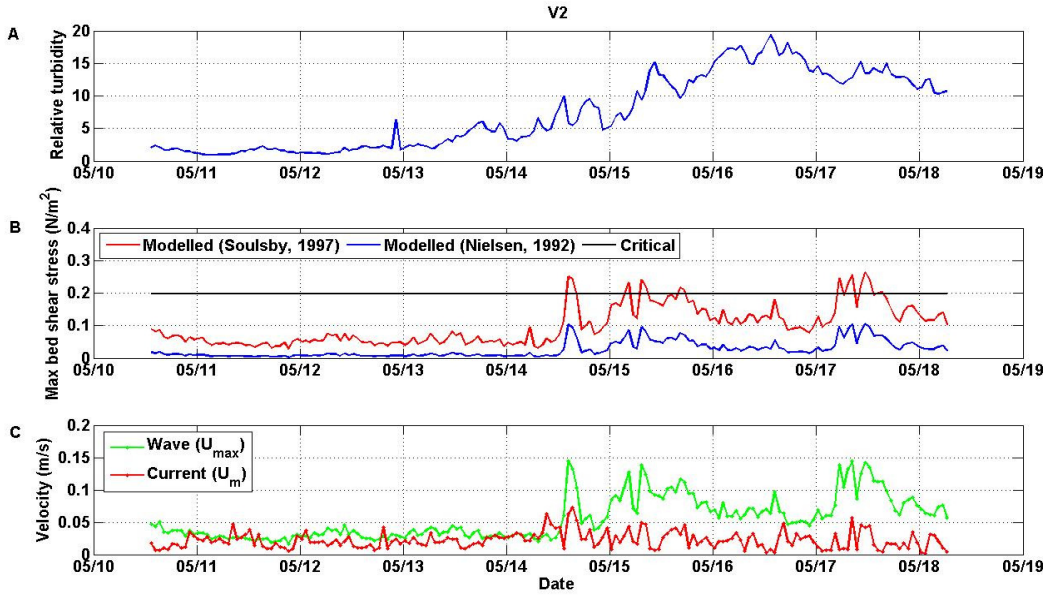

Figure 3.30 As Figure 3.29, for all parameters measured or calculated at V2.

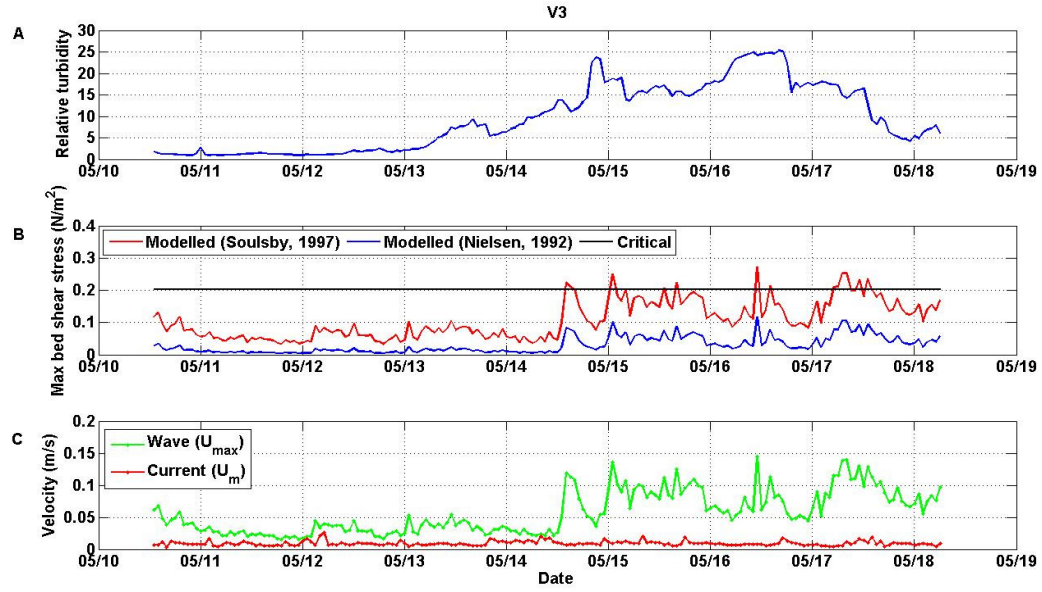

Figure 3.31 A) As Figure 3.29, for all parameters measured or calculated at V3.

3.6 Concluding remarks

The *Posidonia oceanica* seagrass meadow in the study area had a patchy distribution, with smaller patches in shallow waters, reaching the 3 m depth isobath. Canopy density was, on average, 251±51 shoots/m^2 and canopy height was, on average,

24±4.3 cm, reaching up to 48 cm. In the central areas, near the 5 m isobath, the meadow had a larger canopy height. However canopy height was not related to water depth, probably because of the patchy nature of the meadow. A distinctive feature was the deep channel cut through the *Posidonia* meadow oriented in the direction of the dominant NW winds. The area to the north of the harbour of S'Ena Arrubia was characterised by a 6-7 m deep non-vegetated area, with some *Posidonia* debris from the beach to about 700 m offshore. The area around the harbour breakwaters was also sandy and non-vegetated. Some patches of pioneering seagrass *Cymodocea nodosa* were also observed at shallow depths and near the breakwaters.

The sand size and composition varied throughout the study region. Grain size varied from coarse to fine sand, and from poorly sorted to well sorted. Organic matter content was highest within the harbour and offshore, especially where *Posidonia* plants were present.

The SIS (Sediment Imaging Sonar) proved to be a valuable tool for mapping *Posidonia* beds: it was able to detect efficiently areas where the seagrass was absent, or patchy, and most importantly it provided an indication of the canopy height. This information cannot be obtained from conventional methods, such as satellite imagery, aerial photography or side-scan sonar imagery.

The ABL's were able to record wave and current information during a low energy periods, governed by the typical breeze regime, and during 2 moderate wind perturbations, from the SW (reaching 15 knots) and NW (Mistral, the dominant wind in the region, reaching 23 knots). Waves were generated locally and during high winds they had a more constant period, of 2.5 s on average, reaching 0.45 m in height. Wave Reynolds number (Re_w) during the deployment reached 7.1×10^3 at the *Posidonia* site, in a 5 m water depth, and 1.2×10^4 at the shallowest location (4.3 m). Amongst the *Posidonia,* the Reynolds vegetation number (Re_v) was, on average, 414; it reached a maximum of 1006 during the deployment period.

A wave height reduction (of about 5% over 132 m) was measured for waves travelling over the seagrass meadow during mild breeze regimes. There was no evidence of wave height attenuation during windy conditions. The active effect of strong winds on sea surface elevation, wave reflection and/or an increase in seagrass bending under higher energy conditions might have contributed to the small wave height attenuation.

The wave energy dissipation factor was 0.26, on average, which is similar to values for other rough [*Lowe et al.*, 2005a] and vegetated beds [*Möller et al.*, 1999], assuming that it can be considered equal to the friction factor at the bed, as over rippled beds [*Nielsen*, 1992]. Generally, the largest wave dissipation factors were found for waves with the smallest orbital length (A), as observed for waves travelling over coral reefs [*Lowe et al.*, 2005a] and other seagrass species [*Bradley and Houser*, 2009]. However, the trend between A and f_e was not very clear, due to a large scatter in the data.

Unidirectional currents were reduced at the *Posidonia* station during both breezy and windy conditions, confirming previous findings [*Granata et al.*, 2001] in a deep *Posidonia* meadow. Unidirectional flows in the upper canopy/canopy top of the *Posidonia* were halved compared to velocity at the edge of the seagrass bed and reduced by one third compared to the site in shallow water. The currents within the meadows were directed north only for a few hours; most of the time, they were directed towards the south; a trend that was independent of the wind conditions, or the sea state. Conversely, elsewhere, even the breeze regime was able to affect the current direction, which reversed in the late evening, for a few hours, when the breeze was coming from the land. Currents were directed southwards for most of the time; confirming the field observations that the main longshore current (and longshore sediment transport) was directed towards the south.

Whilst unidirectional currents were affected significanly by the *Posidonia* plants, in contrast there was not a difference in wave orbital velocities (U_{max}) between the *Posidonia* site and the site at the shoreward edge of the bed. There is some evidence that attenuation of oscillatory flows at the edge of the patch might have taken place for the longest waves (large A). However, because of the large scatter in the data, such a trend could not be confirmed.

A turbid plume was advected into the study area during the monitoring period. It dominated the turbidity signal recorded at all of the sites. However, most of the smaller peaks could be related to peaks in wave energy, even over the *Posidonia* bed station. As oscillatory flows were not reduced significantly, they might have been able to resuspend the fine sand and mud/silt present at the site.

It was clear also that weaker near-bed unidirectional currents were not able to induced sediment motion, at all of the stations. Thus, waves play a much more

important role in sediment transport (and hydrodynamics) in the Gulf and, probably, within the *Posidonia oceanica* beds.

A narrow belt of fine, potentially highly mobile, sand was located shoreward of the main *Posidonia* meadow edge; its distribution suggests that the mobile sand did not significantly penetrate the established *Posidonia* beds. Therefore, offshore sediment transport might be inhibited by the presence of the canopy. Indeed previous laboratory experiments [*Price et al.*, 1968], have shown that seagrass was able to induce a net shoreward drift in the nearshore. There is evidence that, at the *Posidonia* site, wave orbital asymmetries were mostly positive (directed shoreward), whilst the same did not occur elsewhere. This observation supports previous published evidence, obtained from laboratory experiments, of a potential shoreward drift induced by seagrass meadows [*Price et al.*, 1968] and kelp beds [*Lovas and Torum*, 2001]. This pattern would explain the reduced offshore sediment dispersal (offshore of the meadow's shallowest edge), which would help protect the beach from erosion.

Shorefaces characterised by *Posidonia* beds are very complex environments, with large variability in the topography, sediment composition and hydrodynamics. This complexity probably contributed to the large variability in the data, potentially masking trends. In order to evaluate the real capacity of the plants to reduce wave energy, and to understand the basic mechanisms behind the interaction between plants and waves, it is important to perform experiments under controlled conditions. Nonetheless, this field dataset was useful in defining real conditions in natural beds and was very valuable when planning the laboratory experiments and designing the plants mimics (described in the following Chapters).

.

4 Chapter 4: Large-scale experiments on wave propagation over artificial *Posidonia oceanica*

4.1 Introduction

The relationship between waves and submerged canopies is complex due to the interaction of a range of processes acting simultaneously [*Möller et al.*, 2002; *Mendez and Losada*, 2004; *Koch et al.*, 2009]. Changes in bottom topography, variation in canopy characteristics and changes in wave and current directions are some of the main factors affecting the interaction between a canopy and its surroundings. Thus, understanding these mechanisms in a natural setting is not straightforward. Controlled experiments undertaken in a laboratory flume are useful to improve our understanding of the processes of wave-seagrass interactions and to isolate the contribution of different variables. Few such experiments have been performed in wave flumes; most have been restricted to small flumes, in which scale effects are notoriously difficult to quantify [*Sarpkaya and Isaacson*, 1981; *Hughes*, 1993].

In the present study, wave energy dissipation and wave-induced flow transformation over a submerged artificial *Posidonia oceanica* seagrass meadow were investigated at full scale in the 100 m long wave channel CIEM (Canal d'Investigació i Experimentació Marítima) at Universitat Politècnica de Catalunya, Barcelona, Spain. Access to this large and unique facility was funded by the European project Hydralab 3. The project was carried out in collaboration with several institutions: Aristotle University of Thessaloniki (Greece); University of Cantabria (Spain) the Institute of Marine Sciences, (ISMAR, Italy); as well as the facility providers). [1]

[1] The author was involved in all phases of the project, including: writing the grant proposal, designing the seagrass mimics and experiments, data collection and the decision-making during the experiments and the analysis of the dataset and the interpretation of the results (which will be the focus of Chapter 5 and 6). The author travelled to CIEM in Barcelona on four occasions, for more than 10 weeks in total; this was four times longer than any other individual involved in the project.

The experiments had the following aims:

(a) To quantify wave energy dissipation over a patch of artificial *Posidonia oceanica*, in intermediate water depths, under regular and irregular (also called spectral) waves;

(b) to investigate how artificial *Posidonia oceanica* canopies affects both wave-induced flows and turbulence, within and above the canopy;

(c) to determine the effects of submergence ratio h_s/D (h_s=height of seagrass canopy, D=water depth), seagrass density (number of shoots/m^2) and wave characteristics on the wave-canopy and flow-canopy interactions;

(d) to characterise the wave boundary layer in artificial *Posidonia oceanica* canopies; and

(e) to observe the effects of the canopy on sediment motion.

In order to address these aims, a series of tests were performed, with regular and random waves and several combinations of wave heights and wave periods. The tests were repeated for 4 water depths and for 2 plant densities (see Table 4-9 and 4.10).

This Chapter describes the experiments undertaken in the flume. The results are presented and discussed in Chapters 5 and 6. Section 4.1.1 briefly introduces physical modelling of waves. Section 4.2 forms the majority of the Chapter and provides a description of the flume set-up, the instrumental set-up and the tests performed. For more details on the experiments the reader is referred to *Manca et al*. [2009, included in Appendix D]. The experiments are also described in the publications produced in collaboration with the project partners [*Stratigaki et al.*, 2009a; *Stratigaki et al.*, 2009b; *Manca et al.*, 2010; *Prinos et al.*, 2010; *Stratigaki et al.*, accepted].

The selection of *Posidonia oceanica* plant mimics was an important part of this work. A brief description of the plant mimics is given in this Chapter. A full account of the preliminary work on selecting the mimics, is reported in Appendix B.

4.1.1 Waves in physical models and the advantages of full scale tests

Physical models are used commonly in studies of fluid-structure interactions, being very valuable in understanding problems for which an analytical solution is not available or to verify results from a conceptual or numerical model [*Sarpkaya and Isaacson*, 1981]. However, there are two main disadvantages when creating waves in laboratory flumes, which were classified by *Hughes* [1993] as laboratory effects and scaling effects. The assessment of both is crucial, as each can affect the reliability of the results [*Sarpkaya and Isaacson*, 1981].

Some laboratory effects can be related to the physical constraints of the flume boundaries on the waves and flows, such as diffraction and increased energy loss due to friction induced by the sidewalls. Also cross-waves can develop, especially under energetic wave conditions. Another common problem in flume tests is wave reflection by wave paddles, where waves propagating towards the far end of the flume, opposite to the paddle, are reflected back towards the wave paddle, where they can be reflected again.

Several techniques are used commonly to avoid reflection: the construction of a sandy or gravelly beach at the opposite end to the paddle is common [*Sarpkaya and Isaacson*, 1981]. Often, newer wave paddles are equipped with an active absorbing system. In these modern flumes the wave paddle is programmed to detect and absorb unwanted reflected wave energy. Undesired effects can also be introduced during wave generation. These effects may be manifested as higher harmonics in finite amplitude regular waves or spurious long waves when creating irregular waves using a paddle motion based on a linear theory transformation function [*Sarpkaya and Isaacson*, 1981; *Hughes*, 1993]. The simplification of the natural forcing conditions can also be classified as a laboratory effect. For example, flume waves can only be unidirectional and some forcing functions (such as wind stresses acting on the water surface) are missing. During the programming of experiments it is important to determine whether such simplifications are reasonable approximations of real conditions [*Sarpkaya and Isaacson*, 1981; *Hughes*, 1993].

Scaling effects occur in models that are not at 1:1 scale, when the relevant processes and their variables cannot be simulated in correct relationships to each other [*Hughes*, 1993]. Scale effects in physical models are analogous to the decreased accuracy induced in numerical models, when simplified simulations are applied to represent complex processes [*Kamphuis*, 1991]. Similitude laws are used to enable measurements made in the model tests to predict prototype values, by providing a relationship between variables in the prototype and the model [*Sarpkaya and Isaacson*, 1981]. The Froude similitude law (ratio of the inertial to gravity forces) is used often for the scaling of laboratory tests involving wave motion [*Sarpkaya and Isaacson*, 1981; *Hughes*, 1993]. The Froude scaling is based upon the assumption that gravity is the main physical force balancing the inertial forces and that all other physical forces (such as viscosity and elasticity) are incorrectly scaled [*Hughes*, 1993]. Other properties that might be important in vegetated beds, such as turbulence, are not considered in Froude

scaling, increasing the uncertainties on the relevance and reliability of scaled tests. Turbulence, in particular, is a three-dimensional process that can be studied in a bi-dimensional physical model, but it is best to modelled at full scale [*Hughes*, 1993].

It is well known that the presence of submerged canopies will have a large effect on flow velocities and will affect the structure of the bottom boundary layer [*Løvås and Tørum*, 2001; *Lowe et al.*, 2005b; *Koch et al.*, 2006a]. Froude scaling does not provide a correct estimate of the scaled bed shear stresses, distorting the bottom boundary layer [*Cáceres et al.*, 2008]. In addition, a disadvantage of employing scaled models when investigating problems which require the use of a mobile bed (such as canopy-wave-sediment interactions) is that while the dimensions of the mimics and the size of the waves can be scaled, the sand grain-size can not be reduced without changing its cohesive properties. Therefore large–scale facilities are therefore valuable because they are better suited for sediment transport investigations, especially when suspension is the main sediment transport mechanism [*Cáceres et al.*, 2008]. Furthermore, adequately large values of the Reynolds number can be difficult to obtain in channels of limited size, therefore limiting the understanding of the boundary layer processes [*Nielsen*, 1992]. Another advantage of tests undertaken at full scale has been the direct comparison of the oscillation of full-scale mimics in the flume, with videos of natural seagrass under waves, facilitating the challenging task of selecting accurate *Posidonia oceanica* mimics.

4.2 Description of the experiments

4.2.1 The CIEM flume

The CIEM wave flume, located at the Maritime Engineering Laboratory of the Universitat Politècnica de Catalunya (LIM/UPC), is a unique large-scale research installation both in terms of its dimensions (100 m length, 3 m width and 5 m depth) and its performance capabilities. The CIEM flume is a proven tool for large-scale and full-scale investigations in coastal engineering and coastal morphodynamics [*Cáceres et al.*, 2008; *Oliveira et al.*, 2009; *Cuomo et al.*, 2010].

Waves are generated by a wedge type paddle (Figure 4.1), with a 30º slope and 2 m horizontal stroke. The design is particularly suited for intermediate-type waves ($1/20<D/\lambda<1/2$, see Chapter 2). The wave generation system is hydraulically-activated

by 3 pumps and is PC-controlled. Sophisticated software controls an active wave absorption system (SAWAS, developed at LIM/UPC for the CIEM flume), which is designed to limit wave reflection and seiching within the channel. The system is capable of producing regular and irregular waves, using parametric or user-defined spectra, as well as time-series. The maximum wave height that can be generated at the wave paddle is 1.6 m (0.9 m significant wave height), corresponding to a wave exceeding 2 m in height at the test section. The paddle can generate waves of frequencies ranging from 0.125 to 1 Hz.

Figure 4.1 The CIEM wave generator (Photo courtesy LIM/UPC)

The flume has seven lateral windows along its length and the flume waters are kept clear by a continuous filtering system, enhancing the observation and filming of particle movements. The flume is equipped with software for data acquisition and management, together with online quality control tests during the execution of experiments.

4.2.2 Set-up of the flume

The experiments were undertaken in the CIEM wave flume, between 20th October 2008 and 7th November 2008.

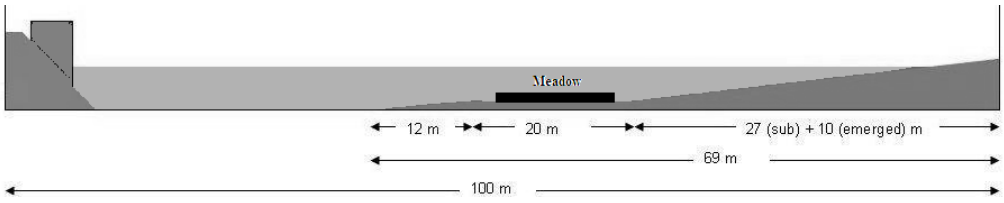

Figure 4.2. Cross-section of the profile in the CIEM flume at the start of experiments.

A sandy slope, of about 1/15, was built at the opposite end of the flume to the wave paddle to reduce wave reflection. A 20 m long flat sandy region was created in the central part of the flume. In this region the sand layer was 0.7 m in thickness. A gentle slope, about 12 m long, connected the flat part to the flume bed towards the wave paddle. An illustration of the bottom profile at the start of experiments is shown in Figure 4.2.

The artificial seagrass meadow was 10.7 m long, (Figure 4.2 and Figure 4.3) and located in the flat horizontal area of the flume at a distance of 38.4 m from the wave paddle (its trailing edge was located at a distance of 49.1 m). All the measurements described in this thesis are referred to an XYZ coordinate system. The X coordinate is in the along-flume direction, which is positive in the direction of wave travel. The origin is at the edge of the wave paddle at rest. Lower case x (which is the main measurement used when the data are described and analysed in Chapters 5 and 6) is used to define the distance in the X direction from the start of the artificial seagrass patch, as indicated in Figure 4.3. The Y direction is the distance from the side wall, from which all the equipment is secured (the left wall looking towards the wave paddle). The Z distance is the vertical distance from the sandy bottom, positive values denote the upwards direction (Figure 4.3).

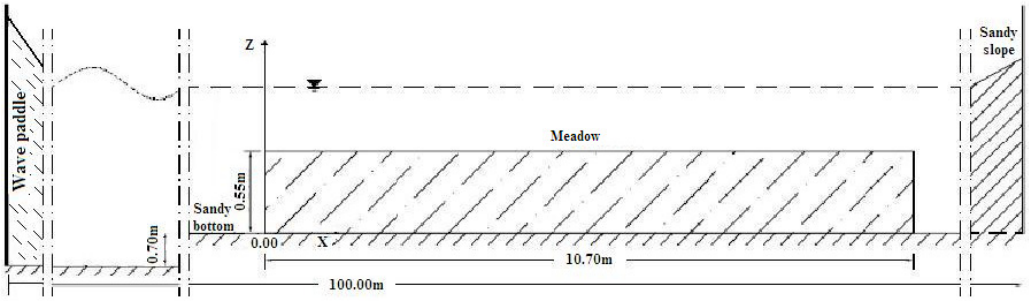

Figure 4.3 Schematic diagram of the artificial seagrass patch used in the experimental set-up [from *Stratigaki et al.*, 2009b].

4.2.3 Artificial seagrass mimics and patch

A major challenge in these experiments was the design of a mimic for the seagrass *Posidonia oceanica*. The composition and shape of the mimics were chosen to have a comparable hydraulic behaviour in the fresh water inside the flume, with that of natural plants in seawater. The criteria used in the choice of the material to mimic the seagrass leaf were:

flexibility and density comparable to real seagrass;

cost within the limits of the budget;

non-absorbent to water;

no elastic memory/resistant to fatigue, so that the properties wouldn't change after being in the water and being bent several times; and

ease of cutting and handling.

The material that best satisfied these criteria was found to be a PVC foam, as used in the advertising industry. It was available as large sheets and could be efficiently cut into strips by the manufacturer. The physical properties of the *Posidonia oceanica* leaves, with those of the PVC foam strips are compared in Table 4-1. Using these properties a dimensional analysis was performed, in order to determine the characteristic parameters for prototype and laboratory conditions. The mimics (indicated with subscript m) were required to have similar morphological and dynamic properties, to those of the prototype (subscript p).

Table 4-1 Properties of the PVC foam blades used in the construction of the mimics, compared with those of the natural *Posidonia oceanica* seagrass from the literature.

Property	PVC foam strips	*Posidonia oceanica leaves [Folkard, 2005]*
Modulus of Elasticity (E) x 10^9N/m^2	0.90	*0.41-0.53*
Density of the material (ρ_s) kg m^{-3}	550-700	*800-1020*
Thickness (l) mm	1	*0.2*
Width (b) cm	*1.2*	*1*

Ghisalberti and Nepf [2002] introduced two parameters λ_1 and λ_2 for the design of vegetation mimics for hydrodynamic studies. The parameter λ_1 was derived from the ratio of blade buoyancy to blade rigidity and is defined as:

$$\lambda_1 = \frac{(\rho_S - \rho)h_s^3}{El^2} \qquad \textbf{Eq. 4-1}$$

where h_s and l are the length and thickness of the leaves, respectively; ρ is the fluid density and ρ_s the density of the material. It was assumed that the average density of freshwater was ρ=1000 kg/m³ (laboratory) and the density of seawater was 1025 kg/m³ (prototype). $\lambda_{1,p}$ should be as close as possible to $\lambda_{1,m}$. Based upon the above relationship the parameter $\lambda_{1,m}$ is within the limits $0.33\ h_s^3 < \lambda_{1,m} < 0.5\ h_s^3$ and the $\lambda_{1,p}$ is within $0.23\ h_s^3 < \lambda_{1,p} < 13.7\ h_s^3$. Leaf length is quite variable in the field and reaches a maximum value of 0.75 m [*Buia et al.*, 2004]. In these experiments $\lambda_{1,m}$ varied between

0.055 and 0.083 s^2/m which confirms that the model dynamic characteristics lie within the range of the prototype values for seagrass [between 0.001 and 1 s^2/m, *Ghisalberti and Nepf*, 2002]). The second design criteria (λ_2) is derived from the ratio between blade rigidity and the drag forces acting on the blade; therefore, it is a function of the characteristic velocity acting on the canopy (U_c).

$$\lambda_2 = \frac{El^3}{h_s^3 U_c^{\ 2}} \qquad \textbf{Eq. 4-2}$$

Test conditions and orbital velocities were selected, taking into consideration that $\lambda_{2,\,m}$ had to be within the range of $\lambda_{2,\,p}$, as found in nature.

These formulae assume a cantilever movement of the plant. A similar approach has been used in other studies on wave-vegetation interactions [*Fonseca et al.*, 2007; *Bradley and Houser*, 2009].

Preliminary tests at small-scale were carried out to evaluate the hydraulic behaviour of the plant mimics. The bending angle of the *Posidonia* mimics was compared against the bending angle of the natural *Posidonia* shoots exposed to the same unidirectional flow and were seen to be similar (for more detail see Appendix B). The mimics were then positioned in the CIEM flume and tested under several wave conditions. A video of these tests was compared with videos of natural *Posidonia* patches taken at a similar water depth, under normal wind wave conditions. The characteristic oscillatory "whip-like" movement of the plants observed in the field and reported in literature [*Ghisalberti and Nepf*, 2002; *Bradley and Houser*, 2009] was well reproduced by the artificial plants (Figure 4.5).

In order to simulate the morphology of the *Posidonia* shoots (see Figure 2.5 in Chapter 2 and Appendix B), each mimic was a composite of four blades of two lengths (one pair of 40 cm length, and another pair of 60 cm length, Figure 4.4). The variable leaf length was selected in order to mimic the natural variation with height of the canopy density, defined by *Folkard* [2005] and *Maltese et al.* [2007]. Mimics with variable leaf length configuration were found to simulate better the oscillation and morphology of *Posidonia oceanica,* in preliminary tests (see Appendix B for more detail). The leaves were inserted into a stiff 10.0 cm long rod, made of PVC (Figure 4.4). The rods were introduced into to 2 cm thick perforated metal boards. The boards were pushed into the sandy bed for stability, then covered with about 4 cm of sand; hence, about 4 cm of the rod was protruding from the sandy bed, to simulate the stiff

rhizome of the plant. The canopy reached a maximum elevation of 55 cm from the sandy bed, when not exposed to waves.

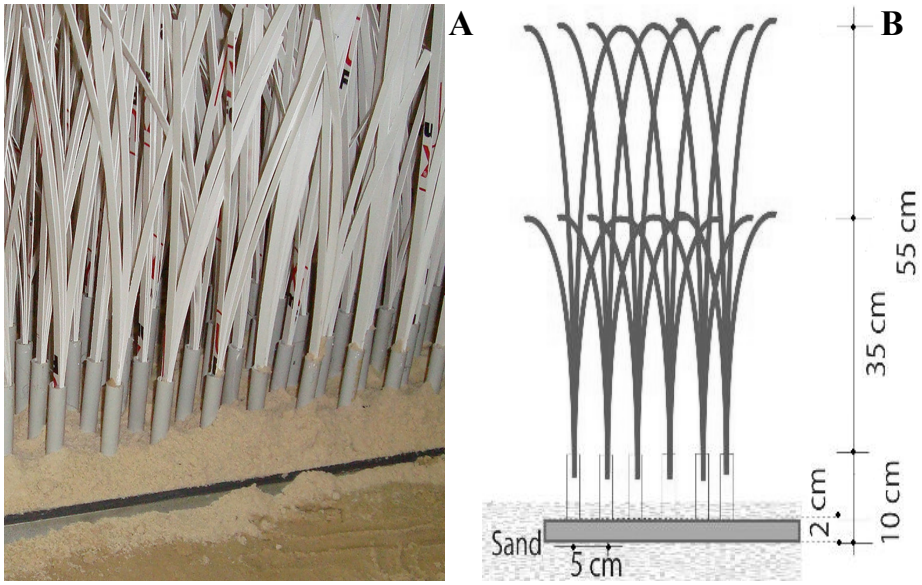

Figure 4.4 A) Detail of the canopy during construction of a seagrass patch; and B) A sketch of the geometry of the artificial *Posidonia oceanica* canopy.

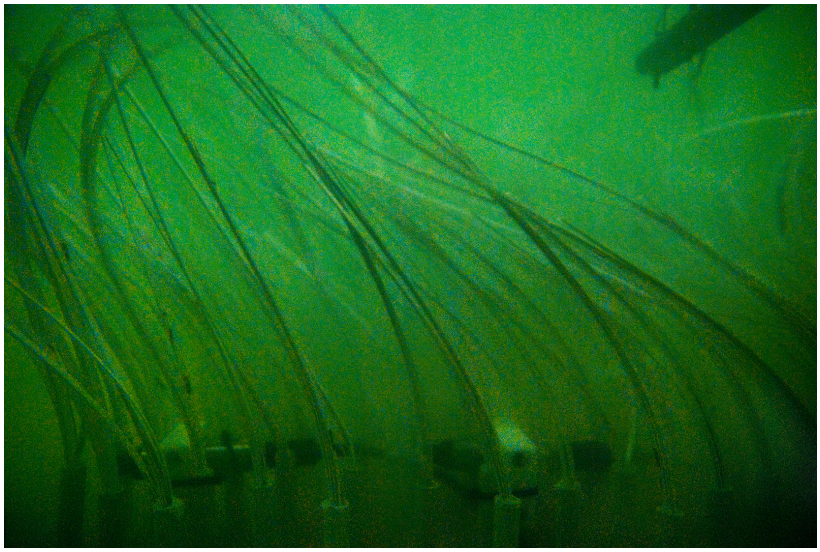

Figure 4.5 *Posidonia oceanica* mimics seen from the side window of the CIEM flume. The "whip-like" motion of the mimics under waves is apparent.

The experiments were carried out using two different meadow configurations:

1. high density (360 stems m^{-2} arranged in a non-staggered pattern); and
2. low density (180 stems m^{-2} arranged in a staggered pattern).

These densities lie within the typical range of densities measured in the field (Chapter 3). They are representative of a sparse and very sparse *Posidonia* meadow, following *Giraud's* [1977] classification.

The seagrass patch was built as a series of modules on boards that were fixed firmly together. The total length (L) of the patch was 10.7 m and the width was 2.5 m. A gap between the flume walls and the patch (Figure 4.6) was created for a better simulation of a patchy seagrass distribution [*Fonseca and Koehl*, 2006], typical of shallow waters (see Chapter 3) and to avoid any disruptions to the movement of the mimics, by the sidewalls. The gap between the instrumented flume wall and the patch was kept at a minimum (0.3 m), to ensure that the flows recorded were undisturbed.

Figure 4.6 Overview of the patch and the instrument layout within the CIEM flume (looking towards the wave paddle). Wave gauges and velocimeters are secured to the sidewall.

4.2.4 Instrumentation

A series of wave gauges were deployed along the flume, to monitor wave passage. Three vertical arrays of current-meters and one current profiler were also installed in the flume, to detect the flow velocities induced by the seagrass patch at different elevations and positions. Turbidity was measured also in front and within the patch by Optical

Backscatter Sensors (OBS). All measuring devices were synchronized and provided continuous measurements at 20 Hz. The motion of the mimics during the experiments could be observed through the windows of the flume. All details of these instruments are provided in the following paragraphs and the major specifications are reported in Table 4-2.

4.2.4.1 Wave measurements

Ten pre-calibrated twin-wires resistance wave gauges were used during this project (in the foreground, on the left, in Figure 4.6). These instruments record changes in water surface elevations by measuring changes in conductance. They are made of two parallel stainless steel wires, aligned perpendicular to the direction of wave travel and separated by a known fixed distance. The wires have been custom-built for the CIEM flume with an active length of 2 m in order to measure waves up to 2 m in height [*LIM/UPC*, 2010]. Conductance between the wires is recorded by the acquisition board (General Instruments). The instantaneous depth of immersion is proportional to conductance, which depends upon the conductivity of the water [*Hughes*, 1993].

Table 4-2 Specification of the sensors used in the laboratory experiments [data from *LIM/UPC*, 2010].

Instrument	Type	Accuracy	Sampling frequency
ADV-Vectrino- Nortek Ltd	Acoustic velocimeter	±0.05% of the measured value	20 Hz
S-type EMC Delft Hydraulics	Electromagnetic spherical biaxial velocimeter	±3% of measured value	20 Hz
OBS-3+	Turbidity Sensor	±1% of measured value	20 Hz
National instruments (board) LIM/UPC (cables)	Resistive wave gauges	up to ±10 mm	20 Hz
Ultralab ULS-40D, General Acoustics	Acoustic wave gauges	±1 mm	20 Hz

The wave gauges are capable of producing very high resolution data (±1 mm accuracy , see Table 4-2); they are reliable and easy to calibrate, as they have a good linear response [*Hughes*, 1993]. Since the submerged part of the instrument consists of

only 2 thin (1.5 mm diameter) stainless steel wires, the interaction between the device and the incoming/reflected waves is low. Calibrations were performed before the start of each experiment, since measurements are affected by changes in water conductivity (salinity and temperature). The calibration function from voltage to depth was obtained by varying the mean water level within the flume and comparing the voltage output of the instruments. The transformation of the data from each wave-gauge was performed by the acquisition software of the flume.

The distance along the flume (X) from the edge of the wave paddle and the relative distance from the leading edge of the meadow (x) of each instrument are indicated in Table 4-3 and their position is sketched in Figure 4.13.

Table 4-3 Location of the resistive wave gauges: X is the distance along the flume from the wave paddle at rest; x is the distance from the leading edge of the seagrass patch, positive in the direction of wave travel.

Sensor	X (m)	x (m)
WG14	5	-33.36
WG0	15.01	-23.35
WG1	15.73	-22.63
WG2	16.7	-21.66
WG3	17.41	-20.95
WG4	37.86	-0.5
WG5	38.86	0.5
WG6	39.86	1.5
WG7	40.86	2.5
WG8	46.86	8.5
WG9	48.86	10.5
WG10	42.86	4.5
WG11	44.86	6.5
WG12	49.86	11.5
WG13	50.86	12.5

Also a series of 12 acoustic wave gauges (Ultralab ULS-40D, General Acoustic) were placed along the flume (see Table 4-4 and the sketch in Figure 4.13 for details on their exact locations) to monitor wave height variations.

These devices emit ultrasonic pulses, which are reflected by the water surface and received by the instrument as an echo. The instruments output a voltage between 0 and 10 V, proportional to the distance between the probe and the water surface. Each instrument has as known transformation function (a linear relationship between signal intensity to distance). Their application range is 0.18 m to 3.5 m and their accuracy is up to ± 1 mm under stable conditions. During the first tests, some spurious peaks in the acoustic wave gauge signal were noticed. These problems were attributed to the interference between the gauges. In order to overcome this problem, some of the acoustic gauges were de-activated, to increase the spacing between them and avoid such interference. Calibration was performed and the reliability of the measurements with the new instrument configuration was also verified before further tests were carried out. During most of the tests 6 of the 12 acoustic wave gauges were in use.

Table 4-4 Probe number, status and location of the acoustic wave gauges, where: X is the distance along the flume from the wave paddle at rest and x is the distance from the leading edge of the seagrass patch, positive in the direction of wave travel

Sensor	Status	X (m)	x (m)
AWG0	on	38.36	0
AWG1	off	39.36	1
AWG2	on	40.36	2
AWG3	off	41.86	3.5
AWG4	on	43.86	5.5
AWG5	off	45.86	7.5
AWG6	on	47.86	9.5
AWG7	off	49.36	11
AWG8	on	50.36	12
AWG9	off	51.36	13
AWG10	on	52.81	14.45
AWG11	off	53.71	15.35

4.2.4.2 Flow measurements

Eight 3D Acoustic Doppler Velocimeters (ADV, Vectrino, Nortek Ltd.) and four bi-axis electromagnetic current meters (EMCM, S-type, Delft Hydraulics) were used to measure flow velocities in front, above and within the patch. Shoreward of the trailing

edge of the patch, a velocity profiler recorded velocities at several elevations in the water column.

The Vectrino ADV (Figure 4.7) is a high resolution 3D velocity probe that uses the Doppler effect to measure current velocity by transmitting short pairs of sound pulses, listening to their echoes and, ultimately, measuring the change in pitch or frequency of the returned signal [*Nortek*, 2005]. The probe consists of a transducer that transmits the pulses located in the centre of the probe, together with four receivers transducers, each mounted inside the receiver arm. The sound is reflected by particles in the water. When water is very clear the quality of measurements is poor. However, the quality of each data sample can be monitored and obtained from information on the signal to noise ratio (SNR), amplitude and correlation of the signal, recorded in a separate file. According to the user manual [*Nortek*, 2005], when the signal amplitude is larger than 70 counts (each count is 0.45dB in signal strength) the signal can be considered as "good". This was the case throughout the experiment. Moreover, the SNR and the correlation of the raw data were checked during data processing (see Chapters 5 and 6).

Figure 4.7 The velocimeter array located in front of the leading edge of the patch.

The sampling diameter of the ADVs was 6 mm and was located about 5 cm in front of each probe (i.e. where the beams intersect). The nominal velocity range was set to 2.5 m/s and the transmit pulse length to 2.4 mm. With this velocity range the internal

ping rate was 125 Hz. The salinity was set to zero (freshwater) and the temperature of the water was detected automatically by the instruments. The correction for the speed of sound and calibration was performed automatically by the instruments.

The EMCMs (electromagnetic current meters, S-Type, Delft Hydraulics, Table 4.2) were used inside the canopy. The principle behind the functioning of EMCM-type current meters has been described in Chapter 3. EMCM has a sampling volume with a diameter that is typically two to three times the diameter of the probe (40mm) [*LIM/UPC*, 2010]. The devices are calibrated by the manufacturer, and the calibration function is set before use. The instrument output signal is already converted from voltage to velocity signal.

All the ADVs and EMCMs were placed in the horizontal central area of the flume, at 3 different locations along the flume: 0.7 m in front of the leading edge of the patch (x/L=-0.07 indicated as P1 in Figure 4.14, L=10.7 m and is the total length of the patch); 1.8 m within the seagrass patch (x/L=0.17 indicated as P2 in Figure 4.14) and 8 m further inside the seagrass patch (x/L=0.80 indicated as P3 in Figure 4.14). These positions are referred to in Chapters 5 and 6. The velocimeters were arranged in three vertical profiles, at four elevations (Z) from the flume bed (measured from the top of the sand layer), as indicated in Table 4-5.

Table 4-5 List of ADV measuring devices and their position (X being the distance along the flume from the wave paddle at rest; and x is the distance from the leading edge of the seagrass patch, positive in the direction of wave travel).

Sensor	X (m)	x (m)	Y (m)	Z (m)
ADV0	37.66	-0.7	0.84	0.2
ADV1	37.66	-0.7	0.84	0.4
ADV2	37.66	-0.7	0.84	0.6
ADV3	37.66	-0.7	0.84	0.8
EMF0	40.16	1.8	0.84	0.2
EMF1	40.16	1.8	0.84	0.4
ADV4	40.16	1.8	0.84	0.6
ADV5	40.16	1.8	0.84	0.8
EMF2	46.96	8.6	0.84	0.2
EMF3	46.96	8.6	0.84	0.4
ADV6	46.96	8.6	0.84	0.6
ADV7	46.96	8.6	0.84	0.8

Inside the canopy (at elevations $z < 0.55$; $x/L=0.17$ and $x/L=0.80$), the plant leaves interfered with the ADV measurements; thus, EMCMs were used instead. The installation of ADVs amongst the mimics and the creation of a clearing around the ADV sensors was considered, but, in order to avoid damage to the sensors under the most energetic tests, the clearing would have had to have a minimum diameter of 1 m. This option was rejected as it would have caused excessive disruption to the flow and dataset.

The velocimeters were located well inside the patch, where neither side wall effects nor effects due to the presence of the lateral gap would be observed in the velocity measurements.

4.2.4.3 Optical backscatter sensors (OBS)

Seven Optical Backscatter Sensors (OBS-3+, D&A Instrument Company) were used for the measurements of turbidity and suspended sand concentration in front of the leading edge of the patch, and within it. Chapter 3 provides a detailed description of the OBS technology. The sensor responses depends upon the composition, size and shape of the particles in suspension [*Van Rijn*, 2007]. Therefore, the instruments were calibrated using the sand used for the flume (which will be described in Section 4.2.5). The calibration was underataken at the LIM laboratory using *Butt et al.'s* [2002] approach. Glycerol, a clear fluid with higher viscosity than water was used as it has the advantage of decreasing the settling velocity. Several known sand concentrations were introduced into the control volume and the signal output was recorded. The sand and glycerol mixture was kept in a well-mixed suspension, by stirring throughout the procedure. Using this high viscosity fluid, the suspension is spatially and temporally more homogeneous than using traditional methods with water, thus improving the reliability of the signal.

The location of each OBS is listed in Table 4-6, where the relative distances of each OBS from the leading edge of the patch are indicated.

The elevation of the OBS (Z) from the sandy bed changed during tests, because of the movement of sand. OBS 0 and OBS 1 (see Table 4-6) were located in front of the patch, secured to the pole holding the resistive wave gauge WG4. All other OBSs were located inside the patch and fixed securely at the base, at a distance of 60 cm from the instrumented wall. Sand transport was expected to be small in the central area of the

flume and in particular inside the seagrass patch very limited sediment transport was anticipated. For this reason, all the OBS instruments were located near the edge of the seagrass patch. However, during the first tests, movement of sand caused "starvation" of OBS 2 and OBS 3 and burial of OBS 4.

Table 4-6 Location and name of the optical backscatter sensors at the start of the experiments.

Sensor	X (m)	x(m)	Y (m)	Z (m)
OBS 0	37.86	-0.5	0.6	0.04
OBS 1	37.86	-0.5	0.6	0.09
OBS 2	38.385	0.025	0.6	0.03-0.04
OBS 3	38.66	0.3	0.7	0.03-0.04
OBS 4	38.96	0.6	0.7	0.03-0.04
OBS 5	39.36	1	0.7	0.03-0.04
OBS 6	39.86	1.5	0.7	0.03-0.04

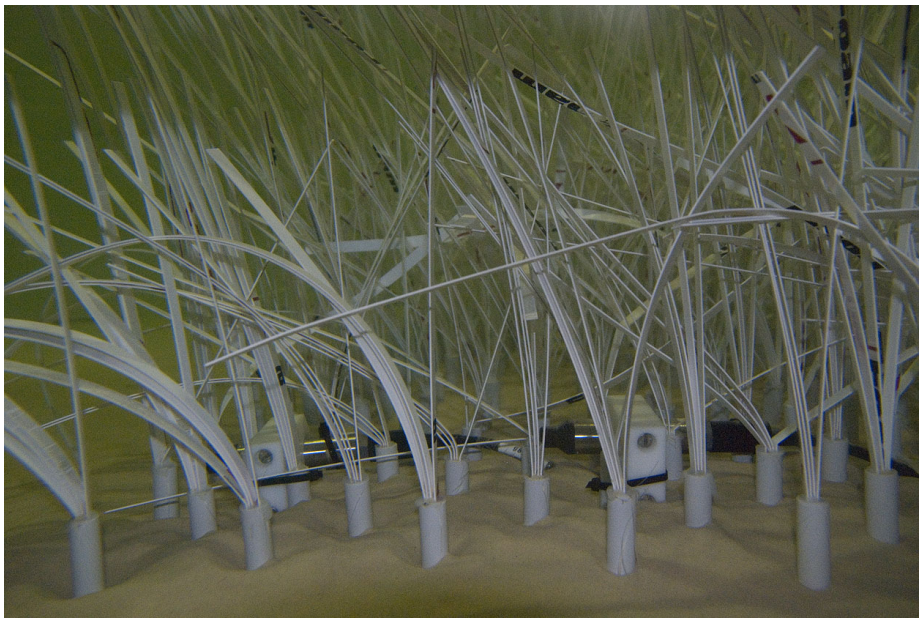

Figure 4.8 Location of an OBS within the mimic canopy.

4.2.4.4 Bed profiles

A mechanical profiler was used to detect and record changes in the bed profile both in the exposed and submerged beach. A sketch of the profiler is shown in Figure 4.9. The profiler was located on a mobile platform that moved on rails along the flume at a

constant, known, speed. A 3 m long articulating arm with a small wheel (0.2 m diameter) at its end was attached to the platform, so that the wheel followed the bed profile. The distance (r in Figure 4.9) between the centre of the wheel and the lower arm hinge was 3.15 m and the Z_{offset} was 3 m. The angle α(x) (in Figure 4.9) was measured constantly by an inclinometer located on the arm. Dedicated software returned the wheel's position in X and Z coordinates, calculated from the profiler's geometry, the speed of movement of the platform and the measurements of α(x). The profiler was calibrated by measuring the position of different control points of known coordinates. It operated on a profile with a maximum vertical excursion of 2.5 m. Changes in bed elevation of the sand profile were monitored after each water depth change. For practical reasons the profiler could not be operated over the meadow.

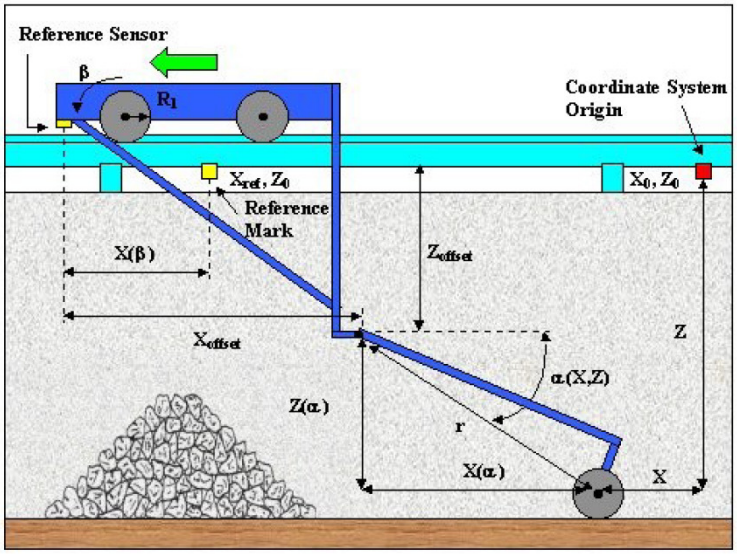

Figure 4.9 Sketch of the mechanical bed profiler [From *LIM/UPC*, 2010].

The profile could be measured from X=56 m (6.9 m shoreward of the trailing edge of the seagrass patch) to the start of the flat part of the emerged beach (X=86 m). Some typical profiles of the beach are shown in Figure 4.10, for the test series with 180 stems/m^2. The vertical axis is the vertical distance from Z0 (defined in Figure 4.9). The 1:15 slope did not change during the tests, only the position of the bar deepened as the water depth was decreased.

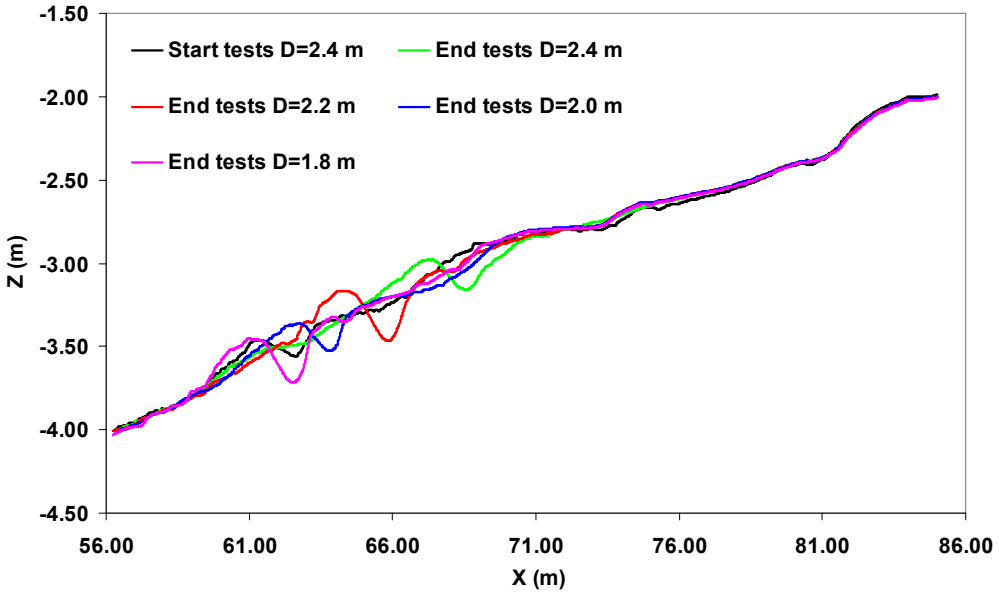

Figure 4.10 Submerged and emerged beach profile at the start and end of tests with 180 stems/m^2. Z is the depth referred to as Z0 defined in Figure 4.9. X is the horizontal distance from the wave paddle at rest. (adapted from the profile data analysis by LIM/UPC provided during the experiments). The location of the sand bar depended upon water depth is evident, whilst the profile slope was practically constant.

4.2.5 Sediment characteristics

The bed was composed of medium well-sorted sand (commercial name J5060S). The measured statistical parameters obtained with both the Method of Moments [*Riviere*, 1977] and the *Folk and Ward* method [1957] are listed in Figure 4.11 (measured by the LIM laboratory). The measured median grain-size of the sand sample was 246 μm and the measured settling velocity was 34 mm/s. Thus, the sediment used was a medium, moderately well sorted, sand.

	METHOD OF MOMENTS			FOLK & WARD METHOD		
	Arithmetic	Geometric	Logarithmic	Geometric	Logarithmic	Description
	μm	μm	ϕ	μm	ϕ	
MEAN ($\bar{x}$):	266,6	251,7	1,990	241,7	2,049	Fine Sand
SORTING (σ):	83,87	1,401	0,486	1,415	0,501	Moderately Well Sorted
SKEWNESS (Sk):	0,089	-0,372	0,372	-0,066	0,066	Symmetrical
KURTOSIS (K):	2,191	2,011	2,011	0,678	0,678	Platykurtic

Figure 4.11 Grain-size statistical parameters of the sand used in these experiments (provided by LIM/UPC)

The characteristic grain size and the absence of fines in the sample made this sand suitable for mobile-bed tests, with predominant suspended load regimes under the wave conditions that can be generated in the CIEM flume.

4.2.6 Description and selection of the test conditions

The artificial seagrass patch was exposed to waves of different steepnesses under 4 different water depths, with both regular and irregular waves. For a list of the tests and a description of the wave conditions created see Table 4-9 and Table 4-10. All of the tests were repeated for a patch with the low density configuration. A total of 200 regular waves were generated during each test. The irregular waves were created using a parametric spectra. Measured wave spectra in the sea are often very similar to each other and can be simulated by using a parametric expression [*Kamphuis*, 2002]. The Pierson-Moskowitz spectrum is often used for fully-developed seas, whilst other spectra have been used for developing seas. The Jonswap spectrum is used most commonly to represent developing wind waves with a peak enhancement factor γ=3.3, (Figure 4.12) [*Soulsby*, 1997; *Kamphuis*, 2002]; this was used in all of the irregular wave experiments.

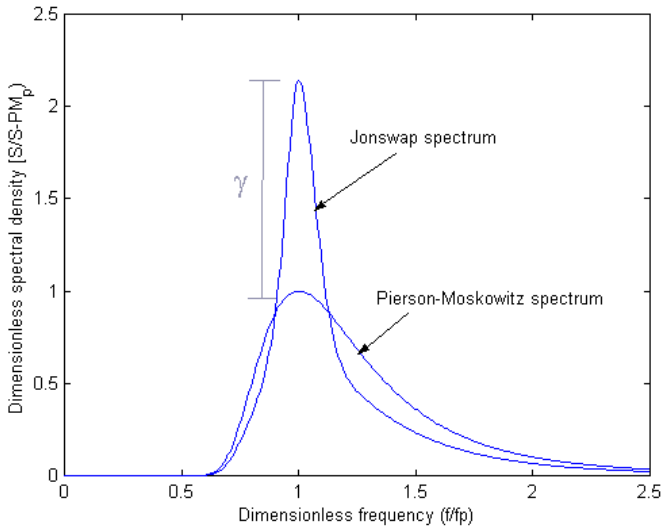

Figure 4.12 The Jonswap spectrum and the Pierson-Moskowitz spectrum for fully-developed seas. The peak enhancement factor (γ) is indicated and it is defined as the ratio between a peak spectrum and a peak spectrum of the Pierson-Moskowitz spectrum.

The wave conditions used, were selected to represent realistic wind-wave conditions found in the Mediterranean [*Franco et al.*, 2004]. The selection of target wave heights (H_T) was also dictated by the maximum wave height that the wave generator could produce for each given combination of period (T) and water depth (D). Non-breaking wave conditions over the seagrass patch were simulated; wave steepness was calculated for the prediction of wave breaking conditions. The Ursell number (*UR*)

was computed, to predict wave conditions that could give rise to significant wave non-linearity:

$$UR = \frac{H\lambda^2}{D^3} \qquad \textbf{Eq. 4-3}$$

where H is the wave height; λ is the wave length; and D is the water depth. Sediment motion was used as one of the criteria in the selection of the wave conditions. The threshold of motion of the sand in the flume, in freshwater, was evaluated in terms of bed shear stress (τ_0). The threshold bed shear stress (τ_{cr}) was compared against the predicted bed shear stress for each test. The critical Shield's parameter for bed-load (θ_{cr}) was obtained from:

$$\theta_{cr} = \frac{0.24}{D_*} + 0.055\left[1 - \exp(-0.020 D_*\right] \qquad \textbf{Eq. 4-4}$$

[*Soulsby*, 1997], with the dimensionless grain diameter (D_*) defined as:

$$D_* = \left[\frac{g(s-1)}{\upsilon^2}\right]^{\frac{1}{3}} d_{50} \qquad \textbf{Eq. 4-5}$$

where: d_{50} is the median diameter of grains; s is the ratio of density of quartz grain (2650 kg m^{-3}) and density of water (ρ=1000 kg m^{-3}); υ is the kinematic viscosity of water (assumed to be equal to 1.0 X 10^{-6} m^2 s^{-1}).

This parameter was applied in the Shield's formula (as in Soulsby, 1997), to obtain the threshold bed shear stress predicted inside the flume. This resulted in a threshold stress of 0.18 N m^{-2} (Table 4-8).

The shear stress at the bed, over a wave cycle, was calculated using:

$$\tau_w = 0.5\rho f_w U_w^{\ 2} \qquad \textbf{Eq. 4-6}$$

The friction factor under waves f_w was obtained using *Nielsen*'s method [1992].

$$f_w = \exp\left(5.5\left(\frac{r}{A}\right)^{0.2} - 6.3\right) \qquad \textbf{Eq. 4-7}$$

Where A is the orbital amplitude of fluid obtained from linear wave theory and assuming the flow regime to be rough turbulent and the hydraulic roughness (r) to be equal to the grain size (d_{50}). The friction factor (f_w) is then substituted to obtain τ_w (Table 4-8).

The friction factor under waves was also calculated using the *Soulsby and Clarke* [2005] method, which provides the maximum value of bed shear stress (see Table 4-8).

According to this method, friction factors in smooth turbulent flow conditions (f_w^r) and rough turbulent flow conditions (f_w^s) are calculated respectively as:

$$f_w^r = 1.39\left(\frac{A}{z_0}\right)^{-0.52} \quad \textbf{Eq. 4-8}$$

$$f_w^s = 0.0521\,\mathrm{Re}_w^{-0.187} \quad \textbf{Eq. 4-9}$$

with the bed roughness length defined as:

$$z_0 = \frac{1}{12} d_{50} \text{ [*Soulsby and Clarke*, 2005]} \quad \textbf{Eq. 4-10}$$

For $Re_w > 1.5 \times 10^5$, the flow is considered to be turbulent and the maximum value between f_w^r and f_w^s is applied in the calculation of $\tau_{wmax.}$. When $Re_w \leq 1.5 \times 10^5$ laminar flow is assumed and $\tau_{wmax.}$ is derived using:

$$\tau_{w\max} = \rho\,\mathrm{Re}_w^{-0.5} U_w^2 \quad \textbf{Eq. 4-11}$$

Sediment motion is predicted when the bed shear stress exceeds the critical value τ_{cr}. This condition is indicated with the number "1" in Table 4-8. The condition of no sediment transport is indicated with "0". Sediment transport was predicted to occur in all of the tests, except for the wave period T=1.5 s. The first tests to be performed were those with monochromatic waves and in deeper waters (D=2.4 m). Scour in the sand started to appear at the edge of the patch when a test was performed with a target wave height (H_T) greater than 0.65 m and target wave period greater than T=3 s. The test with H_T=0.90 was aborted, as it lifted the seagrass patch! To avoid complications, tests with a target wave height greater than 0.5m were not performed, as even larger stresses would be produced when the water level was lowered. A list of the tests that were performed and their characteristics can be found in Table 4-9 (for regular waves) and Table 4-10 (for irregular waves).

4.2.7 Data acquisition

Wave generation and part of the data acquisition (wave gauges, OBSs, electro-magnetic current-meters) were controlled by the General Acquisition Software developed for the CIEM flume. The software used to acquire the ADV information was the Polysink, provided by the ADV manufacturer. The software was used to synchronise the ADV probes to a selected master probe (ADV3/Probe 4 in all tests) and to log information on the intensity of the signal.

The data from each test was stored in 3 groups of files:

- Acquisition file (.res files). These files were produced directly by the acquisition system of the wave paddle and contain: the absolute time reference, the water depth at the paddle, the frequency of acquisition, the signals from the wave gauges (both acoustic and resistive), the data from the electro-magnetic current-meters, the OBS signals and the data acquired by one of the ADVs (ADV3). All of the signals in these files were synchronised. The signal of ADV3 was used to synchronise the data in the .res file with the other type of files.
- Polysink files (.vno files). The raw Vectrino files from the Polysink software, where the velocity data in the 3 directions from each ADV was synchronised and stored. For each ADV, the signal to noise ratio, correlation of the signal and signal amplitude was available (see Chapter 3).

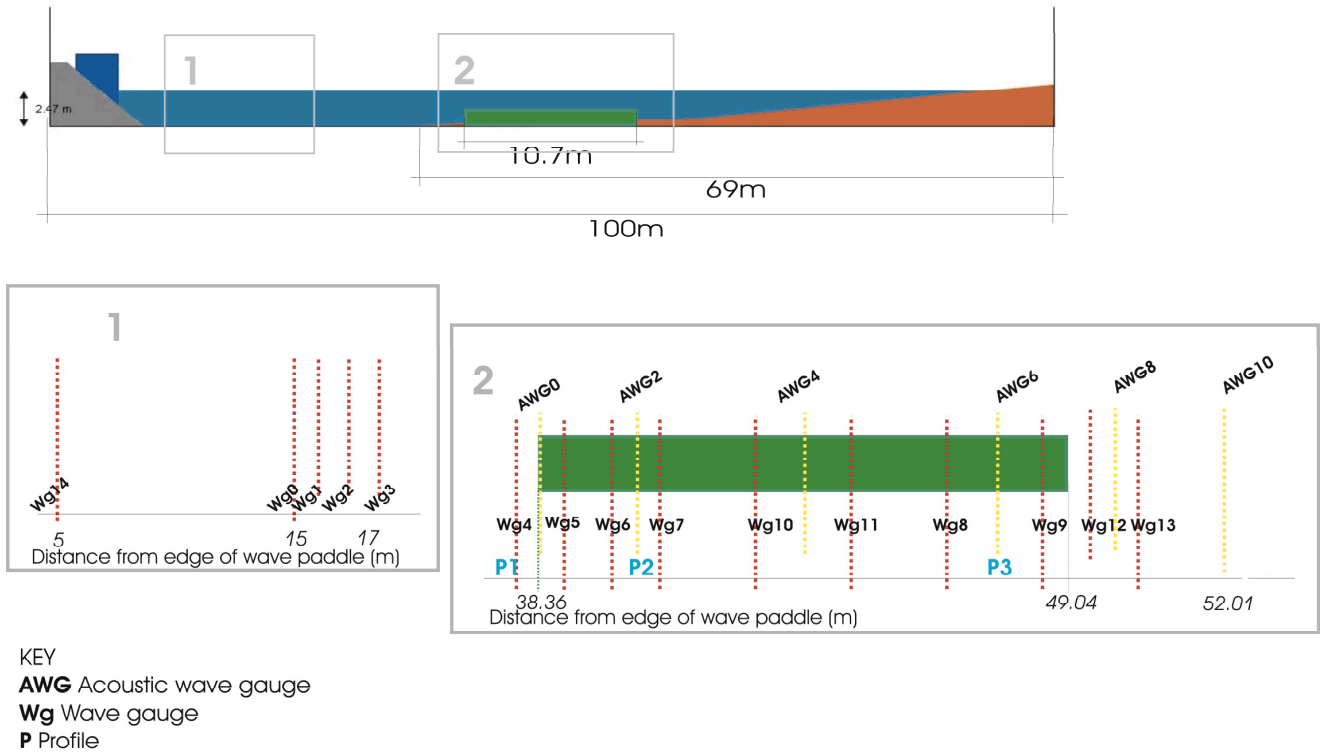

Figure 4.13 Layout of the acoustic and resistance wave gauges and location of the velocity profiles in the wave flume. The beach at the opposite end of the wave paddle had a profile slope of 1:15.

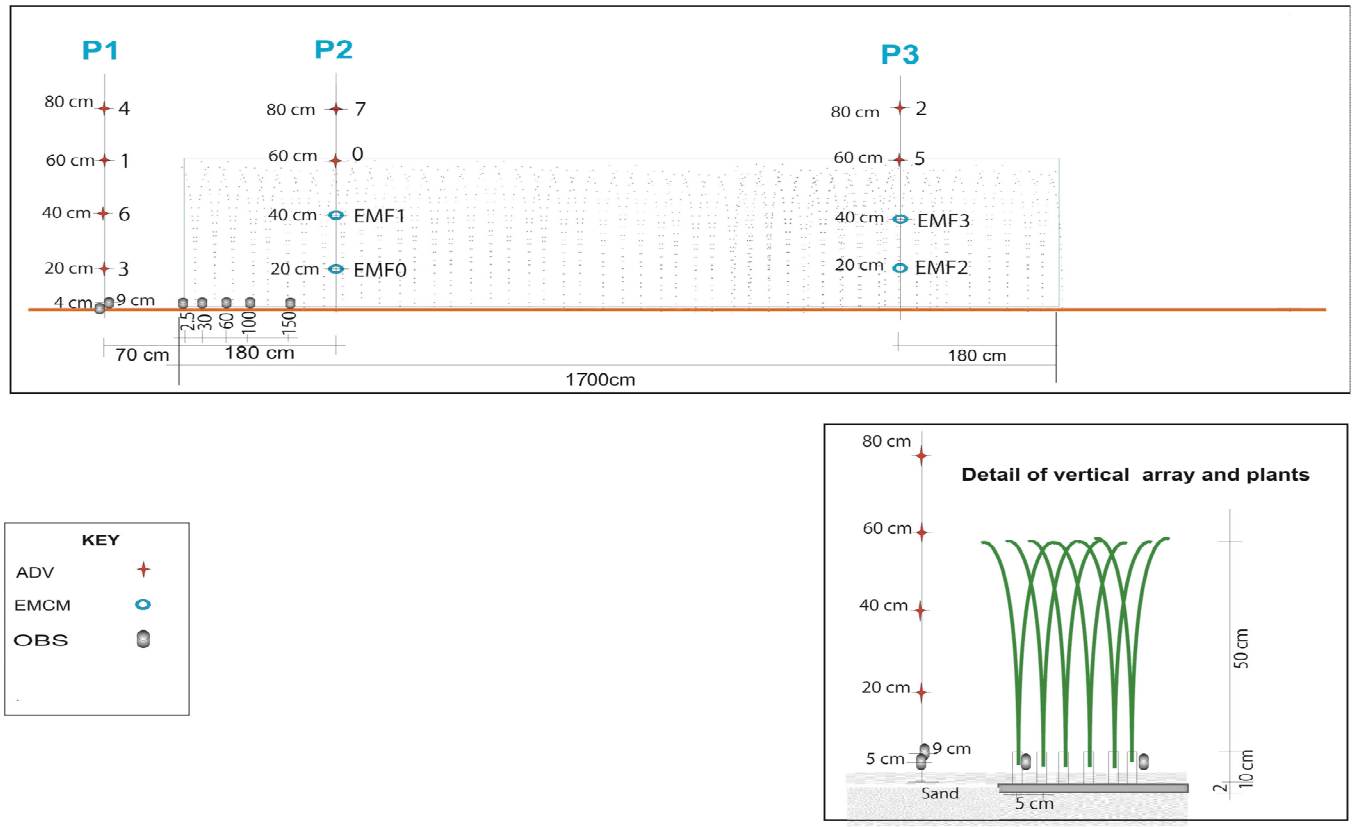

Figure 4.14. Layout of the OBS, ADV and electro-magnetic current-meters. Detail of the leading edge of the patch is shown.

Table 4-7 Predicted steepness and Ursell number for the programmed tests. Note: REG stands for regular waves and IRR for irregular wave type.

Dp (m) Depth at paddle	D (m) Depth at patch	TT (s)	HT (m) REG	HT (m) IRR	λ (m) Wave length	L/ λ	Steepness REG	Steepness IRR	H/D REG	H/D IRR	Ursell REG	Ursell IRR	C (m/s)
1.8	1.1	2	0.4500	0.2800	5.36	2.00	0.0839	0.0522	0.4091	0.2545	9.72049	6.0483	2.681
1.8	1.1	3	0.5000	0.4000	9.04	1.18	0.0553	0.0442	0.4545	0.3636	30.7129	24.5703	3.014
1.8	1.1	3.5	0.5000	0.3500	10.80	0.99	0.0463	0.0324	0.4545	0.3182	43.8086	30.666	3.08543
1.8	1.1	4	0.5000	0.3100	12.53	0.85	0.0399	0.0247	0.4545	0.2818	58.9785	36.5667	3.1325
1.8	1.1	3	0.4000		9.04	1.18	0.0442		0.3636		24.5595		3.01333
1.8	1.1	4	0.4000		12.53	0.85	0.0319		0.3636		47.1753		3.13225
2	1.3	2	0.4500	0.2800	5.60	1.91	0.0803	0.0500	0.3462	0.2154	6.42789	3.99958	2.801
2	1.3	3	0.5000	0.4000	9.67	1.11	0.0517	0.0414	0.3846	0.3077	21.2766	17.0213	3.223
2	1.3	3.5	0.5000	0.3500	11.60	0.92	0.0431	0.0302	0.3846	0.2692	30.6394	21.4476	3.31514
2	1.3	4	0.5000	0.3100	13.50	0.79	0.0370	0.0230	0.3846	0.2385	41.477	25.7157	3.375
2	1.3	3	0.4000		9.67	1.11	0.0414		0.3077		17.0248		3.22333
2	1.3	4	0.4000		13.50	0.79	0.0296		0.3077		33.1816		3.375
2.2	1.5	2	0.4500	0.2800	5.78	1.85	0.0778	0.0484	0.3000	0.1867	4.45754	2.77358	2.891
2.2	1.5	3	0.5000	0.4000	10.21	1.05	0.0490	0.0392	0.3333	0.2667	15.4557	12.3645	3.40467
2.2	1.5	3.5	0.5000	0.3500	12.32	0.87	0.0406	0.0284	0.3333	0.2333	22.4717	15.7302	3.51886
2.2	1.5	4	0.5000	0.3100	14.37	0.74	0.0348	0.0216	0.3333	0.2067	30.5921	18.9671	3.5925
2.2	1.5	3	0.4000		10.21	1.05	0.0392	0.0000	0.2667		12.3549		3.40333
2.2	1.5	4	0.4000		14.37	0.74	0.0278		0.2667		24.4805		3.593
2.4	1.7	2	0.4500	0.2800	5.92	1.81	0.0761	0.0473	0.2647	0.1647	3.20461	1.99398	2.9575
2.4	1.7	3	0.5000	0.4000	10.69	1.00	0.0468	0.0374	0.2941	0.2353	11.6343	9.30746	3.564
2.4	1.7	3.5	0.5000	0.3000	12.95	0.83	0.0386	0.0232	0.2941	0.1765	17.0778	10.2467	3.70114
2.4	1.7	4	0.5000	0.2200	15.16	0.71	0.0330	0.0145	0.2941	0.1294	23.3895	10.2914	3.79
2.4	1.7	3	0.4000		10.69	1.00	0.0374		0.2353		9.30398		3.56333
2.4	1.7	4	0.4000		15.16	0.71	0.0264		0.2353		18.719		3.79075
2.4	1.7	4	0.6500		15.16	0.71	0.0429		0.3824		30.4184		3.79075

Table 4-8 Predicted threshold of sand motion, friction factors and bed shear stress, using *Nielsen* [1992] and *Soulsby and Clarke* [2005] methods for the regular waves tests. A value of 1 for sand motion indicates that sediment motion is predicted.

Depth D (m)	H_T (m)	T_T (s)	τ_{wmax} Soulsby (N m^{-2})	τ_w Nielsen (N m^{-2})	T_{cr} (N m^{-}	Sand motion Soulsby	Sand motion Nielsen	f_w Nielsen	f'_w Soulsby (rough turb.)	Wave Reynolds Number (Re_w)
1.1	0.45	2	0.745	0.774	0.179	1	1	8.736E-03	1.441E-02	5.653E+04
1.1	0.4	3	0.720	0.915	0.179	1	1	7.378E-03	1.070E-02	1.186E+05
1.1	0.5	3	1.845	1.345	0.179	1	1	6.943E-03	9.527E-03	1.853E+05
1.1	0.4	4	1.293	0.979	0.179	1	1	6.679E-03	8.820E-03	1.870E+05
1.1	0.5	3.5	1.839	1.414	0.179	1	1	6.581E-03	8.559E-03	2.398E+05
1.1	0.5	4	1.798	1.445	0.179	1	1	6.313E-03	7.854E-03	2.921E+05
1.3	0.45	2	0.615	0.561	0.179	1	1	9.285E-03	1.593E-02	3.852E+04
1.3	0.4	3	0.638	0.743	0.179	1	1	7.633E-03	1.139E-02	9.314E+04
1.3	0.5	3	0.797	1.091	0.179	1	1	7.173E-03	1.014E-02	1.455E+05
1.3	0.4	4	1.111	0.819	0.179	1	1	6.860E-03	9.302E-03	1.524E+05
1.3	0.5	3.5	1.564	1.169	0.179	1	1	6.769E-03	9.059E-03	1.928E+05
1.3	0.5	4	1.546	1.208	0.179	1	1	6.476E-03	8.283E-03	2.381E+05
1.5	0.45	2	0.510	0.410	0.179	1	1	9.879E-03	1.756E-02	2.647E+04
1.5	0.4	3	0.571	0.615	0.179	1	1	7.880E-03	1.207E-02	7.470E+04
1.5	0.5	3	0.714	0.902	0.179	1	1	7.394E-03	1.074E-02	1.167E+05
1.5	0.4	4	0.559	0.700	0.179	1	1	7.027E-03	9.752E-03	1.271E+05
1.5	0.5	3.5	1.353	0.986	0.179	1	1	6.946E-03	9.533E-03	1.584E+05
1.5	0.5	4	1.351	1.031	0.179	1	1	6.627E-03	8.683E-03	1.985E+05
1.7	0.45	2	0.423	0.301	0.179	1	1	1.053E-02	1.935E-02	1.822E+04
1.7	0.4	3	0.515	0.516	0.179	1	1	8.122E-03	1.273E-02	6.081E+04
1.7	0.5	3	0.644	0.756	0.179	1	1	7.612E-03	1.133E-02	9.502E+04
1.7	0.4	4	0.515	0.607	0.179	1	1	7.185E-03	1.018E-02	1.078E+05
1.7	0.5	3.5	0.652	0.844	0.179	1	1	7.115E-03	9.989E-03	1.324E+05
1.7	0.5	4	1.196	0.894	0.179	1	1	6.770E-03	9.063E-03	1.684E+05
1.7	0.5	4.5	1.185	0.921	0.179	1	1	6.510E-03	8.372E-03	2.031E+05
1.7	0.65	4.5	1.747	1.459	0.179	1	1	6.102E-03	7.304E-03	3.433E+05
1.7	0.4	6	0.795	0.638	0.179	1	1	6.319E-03	7.870E-03	1.932E+05

Table 4-9 List of the performed regular wave tests. Tests that were not analysed because of a corrupted raw file are indicated in red.

Posidonia Experiments----------REGULAR WAVES TESTS									
Mimic density: 360 stems/m^2				Mimic density: 180 stems/m2					
0.32	0.37	0.42	0.50	0.32	0.37	0.42	0.50		
Depth 2.4m	Depth 2.2m	Depth 2.0 m	Depth 1.8m	Depth 2.4m	Depth 2.2m	Depth 2.0m	Depth 1.8m		
Test Number								H_T (m)	T (s)
5	19	29	36	48	67	75	93	0.45	2
	23	30	37	49	68	76	94	0.4	3
1	20	31	38	50	69	77	95	0.5	3
	24	32	39	51	70	78	96	0.4	4
	21	33	40	52	71	79	97	0.5	3.5
2	22	34	41	53	72	80	98	0.5	4
				54	73	81	100 & 99	0.5	2.3
2								0.5	4.5
7								0.65	4.5
3								0.4	6

Table 4-10 List of the performed irregular wave tests. Tests that were not analysed because of a corrupted raw file are indicated in red

Posidonia Experiments----------IRREGULAR WAVES TESTS									
Mimic density: 360 stems/m^2				Mimic density: 180 stems/m^2					
0.32	0.37	0.42	0.50	0.32	0.37	0.42	0.50		
Depth 2.4m	Depth 2.2m	Depth 2.0 m	Depth 1.8m	Depth 2.4m	Depth 2.2m	Depth 2.0m	Depth 1.8m		
Test Number								H_T (m)	T (s)
9	14	25	42	55	61	82	88	0.28	2
10	16	26	43	56	63	83	89	0.4	3
	17	27	44	57	64	84	90	0.35	3.5
	18	28	45	58	65	85	91	0.31	4
				59	66	86	92	0.3	2.3

5 Chapter 5: The effects of artificial *Posidonia oceanica* on regular waves and flows

5.1 Introduction

This Chapter presents the analysis, results and discussion of a set of full-scale experiments, on the effects of a *Posidonia oceanica* meadow on regular waves performed in the CIEM flume, following the methodologies described in the previous Chapter.

Wave propagation was monitored along the flume length and flow measurements were taken at the three locations within an artificial seagrass meadow (referred to herein as x/L=-0.07, in front of the artificial *Posidonia oceanica* patch; x/L=0.17 in the patch near the edge, and x/L=0.80 into the patch). The methods used in the data analysis of wave and flow data are described in Section 5.2.

The present experiments are the first attempt to quantify frictional drag and roughness (r) induced by an (artificial) *Posidonia oceanica* meadow, under different submergence ratios, plant densities, and wave characteristics, without the uncertainties associated with small-scale experiments. Friction over vegetated beds has often been parameterised as a drag coefficient [*Kobayashi et al.*, 1993; *Mendez et al.*, 1999; *Mendez and Losada*, 2004; *Bradley and Houser*, 2009; *Myrhaug et al.*, 2009], in order to predict coastal flows in the presence of waves [*Myrhaug et al.*, 2009]. Drag coefficients are generally obtained by applying Dalrymple's rigid model (Eq. 2-24 of Chapter 2), taking into consideration the characteristics of the canopy (canopy density and geometry). However, friction at the seabed varies with orbital wave amplitude [*Nielsen*, 1992; *Soulsby*, 1997] and drag coefficients do not take into account the effect of orbital amplitude on wave friction [*Lowe et al.*, 2007]. The friction induced by a rigid canopy can be expressed by a hydraulic roughness coefficient, typical of that canopy, derived from the calculation of wave dissipation factors [*Lowe et al.*, 2005a]. In Section 5.3, wave energy loss due to *Posidonia* is evaluated both as a drag coefficient

and a wave dissipation factor, from the decay in wave height along the patch. Hydraulic roughness for two different canopy densities is also derived.

In Section 5.4, the transformation of the oscillatory flow within and above the artificial seagrass patch is analysed. Changes in the horizontal oscillatory velocity magnitude and phase shifts induced by the canopy are presented and compared to the classic [*Sleath*, 1987; *Nielsen*, 1992] wave boundary layer structure. The effects of wave period, submergence ratio and seagrass density on wave-induced flow structure are discussed (Section 5.4.3). Flow asymmetries are examined (Section 5.4.5) to compare with the field results (presented in Chapter 3), indicating a positive oscillatory flow asymmetry at the *Posidonia* station, which might result in a net shoreward drift. Wave flow attenuation within submerged rigid canopies is largest for the largest waves [*Lowe et al.*, 2007]. The relationship between orbital amplitude and flow reduction/intensification inside and above the canopy is examined in Sections 5.4.6 and 5.4.7, for the horizontal and vertical component of the flow, respectively.

Section 5.5 presents and discusses the results obtained on turbulence induced by *Posidonia*. The distribution of turbulent kinetic energy above and within the canopy (Section 5.5.1) and shear at the canopy top (Section 5.5.2) are reported. The results are summarised in a final section (Section **Error! Reference source not found.**)

5.2 Data Analysis: Regular wave tests

5.2.1 Wave data processing

The data from the wave gauges (see previous Chapter) were quality-checked to remove gaps in the data. The initial part of the time-series, when the flume system had not yet reached an equilibrium state, was eliminated. Also the end part of the time-series, when unwanted waves were produced while the wave paddle was returning to rest, was rejected. An example of raw data from the wave gauges is shown in Figure 5.1.

A zero-crossing method was used to calculate the significant wave height (H) and peak wave period (T_p) from each water oscillation time series. Wave reflection analysis was performed to estimate reflection coefficients within the flume using the method of *Mansard and Funke* [1980]. This method uses both the wave height information and the phase angles. It was determined from three resistive wave gauges

(in particular the wave gauges used were: Wg 0; Wg 2; and Wg 3, see Figure 4.13 of Chapter 4) located in front of the seagrass patch at a minimum distance of 15 m from the wave paddle. Their characteristic spacing was 2.4 m between Wg 0 and Wg 3 and 1.69 m between Wg 0 and Wg 2.

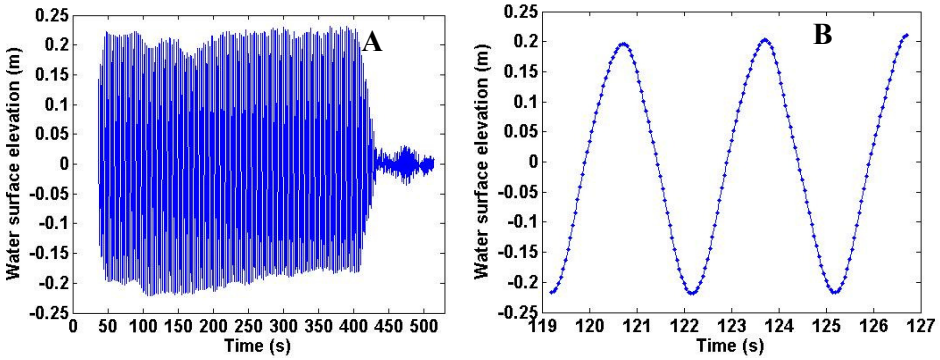

Figure 5.1 A) Example of water surface elevation time series (raw data); and B) Detail from previous plot (A).

The wave height decay, defined as the ratio H/H_0 (where H is the significant wave height at each location along the seagrass patch and H_0 is the significant wave height at X=-0.46), was calculated for all of the tests. As wave heights over vegetated beds decay exponentially with distance from the leading edge, the H/H_0 ratio was fitted (least square fit) to an exponential decay model:

$$\frac{H(x)}{H_0} = \exp^{-k_i \Delta x} \qquad \textbf{Eq. 5-1}$$

to obtain k_i, the wave height decay coefficient. The drag coefficient (C_d) was calculated, using the modelled wave height decay, by means of Dalrymples's rigid model (see Chapter 2), reported below:

$$\frac{H(x)}{H_0} = \frac{1}{\left\{\left[\frac{g^2 C_d N b H_0 (\cosh^3 kh_s + 2)\sinh kh_s}{9\pi C_g C^3 \cosh^3 kD}\right]x + 1\right\}} \qquad \textbf{Eq. 5-2}$$

Where: b is the maximum dimension of the mimics in the flow direction (b=0.01 m); υ is the kinematic viscosity of water (υ =1.0x10^{-6} m^2/s); D is the water depth and N is the number of stems/m^2 (180 or 360 stems/m^2 depending on the test). The other parameters in the formula were calculated using Stokes's wave theory.

Furthermore, the friction induced by the seagrass patch was evaluated in terms of the wave dissipation factor (f_e), assuming exponential wave height decay, was determined from the wave energy loss along the patch, as described already in Chapter 3.

The rate of energy dissipation per unit area, due to friction (ε_f), is the change in the wave energy flux with distance along the patch

$$\frac{\delta EC_g}{\delta x} = -\varepsilon_f \qquad \textbf{Eq. 5-3}$$

Where E is the wave energy density and Cg the group velocity, both obtained from the equations below, which is valid for both linear and second order wave theory [*Sarpkaya and Isaacson*, 1981]

$$C_g = \frac{1}{2}c\left[1 + \frac{2kD}{\sinh(2kD)}\right] \qquad \textbf{Eq. 5-4}$$

$$E = \frac{1}{8}\rho g H^2 \qquad \textbf{Eq. 5-5}$$

From the rate of energy dissipation, the friction factor (f_e) was derived using (Chapter 2 Eq. 2-4) of Jonsson (1966) reported below

$$\varepsilon_f = \frac{2\pi}{3}\rho f_e u_\infty^3 \qquad \textbf{Eq. 5-6}$$

5.2.2 Flow data processing

The raw data from the ADV (Acoustic Doppler Velocimeter) and EMCM (Electro Magnetic Current Meter) were quality-checked (including de-spiking) and synchronised to the wave data (see Chapter 4, Figure 4.14, for the location of the instruments). An example of raw data from an ADV is shown in Figure 5.2 and raw data from an EMCM is shown in Figure 5.3.

The correlation coefficient and the signal to noise ratio (SNR) of the ADV data were analysed, as instructed by the user manual [*Nortek*, 2005, see also Chapter 4]. The correlation was always higher than 85% (often > 90%) and the SNR was larger than 15, indicating the signal was of good quality. The data were de-spiked using the phase-space method [*Goring and Nikora*, 2002]. This method is used widely [*Graham and Manning*, 2007; *Mori et al.*, 2007] and has been found to be the best suited for high resolution velocity data [*Goring and Nikora*, 2002; *Wahl*, 2003]. The method is based upon the concept that good data cluster within a dense cloud, in phase space. An ellipsoid in three-dimensional phase space is constructed and all the points lying outside

the ellipsoid were considered as spikes. The missing data points, after spike removal, were substituted by fitting a cubic polynomial between the data points, across the spike, and interpolating the data.

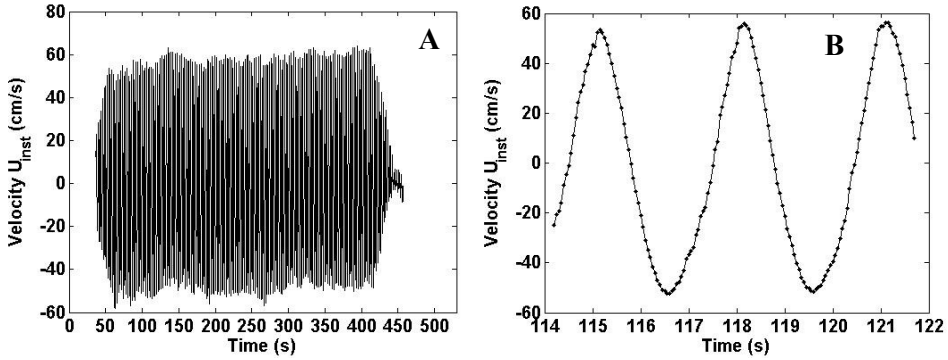

Figure 5.2 A) Example of ADV raw data; and B) Detail of A.

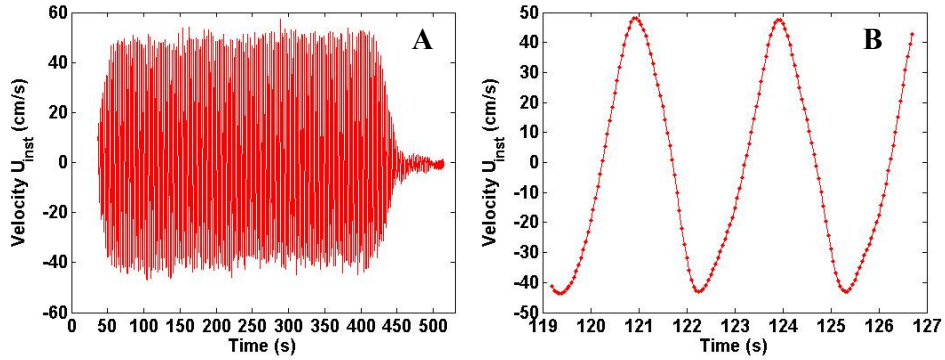

Figure 5.3 A) Example of EMCM raw data; and B) Detail of A

The measured horizontal velocity time-series ($U_{inst}(t)$) can be described as the sum of the time-averaged flow (U_m), the random turbulent fluctuations ($U'(t)$) and the periodic component generated by waves $U_w(t)$ (Reynolds decomposition).

$$U_{inst}(t) = U_w(t) + U_m + U'(t) \qquad \textbf{Eq. 5-7}$$

Under regular waves, the horizontal component of the oscillatory velocity was obtained by ensemble-averaging the de-meaned velocity data (U), over successive waves [*Pedersen et al.*, 1998]:

$$< U > (\omega t) = \frac{1}{N}\sum_{i=1}^{N} U(\omega(t + (i-1)T)) \qquad \textbf{Eq. 5-8}$$

where:

$$U(t) = U_{inst}(t) - U_m = U_w(t) + U' \qquad \textbf{Eq. 5-9}$$

U(t) stands for the de-meaned instantaneous velocity measurements, ωt is the wave phase, T is the wave period and N the number of wave periods sampled. The ensemble-averaging operation groups the velocities with respect to their wave phase, averaging the values of equivalent phase. The wave phase and period were determined from the measured local wave data. The same method was applied to obtain the vertical phase-averaged component of the wave-induced flow (<W>). At each elevation (z), the maximum vertical and horizontal component of the orbital velocities (U_{max} and W_{max}) were obtained from the peak value of <U> (Figure 5.4) and <W>, respectively. Similarly U_{min} and W_{min} were calculated from the minimum value of <U> and <W>, respectively. The root mean square values of U_{rms} (t) and W_{rms} s were also calculated.

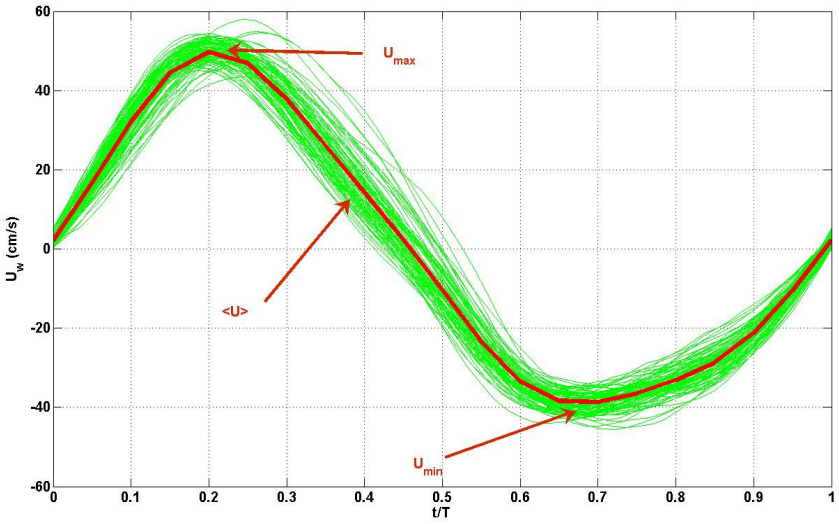

Figure 5.4 Example of the method of computation of the wave-induced flow from a measured velocity times series. In green are the de-meaned ensemble horizontal velocity values, corresponding to each wave. The red line is the ensemble averaged <U>. U_{max} corresponding to the peak value of <U>and U_{min}, the minimum value of <U>, are also indicated.

The ensemble-averaged turbulence was calculated from the fluctuating component of the velocities, by subtracting the ensemble averaged value of the velocity from the de-meaned data

$$< U' >= \frac{1}{N}\sum_{i=1}^{N}[U(\omega(t+(i-1)T)) - < U > (\omega(t+(i-1)T))] \qquad \textbf{Eq. 5-10}$$

The turbulence intensities are the root mean square values of the fluctuating component of the velocity signal U'_{rms} and $W'_{rms,}$ and are obtained as a function of the wave phase from:

$$U'_{rms}(\omega t) = \sqrt{\langle U'^2 \rangle}(\omega t) = \left[\frac{1}{N} \sum_{i=1}^{N} [U(\omega(t+(i-1)T)) - < U > (\omega(t+(i-1)T))]^2 \right]^{1/2}$$

Eq. 5-11

after *Pedersen et al*. [1998] and *Ting and Kirby* [1996]. The same method was used to obtain the vertical component of the turbulence intensities, W'_{RMS}. The product <U'W'> of the bi-dimensional Reynolds stress (See Section 2.5.3 Chapter 2), as a function of the phase, was derived from deviations from the ensemble-averaged velocities, using:

$$\langle U'W' \rangle (\omega t) = \frac{1}{N} * \\ * \sum_{i=1}^{N} \{ [U(\omega(t+(i-1)T)) - Uens(\omega(t+(i-1)T))] * [W(\omega(t+(i-1)T)) - Wens(\omega(t+(i-1)T))] \}$$

Eq. 5-12

A similar method was used to obtain the other two bi-dimensional Reynolds stresses <U'U'> and <W'W'> at the XZ plane.

Turbulent kinetic energy (TKE) was calculated from the horizontal and vertical component of turbulence

$$TKE = 0.5\left(< U' >^2 + < W' >^2 \right)$$ **Eq. 5-13**

The total turbulent kinetic energy (TKE_t) is proportional to the component evaluated at the XZ plane (TKE)

$$TKE_t = 1.33 TKE$$ **Eq. 5-14**

In most turbulent flows the error associated with the approximation of the total turbulent kinetic energy using, Eq.5-14, is considered to be small [*Svendsen*, 1987].

5.3 Results and discussion: Wave dissipation

5.3.1 Wave height decay

Wave parameters (wave height (H), peak period (T_p)) were calculated at each measurement location. A significant difference (an almost constant offset) was found between the wave data recorded by the acoustic wave gauges and the resistive wave gauges Thus, only the results from the resistive wave sensors were considered in this study (the resistive are known to be more reliable, (I. Caceres CIEM staff, personal communication). It is not clear what created this offset in the acoustic wave gauges

output. A list of the test conditions and the main wave parameters measured at X=-0.46 (in front of the leading edge of the patch) is given in Table 5-1.

The Miche no-breaking criterion (Eq 2-1, Chapter 2) was verified for all tests and wave breaking was not observed above the patch of mimics, during the tests.

The wave reflection coefficient (r_w) in the flume, for the regular wave tests was estimated to be on average 0.070±0.02. As this value is relatively small, lying close to the characteristic reflection coefficient of 5% for a flume with the sandy slope (oral communication, CIEM Staff), wave reflection induced by the seagrass was neglected. Since reflected energy is proportional to r_w^2, only about 2.6% of the wave energy was reflected back to the paddle. As a result the velocity data measured at the control profile (x/L=-0.07) are expected not to be affected significantly by waves reflected by the patch.

The wave period was constant as waves propagated over the seagrass. However, wave amplitude was reduced with distance along the patch, in all of the tests (up to 35% over 10.7 m). A localised increase in wave height was observed at the edge of the patch (from x/L=0.46, within the first 2 m of the patch), in most tests; this was due probably to the sudden obstacle encountered by the wave, or local wave reflection induced by the edge of the patch. An increase in wave height at the edge of a shallow seagrass meadow together with an exponential decay fuarther shoreward has been observed in the field [*Bradley and Houser*, 2009]. The wave height decay (H/H_0, defined as the ratio between the significant wave height at each location along the seagrass patch and the significant wave height at X=-0.46) was found to depend upon the submergence ratio and mimic density. In collaboration with the project partners, it was found that wave height attenuation increased with submergence ratio and was largest for the denser patch [*Stratigaki et al.*, accepted].

Table 5-1 Key wave parameters measured in front of the leading edge of the seagrass patch (x/L=-0.07) for all tests. L is the total length of the patch; x is the distance along the flume from the leading edge of the patch. All other symbols are listed in the abbreviations section.

TEST	Density (stems /m^2)	hs/D	Tp (s)	H0 (m)	Wave length (m)	Ursell N	Vertically Averaged Umax (m/s) x/L=-0.07
1	360	0.32	3.00	0.40	10.69	9.43	0.41
2	360	0.32	4.00	0.46	15.17	21.72	0.53
3	360	0.32	6.00	0.36	22.94	39.00	0.53
5	360	0.32	2.00	0.38	5.93	2.73	0.26
7	360	0.32	4.50	0.65	17.35	39.67	0.76
19	360	0.37	2.00	0.36	5.79	3.56	0.29
21	360	0.37	3.50	0.44	12.32	19.61	0.62
22	360	0.37	4.00	0.43	14.38	26.18	0.65
23	360	0.37	3.00	0.36	10.22	11.05	0.46
24	360	0.37	4.00	0.35	14.38	21.47	0.46
29	360	0.42	2.00	0.38	5.61	5.43	0.38
30	360	0.42	3.00	0.32	9.67	13.81	0.46
31	360	0.42	3.00	0.43	9.68	18.14	0.59
33	360	0.42	3.49	0.46	11.61	28.10	0.67
34	360	0.42	4.00	0.42	13.51	35.03	0.73
36	360	0.5	1.99	0.42	5.36	9.18	0.47
37	360	0.5	3.00	0.34	9.05	20.83	0.53
38	360	0.5	3.01	0.45	9.05	27.48	0.66
39	360	0.5	4.00	0.40	12.54	46.69	0.64
40	360	0.5	3.49	0.48	10.80	42.01	0.70
41	360	0.5	4.01	0.48	12.39	54.90	0.81
48	180	0.32	2.00	0.38	5.93	2.71	0.26
49	180	0.32	2.99	0.37	10.69	8.60	0.34
50	180	0.32	2.99	0.46	10.69	10.63	0.41
51	180	0.32	4.00	0.40	15.17	18.63	0.45
52	180	0.32	3.50	0.46	12.96	15.76	0.50
53	180	0.32	3.99	0.47	15.18	21.82	0.52
54	180	0.32	2.30	0.39	7.39	4.32	0.36
67	180	0.37	2.00	0.35	5.79	3.47	0.31
68	180	0.37	3.00	0.35	10.22	10.68	0.38
69	180	0.37	3.00	0.40	10.22	12.53	0.51
70	180	0.37	4.00	0.38	14.38	23.20	0.44
71	180	0.37	3.50	0.44	12.32	19.83	0.64
72	180	0.37	4.00	0.44	14.38	26.76	0.61
75	180	0.42	2.00	0.38	5.61	5.45	0.38
76	180	0.42	3.00	0.31	9.67	13.30	0.47
77	180	0.42	3.00	0.40	9.68	17.21	0.59
78	180	0.42	4.00	0.31	13.51	25.68	0.56
79	180	0.42	3.49	0.51	11.61	31.29	0.67
80	180	0.42	4.00	0.41	13.51	33.74	0.74
81	180	0.42	2.30	0.39	6.86	8.43	0.52
93	180	0.5	2.00	0.38	5.36	8.17	0.47
94	180	0.5	3.00	0.33	9.05	20.00	0.53
95	180	0.5	3.01	0.42	9.05	25.86	0.66
96	180	0.5	4.01	0.33	12.54	39.34	0.64
97	180	0.5	3.49	0.46	10.80	39.92	0.70
98	180	0.5	4.00	0.42	12.54	49.52	0.82
99	180	0.5	2.30	0.42	6.50	13.19	0.61
100	180	0.5	2.00	0.41	5.36	8.85	0.47

In the present study, the wave height decay H/H_0, was calculated for all of the tests, and fitted (least square fit), to an exponential decay model to obtain k_i, the wave decay coefficient:

$$\frac{H(x)}{H_0} = \exp^{-k_i \Delta x} \qquad \textbf{Eq. 5-15}$$

The results for all of the tests performed are presented in Table 5-2, where both k_i and the corresponding R^2 of the fit are shown (with a significance level P=0.05). The exponential decay model had a goodness of fit (see example shown in Figure 5.5), comparable to the results of Kobayashi (1993). However, in some of the tests, the natural wave height modulation recorded along the patch was large; therefore, producing a bad fit to the exponential function. Only the tests for which the exponential decay theory is considered valid (with an exponential fit correlation coefficient larger than 0.60) were considered here. The wave decay coefficient k_i ranged between 0.0120 and 0.0340, which is within the range of k_i found in previous studies for flexible vegetation such as kelp [*Asano et al.*, 1988] and mixed seagrass in the field [*Bradley and Houser*, 2009] (see Table 2-2 in Chapter 2).

Wave energy loss induced by the walls and bed of the flume contribute to the wave height decay measured at the patch. The wave decay in the absence of the seagrass patch could not be measured in these experiments; however the flume-induced wave decay coefficient (k_f) was estimated from the wave data measured in front of the patch, assuming exponential wave height decay with distance. The flume-induced decay coefficient k_f is defined as follows:

$$\frac{H(X)}{H_1} = \exp^{-k_f \Delta X} \qquad \textbf{Eq. 5-16}$$

Where H_1 is the wave height measured by the wave gauge closest to the wave generator (Wg 14, see Figure 4.13 Chapter 4), H(X) is the wave height (measured between the wave paddle and the leading edge of the patch) and ΔX is the distance between the wave gauges considered. For example, for Test 33 (Figure 5.5), k_f=0.0002 and k_i=0.0205.

In some cases, the wave height between the wave paddle and the leading edge of the patch slightly increased as a result of wave shoaling over a mild (<1:10) sandy slope from the flume's bed to the higher horizontal sandy bed (where the patch was located, see Figure 4.2, Chapter 4). Thus, the estimate of k_f is only indicative, as it is also affected by shoaling. In general, k_f was much smaller than k_i at the patch (two orders of magnitude). Previous experiments underataken in the CIEM flume have found a negligible effect of friction, by the sidewalls and the flume's sandy bottom, on wave height decay (personal communication, CIEM staff), confirming that the vegetation was

responsible for most of the wave decay measured at the patch. Furthermore, other authors have found that, for a vegetated seabed, bottom friction (by sediment) is negligible compared to the drag induced by the canopy [*Asano et al.*, 1992; *Kobayashi et al.*, 1993; *Nepf*, 1999; *Mendez and Losada*, 2004].

Table 5-2 Wave dissipation, drag and wave parameters calculated for all of the regular wave tests: Wave height at x/L=-0.046, R^2 coefficient for the wave decay exponential fit, decay coefficient (k_i). The table contains also values averaged along the patch of: drag coefficient (C_d), Reynolds vegetation number (Re_v), Keulegan-Carpenter number (KC), orbital amplitude above the canopy (A), wave Reynolds number (Re_w) and wave dissipation factor. The results above the bold line (associated with all of the tests having R^2>0.60) are considered to be more reliable.

Test	H0 (m)	R2	ki	Cd	Rev	KC	A (m)	Rew	fe
31	0.43	0.93	0.022	0.506561	5159	110.6	0.246	1.371E+05	0.427
38	0.45	0.89	0.027	0.386	6370	136.6	0.304	2.062E+05	0.325
37	0.34	0.88	0.028	0.523	4648	99.6	0.222	1.159E+05	0.481
40	0.48	0.86	0.029	0.429	7384	184.7	0.412	3.435E+05	0.247
93	0.38	0.85	0.027	0.802	3919	56.0	0.125	5.383E+04	0.574
24	0.35	0.82	0.017	0.857	4250	121.4	0.270	1.208E+05	0.232
39	0.40	0.80	0.018	0.345	6855	195.9	0.436	2.998E+05	0.173
99	0.42	0.78	0.018	0.474	4968	81.5	0.182	1.045E+05	0.297
30	0.32	0.78	0.015	0.469	3875	83.1	0.185	8.026E+04	0.356
81	0.39	0.78	0.012	0.575	4088	67.2	0.150	6.812E+04	0.448
29	0.38	0.77	0.034	0.994	3009	43.0	0.096	3.266E+04	1.474
23	0.36	0.75	0.015	0.624	3781	81.1	0.181	7.458E+04	0.499
79	0.51	0.70	0.031	1.370	6540	163.4	0.364	2.517E+05	0.187
33	0.46	0.70	0.020	0.484	6214	155.4	0.346	2.342E+05	0.242
95	0.42	0.65	0.016	0.457	6405	137.3	0.306	2.036E+05	0.217
41	0.48	0.61	0.016	0.253	9279	264.2	0.589	5.303E+05	0.099
36	0.42	0.59	0.044	0.624	3861	55.2	0.123	5.472E+04	1.098
77	0.40	0.58	0.008	0.376	5216	111.8	0.249	1.338E+05	0.189
94	0.33	0.57	0.015	0.541	4774	102.3	0.228	1.155E+05	0.314
100	0.41	0.56	0.025	0.678	4134	59.1	0.132	6.099E+04	0.495
49	0.37	0.56	0.015	1.748	3283	70.2	0.156	5.546E+04	0.895
5	0.38	0.48	0.015	1.328	2232	31.9	0.071	1.653E+04	2.061
51	0.40	0.45	0.015	1.853	4328	123.6	0.275	1.210E+05	0.519
1	0.40	0.43	0.018	1.018	3588	76.9	0.171	6.600E+04	0.860
48	0.38	0.43	0.006	1.070	2373	33.9	0.076	1.843E+04	0.681
34	0.42	0.42	0.007	0.192	6886	196.9	0.439	3.009E+05	0.127
72	0.44	0.40	0.011	0.817	5632	160.9	0.358	2.012E+05	0.162
52	0.46	0.37	0.013	1.244	4772	119.2	0.266	1.316E+05	0.324
97	0.46	0.36	0.021	0.635	7177	179.3	0.400	3.271E+05	0.209
19	0.36	0.33	0.006	0.326	2693	38.5	0.086	2.505E+04	0.141
71	0.44	0.31	0.009	0.663	5482	137.0	0.305	1.781E+05	0.222
75	0.38	0.28	0.019	1.027	3291	47.0	0.105	3.697E+04	0.863
98	0.42	0.27	0.008	0.280	8505	242.8	0.541	4.381E+05	0.098
21	0.44	0.24	0.008	0.303	5561	139.1	0.310	1.801E+05	0.123
50	0.46	0.18	0.021	2.095	3951	84.6	0.188	8.164E+04	1.062
96	0.33	0.15	0.008	0.338	6004	171.6	0.382	2.411E+05	0.256
70	0.38	0.15	0.012	1.098	4657	133.2	0.297	1.380E+05	0.276
53	0.47	0.13	0.016	1.681	5102	145.8	0.325	1.664E+05	0.315
69	0.40	0.10	0.004	0.259	4451	95.4	0.213	9.963E+04	0.065
76	0.31	0.09	0.002	0.120	4067	87.1	0.194	8.145E+04	-0.020
67	0.35	0.04	0.001	0.068	2731	39.0	0.087	2.519E+04	-0.054
68	0.35	-0.01	0.013	1.138	3529	75.6	0.168	6.457E+04	0.545
22	0.43	-0.02	0.002	0.066	6090	173.9	0.387	2.301E+05	0.059
80	0.41	-0.03	0.002	0.121	6842	195.3	0.435	2.888E+05	0.114
54	0.39	-0.07	-0.004	-0.482	3042	50.0	0.111	3.701E+04	-0.376
78	0.31	-0.25	-0.002	-0.129	5107	145.9	0.325	1.585E+05	0.025
3	0.36	-0.51	-0.004	-0.319	5698	234.8	0.523	2.987E+05	-0.010
2	0.46	-0.52	0.013	0.700	4982	142.3	0.317	1.623E+05	0.399

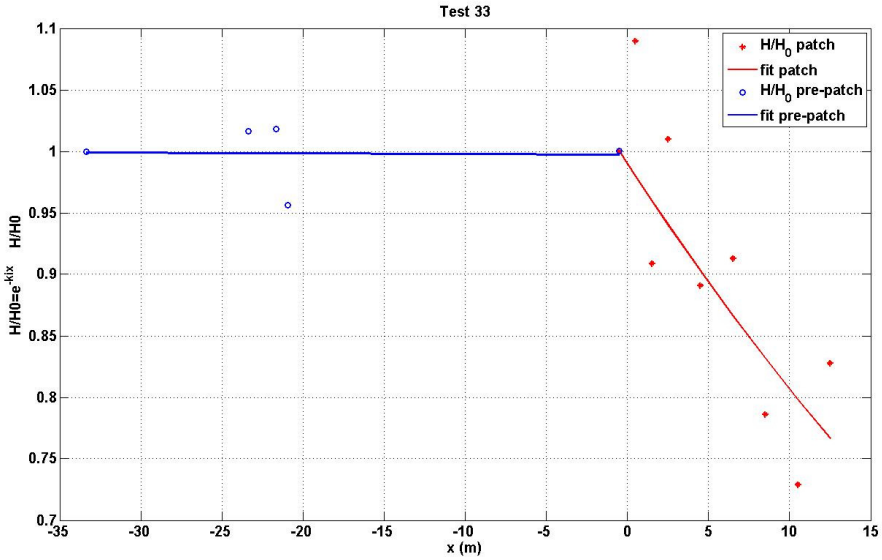

Figure 5.5 Example of wave height decay (Test 33, see Table 5-1). The measured and modelled wave height decay are plotted versus distance. The leading edge of the patch is located at x=0. Red lines and symbols indicate the data measured at the patch, whilst the blue line and symbols represent the data measured in front of the leading edge of the patch (indicated in the legend as pre-patch).

5.3.2 The drag coefficient

The drag coefficient (C_d), obtained from the Dalrymple rigid model equation [*Dalrymple et al.*, 1984] was averaged along the patch, for each test condition. It varied between 0.25 and 1.37 (see Table 5-2). The relationship between C_d and the Reynolds vegetation number (Re_v) was investigated. Re_v is defined as in previous studies (Eq.2-26, of Chapter 2):

$$\mathrm{Re}_v = \frac{bU_c}{\upsilon} \qquad \textbf{Eq. 5-17}$$

with the characteristic orbital velocity (U_c) taken as the theoretical U_{max} at the top of the canopy and obtained by applying Stoke's second-order theory (measurements of U_{max} were not available at all wave gauge locations). The values of Re_v for each test in Figure 5.6 and Table 5-2 are an average of the values calculated for each wave gauge along the patch. Drag coefficients decreased with increasing Reynolds vegetation number (Re_v), in agreement with findings for kelp [*Kobayashi et al.*, 1993; *Mendez et al.*, 1999; *Mendez and Losada*, 2004] and natural seagrass beds [*Bradley and Houser*, 2009].

For the regular waves fitting the exponential decay model, Re_v ranged between 3008 and 9279 and the following relationship with C_d was found:

$$Cd = 0.216 + \left(\frac{2526}{\mathrm{Re}_v}\right)^{1.76} \qquad \textbf{Eq. 5-18}$$

(Figure 5.6) R^2 coefficient was 0.72 (with 16 data points and a level of significance of P=0.05). The above relationship is comparable (in shape) to the modelled C_d found for kelp by *Kobayashi* [1993], with regular waves. However, the values found in this study are higher. Considering that the modelled C_d obtained from the published literature, have been obtained from models calibrated on experiments using 1:10 kelp mimics; these have different structure and stiffness from the full-scale *Posidonia oceanica* mimics used in the present study and, as such, some divergence in the values of C_d can be expected. The model produced by *Mendez et al.,* [1999], obtained considering the oscillation of the mimics, only fits the present dataset for Re_v larger than 6000 Thus, C_d does not grow as fast as predicted by the Mendez et al model for Re_v <6000. The curve obtained on natural seagrass from the *Bradley and Houser* [2009] study, was obtained under random waves and for very low Re_v numbers ($200<Re_v<800$). In Figure 5.6, the Bradley and Houser (2009) relationship was extrapolated for Re_v numbers larger than 800, but its validity for these conditions is not proven, making the results difficult to compare.

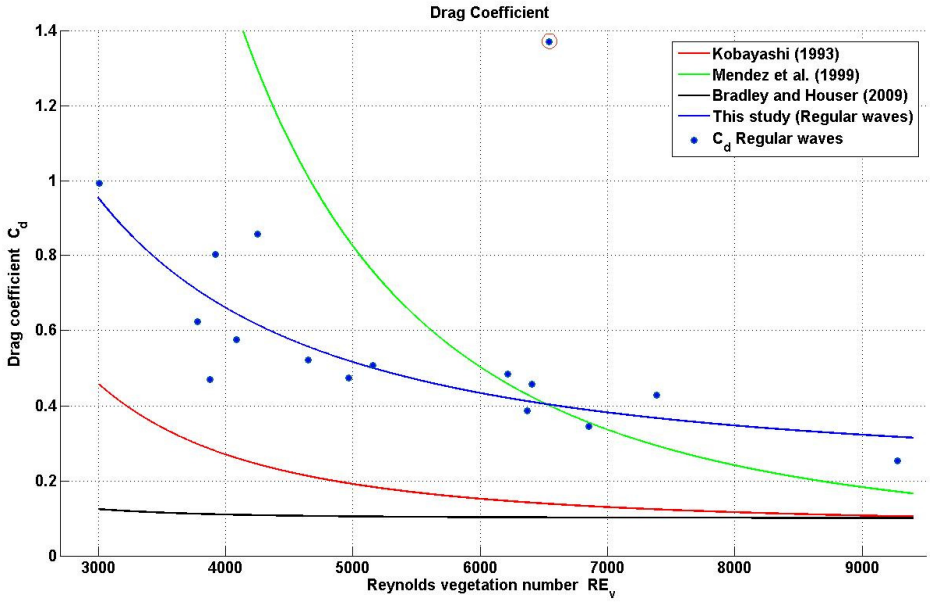

Figure 5.6 Drag coefficients plotted against the Reynolds vegetation number (blue symbols) and the best-fit (blue line, Eq. 5-18). The data are compared with the relationship found in previous studies [*Kobayashi et al.*, 1993; *Mendez et al.*, 1999; *Bradley and Houser*, 2009]. The data point circled in red was excluded from data analysis as it was considered to be an outlier (the residual was more than 3 times larger than the root mean square error of the fit).

The drag coefficient was also plotted against the Keulegan-Carpenter number (See Eq 2-29 in Chapter 2), but the exponential fit obtained was slightly worse than when plotted against the Re_v (R^2=0.70 see Figure 5.7). However C_d decreased with increasing KC and, therefore, with increasing A_c (the orbital amplitude at the top of the canopy), as KC is dependent on A_c:

$$KC = \frac{A_c 2\pi}{b} \qquad \textbf{Eq. 5-19}$$

The Dalrymple model has several limitations, despite being successfully used in the estimation of C_d even for seagrass in the field [*Bradley and Houser*, 2009]; it assumes that linear wave theory applies and that flexible seagrass can be approximated by rigid cylinders. Moreover, the wave decay is assumed to be due only to the frictional drag exerted by the mimics on the flow: other processes, such as cascading of energy through turbulence, are ignored. Nevertheless, the model provided a first estimate of C_d which made possible a comparison of this regular wave dataset, with other studies on vegetation-induced drag.

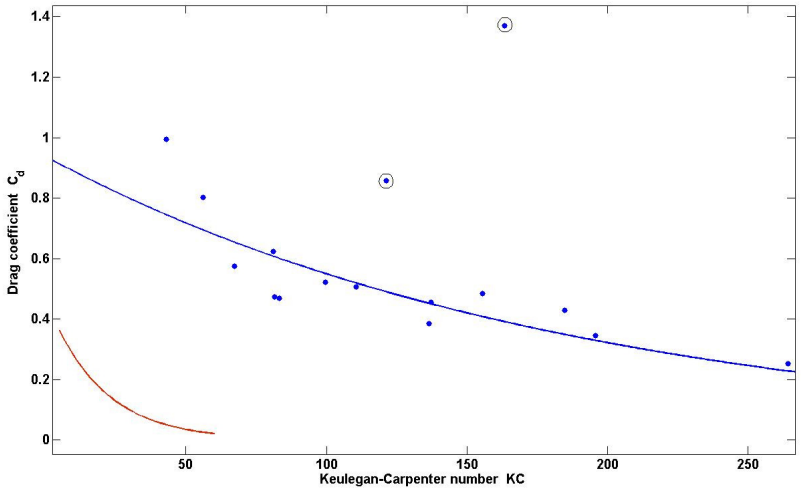

Figure 5.7 Drag coefficients plotted against the Keulegan-Carpenter number (blue symbols) and the best fit (blue line). The data are compared with the relationship found in Mendez and Losada (2004). Two data points were considered to be outliers and excluded from the analysis (indicated by a black circle) because the absolute value of their residuals was more than 3 times greater than the RMSE (root mean square error of the residuals).

5.3.3 Wave friction factors and roughness length from wave energy dissipation

The friction induced by the seagrass patch, expressed by the wave dissipation factor (f_e), was calculated, assuming exponential wave height decay; this was determined from

the wave energy loss along the patch. The values of f_e (obtained from the tests which showed a very good fit with the wave height exponential decay model, R^2 >0.6) varied between 0.10 and 1.47 with an average of 0.46 and 0.41 for the high meadow density and low meadow density tests, respectively. The f_e values were plotted against A (Figure 5.8) and the Reynolds wave number varied between 3.2 x 10^4 and 5.3 x 10^5. The energy dissipation factor decayed with A, for both densities; the values were lower for the same A, when the stem density was 180 stems/m^2. The very high value of f_e (for A = 0.07) in Figure 5.8 was not spurious and the trend of decreasing f_e, with A, was clear when all the tests were considered (even those with a poor fit to the exponential decay model, Figure 5.9). The values of f_e were compared to existing formulae on friction factors, as a function of relative roughness (r/A) (see Chapter 2 Eq 2-13 to Eq. 2-15), assuming $f_e=f_w$. For tests with density 360 stems/m^2 a very good fit (R^2=0.91) to Nielsen's formula (1992) was obtained:

$$f_w = \exp\left[5.2\left(\frac{r}{A}\right)^{0.2} - 6.3\right] \qquad \textbf{Eq. 5-20}$$

where the hydraulic roughness (r) providing the best fit to the data was 0.23 m, (henceforth known as r_{360}). Similarly f_e from the low density mimics (180 stems/m^2) data fitted Eq.5.20 very well (R^2=0.95) when r =0.15 m (henceforth known as r_{180}).

The hydraulic length (r) is used commonly in coastal modelling and provides a yard-stick to compare the roughness of sandy beds to those created by seagrass. The Nielsen (1992) formula was derived for sandy beds, relating the hydraulic roughness length to a physical roughness r=d_{50}, with d_{50} the grain diameter. In coral reefs studied elsewhere, the average value of r was 0.16 ±0.03 m [*Lowe et al.*, 2005a], which is similar to that found in the present study for the low density patch configuration. In the Lowe et al. study, r was related to the physical elevation of roughness elements measures on the reef. However, these authors recognised that the hydraulic roughness depends often upon the spacing of the elements, their configuration as well as their height above the bed. For vegetation, the physical meaning of the parameter r is spurious [*Bradley and Houser*, 2009]. Hydraulic roughness for natural seagrasses varied between 0.03 m and 0.38 m [*Bradley and Houser*, 2009], which is between approximately 0.1 and 1.3 times the canopy height; it was largest for the smallest Reynolds number. The results from these regular wave experiments fit well those

observations. Over *Posidonia* mimics, r was a fraction of the canopy height (r_{180}=0.27h_s and r_{360}=0.42h_s); it depended upon the canopy density (r_{360}=1.6 r_{180}).

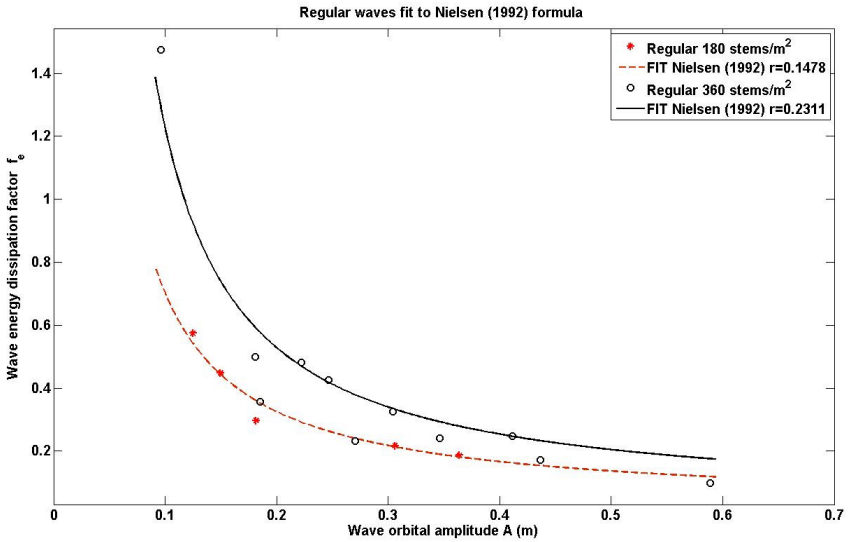

Figure 5.8 Friction factors plotted against the wave orbital amplitude for the two stem densities. The red dashed line shows the curve obtained setting r=0.15 m to the Nielsen [1992] formula; whilst the black solid line shows the same curve with r=0.23 m. Data from regular wave test having wave height exponential decay fit R^2>0.60 are shown.

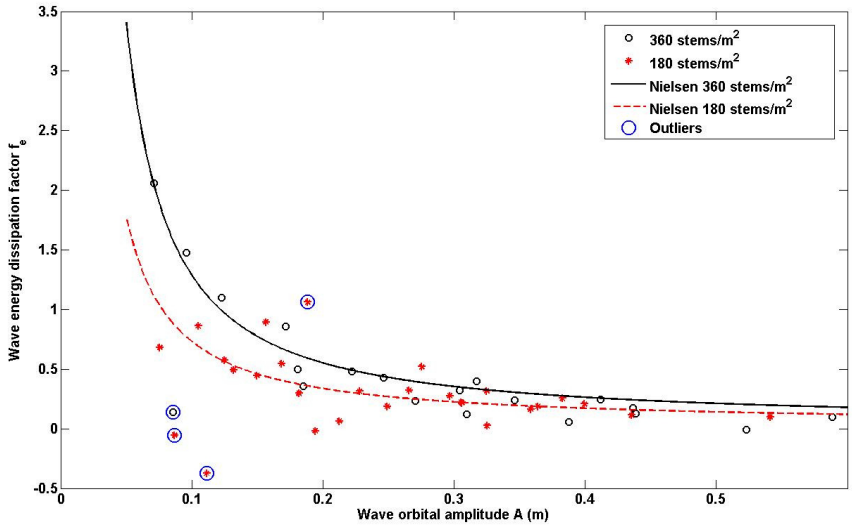

Figure 5.9 Friction factors plotted against the wave orbital amplitude for the two stem densities. The red dashed line shows the curve obtained setting r=0.15 m to Nielsen (1992) formula; whilst the black solid line shows the same curve with r=0.23 m. Data from all regular wave tests. Four data points were considered to be outliers and excluded from the analysis (indicated by a blue circle), because the absolute value of their residuals was more than 3 times greater than the RMSE.

For the high-density, non-staggered configuration, the canopy element spacing was S_{360}=0.44 m; whilst for the low-density staggered configuration it was different in the x and y directions 0.62 m<S_{180}<0.88 m, on average S_{180}=0.75 m. Assuming r_{360}= (S_{180}/ S_{360})r_{180}, r_{360}= 0.25 m was obtained, which is similar to the r_{360}=0.23 m found

from the data. Therefore, it might be therefore possible, under the tested Re_w, to parameterise the roughness of flexible canopies in terms of the canopy height and canopy element spacing.

5.4 Results and discussion: Oscillatory velocities

5.4.1 Preliminary observations

The velocity data were compared to theoretical values to check that the methodology used in the data processing was correct; likewise, to ensure that the data at the control profile (x/L=-0.07) were not affected by the presence of the patch.

Linear wave theory, with small U_{max}, fitted well the data outside the patch. However, a better fit for the range of U_{max} was found when velocities were predicted using Stokes second order theory (Figure 5.10). Tests, whose the velocity profiles deviated significantly from the Stokes's theory, were not considered as the velocities measured at x/L=-0.07 may have been affected by the presence of the patch (or require the application of a higher-order theory). As the velocities in front of the patch followed theory, it was concluded that they were not significantly affected by the presence of the patch. The repeatability of the tests was evaluated by comparing the velocities measured at the control site for different patch densities. An average difference of 1 cm/s (2.89 % of the velocity magnitude) was found for the U component and 2 cm/s (2.75%) for the W component. The differences between the measured data at the patch (x/L>0) and those at the control profile were significantly greater than the natural variability in the experiments.

The theoretical free stream velocity, $U_\infty(\omega t)$ at the surface (dotted black line in Figure 5.11), was obtained as a function of wave phase, from the local measurement of the water surface oscillation using:

$$U_\infty(wt) = <\xi> \omega \frac{\cosh(kD)}{\sinh(kD)} \qquad \textbf{Eq. 5-21}$$

Where: $<\xi>$ is the measured ensemble-averaged surface elevation; ω is the radian frequency; k is the wave number and D is the water depth. To obtain a value of the free-stream velocity at each wave phase, linear wave theory was used following a common practice [*Nielsen*, 1992; *Lowe et al.*, 2005a]. Although this is only a first approximation

for the tests that were non-linear, it provides an insight into the processes involved in the interaction between the canopy and the oscillatory flow. The measured <U> at the control location (x/L=-0.07, in front of the leading edge of the patch), was in phase with the wave signal for all z/h_s. As expected, the velocities peaked at the wave crest and reached their minimum values in the wave trough (Figure 5.11 A). <W> was approximately 90 degrees out of phase with respect to <U>, which is also in good agreement with theory.

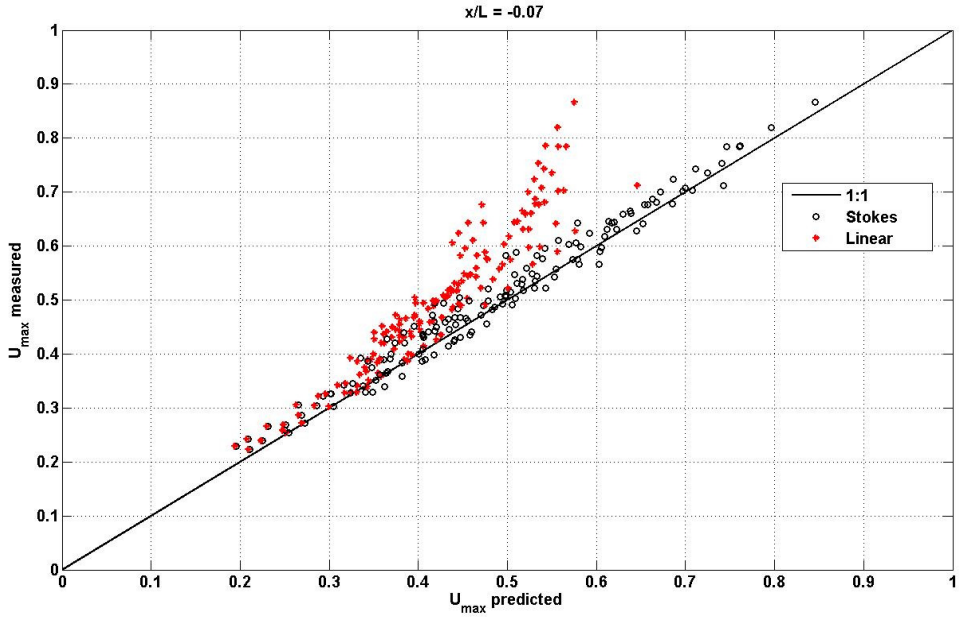

Figure 5.10 U_{max} measured at all elevations at x/L=-0.07 plotted against the predicted value obtained using linear theory (red symbols) and Stoke's second-order theory (black circles).

The ensemble velocity time-series followed a classic behaviour in front of the leading edge of the patch (x/L=-0.07). Within the patch (x/L=0.17 and x/L=0.80 Figure 5.11 B and C), the <U> and <W> showed a significant deviation from linear wave theory (the dotted black line in Figure 5.11), in both magnitude and phase. This was observed especially in the in-canopy velocities, (where the relative height (z/h_s) was smaller than 1). A more detailed analysis of how the oscillatory flow structure is affected by the canopy is presented in Sections 5.4.2 to 5.4.4.

In all of the tests (especially those with Ursell numbers >12.5, see Table 5-1), waves showed a positive asymmetry; this was observed also in the measured velocities i.e. U_{max} greater than U_{min}, (see for example Figure 5.11). Flow asymmetry will be examined in more detail in Section 5.4.5.

From Figure 5.11, it is clear also that the magnitude of <U> in the canopy (at x/L=0.17 and at x/L=0.80) was reduced compared to the <U> at the same elevation outside the canopy (x/L=-0.07); whilst, in this particular run, <U> was enhanced just above the canopy (h_s/D=1.09). The component <W> was reduced mostly compared to measurements obtained outside the canopy. The changes to the oscillatory flows will be presented and discussed, for all of the tests, in Section 5.4.6 and 5.4.7.

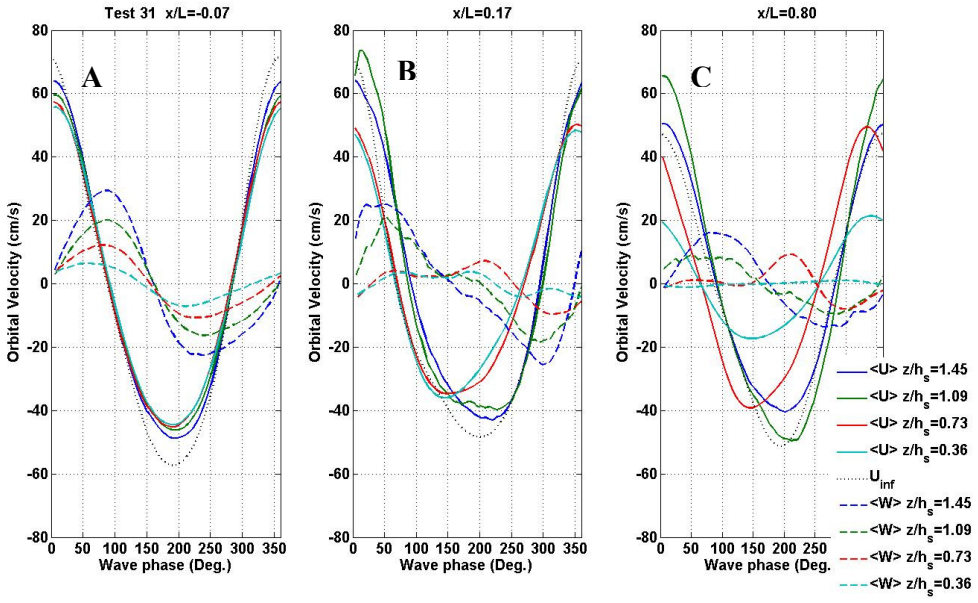

Figure 5.11 Measured <U> (ωt, z), and <W>(ωt, z) U∞(ωt) for Test 31 (see Table 5-1) at X/L=-0.07 in front of the patch (A); at the patch near the leading edge x/L=0.17 (B) and x/L=0.80, at the patch further shoreward (C).

5.4.2 The oscillatory velocity structure

The magnitude of the vertical component <W> inside the patch (at both x/L locations) decreased from the surface towards the bed, as it did outside the patch. The <U> component showed a much more complicated pattern. The vertical profiles of <U> of selected tests have been plotted (Figure 5.12 to5.15), for several phases of the wave cycle. At x/L=-0.07 (in front of the leading edge of the patch), the velocities followed a normal vertical distribution at all phases, reaching a maximum value near the water surface (z/h_s=1.45) and a minimum near the bed. Within the patch, the <U> values in the lower canopy were reduced significantly compared to those measured in front of the leading edge, particularly at x/L=0.80, farther inside the patch. Interestingly, the velocity peak in the patch was not found at the water surface but near the canopy top (z/h_s=1.09) or, in some cases, in the upper canopy (z/h_s=0.73) (see Figure 5.12). This

peak was observed both for the shoreward- and backward-directed velocities (phase >270 degrees and phase <270 degrees respectively).

The presence of the peak of <U>, in both directions, confirms that it is a feature of the oscillatory motion (not induced by a steady current) and is similar to the "overshoot" (the peak of U(z,t)) at the top of the wave boundary layer, typical of harmonic flow described by Nielsen (1992) (Figure 2.3 of Chapter 2). Moreover, as in a classical wave boundary layer, the velocities near the flume bed changed direction before the velocity measured near the surface and the predicted $U_\infty(\omega t)$ (which is an approximation of the free-stream velocity). The phase shift and the vertical structure of the oscillatory flow were further investigated for the entire regular wave dataset (Section 5.4.4).

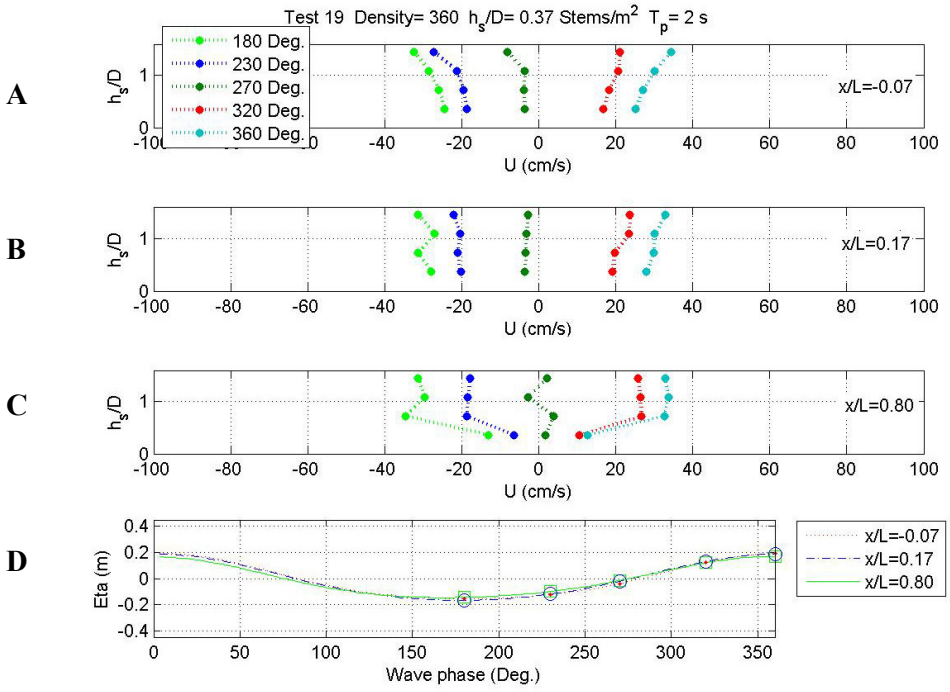

Figure 5.12 The variation of <U> with relative height at different wave phases (x/L=-0.07 in plot A, x/L=0.17 in plot B and x/L=0.80 in plot C). Plot D shows the measured water surface oscillation. The symbols indicate the surface elevation at the wave phase for the velocities profiles in plots A-C: Test 19 (T_p=2 s, H_o=0.36 m, h_s/D=0.37 and 360 stems/m^2).

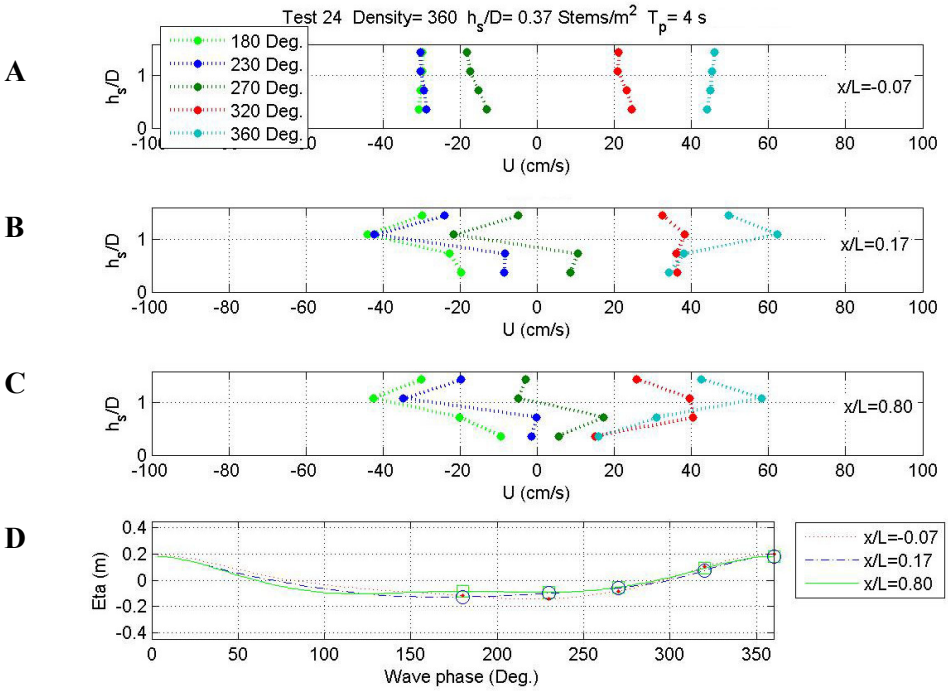

Figure 5.13 The panels correspond to Figure 5.12:Test 24 (T_p=4 s, H_o=0.35 m, h_s/D=0.37 and 360 stems/m^2).

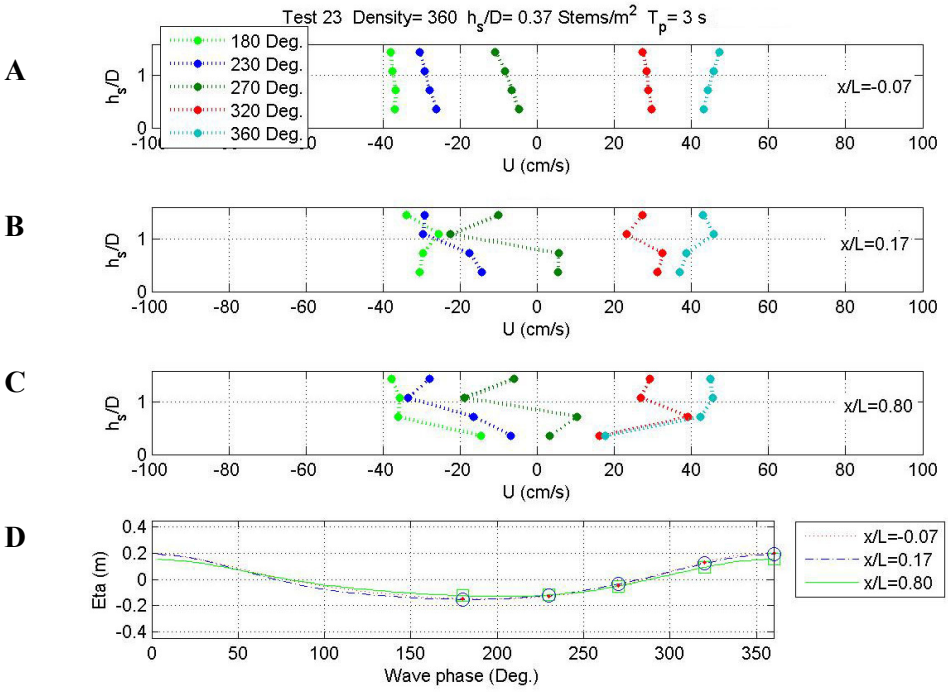

Figure 5.14 The panels correspond to Figure 5.12: Test 23 (T_p=3 s, H_o=0.36 m, h_s/D=0.37 and 360 stems/m^2).

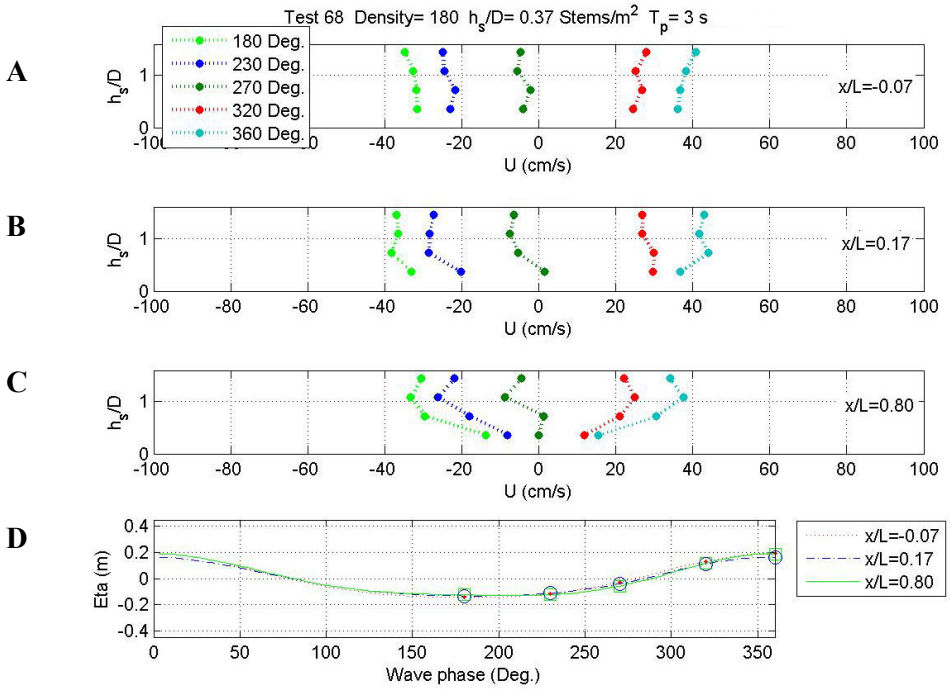

Figure 5.15 See above: Test 68: (T_p=3 s, H_o=0.35 m, h_s/D=0.37 and 180 stems/m^2).

5.4.3 The vertical structure of the oscillatory flow: Effects of submergence ratio, stem density and wave period.

The maximum value of the ensemble velocities (<U> and <W>) were obtained in order to identify the changes in the vertical distribution of the orbital velocities induced by the canopy in the different runs. The U_{max} and W_{max} velocities were normalised against the corresponding theoretical values at the water surface (U_{free} and W_{free}), obtained by applying Stokes theory to the local wave parameters.

Figure 5.16 and Figure 5.17 show the effect of stem density ratio on the distributions of the normalised U_{max} and W_{max}. Figure 5.18 and Figure 5.19 show the effect of submergence ratio, on normalised U_{max} and W_{max}. Figure 5.20 and Figure 5.21 show the effect of wave period on normalised U_{max} and W_{max}, respectively. The denser patch produced a larger "overshoot" above the seagrass and a more pronounced reduction in U_{max} in the lower canopy, especially at the edge of the patch (x/L=0.17). When the submergence ratio was increased, a similar effect was observed on normalised U_{max}: i.e. an increased "overshoot" at the canopy top, with increasingly reduced velocities in the lower canopy. An increase in period produced also the same effect (except for the 4 s waves).

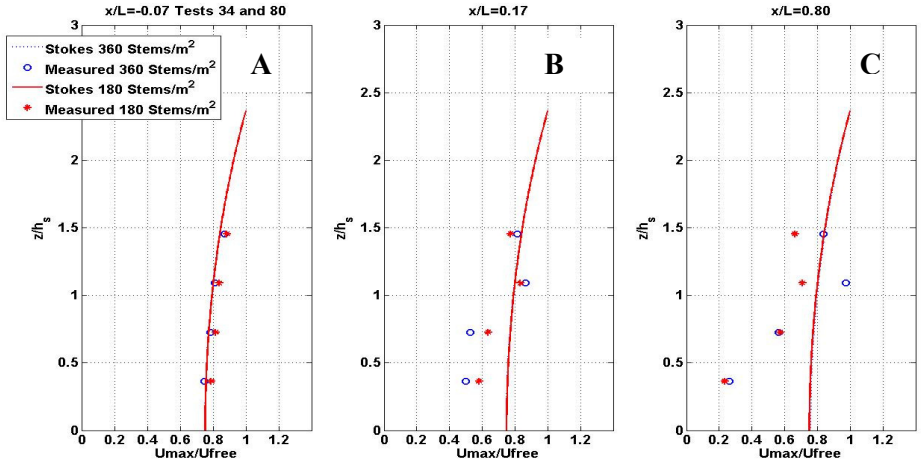

Figure 5.16 Effect of stem density on the vertical structure of U_{max}, (T_p=4s h_s/D=0.42) A) in front of the leading edge of the patch (x/L=-0.07); B) near the edge (x/L=0.17); and C) in the patch (x/L=0.80) (T_p=4 s, H_0=0.41±0.007 m and h_s/D=0.42)

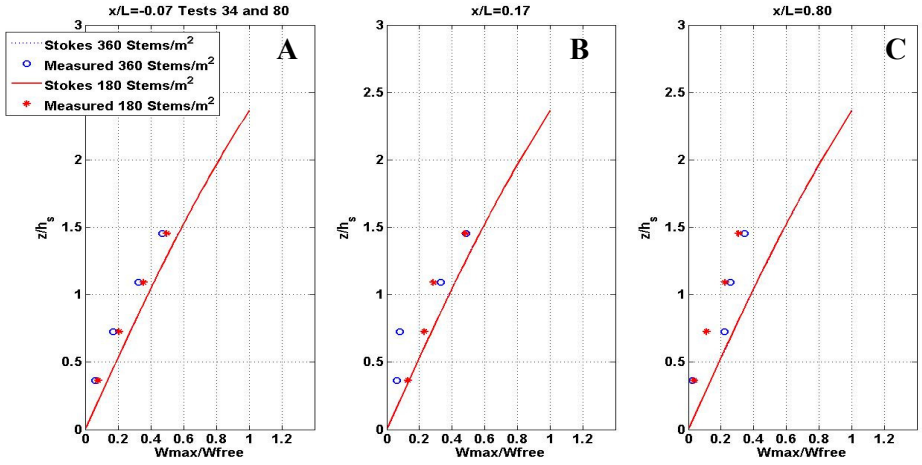

Figure 5.17 Effect of stem density on the vertical structure of W_{max}. A) in front of the leading edge of the patch (x/L=-0.07); B) near the edge (x/L=0.17); and C) in the patch (x/L=0.80) (T_p=4 s, H_0=0.41±0.007 m and h_s/D=0.42)

Within the canopy U_{max}/U_{free} decreased exponentially with increasing orbital amplitude A (plot Figure C. 1, in Appendix C).

$$A = \frac{U_c T_p}{2\pi} \qquad \textbf{Eq. 5-22}$$

U_c is defined as the maximum orbital velocity above the canopy, obtained from Stokes theory.

The W_{max} velocities were reduced at all elevations, compared to the predicted values, without a significant variation to the shape of the profile. The largest deviations

were observed in the upper canopy. However, the effects of density and period were not as clear as for U_{max}/U_{free}.

These results on the effects of submergence ratio, stem density, and wave period on the oscillatory velocity structure confirm preliminarily observations [obtained by the author by using a more simplistic linear wave theory, reported in *Stratigaki et al.*, Submitted], despite Stokes theory was more appropriate at describing flows outside the canopy (see Figure 5.10).

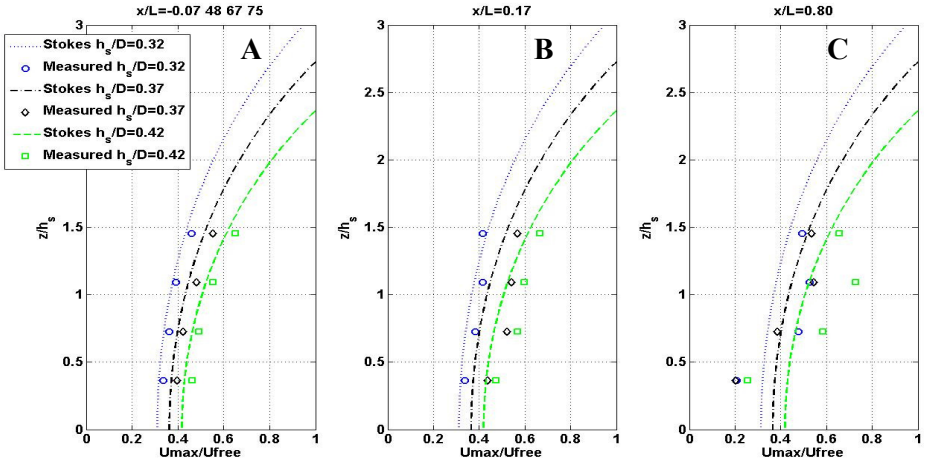

Figure 5.18 Effect of submergence ratio (h_s/D) on the vertical structure of U_{max},,: A) in front of the leading edge of the patch (x/L=-0.07); B) near the edge (x/L=0.17); and C) in the patch (x/L=0.80) (T_p=2 s, H_0=0.37±0.017 m and density 180 stems/m^2)

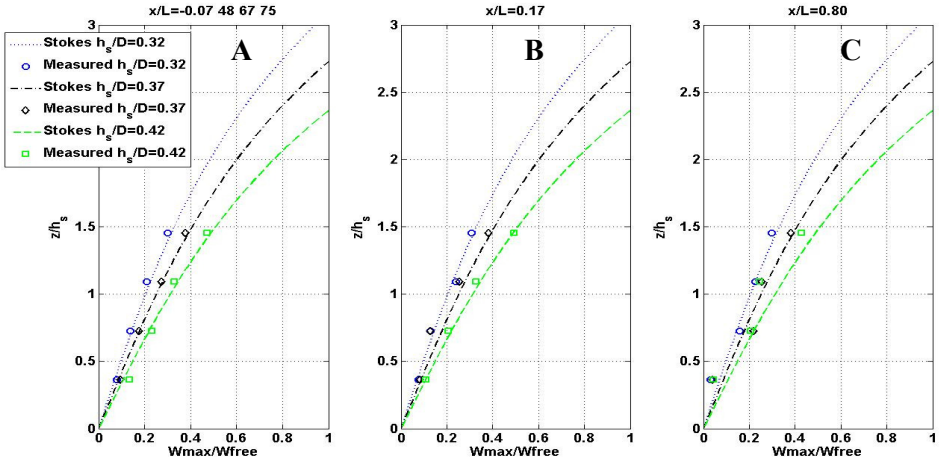

Figure 5.19 Effect of submergence ratio (h_s/D) on the vertical structure of W_{max},: A) in front of the leading edge of the patch (x/L=-0.07); B) near the edge (x/L=0.17); and C) in the patch (x/L=0.80). (T_p=2 s, H_0=0.37±0.017 m and density 180 stems/m^2)

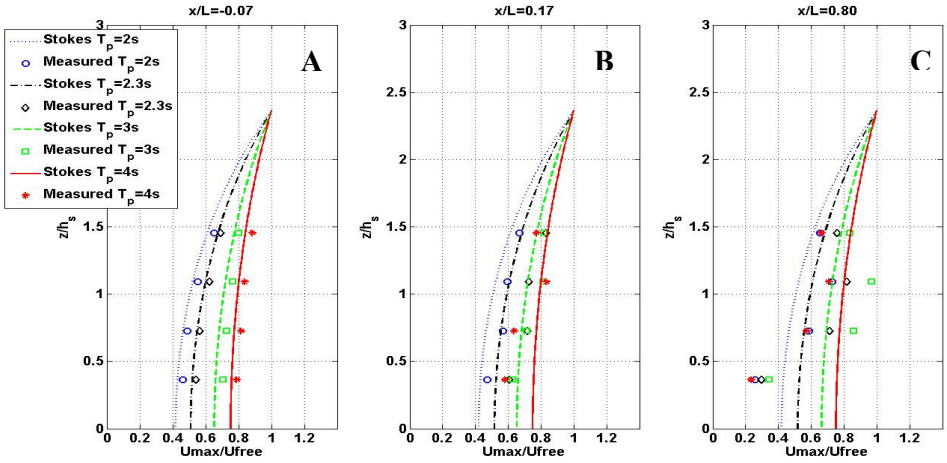

Figure 5.20 Effect of period on the vertical structure of U_{max}: A) in front of the leading edge of the patch (x/L=-0.07); B) near the edge (x/L=0.17); and C) in the patch (x/L=0.80) (T_p=4 s h_s/D=0.42) (density 180 stem/m^2, H_0=0.39±0.013 m and h_s/D=0.42)

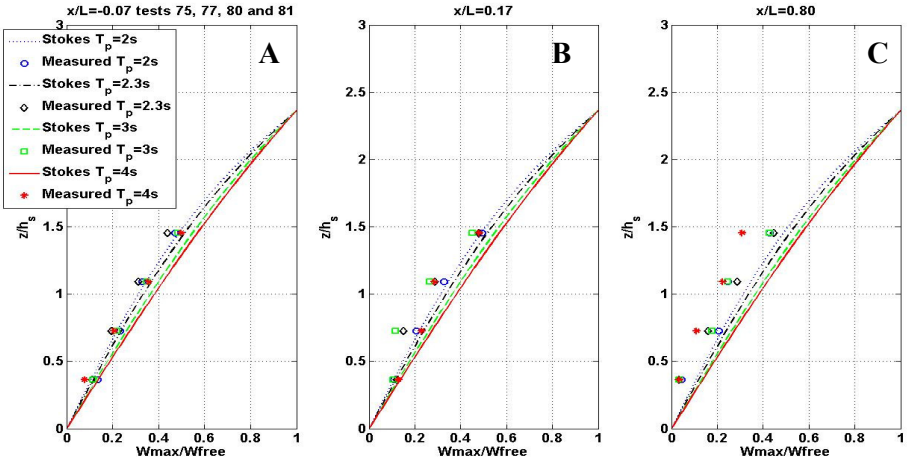

Figure 5.21 Effect of period on the vertical structure of W_{max}: A) in front of the leading edge of the patch (x/L=-0.07); B) near the edge (x/L=0.17); and C) in the patch (x/L=0.80) (density 180 stem/m^2, H0=0.39±0.013 m and h_s/D=0.42)

5.4.4 The phase shift

The phase difference (φ) between U_{max} and the maximum value of the surface velocity U_∞ (defined in Eq. 5-21) was obtained for all of the tests and have been plotted against the wave orbital amplitude (A). At the control profile, φ (red symbols in Figures 5.22 and 5.23) was small and did not change with A. This result was expected as, outside of the patch, the wave boundary layer is only few cm's thick (Chapter 2, Section 2.2.3) and all measurements were made in the free-stream region. For the tests with a shoot density of 360 stems/m^2, φ was positive inside the canopy (z/h_s<1), varying from 0 to about 45 degrees. This pattern indicates that, inside the canopy, the velocity

maximum occurred before the passage of the wave crest, as predicted by classical wave boundary layer theory.

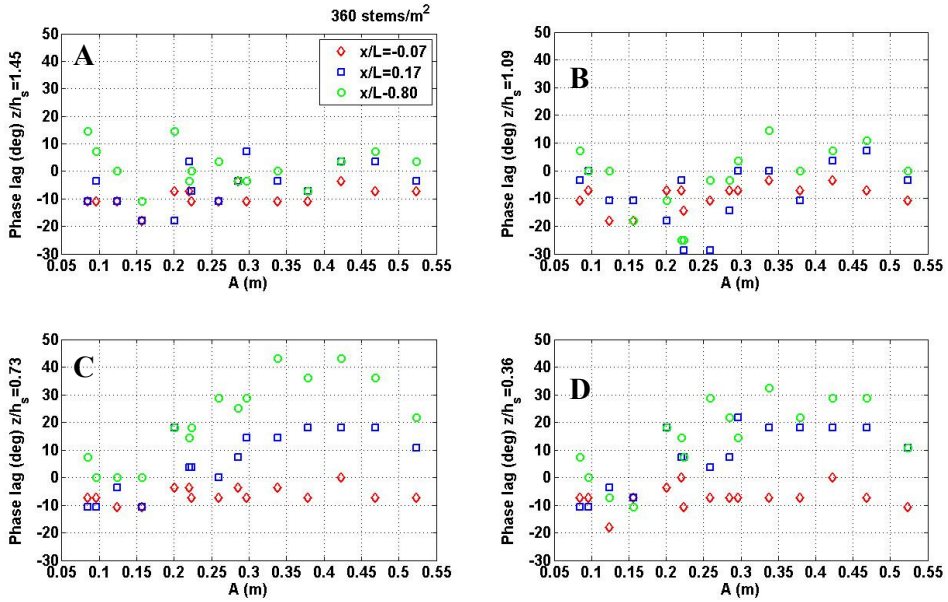

Figure 5.22 Phase lag between the passage of the wave crest and the maximum velocity plotted against A (wave orbital amplitude), for tests having 360 stems/m^2. Plots A-D shown the data measured at various elevations from the bed, at the three x/L locations.

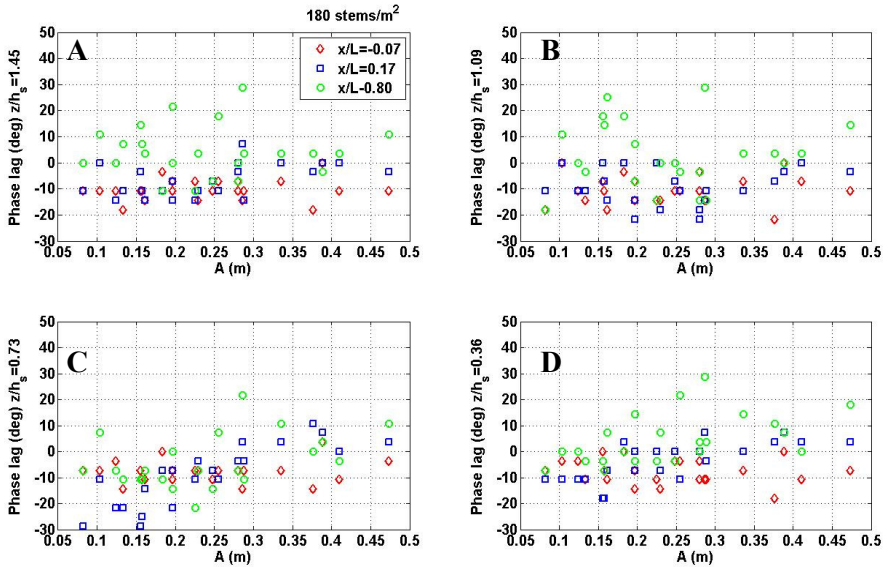

Figure 5.23 Phase lag between the passage of the wave crest and the maximum velocity plotted against A (wave orbital amplitude), for tests having 180 stems/m^2. . Plots A-D shown the data measured at various elevations from the bed, at the three x/L locations.

The phase difference increased with A, for A>0.20 m. At x/L=0.17, within the canopy near the leding edge, the magnitude of the phase difference was on average smaller than at x/L=0.80 (Figure 5.22). In contrast, above the canopy (at z/h_s=1.45) φ varied between 15 and -20 degrees; it did not show any trend with A (Figure 5.22A).

The trends observed between A and φ, for tests with the denser patch (Figure 5.22), were also evident for the less dense patch (data shown in Figure 5.23); however, not as clear, as the phase shift is smaller and the scatter is larger. Some of this scatter might be due also to the different behaviour of the mimics under different submergence ratios.

The increase in phase shift with A inside the canopy indicates that the response of the mimics and the velocity structure depended largely upon the orbital amplitude.

5.4.5 The flow asymmetry

The asymmetry of the oscillatory flow beneath the waves has been plotted against the Ursell number. Here, the Stokes asymmetry (R) coefficient was used to quantify the flow asymmetry:

$$R = \frac{U_{\max}}{U_{\max} - U_{\min}} \qquad \textbf{Eq. 5-23}$$

The Ursell number (UR) was obtained from

$$UR = \frac{H_0 \lambda^2}{D^3} \qquad \textbf{Eq. 5-24}$$

With: H_0 wave height in front of the patch; λ wave length and D water depth.

In the perfect sinusoidal case R=0.5. As R increases, with increasing UR, it indicates that the wave orbits are not symmetric and that a shoreward direction prevails. This shoreward drift for test with Ursell numbers >12.5 was largest just above the canopy and larger than on rippled sand in front of the seagrass patch, consistent with the observations of Price et al (1968). Also, from field measurements in the upper part of the canopy (Chapter 3) it was shown that *Posidonia* induced a net shoreward drift. However, from the present results there is evidence that inside the canopy the shoreward drift is not enhanced; instead it appears reduced compared to the area in front of the patch.

The plots in Figure 5.24 show that upstream of the seagrass patch (at x/L=-0.07) R was larger than 0.5 in all of the tests; it increased with increasing *Ur*, as expected. The asymmetries near the bed were smaller than near the surface. This difference was enlarged over the seagrass patch for Ursell numbers larger than 12.5. At the edge of the canopy (x/L=0.17), the velocity asymmetries were generally larger than observed elsewhere. At the canopy top, R was larger than upstream of the patch (at both x/L

locations, see Figure 5.24B). Within the canopy, the orbital velocities became less asymmetrical than upstream of the patch, especially at the highest Ursell numbers. At high Ursell numbers the data show a large scatter.

For the tests with Ursell numbers smaller than 12.5, the differences between R at the front of the patch and inside the patch were not significant; they very close to 0.5 such that the waves can be considered as linear.

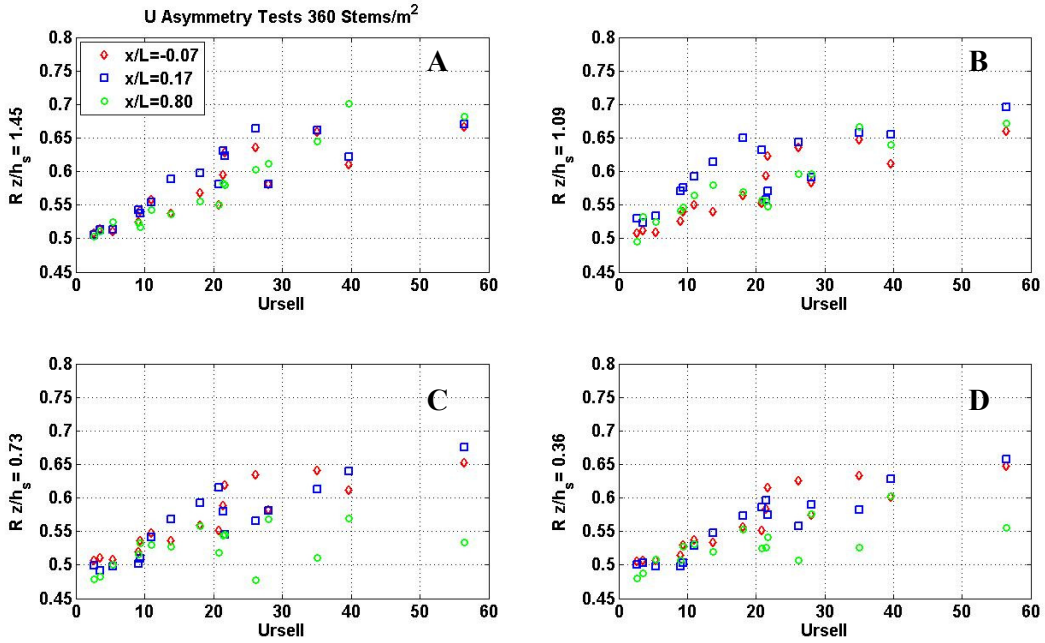

Figure 5.24 Stokes asymmetry (R) plotted against Ursell number at different elevation above the bed (plots A-D) (tests having 360 stems/m^2).

5.4.6 Changes induced by the canopy to the oscillatory flows: horizontal component

The orbital velocities measured at the control profile (x/L=-0.07) fitted well the Stokes theory; therefore, it is assumed that they are not affected significantly by the presence of the meadow.

In order to quantify the changes in the horizontal component of the oscillatory flow, induced by the seagrass patch, the velocities measured at x/L=0.17 and x/L=0.80 were normalised against the velocities measured at x/L=-0.07 (U^0_{rms}) at the same elevation; thus resulting in a dimensionless parameter (α, hereafter referred to as the flow attenuation coefficient), defined as:

$$\alpha(z) = \frac{U_{rms}}{U^{0}_{rms}} \qquad \textbf{Eq. 5-25}$$

The root mean square value of <U> (called U_{rms}) was used, in preference to the maximum value, so that both regular and irregular waves could be compared (in the next Chapter). The α(z) values from the tests with the high density patch are shown in Figure 5.25 (A and B); those from the low density patch are shown in Figure 5.26.

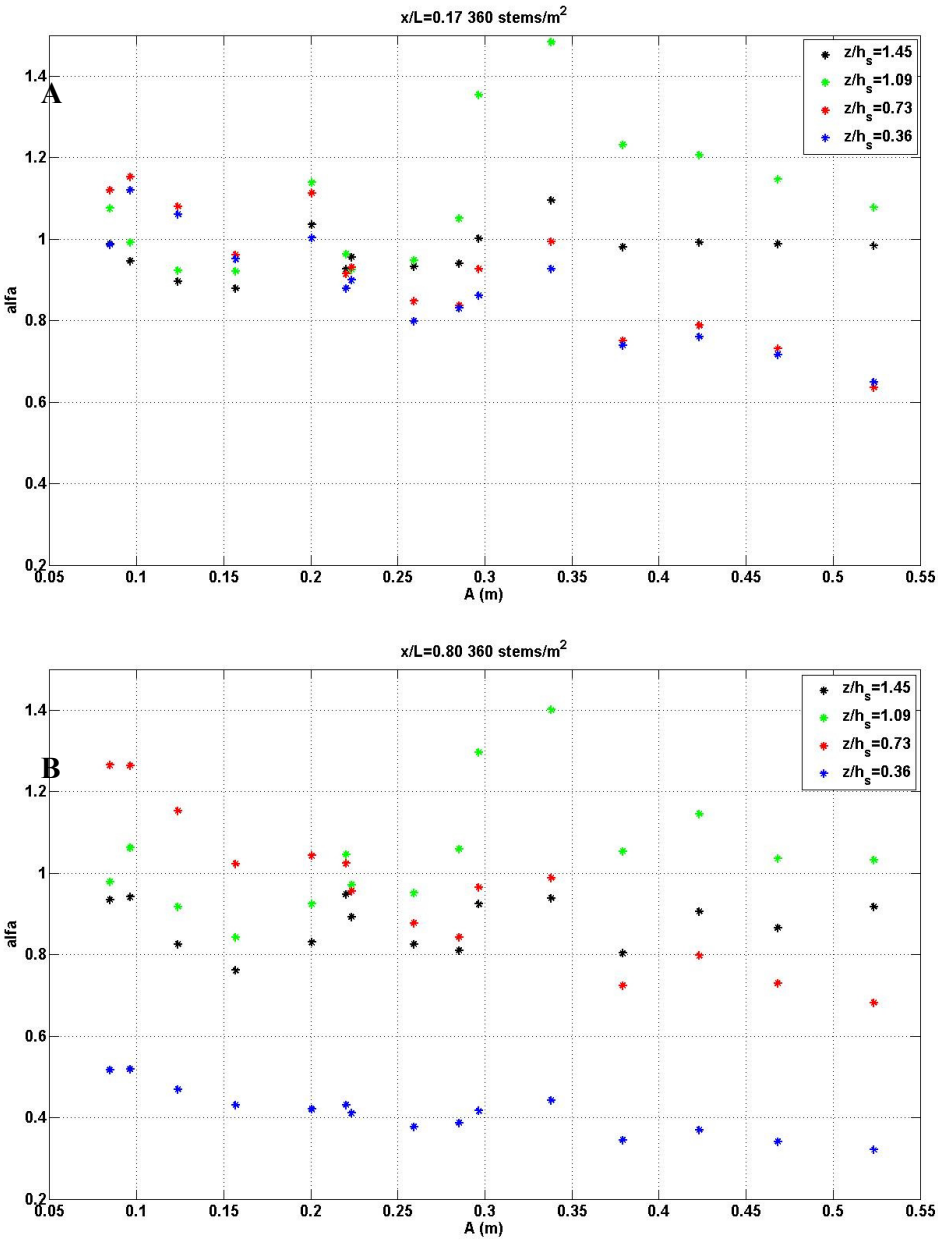

Figure 5.25 Variation in flow attenuation coefficient (α), with A, at 4 elevations above the bed for the tests with 360 stems/m^2, at x/L=0.17 (plot A) measurements at x/L=0.80 (plot B).

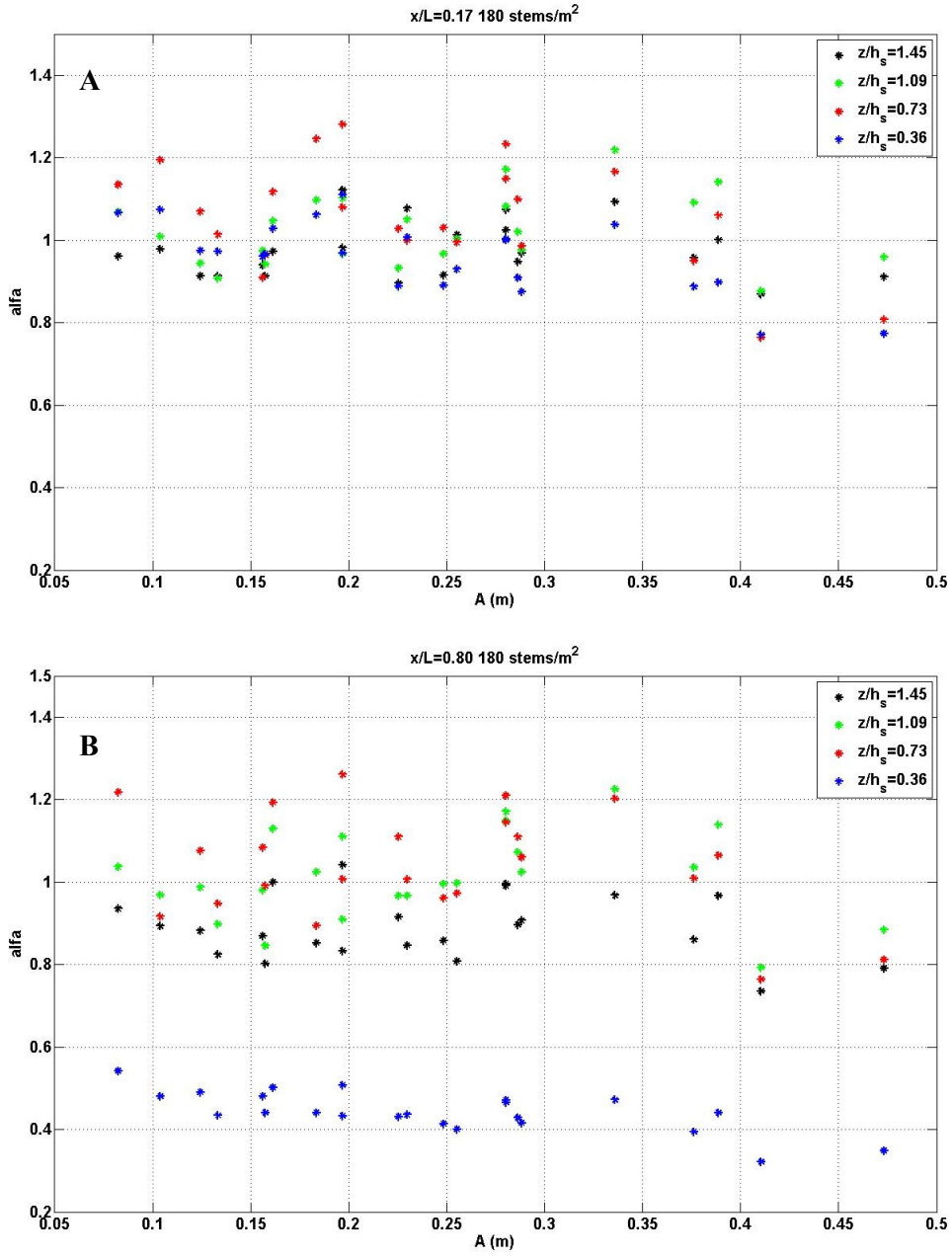

Figure 5.26 Variation in the flow attenuation coefficient (α), with A, at 4 elevations above the bed for the tests with 180 stems/m^2 at x/L=0.17 (plot A) measurements at x/L=0.80 (plot B).

The waves characterised by large A (A>0.20 m) tended to become non-linear at the depths tested (*Ur*>15) and, potentially, a Stokes drift was produced. This factor might have contributed also to the intensification of shoreward oscillatory flows at the canopy top.

Flows within the canopy (at $z/h_s<1$) were reduced, compared to those measured in front of the patch for the tests with a large orbital amplitude (approximately A>0.20

m for tests with a density of 360 stems/m^2 and A>0.30 m for tests with a density of 180 stems/m^2). The in-canopy flow was reduced more by the waves characterised by large orbital amplitudes. These results are in line with findings obtained from oscillatory flows, within rigid canopies [*Lowe et al.*, 2005b; *Lowe et al.*, 2007].

Flow transformation in the lower canopy, was further analysed. The percentage reduction of U_{rms} in the lower canopy ((1- α_L)*100) was calculated for all of the tests and averaged. The results and the variations amongst the tests are reported in Table 5-3. The percentage reduction of flow within the patch (x/L=0.80) is on average larger for the tests with 360 stems/m^2 (58.7%), than for those tests with half the mimic density (55.7%). Also, at the edge of the patch the denser meadow reduced the wave-induced flows more than the less dense patch; however, here the reduction is much smaller and the variation amongst the tests is very large. The variation amongst all tests is only 5%-5.7%, at x/L=0.80.

Table 5-3 Percentage flow reduction (horizontal component) in the lower canopy (z/h_s=0.36). Average values (mean) and standard deviations (S.D.) amongst the tests with two different densities are indicated.

Mimic density (stems/m^2)	Mean %U_{rms} reduction x/L=0.17	Mean %U_{rms} reduction x/L=0.80	S.D. %U_{rms} reduction x/L=0.17	S.D. %U_{rms} reduction x/L=0.80
360	12.1	58.7	13.3	5.7
180	4.1	55.7	8.9	5.0

Flow reduction (horizontal component) in the lower canopy was expressed by the exponential function:

$$\alpha(z) = a\exp(bA) \qquad \textbf{Eq. 5-26}$$

with α(z) defined in Eq. 2-25 and A the wave orbital amplitude.

The values of the fitted coefficient *b* and *a* in the lower canopy (z/h_s=0.36) are summarised in Table 5-4, for the different locations along the patch and for the two shoot densities. The fit and the uncertainties in the fit estimate (95% confidence bounds) are shown in Figure 5.27, for tests with 360 stems/m^2 at x/L=0.17 (A) and at x/L=0.80 (B). The fit was very good for the higher density configuration tests, whilst the tests with lower density (180 stems/m^2) were characterised by a much larger scatter of data (Figure 5.28). The values of *b* were less negative in the test with 180 stems/m^2 compared with 360 stems/m^2, at both locations in the patch (Table 5-4); this indicates that the more dense patch induced a larger flow reduction than the less dense patch, in

agreement with Lowe et al.'s (2005b) model for rigid canopies. In particular, the effect of increased density is to accelerate the rate of change (b) of α, with increasing A (i.e. steeper slope for tests with 360 than 180 stems/m^2). The factor *a* of the exponential curve decreased with increasing distance from the edge of the patch for both densities, i.e. the flow attenuation increased with distance from the leading edge of the patch.

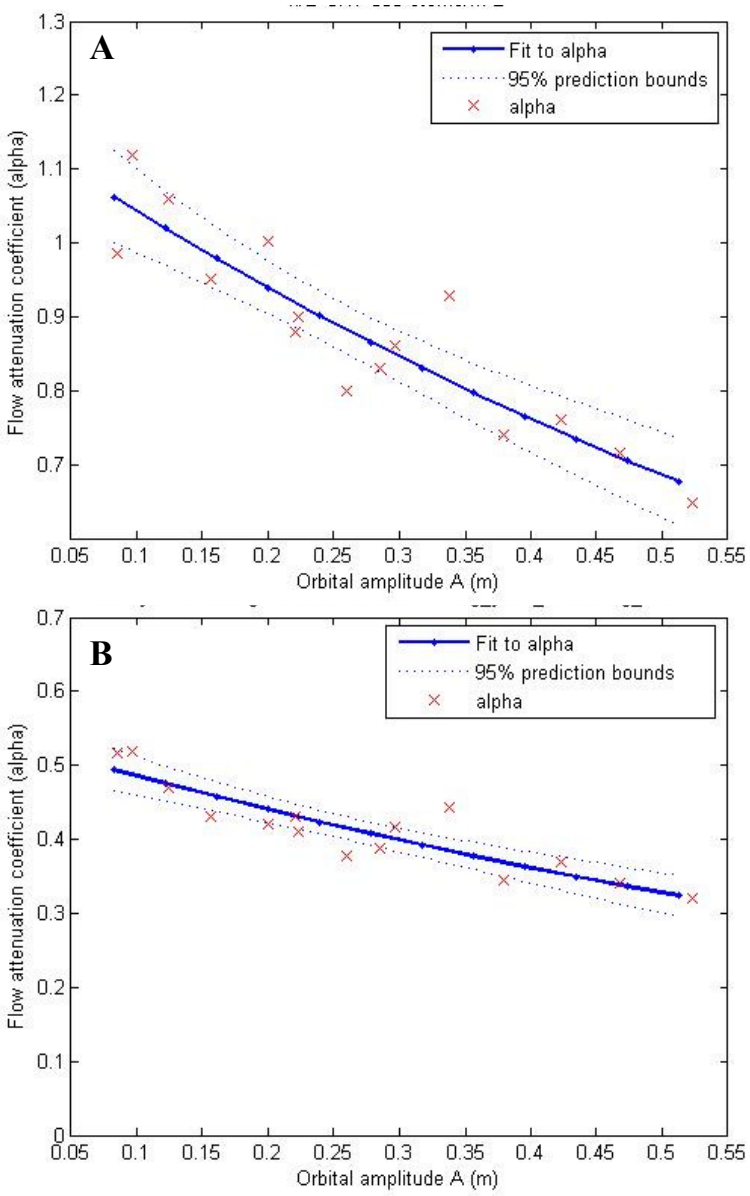

Figure 5.27 Analysis of fit of the flow attenuation coefficient (α) measured in the lower canopy, to the exponential model (z/h_s=0.36), for tests with 360 stems/m^2 at x/L=0.17 (A) and at x/L=0.80 (B). The 95% confidence bounds are indicated by the dotted lines.

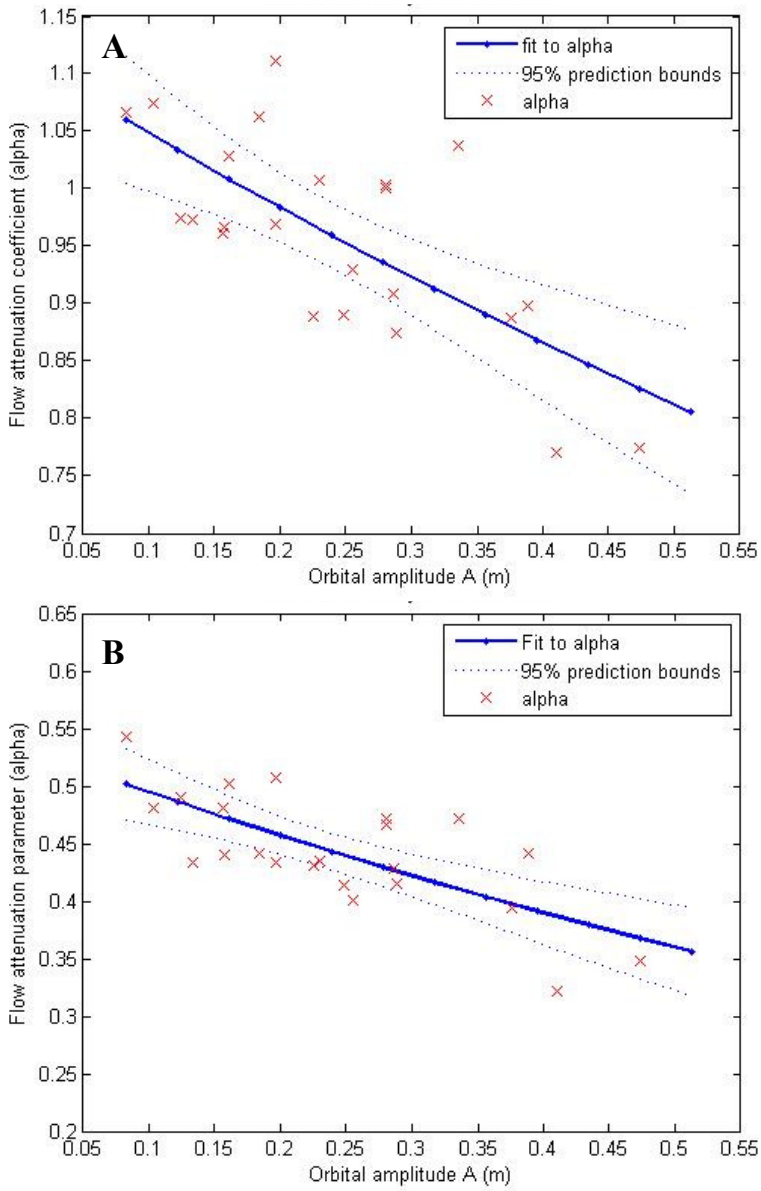

Figure 5.28 Analysis of fit of the flow attenuation coefficient (α) measured in the lower canopy, to the exponential model (z/h_s=0.36), for tests with 180 stems/m^2 at x/L=0.17 (A) and at x/L=0.80 (B). The 95% confidence bounds are indicated by the dotted lines.

Table 5-4 Flow reduction as a function of A in the lower canopy (z/hs=0.36) for regular waves. The a and b coefficients of the fits to Eq. 5-25 are indicated, as well as their confidence limits (calculated as twice the standard error, with 95% level of confidence) and the correlation coefficient (R^2).

		x/L=0.17			x/L=0.80		
Wave type	**Density (stems/m^2)**	**a**	**b**	**R^2**	**a**	**b**	**R^2**
Regular	360	1.16 ±0.09	-1.05 ±0.30	0.83	0.54 ±0.08	-0.98 ±0.29	0.81
	180	1.12 ±0.08	-0.64 ±0.30	0.52	0.54 ±0.05	-0.80 ±0.35	0.50

5.4.7 Changes induced by the canopy to the oscillatory flows: vertical component

An equivalent α parameter was calculated for the vertical component of the oscillatory flow, as for the horizontal component:

$$\alpha^{w}(z) = \frac{W_{rms}}{W^{0}_{rms}} \qquad \textbf{Eq. 5-27}$$

No clear trend was observed with the orbital amplitude, A (see plots C.2 and C.3 in Appendix C). At x/L=0.80, W_{rms} was generally smaller than that measured in front of the patch at all elevations (as found for the horizontal component). In the lower canopy at x/L=0.80, the flow reduction was very large, especially for the denser patch where it averaged 80±6.3% (see Table 5-5). The value of α^{w} varied little between the different tests. There was a much larger scatter for the measurements at the edge of the patch, than for those measured into the patch.

Table 5-5 Percentage flow reduction (vertical component) in the lower canopy (z/h_s=0.36). Average values (Mean) and standard deviations (SD) between the tests with two different densities, are indicated.

Mimic density stem/m^2	Mean %W_{rms} reduction x/L=0.17	Mean %W_{rms} reduction x/L=0.80	SD %W_{rms} reduction x/L=0.17	SD %W_{rms} reduction x/L=0.80
360	28.2	79.4	24.6	6.3
180	5.6	69.1	16.6	5.7

5.5 Results and discussion: Turbulence

5.5.1 Turbulence intensities and turbulent kinetic energy

Horizontal turbulence intensities (U'_{rms}) were found to increase with height above the bed, in front of the leading edge of the seagrass (see, for example, plot C in Figure 5.29 and Figure 5.30, x/L=-0.07, red symbols). Above the patch, the turbulence was higher than in front of the patch. Conversely, in the lower canopy smaller values of U'_{rms} were recorded, in particular at x/L=0.80; here, the levels of U'_{rms} were in some tests even less than those at the same elevation in front of the patch (at x/L=-0.07). Just above the canopy, the levels of U'_{rms} were always larger than those measured in front of the seagrass, or above this level. Inside the canopy, the levels of horizontal turbulence were always lower than those above; this can be attributed to lower turbulence

production associated with the reduced wave-induced flow (see plot A in Figure 5.29 and in Figure 5.30) measured in this area (less than 13 cm/s at x/L=0.80).

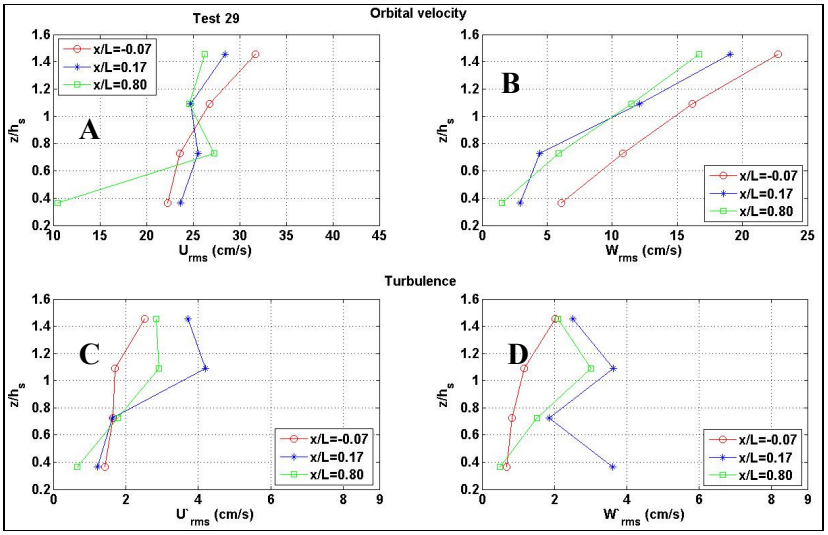

Figure 5.29 Plots of the vertical profiles of horizontal (A) and vertical (B) wave-induced velocities and of horizontal (C) and vertical (D) turbulence. In each plot, the red dots represents measurements at x/L=-0.07; blue stars at x/L=0.17 and green squares at x/L=0.80. Test with T_p=2 s, H_0=0.38 m, density 360 stems/m^2 and h_s/D=0.42.

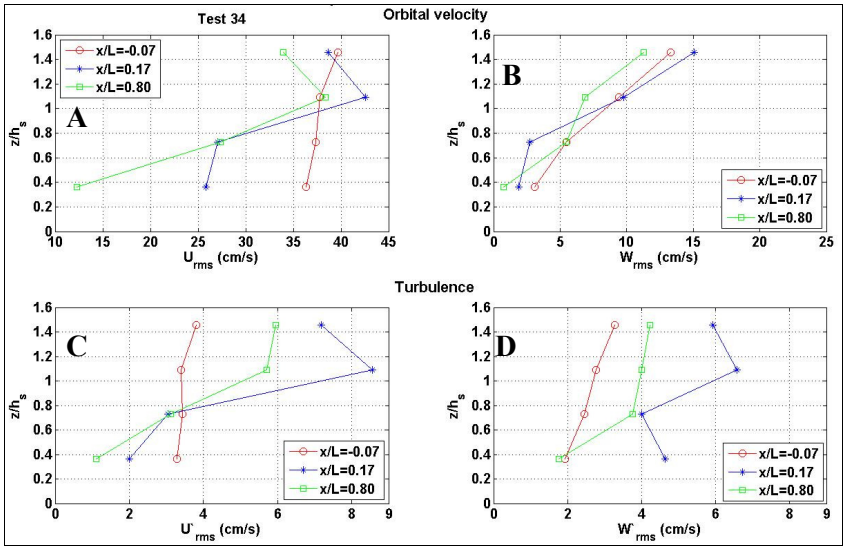

Figure 5.30 Plots of the vertical profiles of horizontal (A) and vertical (B) wave-induced velocities and of horizontal (C) and vertical (D) turbulence. In each plot , the red dots represents measurements at x/L=-0.07; blue stars at x/L=0.17 and green squares at x/L=0.80. Test with T_p=4 s, H_0=0.42 m, density 360 stems/m^2 and h_s/D=0.42.

The magnitude of the rms vertical component of turbulence (W'_{rms}) was considerably larger than in front of the canopy, both above and inside the canopy (plot

D, in Figure 5.29 and in Figure 5.30). At the edge of the canopy, in particular, high levels of vertical turbulence were observed. Reduced vertical turbulence was only observed in the lower canopy at x/L=0.80, a similar trend to U'_{rms}. This pattrn is due to the deceleration at this location (plot B, in Figure 5.29 and in Figure 5.30). These observations were consistent throughout the tests.

Turbulent kinetic energy (TKE) was calculated and plotted against the wave orbital amplitude (A), in order to compare the different tests. TKE increased consistently with increasing wave orbital amplitude, A (see plots in Appendix C for the 360 stems/m^2 and 180 stems/m^2 canopy, respectively). Generally, the TKE peaked at the canopy top (z/h_s=1.09) and the largest values were found at the edge of the canopy (x/L=0.17), at all elevations. The TKE, at the top of the canopy, for 360 stems/m^2 was more than double the values for 180 stems/m^2. However, the opposite pattern occurred in the upper canopy, where tests with 180 stems/m^2 were characterised by a larger turbulent energy, than tests with 360 stems/m^2.

Normalised values of TKE (α_{TKE}) are shown in Figure 5.31 and Figure 5.32 (for the 360 stems/m^2 and 180 stems/m^2 canopy respectively) plotted against wave orbital amplitude. The parameter αTKE is defined as the ratio:

$$\alpha_{TKE} = \frac{TKE}{TKE_0} \qquad \textbf{Eq. 5-28}$$

where TKE_0 is measured in front of the canopy (at x/L=-0.07), at the same elevation as the TKE. In all of the tests, in the lower canopy the TKE was reduced compared with the values at the front of the patch. Conversely, the TKE above the canopy and in the upper canopy was larger than in front of it, at the same elevation.

There is not a clear trend between normalised turbulent kinetic energy (α_{TKE}) and wave orbital amplitude. This is because the depth of submergence (h_s/D) is affecting significantly turbulence levels, both above and inside the canopy. In particular normalised α_{TKE} decrease with increasing submergence ratio, for tests with values of A larger than 0.20 m (see for example Figure 5.33, tests T_p=4 s). This trend is not clear for A<0.20 m (see tests with Tp=2 s, in Figure 5.34); it almost appears reversed. Probably, this is linked to the amount of "plant" oscillation. Under these conditions (A<0.2 m), particularly under low submergence ratios, the oscillatory flow was very weak and the amplitude of the mimics oscillation was very small, probably creating relatively less turbulence within the canopy.

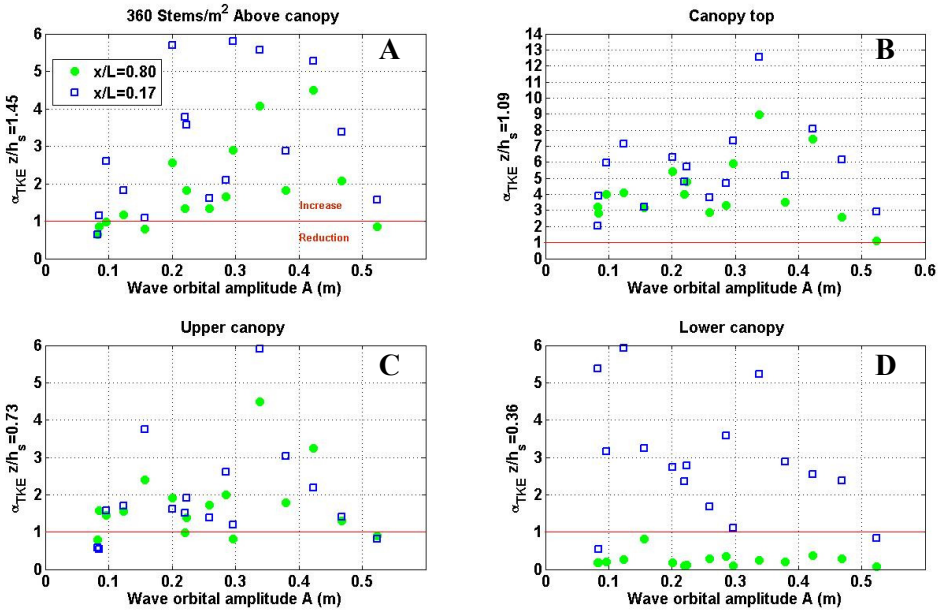

Figure 5.31 Normalised values of turbulent kinetic energy (α_{TKE}) at various elevations (plots A-D) and at two x/L locations (represented by different symbols). Tests with 360 stems/m^2.

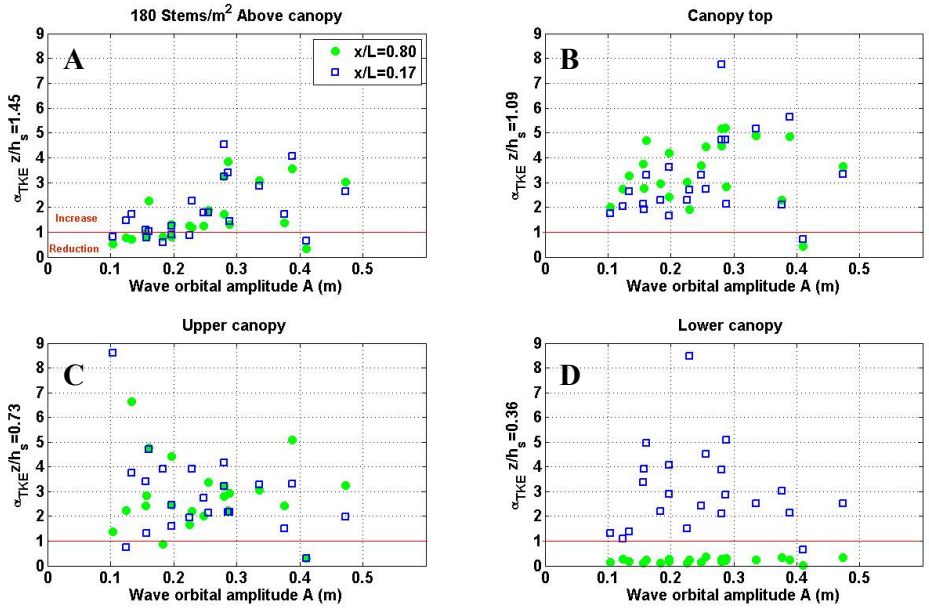

Figure 5.32 Normalised values of turbulent kinetic energy (α_{TKE}) at various elevations (plots A-D) and at two x/L locations (represented by different symbols). Tests with 180 stems/m^2.

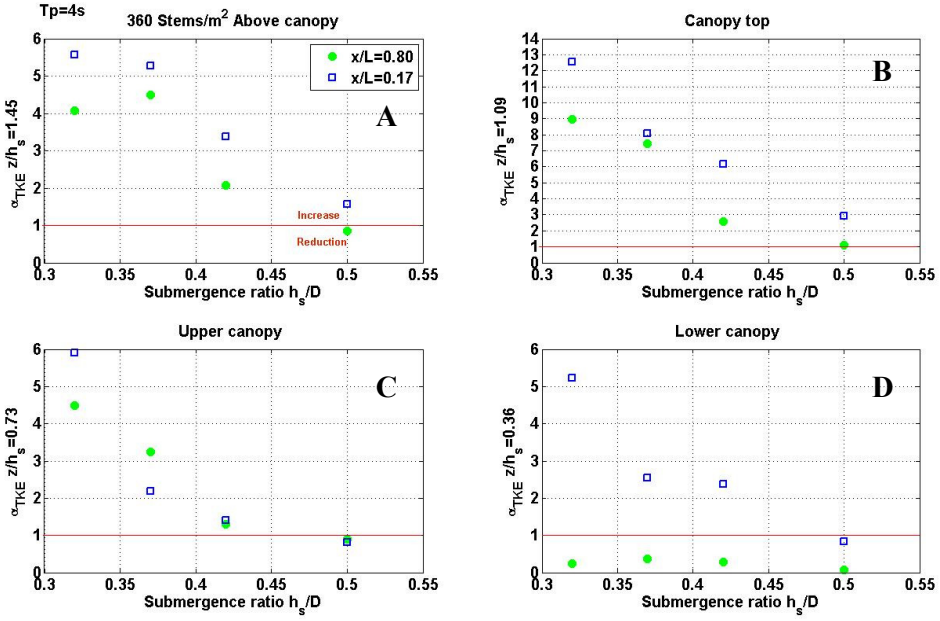

Figure 5.33 Normalised values of turbulent kinetic energy (α_{TKE}) at various elevations (plots A-D) plotted for tests with different submergence ratios Different symbols represent the two x/L locations. Tests with 360 stems/m^2, T_p=4 s and H_0=0.45±0.02 m.

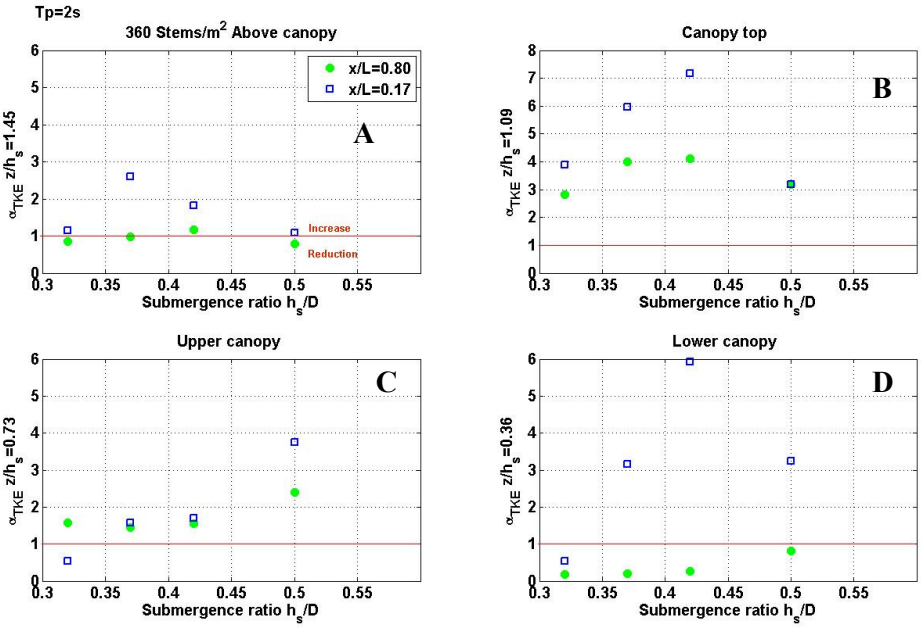

Figure 5.34 Normalised values of turbulent kinetic energy (α_{TKE}) at various elevations (plots A-D) plotted for tests with different submergence ratios Different symbols represent the two x/L locations. Tests with 360 stems/m^2, T_p=2 s and H_0=0.39±0.03 m.

Interestingly, for values of orbital amplitude less than 0.20 m, TKE levels above the canopy were comparable to those in front of the leading edge (at X/L=0.80, far from the edge of the patch, which is generally a more turbulent location, see Figure 5.31A

and Figure 5.32A. This pattern indicates that, for small amplitude waves the turbulence levels in the water column above the canopy (z/h_s=1.45) are not affected by the presence of the canopy.

The flow inside the canopy was measured by electromagnetic current-meters (EMCMs), as the ADV measurements would be affected by the presence of the leaves of the mimics (see Chapter 4). The ADVs have a smaller sampling volume than the EMCMs and are able to measure turbulence levels of the smaller vortices that the EMCM might not detect. For this reason turbulence intensities could be under-predicted within the canopy. Nevertheless, the EMCMs often measured higher turbulence levels in the upper canopy than in front of the patch, whilst in the lower canopy the values were much reduced; this became more apparent farther downstream.

A few measurements exist in the published literature on turbulence within canopies generated by waves. Most studies confirm a reduction of turbulence intensities inside canopies. Importantly, in a wave-exposed *Posidonia oceanica* meadow, near-bed turbulence (at 10 cm from the bed) was found to be reduced significantly with respect to the turbulence outside the meadow [*Granata et al.*, 2001], similarly wave turbulence was reduced in coral canopies [*Lowe et al.*, 2008]. Despite possible differences amongst the instruments, the peak in turbulence at the top of the canopy is a significant and consistent feature of the tests. It has been observed also in previous studies of seagrass under long waves [*Verduin and Backhaus*, 2000], as well as above coral canopies [*Reidenbach et al.*, 2007; *Lowe et al.*, 2008].

For waves with large orbital (and period) amplitude, turbulent energy induced by the presence of the canopy was greatest for low submergence ratios (h_s/D) and it increased for high submergence ratios. This conclusion is in agreement with the findings for vegetated beds under unidirectional flows [*Nepf and Vivoni*, 2000]. The Nepf and Vivoni study found that the vertical exchange zone, defined as the region influenced by the highly turbulent layer that forms at the top of the canopy, extends progressively into the canopy as the submergence ratio (h_s/D) decreases. This might be the case for the largest waves; however, this does not apply to artificial *Posidonia* canopies, under small amplitude waves (Figure 5.34).

5.5.2 Reynolds stresses and shear coefficient at the canopy top

The bi-dimensional turbulence stresses (<U'W'>, <U'U'>and <W'W'>) in the *xz* plane were derived using Eq. 5-12, as a function of wave phase (see as an example in

Figure 5.35). It is clear that the vertical variation in Reynolds stresses was very large and a constant stress layer (see Chapter 2) does not exist in *Posidonia* canopies under waves.

The vertical distribution of the maximum values of <U'W'> was analysed further in order to observe changes in the Reynolds stress between the different test conditions and locations along the patch. The peak in the vertical profile of the Reynolds stress term <U'W'> was at z/h_s=1.09 (i.e. just above the canopy), for all of the tests. Some typical profiles of the maximum value of the phase-averaged <U'W'> are shown in Figure 5.36 for a patch density of 360 stems/m^2 and a constant submergence ratio. It was observed also that, for the tests with small A, the value of <U'W'> at z/hs=1.45 (20 cm above the canopy top) was very small; it was comparable to that measured in front of the patch. For a higher A <U'W'> (representing the shear across the xz plane, see Chapter 2), it was considerably higher. The values of $<U'W'>_{rms}$ at h_s/D=1.09 are assumed to be equivalent to the shear stress at the canopy-water interface.

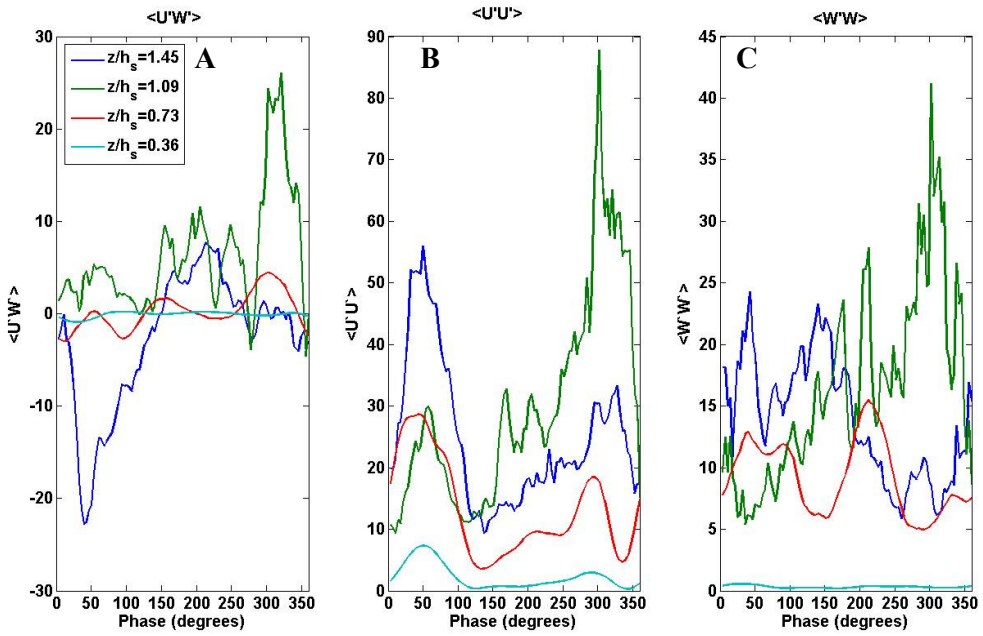

Figure 5.35 Bi-dimensional turbulence stresses <U'W'> (A), <U'U'> (B) and <W'W'> (C), as a function of wave phase at x/L=0.80. Test 31 (T_p=3 s, H_0=0.43 m, h_s/D=0.42 and density =360 stems/m^2).

The <U'W'> measured at the canopy top was normalised against the square of the free-stream orbital velocity value predicted from the local wave parameters applying Stoke's second order theory (U_{free}^2).

The values of $<U'W'>_{max}/U_{free}^2$ at the canopy top (from the tests with density 360 stems/m^2), were large both at x/L=0.17 (Table 5-1), ranging between 0.0028 and 0.041, and at x/L=0.80 (ranging between 0.0058 and 0.061). Conversely, at an equivalent elevation on the control profile, they were small (between 0.0004 and 0.0057) and showed little variation amongst the different tests.

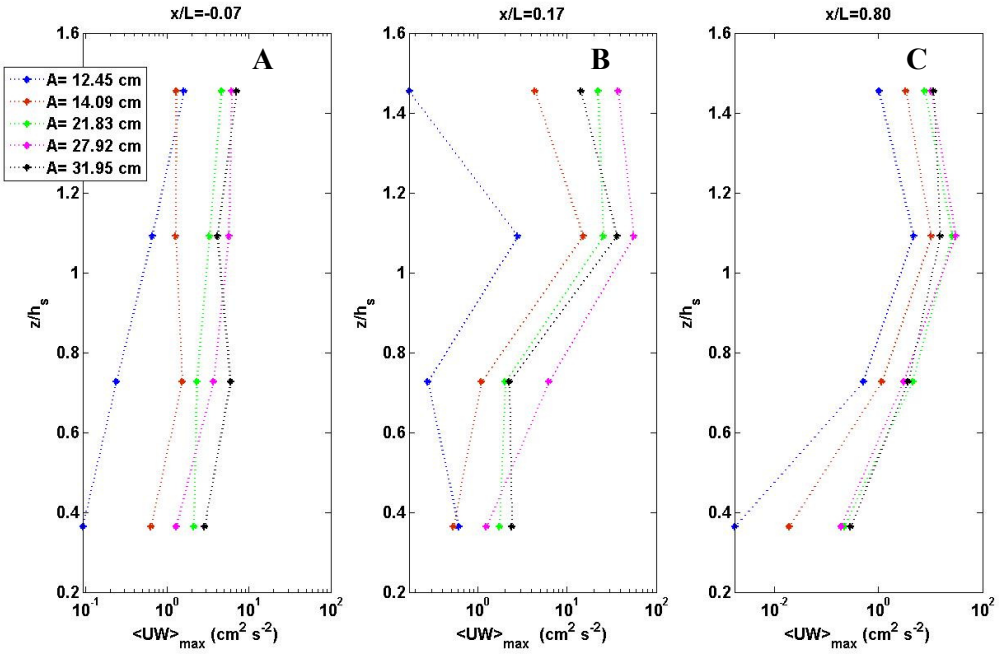

Figure 5.36 Vertical profiles of maximum phase-averaged shear stress, at different locations along the flume (tests with 360 stems/m^2; h_s/D=0.42) at x/L=-0.07 (A); at x/L=0.17 (B); and at x/L=0.80. Note: the different scales on the x axis .

Canopy density has a significant effect on the above-canopy shear stresses: the shear stresses produced above a canopy with 360 stems/m^2 was about 3 times larger than that created by a canopy with half this density (and as much as 4.5 times greater near the canopy edge). For the tests with lower mimic densities (180 stems/m^2), the normalised stress $<U'W'>_{max}/U_{free}^2$ was much lower than that found for tests with 360 stems/m^2 (the range of values were 0.0017-0.018 at x/L=0.17 and 0.0018-0.019 at x/L=0.80). The normalised shear stress values measured were within the range of those measured above coral canopies [*Reidenbach et al.*, 2007; *Lowe et al.*, 2008].

An estimate of the shear stress coefficient (C_f) at the canopy top was obtained from the normalised Reynolds shear stress, by combining Eq 2-31 and 2-32 (see Chapter 2). For the tests with a plant density of 360 stems/m^2, C_f was an average of 0.041±0.0041 at x/L=-0.017 and 0.046±0.0036 at x/L=0.80 (see plot, in Appendix C). For the tests with 180 stems/m^2, the values of C_f were 0.009±0.0010 at x/L=-0.017 and 0.016±0.0012 at x/L=0.80 (Table 5-6 and Figure C. 6 in Appendix C).

Table 5-6 Normalised shear stress and shear stress coefficient at the top of the canopy (z/h_s=1.09), at x/L=0.17 and x/L=0.80 for each test

Test	Stems/m^2	h_s/D	Tp	<U`W`>/U$^2_{free}$ x/L=0.17	<U`W`>/U$^2_{free}$ x/L=0.80	c_f x/L=0.17	c_f x/L=0.80
1	360	0.32	3	0.0405	0.0164	0.0809	0.0328
2	360	0.32	4.5	0.0402	0.0507	0.0804	0.1014
5	360	0.32	2	0.0157	0.0102	0.0314	0.0205
19	360	0.37	2	0.0118	0.0120	0.0235	0.0241
22	360	0.37	4	0.0253	0.0501	0.0507	0.1003
23	360	0.37	3	0.0352	0.0388	0.0705	0.0776
24	360	0.37	4	0.0413	0.0613	0.0826	0.1226
29	360	0.42	2	0.0028	0.0058	0.0055	0.0116
30	360	0.42	3	0.0161	0.0149	0.0322	0.0298
31	360	0.42	3	0.0130	0.0287	0.0260	0.0573
33	360	0.42	3.5	0.0307	0.0219	0.0614	0.0438
34	360	0.42	4	0.0109	0.0060	0.0219	0.0120
36	360	0.5	2	0.0055	0.0070	0.0110	0.0140
37	360	0.5	3	0.0116	0.0149	0.0231	0.0297
41	360	0.5	4	0.0084	0.0075	0.0169	0.0150
48	180	0.32	2	0.0027	0.0074	0.0054	0.0148
49	180	0.32	3	0.0044	0.0151	0.0089	0.0301
50	180	0.32	3	0.0072	0.0083	0.0143	0.0166
51	180	0.32	4	0.0072	0.0189	0.0145	0.0379
52	180	0.32	3.5	0.0108	0.0176	0.0215	0.0353
53	180	0.32	4	0.0059	0.0124	0.0119	0.0248
54	180	0.32	2.3	0.0046	0.0025	0.0093	0.0049
67	180	0.37	2	0.0017	0.0018	0.0033	0.0035
68	180	0.37	3	0.0051	0.0046	0.0102	0.0091
69	180	0.37	3	0.0051	0.0084	0.0101	0.0169
70	180	0.37	4	0.0058	0.0057	0.0117	0.0113
72	180	0.37	4	0.0044	0.0163	0.0089	0.0325
75	180	0.42	2	0.0022	0.0027	0.0043	0.0055
76	180	0.42	3	0.0025	0.0074	0.0049	0.0147
77	180	0.42	3	0.0050	0.0100	0.0099	0.0200
79	180	0.42	3.5	0.0088	0.0126	0.0176	0.0253
80	180	0.42	4	0.0042	0.0047	0.0085	0.0093
81	180	0.42	2.3	0.0018	0.0042	0.0035	0.0083
93	180	0.5	2	0.0022	0.0033	0.0044	0.0066
94	180	0.5	3	0.0050	0.0131	0.0101	0.0262
96	180	0.5	4	0.0041	0.0020	0.0082	0.0040
99	180	0.5	2.3	0.0030	0.0047	0.0060	0.0094
100	180	0.5	2	0.0021	0.0031	0.0043	0.0062

The shear coefficient is an order of magnitude lower than the drag coefficient ($0.320<C_d<1.737$) and the wave energy dissipation factors ($0.128 <f_e<1.676$). These results are consistent also with observations from previous studies [*Lowe et al.*, 2008].

5.6 Concluding remarks

Posidonia mimics affected significantly the propagation of monochromatic waves under all of the conditions tested. A wave height decay of up to 35% was found, which was larger for the denser meadow. Wave height decay was more pronounced for the shorter waves (high density configuration) and the largest submergence ratios. Wave reflection, induced by the meadow and the flume, was estimated to be on average 7%; this could be, in part, responsible for some local variation in wave heights measured along the patch (Mendez and Losada, 2004). In some of the tests, wave height decayed exponentially with distance from the leading edge, whilst decay coefficients (k_i) for these tests varied between 0.34 and 0.0120. These values are within the upper range of values found for seagrass beds in the field, in less energetic conditions [*Bradley and Houser*, 2009]. The drag coefficients varied between 0.25 and 1.37 and, as in previous studies, decreased with increasing Re_v [*Kobayashi et al.*, 1993; *Mendez et al.*, 1999; *Bradley and Houser*, 2009].

The periodic components of the flows created by the regular waves were reduced inside the canopy, whilst the reduction increased exponentially with wave orbital amplitude A. This pattrn has been observed also in other very rough beds (Lowe, 2005), but never for flexible vegetation mimics. The average reduction in oscillatory flow, at the canopy edge in the lower canopy, was 4% or 12 % (for stem densities of 180 and 360 stems/m^2, respectively); it increased to 54%-58% inside the patch (for stem densities of 180 and 360 stems/m^2, respectively). As presented in the publication produced in collaboration with the project partners, *Stratigaki et al*., [2009b] and *Stratigaki et al.,* [accepted], flow reduction was found to be largest for the denser canopy and for the highest submergence ratio. Under high submergence ratios and longer wave period, the canopy seemed to produce larger flow intensification above the canopy. In the lower canopy, the reduction from the free-stream was at least 5 times larger inside the patch at x/L=0.80, than near the edge of the canopy. This observation

demonstrates the importance of the "distance travelled" through the meadow in near-bed oscillatory flow attenuation.

Flow intensification was located mostly at the canopy/water interface z/h_s=1.09. Flow intensification at the canopy top has been observed for other seagrass species [*Verduin and Backhaus*, 2000; *Wallace and Cox*, 2000] and was not attributed to leaf movement [*Backhaus and Verduin*, 2008]. Interestingly, for the smallest orbital amplitudes (A< 15 m), flow intensification did not occur at the canopy top, but below it. The peak oscillatory flow was also larger than the flow predicted by wave theories and measured near the surface This oscillatory flow peak was observed both at the crest and trough of the waves, and therefore appears similar to the "overshoot" (the peak in the vertical distribution of horizontal velocity, as defined by Nielsen, 1992) observed at the top of wave boundary layers over sandy beds, except that the overshoot on sand is located much closer to the bed. Also, similar to a typical harmonic wave boundary layer, the velocities inside the canopy were ahead of the free stream velocities except at very small values of A. The phase shift and overshoot were larger for the denser meadow; therefore, it might have been related to the canopy characteristics (hydraulic roughness), as well as the wave orbital amplitude. According to classic wave boundary layer theory applied to sandy or rippled beds [*Sleath*, 1984; *Nielsen*, 1992], the characteristics of the wave boundary layer depend (for a certain flow regime) not only on the hydraulic roughness (r), but also on the wave orbital amplitude.

In classic wave boundary layer theory, the thickness of the wave boundary layer is generally larger than the hydraulic roughness length and for a constant hydraulic roughness (r), it increases with A (Sleath, 1987). The height at which the "overshoot" takes place is an indication of the boundary layer thickness [*Jensen et al.*, 1989] as shown in Figure 2.4 of Chapter 2. From the horizontal orbital velocity profiles, there is evidence that the overshoot elevation co-varies with A. The wave dissipation factor (f_e), obtained from wave height decay, decrease with increasing A, confirming these conclusions. Seagrass beds under waves and currents were found to move the boundary layer upwards [*Bryan et al.*, 2007], but there have not been any published data for wave-only conditions. Moreover, these findings indicate that thte classic wave boundary layer theory may be applied to understand hydrodynamic processes in vegetated beds, over the range of conditions tested. For the range of Reynolds numbers tested, the roughness r depends only on the canopy characteristics and can be used to predict wave friction factors (f_w). This result is supported by evidence from studies undertaken on canopy

effects on unidirectional flows, where roughness length (Z_o, the vertical length scale for current boundary layers) was dependent only upon the canopy characteristics [*Neumeier*, 2007]. This result is quite surprising as the response of the mimics (and therefore r) to waves was expected to vary with wave period as the mimics' oscillation and amount of bending could depend on the frequency of the waves. For example, when the wave frequency was equal to that of the natural oscillation of the mimic, a phenomenon similar to resonance occurs in macroalgae (See Gaylord, 2003) affecting greatly the roughness created by the canopy.

Hydraulic roughnesses for this artificial *Posidonia* patch were in the range of those found for other seagrasses [*Bradley and Houser*, 2008] as reported in Table 2.2 of Chapter 2. In the present study, the canopy hydraulic roughness was much larger than expected values for sandy beds, as has been observed in *Posidonia* meadows under unidirectional flows (Gacia and Duarte, 2001). The hydraulic roughness length was found to be a fraction of the canopy height and to be dependent upon the canopy element spacing and to be equal to 0.23 m and 0.15 m for the 360 stems/m^2 and 180 stems/m^2 configurations, respectively.

As for the horizontal component of the oscillatory velocities, the vertical component of the orbital velocity was reduced largely both above and inside the canopy, but the reduction was not related to canopy characteristics or hydrodynamic conditions. The vertical components of turbulence, on the other hand, were enhanced mostly inside the canopy, especially near the leading edge. In some tests, horizontal turbulence intensity (U') was higher inside the canopy than outside the meadow (near the edge of the canopy), as has been observed for salt marshes [*Neumeier*, 2007]. But further inside the canopy, U' was dampened, confirming field evidence on natural *Posidonia oceanica* beds [*Granata et al.*, 2001]. An area of high turbulence was observed near the canopy top, as observed with previous studies on current-vegetation interaction [*Neumeier and Amos*, 2006b] and seagrasses exposed to long waves [*Verduin and Backhaus*, 2000].

Turbulence in oscillating canopies is produced both by drag and by the mimic movements [*Nepf and Ghisalberti*, 2008]; it is re-scaled and also dissipated [*Neumeier and Amos*, 2006b]. Hence, the assumption of a balance between production and dissipation of turbulent energy, within the boundary layer, is not valid; it is difficult to estimate a value of the shear stress at the bed (using the TKE method, see Chapter 2). Moreover, the location of the bed is difficult to establish, as for mobile sediment beds [*Nielsen and Guard*, 2010]. Shear stresses were evaluated at canopy/water interface

where the peak of turbulence intensities was found in all tests. This area is known also to be an area of high turbulence and turbulence production, under unidirectional flows [*Ghisalberti and Nepf*, 2006]. The canopy shear at the canopy-water interface is opposite to the canopy drag, and this results in vertical exchanges between the canopy and the water mass above [*Ghisalberti and Nepf*, 2006]. A layer of intense turbulent exchanges might exist in the canopy top region as has been found for rigid canopies exposed to waves [*Reidenbach et al.*, 2007; *Lowe et al.*, 2008]. In the present work, the turbulent kinetic energy induced by the presence of the canopy (and the Reynolds shear stress at the top of the canopy) increased slightly for the tests with a smaller submergence ratio indicating that a turbulent mixing layer might be more pronounced in deeper waters, as has been found for vegetation exposed to steady flows [*Nepf and Vivoni*, 2000]. This pattern is valid only for the large amplitude waves (A>0.20 m), whilst it does not apply for small amplitude waves. The shear coefficient at the canopy top was larger than that of coral canopies [*Lowe et al.*, 2008] and, as for coral, it was an order of magnitude smaller than the drag coefficient or the wave dissipation factor. These findings suggest that, especially for small waves and for high submergence ratios, shear is not an important driver of flows through the canopy, i.e. drag dominates.

Posidonia canopies reduce oscillatory flows and may be considered as a more sheltered environment than bare sand areas, but the high level of turbulence in the vertical and the high peaks of turbulence observed, even deep inside the canopy, still allows exchanges with the overlying water column, even in the lower part of the canopy. These vertical exchanges are important for ecological processes and sediment motion inside the canopy, as predicted for other seagrass species [*Koch et al.*, 2006a].

6 Chapter 6: Effects of artificial *Posidonia oceanica* on spectral waves and flows

6.1 Introduction

Results from a series of large-scale flume experiments, undertaken on wave propagation over artificial *Posidonia oceanica* seagrass performed with spectral waves, are presented and discussed in this Chapter. The methods used in the analysis of the flow and wave data-sets are covered in Section 6.2 (Chapter 4 presents details on the setup of the experiments). In Section 6.3 wave energy dissipation is analysed. Wave energy dissipation varies amongst the different components of the wave spectrum [*Madsen et al.*, 1988]: this is a finding observed over coral reefs [*Lowe et al.*, 2005a] and seagrass beds in low energy environments [*Bradley and Houser*, 2009]. For this reason, wave dissipation at each component of the spectrum was analysed (Section 6.3.2), deriving a frequency-dependent wave dissipation factor.

Drag coefficients, friction factors representative of specific wave conditions and canopy configurations, were calculated at the most energetic frequencies (Sections 6.3.4 and 6.3.5). An estimate of the spectral roughness of *Posidonia oceanica* meadows was obtained, using the model used successfully for regular waves (Chapter 5), based upon *Nielsen*'s [1992] empirical friction factor formula.

The changes induced by the canopy to the orbital velocities were analysed in Section 6.4, both in terms of a frequency-dependent attenuation parameter (within the canopy) and as a representative value (at the peak frequency) for each test. The effects of canopy density and canopy submergence ratio, both on wave height decay and on in-canopy spectral orbital velocity attenuation, are described. These parameters are known to affect wave dissipation in other vegetation canopies [*Fonseca and Cahalan*, 1992; *Mork*, 1996; *Bouma et al.*, 2005; *Koch et al.*, 2006a]; they influence also canopy-induced flow reduction under unidirectional flows [*Fonseca and Fisher*, 1986; *Gambi et al.*, 1990; *Neumeier and Ciavola*, 2004; *Thompson et al.*, 2004].

The findings are summarised and conclusions are drawn in Section **Error! Reference source not found.**. The results are compared with those from the regular wave experiments (see Chapter 5) and from the literature. Some of the findings presented in this Chapter have been published by the author, in a peer-reviewed publication [*Manca et al.*, 2010; included in Appendix D].

6.2 Data Analysis: Irregular wave tests

6.2.1 Wave data

The wave data were quality checked and de-spiked using the same protocol as for regular waves, in Chapter 5. The data were filtered with a simple rectangular hi-pass cut at frequencies (f_{cut}) between 0.12 and 0.2 Hz. The value of f_{cut} depended upon the test conditions (see Table 6-1 and Chapter 4, for details) and was used to cut-off a small energy peak in the low frequency components of the spectrum. This peak carried energy corresponding to long waves (which were negligible compared to the energies of the main spectrum), with a typical peak period of 20 s, and were considered to be induced by seiching in the wave flume. Therefore, this can be considered as an unwanted laboratory effect (see Chapter 4 Section 4 88); filtering is a common procedure to eliminate this type of effect [*Hughes*, 1993; *Kamphuis*, 2002].

Wave spectra (S_j) were estimated from the water surface elevation time series ($\xi(t)$), with the classic fast Fourier transform, by applying a Welch's modified periodogram approach [*Kamphuis*, 2002]. A window length of 480 samples with 50% overlap of the windows appeared to be the best "trade off" between resolution and smoothing of the spectra.

Table 6-1 Cut-off frequencies (f_{cut}) used in the wave and current data filtering

Test Target T_p (s)	Cut off frequency (Hz)
2	0.2
2.3	0.2
3	0.2
3.5	0.16
4	0.12

The wave spectral parameters were obtained from the wave spectral density, as described in Chapter 3. Wave height decay along the flume was obtained by

normalizing the measured wave height (H) to the wave height (H_0) measured in front of the patch (at x/L=-0.046) as was done for the regular wave tests. The wave height decay induced by the flume bed and the sidewalls was negligible as discussed in Chapter 5. Wave reflection was estimated with the method of *Mansard and Funke* [1980], as described in Chapter 5.

Since wave energy can be dissipated at different rates amongst the different spectral components (Madsen, 1994), wave dissipation was investigated at all components of the wave spectra following *Madsen et al.*'s [1988] approach. This method has been successfully used in the field and in flume tests over rigid and rough, submerged canopies [*Lowe et al.*, 2005a; *Lowe et al.*, 2007]. Assuming that all waves of all frequencies propagate in the same direction along the flume, wave energy dissipation rate per unit area ($\varepsilon_{f,j}$) for the jth component of the wave spectra is equal to:

$$\frac{\Delta F_j}{\Delta x} = -\varepsilon_{f,j} \qquad \textbf{Eq. 6-1}$$

$$E_j = \frac{1}{2}\rho g a_j^2 \qquad \textbf{Eq. 6-2}$$

Where $F_j = E_j Cg_j$ **Eq. 6-3**

is the wave energy flux, and Δx is the distance between the wave gauges. E_j is the wave energy density and Cg_j is the group velocity for the same spectral component j, obtained assuming:

$$Cg_j = \frac{1}{2}\frac{\omega_j}{k_j}\left[1 + \frac{2k_j D}{\sinh 2k_j D}\right] \qquad \textbf{Eq. 6-4}$$

with ω_j the radian frequency ($2\pi f_j$) and k_j the wavenumber ($2\pi/\lambda_j$) at the jth frequency component. The wave amplitude for each frequency was calculated from the wave spectrum (S_j) using:

$$a_j = \sqrt{2S_j \Delta f_b} \qquad \textbf{Eq. 6-5}$$

where Δf_b is the discrete frequency bandwidth. Each spectral component of the wave energy dissipation factor ($f_{e,j}$) can be obtained from the component of the rate of energy dissipation $\varepsilon_{f,j}$ as:

$$f_{ej} = \frac{4\varepsilon_{f,j}}{\rho U_j^2 U_r} \qquad \textbf{Eq. 6-6}$$

With U_j the frequency-dependent horizontal orbital velocity calculated from the local wave spectra as:

$$Ub_j = \frac{a_j 2\pi}{T_j \sinh k_j D} \qquad \textbf{Eq. 6-7}$$

Eq. 6-7 Assumes linear wave theory to be valid.

U_r, the representative wave-induced velocity, was calculated, from the local wave spectrum S_j and defined as:

$$U_r = \sqrt{2}\sqrt{\sum_j \left(S_j \Delta f_b \frac{4\pi^2}{T_j \sinh^2 k_j D} \right)} \qquad \textbf{Eq. 6-8}$$

The representative wave orbital velocity (U_r) is equivalent to the root mean square (RMS) value of the orbital velocity [*Wiberg and Sherwood*, 2008].

6.2.2 Velocity data

The measured velocity data were quality checked and de-spiked using the phase-space method [*Goring and Nikora*, 2002], as described in Chapter 5. The data from the ADVs were synchronised with the EMCMs and the wave data. The initial and final part of the time-series were eliminated, as explained in Chapter 5. The raw data were filtered with the same high-pass filters described in Section 6.2.1. The frequency range of the raw data was 0 to 10 Hz (the Nyquist frequency, half the sampling frequency, was 10 Hz). However, the energy contained at frequencies higher than 1 Hz was always small, and the analysis of the wave-induced flows focussed upon the most energetic part of the spectra (Figure 6.1).

Benilov and Filyushkin's [1970] method was used to separate $U_w(t)$, the wave-induced flow, from the total de-meaned velocity signal (U(t)). The de-meaned measured horizontal velocity time-series (U(t)) can be considered as a random process and expressed as the sum of random turbulent fluctuations and the wave-induced flows [*Benilov and Filyushkin*, 1970]. This method is based upon the concept that the signal $U_w(t)$ is highly correlated to the water oscillation signal ($\xi(t)$), whilst the random fluctuations $U'(t)$ are not correlated to $\xi(t)$ and are taken as the turbulent component of the flow (although they also contain some noise induced by the measuring methods). The method requires the calculation of the spectrum of U(t), the horizontal velocity time-series (SU), the spectrum of $\xi(t)$, the surface elevation time-series, ($S\xi$) as well as their cross-spectra ($XSU\xi$) to obtain the parameter γ_w^2 (the coherence of the signals) which is defined as:

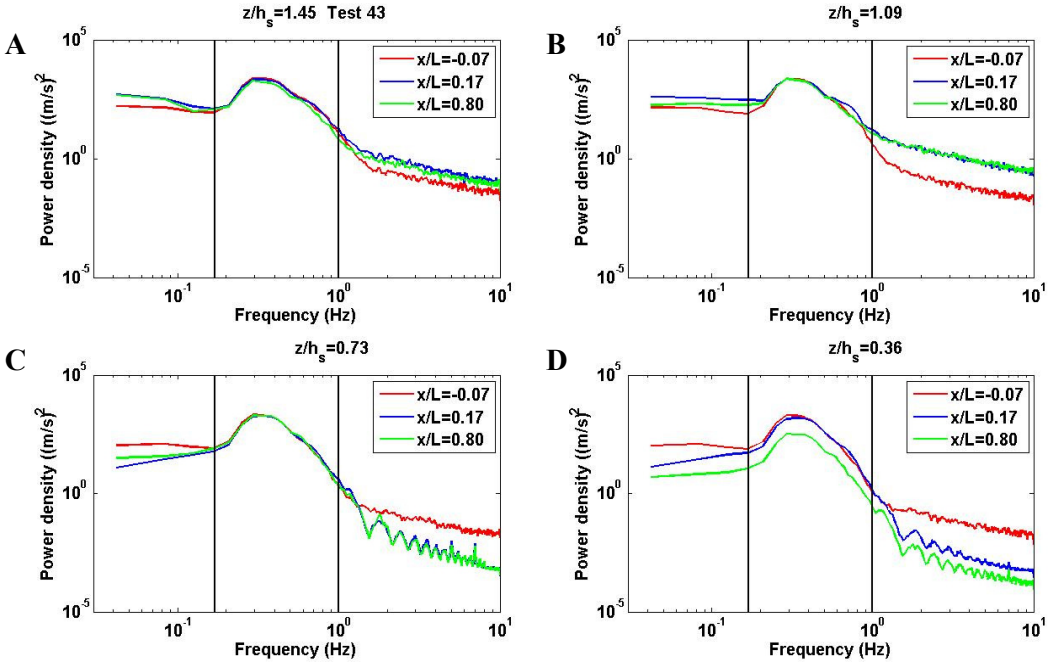

Figure 6.1 Power spectra of the raw velocity data at all four relative elevations (h_s/D) from the bed (A-D). The analysis concentrated upon the most energetic component of the velocity spectra (between the vertical lines).

$$\gamma_w^2 = \frac{XSU\xi^2}{SU \cdot S\xi} \qquad \textbf{Eq. 6-9}$$

The parameter γ_w^2 was then used to separate the two velocity components (mean and wave-induced) and to obtain their spectra:

$$SU_w = \gamma_w^2 SU \qquad \textbf{Eq. 6-10}$$

SU_w is the power spectral density of the wave-induced component of the measured velocity.

$$SU' = (1-\gamma_w^2)SU \qquad \textbf{Eq. 6-11}$$

SU' is the power spectral density of the turbulence-induced fluctuations in velocity. An example of the application of this method is shown in Figure 6.2, where the spectra of the velocity and the wave data measured in front of the patch (x/L=-0.07) are plotted for an example test. The values of SU_w and $S\xi$ are clearly correlated, whilst SU' values are typically 2 or 3 orders of magnitude smaller than the SU_w; furthermore, they are clearly not correlated to the wave signal. The wave-induced velocity spectral densities were calculated for all tests, at all elevations and x/L locations, in front of and along the patch.

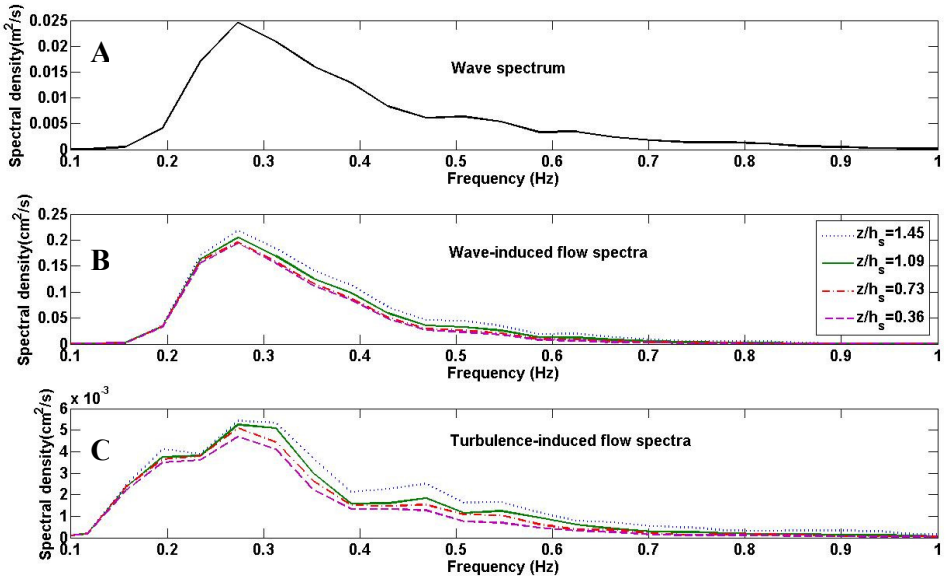

Figure 6.2 Spectral densities plotted as a function of wave frequency. The wave spectra (A) compared to the spectra of the wave-induced velocity (B) and the spectra of the turbulent component (C). Note: different scales of the vertical axes) for test 44 at x/L=-0.07 (Tp= 3.7 s, H_0=0.30 m, h_s/D=0.50 and 360 stems/m^2). Different colours represent spectral densities at different elevations above the bed.

To evaluate the frequency-dependent changes in the flow induced by the canopy, the spectrum of the wave-induced velocity (SU_{jL}) was compared with the spectra of the wave-induced velocity, measured in front of the leading edge of the patch (SU_{jL}^0), in the lower canopy. An attenuation parameter was calculated ($\alpha_j(x,z)$) for each frequency component of the spectrum (Eq. 6-12), both at x/L=0.80 and at x/L-0.17, near the patch edge:

$$\alpha_j = \frac{SU_{jL}}{SU_{jL}^0} \qquad \textbf{Eq. 6-12}$$

A theoretical spectral attenuation coefficient was calculated outside the patch, at x/L=-0.07 (α_j^0), for comparison, using the velocity data measured in the same position near the water surface. This coefficient was calculated at each frequency of the spectrum, following a method similar to that developed for coral reefs [*Lowe et al.*, 2007]:

$$\alpha_j^{\,0} = \left(\phi^2{}_j \frac{SU_{jL}^0}{SU_{jH}^0} \right)^{0.5} \qquad \textbf{Eq. 6-13}$$

Where SU^0_{jH} and SU^0_{jL} are the wave-induced velocity spectra at z/L=-0.07 measured by the highest ADV (z=0.80 m corresponding to h_s/D=1.45) and the lowest ADV (z=0.20

m corresponding to $h_s/D=0.36$), respectively. The parameter ϕ_j is a correction factor that accounts for the predicted vertical increase of flow magnitude with distance from the flume bed. The factor ϕ_j was derived from linear wave theory [*Dean and Dalrymple*, 1991] and obtained by applying the following formulation:

$$\phi_j = \frac{\cosh(k_{jH})}{\cosh(k_{jL})} \qquad \textbf{Eq. 6-14}$$

where k_j is the wave number evaluated for each component of the spectrum. As all ADVs at this location (over a sandy bed) lie above the predicted height of the wave boundary layer, the value of α_j^0 should be 1 for all of the spectral components. The same approach was not applied to the data measured over the patch because the velocity measured by the upper ADV (z=80 cm) was (in some of the tests) affected by the presence of the patch below and cannot be considered to be representative of a free-stream velocity (U_∞). For each test, α_j and α_j^0 were calculated for the upper part of the canopy ($z/h_s=0.73$ m) and for the lower canopy ($z/h_s=0.36$ m).

Only the spectral frequencies containing most of the wave energy (95%) were considered (Figure 6.1). Considering all of the tests, the analysed frequencies ranged between 0.156 Hz and 0.70 Hz, corresponding to a range of wave periods, from 1.4 to 6.4 s.

A representative value of the spectral orbital velocities ($U_r(z)$) was obtained, by summing the contributions of each frequency component of the wave-induced velocity spectra (SU_j), defined as:

$$U_r(z) = \sqrt{2\sum_j SU_j(z)\Delta f_b} \qquad \textbf{Eq. 6-15}$$

It corresponds to the RMS value of the measured wave-induced velocity time-series [*Wiberg and Sherwood*, 2008].

6.3 Results and discussion: Waves and spectral wave dissipation

6.3.1 Preliminary observations

As in the regular wave experiments, only the data from the resistive wave gauges were analysed (see Chapter 5). A summary of the characteristic wave parameters

measured in front of the patch (x/L=-0.07) are presented in Table 6-2, for all the spectral wave tests.

Wave breaking did not occur in any of the irregular wave tests. Wave reflection was negligible. The wave reflection coefficient was on average 10, this was a similar value to the tests carried out with regular waves (7%).

Table 6-2 Wave parameters and vertically-averaged representative horizontal orbital velocity (Ur) measured at x/l=-0.07 for all spectral wave tests.

TEST	Density (stems/m^2)	Submergence ratio (h_s/D)	T_p (s)	H_0 (m)	Vertically averaged U_r (m/s)
9	360	0.32	1.97	0.22	0.09
10	360	0.32	3.20	0.33	0.21
14	360	0.37	1.97	0.23	0.11
16	360	0.37	3.20	0.34	0.23
17	360	0.37	3.66	0.30	0.22
18	360	0.37	4.27	0.27	0.21
25	360	0.42	1.97	0.22	0.13
26	360	0.42	3.20	0.32	0.26
27	360	0.42	3.66	0.29	0.25
42	360	0.50	1.97	0.22	0.16
43	360	0.50	3.20	0.33	0.29
44	360	0.50	3.66	0.30	0.27
55	180	0.32	1.83	0.22	0.09
56	180	0.32	3.20	0.34	0.21
57	180	0.32	3.66	0.30	0.20
59	180	0.32	2.56	0.25	0.12
61	180	0.37	1.97	0.22	0.10
63	180	0.37	3.20	0.33	0.23
64	180	0.37	3.66	0.29	0.22
65	180	0.37	4.27	0.26	0.20
66	180	0.37	2.33	0.25	0.14
82	180	0.42	2.13	0.21	0.13
83	180	0.42	3.20	0.32	0.26
86	180	0.42	2.56	0.24	0.16
88	180	0.50	1.97	0.21	0.16
89	180	0.50	3.20	0.31	0.29
90	180	0.50	3.66	0.28	0.27
92	180	0.50	2.33	0.24	0.20

6.3.2 Frequency-dependent wave dissipation

The frequency-dependent wave dissipation factor ($f_{e,j}$) was calculated for all of the tests, between the site in front of the leading edge of the patch (x/L=-0.07) and the

site over the patch, nearest to the leading edge (x/L=0.17). It was also calculated between x/L=0.17 and the site farther into the patch at x/L=0.80. Some examples of $f_{e,j}$ distribution with T_j are shown in Figure 6.3 to Figure 6.5 for tests with different wave conditions (but the same submergence and stem density). The largest values of $f_{e,j}$ were associated always with the site located nearest to the leading edge (x/L=0.17). Therefore, most wave energy was dissipated in the first few metres of the patch. The least energetic wave conditions (see, for example, Figure 6.3) produced the largest values of $f_{e,j}$, therefore, the largest spectral wave dissipation. Interestingly, in all of the tests, the frequency-dependent wave dissipation factor ($f_{e,j}$) was largest around the peak frequencies of the wave spectrum.

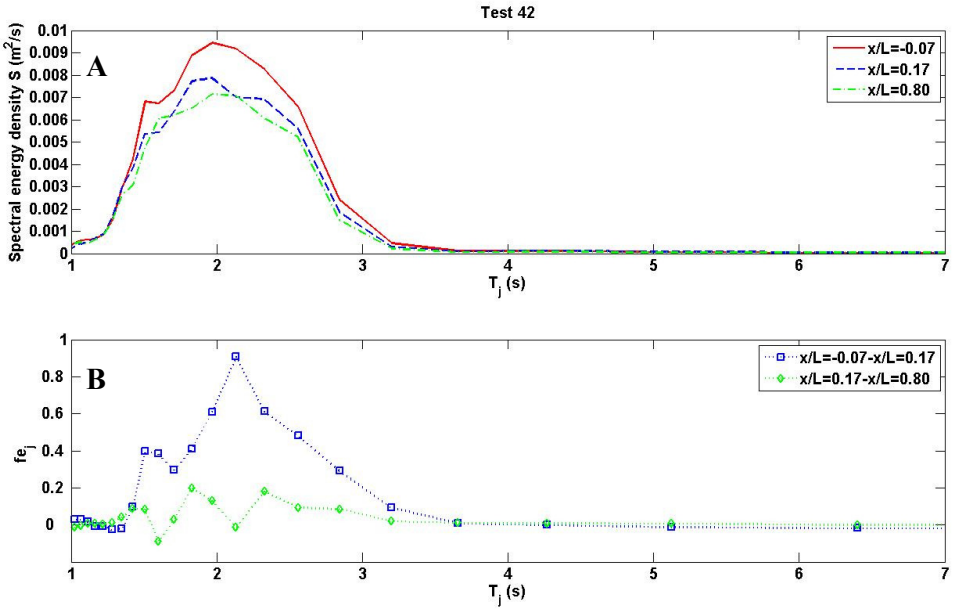

Figure 6.3 (A) Wave energy density spectra at x/L=-0.07 (in front of the patch), x/L=0.17 (over the patch, near the edge) and x/L=0.80 (over the patch). (B) The difference in the frequency-dependent wave energy dissipation factor ($f_{e,j}$) calculated between sites x/L=-0.07 and x/L=0.17 (blue squares) and between sites x/L=0.17 and x/L=0.80, (green diamonds), plotted at each component of the spectra. Test 42 (T_p=1.98 s, H_0=0.22 m, h_s/D=0.50 and 360 stems/m^2)

Moreover, in some of the tests a small energy peak was observed at wave periods less than the peak frequency (see for example Figure 6.3). A peak in $f_{e,j}$ was associated with these short spectral components, indicating that short waves were more easily attenuated by the canopy. These results are supported by field observations over natural mixed seagrasses [*Bradley and Houser*, 2009] under low energy conditions; from these, the authors concluded that waves at the longer periods were not affected by the seagrass and that preferential dissipation occurred at the peak frequency (1.3 s).

Also, over a barrier reef, the largest $f_{e,j}$ corresponded to the high frequency part of the wave spectrum (with peak periods ranging between 7 and 10 s) [*Lowe et al.*, 2005a]. In that study, the data were collected *in-situ* over about a week, and different types of waves (swell, storm waves and normal sea conditions) were recorded. Because simple Jonswap spectra were created in the present study, with just one main peak, the range of periods observed was limited.

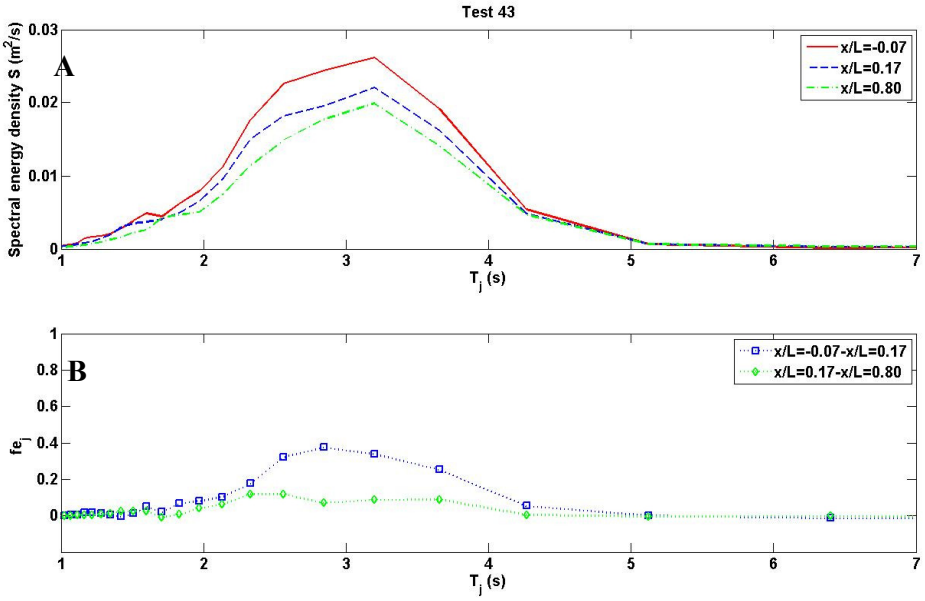

Figure 6.4 As for Figure 6.3; Test 43 (T_p= 3.2 s, H_0=0.33 m, h_s/D=0.50 and 360 stems/m^2)

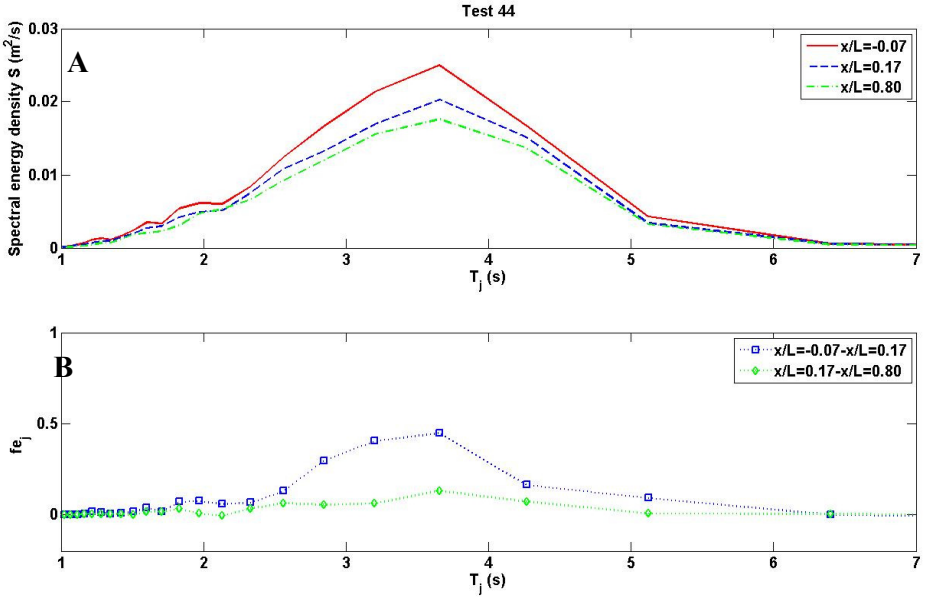

Figure 6.5 As for Figure 6.3; Test 44 (T_p= 3.7 s, H_0=0.30 m, h_s/D=0.50 and 360 stems/m^2)

The same pattern (greatest energy loss around the peak frequency) was observed when examining wave energy loss, defined by a simple analysis of the wave spectra ratios:

$$\frac{S_j(x)}{S0_j} \qquad \textbf{Eq. 6-16}$$

with $S0_j$ being the wave spectrum measured at x/L=-0.046 in front of the leading edge of the patch, as published by *Manca et al*. [2010, in Appendix D].

6.3.3 Wave Height decay along the patch

Wave height reduction (H/H_0) along the artificial seagrass patch was significant for all of the tests, with wave height decreasing with distance along the patch. In all of the tests, the wave height decay induced by the flume bed and the sidewalls was an order of magnitude less than the decay measured above the patch. Therefore, most of the wave attenuation could be attributed to the presence of the seagrass canopy, as observed for regular waves.

Wave height increased at the edge of the patch, especially for the test with the smallest submergence ratio (h_s/D); it started to decay after the first metre. The sudden step created by the edge of the patch might have been responsible for this local wave height increase, which was found also in the regular wave tests. The tests with the highest submergence ratio had the greatest wave height reduction (Figure 6.6).

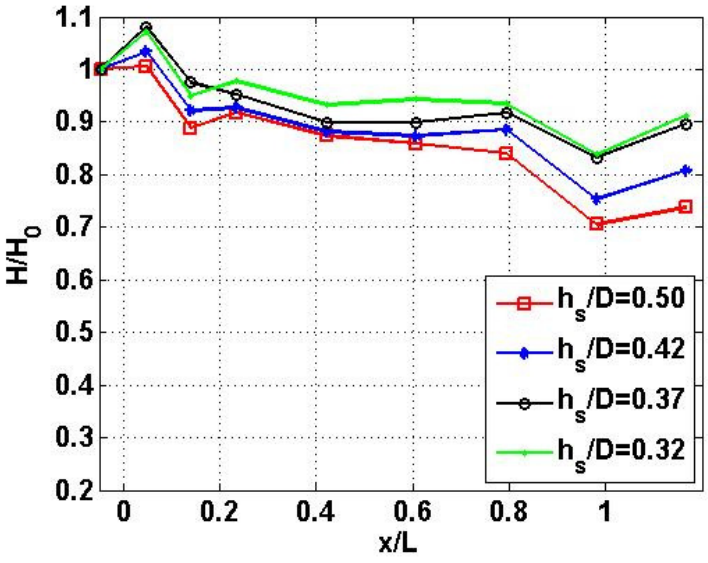

Figure 6.6: Effect of submergence ratio (h_s/D) on wave height decay along the seagrass patch. Tests 16, 26 and 43 (T_p=3.2 s, density 360 plants/m^2 and H_0=0.33±0.01 m).

A larger wave height decay was recorded for tests with 360 stems/m^2 than those with 180 stems/m^2. Figure 6.7 shows an example of the effect of stem density on wave height decay.

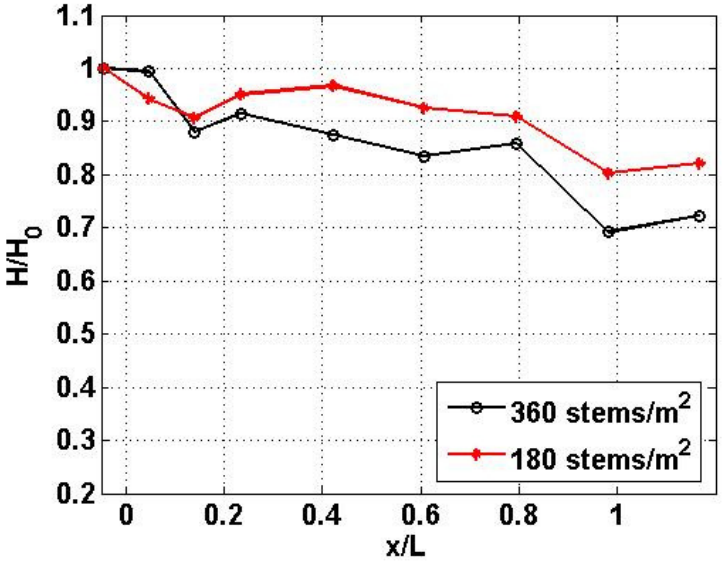

Figure 6.7: Effect of stem density on wave height decay along the seagrass patch. Tests 44 (H_0 =0.30 m, T_p=3.7 s and h_s/D=0.5) and test 90 (H_0=0.28 m, T_p=3.7 s and h_s/D=0.5).

The exponential wave height decay coefficient (k_i) was obtained from the spectral wave height decay, measured in each test by applying the exponential decay model as for regular waves. The parameter k_i ranged between 0.008 and 0.028; it was larger for the tests with 360 stems/m^2 (the average k_i=0.017), than for the tests with 180 stems/m^2 (the average k_i=0.011). Moreover, k_i increased with increasing submergence ratio for both of the stem densities (see Figure 6.8).

The value of k_i (Table 6-3) was in the range of those found in previous studies in natural seagrass beds [ranging between 0.004 and 0.02 in *Bradley and Houser*, 2009]. From these results, it is clear that spectral wave height attenuation was largest for the largest submergence ratio and for the denser canopy (for similar values of A), confirms the results obtained from the monochromatic wave dataset, presented by Stratigaki et al. [accepted], in Appendix D.

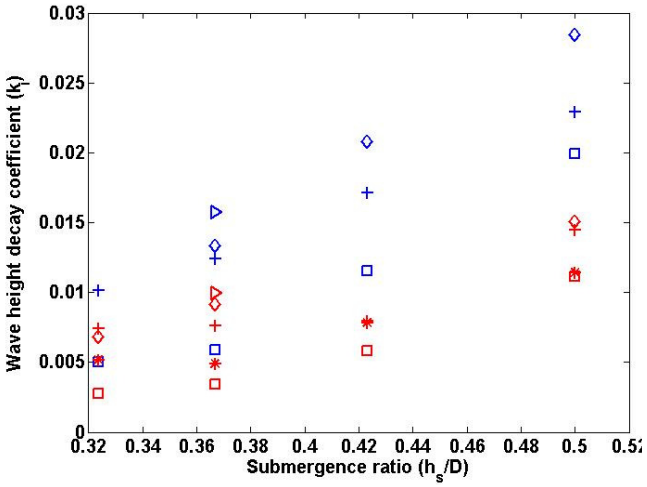

Figure 6.8 Effect of submergence ratio (h_s/D) and stem density on the wave height decay coefficient (k_i), for density=360 stems/m^2 (blue symbols) and density=180 stems/m^2 (red symbols). Different symbol types represent different spectral wave conditions.

Table 6-3 Spectral wave dissipation, drag and wave parameters calculated for all irregular wave tests: wave height at x/L=-0.046; R^2 coefficient for the wave decay exponential fit; decay coefficient (k_i), representative drag coefficient ($C_{d,r}$); Reynolds vegetation number (Re_v); Keulegan-Carpenter number (KC); orbital amplitude above the canopy (A);wave Reynolds number (Re_w); and wave dissipation factor($f_{e,r}$).

Test	H_0 (m)	R^2	k_i	$C_{d,r}$	Re_v	KC	A (m)	Re_w	$f_{e,r}$
44	0.30	0.91	0.028	0.689	4378	114.4	0.255	1.301E+05	0.434
43	0.33	0.89	0.023	0.449	4516	102.3	0.228	1.152E+05	0.421
42	0.22	0.87	0.020	0.489	2338	33.2	0.074	1.827E+04	0.811
25	0.22	0.83	0.012	0.550	1916	27.2	0.061	1.219E+04	0.538
27	0.29	0.82	0.021	0.796	3694	96.5	0.215	8.949E+04	0.545
26	0.32	0.80	0.017	0.539	3904	89.2	0.199	8.848E+04	0.500
17	0.30	0.67	0.013	0.727	3479	90.9	0.202	7.560E+04	0.417
90	0.28	0.67	0.015	0.740	4373	114.2	0.255	1.257E+05	0.264
18	0.27	0.67	0.016	1.061	3288	100.2	0.223	7.840E+04	0.484
64	0.29	0.67	0.009	0.996	3456	90.3	0.201	7.477E+04	0.351
9	0.22	0.66	0.005	0.817	1304	18.3	0.041	5.913E+03	0.929
16	0.34	0.65	0.012	0.559	3721	85.0	0.189	7.596E+04	0.365
83	0.32	0.65	0.008	0.487	4043	91.4	0.204	9.169E+04	0.246
63	0.33	0.62	0.008	0.684	3710	84.8	0.189	7.603E+04	0.284
65	0.26	0.62	0.010	1.341	3285	100.1	0.223	7.782E+04	0.333
89	0.31	0.60	0.014	0.583	4561	104.2	0.232	1.197E+05	0.251
88	0.21	0.59	0.011	0.561	2281	32.4	0.072	1.813E+04	0.520
10	0.33	0.59	0.010	0.682	3179	71.9	0.160	5.586E+04	0.741
57	0.30	0.58	0.007	1.015	3216	84.0	0.187	6.399E+04	0.426
56	0.34	0.54	0.007	0.940	3371	77.0	0.172	6.165E+04	0.363
14	0.23	0.50	0.006	0.478	1722	24.9	0.056	9.681E+03	-0.054
86	0.24	0.46	0.008	0.600	2571	45.7	0.102	2.708E+04	0.438
92	0.24	0.43	0.011	0.510	2912	49.1	0.109	3.313E+04	0.284
66	0.25	0.38	0.005	0.606	2173	36.1	0.080	1.697E+04	0.474
55	0.22	0.34	0.003	0.915	1298	18.0	0.040	5.170E+03	-0.311
82	0.21	0.32	0.006	0.538	1999	29.8	0.066	1.321E+04	0.508
61	0.22	0.24	0.003	0.606	1606	22.6	0.050	8.661E+03	0.446
59	0.25	0.12	0.005	1.013	1927	32.4	0.072	1.449E+04	1.372

6.3.4 The drag coefficient

A representative drag coefficient ($C_{d,r}$) was quantified from the wave height decay coefficient (k_i) using *Dalrymple*'s rigid model [1984] (as described for regular waves), for all the irregular waves tests for which the exponential decay model was considered to be applicable (R^2>0.60). The representative drag coefficients for each test are presented in Table 6-3 and plotted in Figure 6.9, against the Reynolds vegetation number (Re_v). The parameters $C_{d,r,}$ Re_v, A and KC (Table 6-3) are mean values, obtained from the measured wave data along the patch (as described in Chapter 5), spatially averaged. $C_{d,r}$ ranged between 0.45 and 1.34 for Re_v between 1915 and 4560.

The data presented here were calculated at the peak frequency. Wave energy decay was greatest around this frequency; therefore, it can be considered a peak value. The values of C_{dr} drived from the spectral dataset were close to the values of C_d found from regular waves tests, for Re_v>3000. However, the irregular wave dataset was divided in two groups: the data with T_p<=2.3 s and those with T_p>=3s (and Rev>3000).

For Re_v > 3000, the values of $C_{dr,}$ found in the present study, were larger than the published literature values, derived from tests on artificial kelp beds [*Kobayashi et al.*, 1993; *Mendez et al.*, 1999]. However, they were less than modelled values obtained considering swaying in a flexible vegetation canopy [hence ,a flow velocity relative to the seagrass blades, instead of an absolute flow velocity, *Mendez and Losada*, 2004]. Interestingly, the values of $C_{d,r}$ were much lower for Re_v < 2400 (and T_p <= 2.3 s) and they lay relatively close to the values found in natural seagrass beds in the field, under very short waves (T_p = 1.7 and 200 < Re_v< 800). This observation suggests that the response of flexible vegetation elements (the oscillation) is very different under very low energy conditions. Therefore, the model might not be valid over the whole range of Re_v (and, therefore, orbital velocities) that might occur in nature.

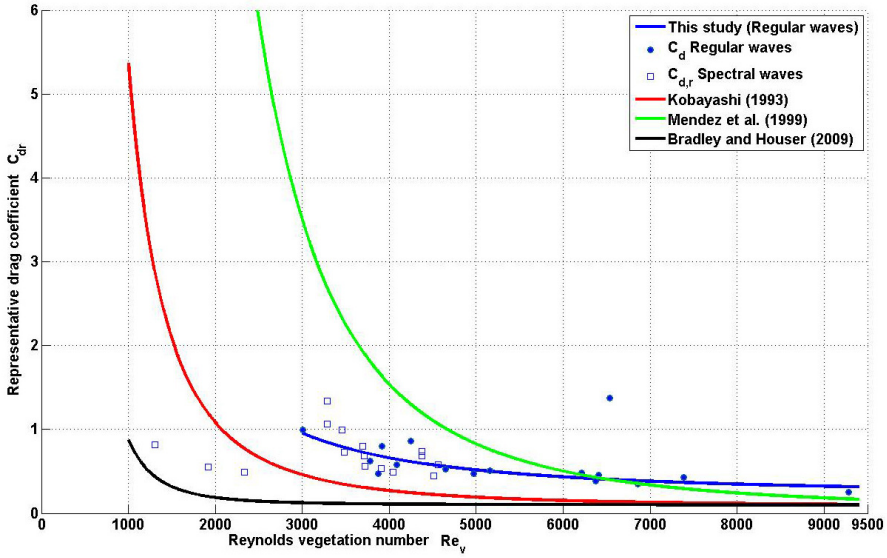

Figure 6.9 Drag coefficients plotted against the Reynolds vegetation number (Re_v): representative drag coefficient ($C_{d,r}$) from spectral waves (blue squares); and drag coefficient (C_d) from regular waves (blue dots). The data are compared with the relationship found in the present study from regular waves (blue line) and with models, from previous studies [*Kobayashi et al.*, 1993; *Mendez et al.*, 1999; *Bradley and Houser*, 2009]. Note: the Bradley and Houser curve is an extrapolation for Re_v>800.

The data were plotted also against the mean Keulegan-Carpenter number KC, (Figure 6.10). The same separation of the data into two populations of drag coefficients was observed; however, the data did not show any trend.

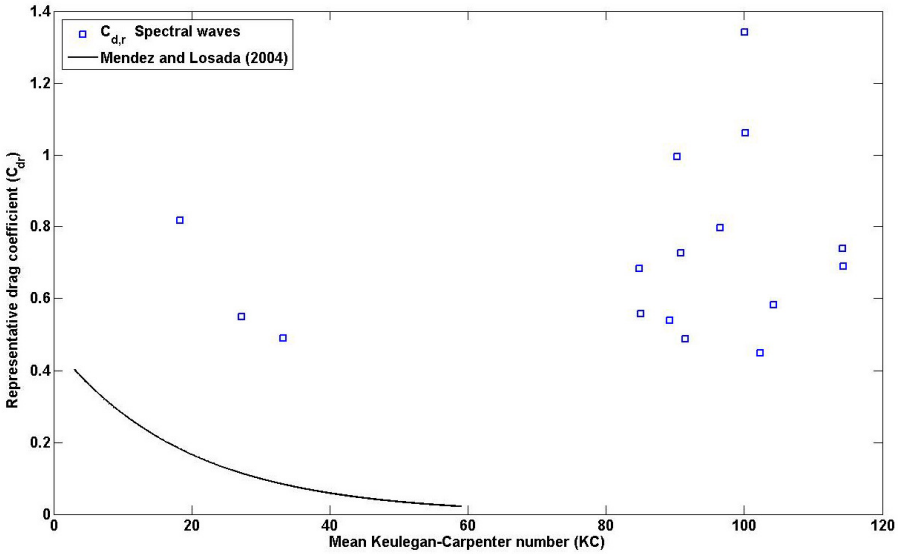

Figure 6.10 Representative drag coefficients for spectral waves plotted against the mean Keulegan-Carpenter number (KC)

6.3.5 Wave dissipation factors and roughness

Representative wave dissipation factors ($f_{e,r}$) were calculated for spectral waves, from the wave energy decay, using the same method, as described in Chapter 5. The $f_{e,r}$ represents the wave energy decay associated with the peak frequencies of the spectra, as most of the energy dissipation occurred there. The results are listed in Table 6-3 and are plotted in Figure 6.11, for all of the tests that fitted the wave decay model (R^2>0.60). It is clear that tests with a lower stem density are characterised by a smaller $f_{e,r}$ for the same A; it appears also that $f_{e,r}$ decreases with A, as found for regular waves.

Assuming that wave energy dissipation factors (f_e) are equal to the wave friction factors (f_w), (Nielsen, 1992), hydraulic roughness values were obtained by applying the model based on the *Nielsen* [1992] formula. Hydraulic roughness values are reported in Table 6-1 for the tests for which the $f_{e,r}$ was considered to be a reliable estimate (where R^2>0.60). Hydraulic roughness was on average 0.237 for the tests with 360 stems/m^2, and 0.188 for 180 stems/m^2. These values are slightly larger than the hydraulic roughness obtained from fitting Nielsen's formula to the f_e values obtained from regular waves tests (r_{360}=0.2311 and r_{180}=0.1478 for stem densities of 360 and 180 stems/m^2 respectively).

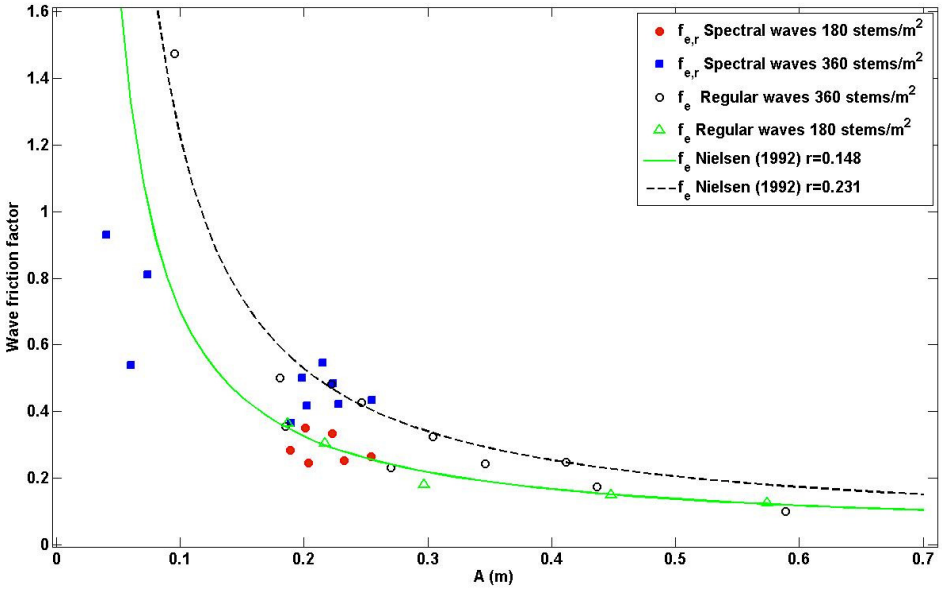

Figure 6.11 Friction factors for regular and spectral waves plotted against A, for both stem densities. The models obtained by fitting Nielsen formula to regular wave data are also plotted: the dashed line is valid for tests with a stem density 360 stems/m^2 and had "best fit" when the hydraulic roughness (r) was 0.231 m. The solid line was valid for tests with a stem density 180 stems/m^2 with r=0.148 m

The Nielsen model did not produce a good fit to the data obtained for 360 stems/$m^{2,}$ under very low A (A<0.1 m) (Figure 6.11). Under very low energy conditions, the system appeared to behave in a different way. Even over sandy beds, friction factors depend not only upon relative roughness (r/A), but also upon the flow regime (indicated by the wave Reynolds number, Re_w) [*Nielsen*, 1992; *Soulsby*, 1997]. The flow regime corresponding to those tests is less turbulent (Tests 9, 25 and 42 with a mean Re_w smaller than $1.8x10^4$); this might explain why the model is invalid under such conditions. Another explanation is that the mimics are responding to very small waves in a different way, for example, bending very little or oscillating at a different frequency than the waves.

Table 6-4 Hydraulic roughness (r) from the Nielsen (1992) formula for spectral wave tests. Mean value and standard deviation (S.D.) for tests with 360 and 180 stems/m^2 are indicated.

Test	stems/m^2	r (m)
90	180	0.203
89	180	0.176
83	180	0.151
65	180	0.223
64	180	0.211
63	180	0.162
mean	180	0.188
S.D.	180	0.026
44	360	0.327
43	360	0.284
42	360	0.163
27	360	0.338
26	360	0.290
25	360	0.094
18	360	0.316
17	360	0.250
16	360	0.207
9	360	0.101
mean	360	0.237
S.D.	360	0.091

6.4 Results and discussion: Spectral wave-induced velocities

6.4.1 Frequency-dependent flow dissipation in the lower canopy

Wave-induced velocity spectra (SUj) at the front of the patch (x/L=-0.07) were compared with those measured within the patch; both near the leading edge (x/L=0.17)

and farther inside the patch (at x/L=0.80), assuming that the flow field at x/L=-0.07 was not affected by the presence of the patch. The data from in front of the leading edge, from the regular wave tests, were not affected by the presence of the patch and wave reflection was similar, in both regular and spectral wave datasets. Therefore, it seems reasonable to assume that the velocities measured at x/L=0.17 are valid for the spectral tests. The resulting spectra of the wave-induced flows in the lower canopy are shown in Figure 6.12. The spectra shown in Figure 6.12A, were measured in front of the patch (x/L=-0.07), inside near the edge of the patch (x/L=0.17) and farther into the patch (x/L=0.80).

The corresponding α_j (frequency-dependent flow attenuation coefficient) are presented in Figure 6.12B. The α_j at each component of the spectra are shown in Figure 6.13 for all spectral tests with densities of 360 stems/m^2 (A) and 180 stems/m^2 (B).

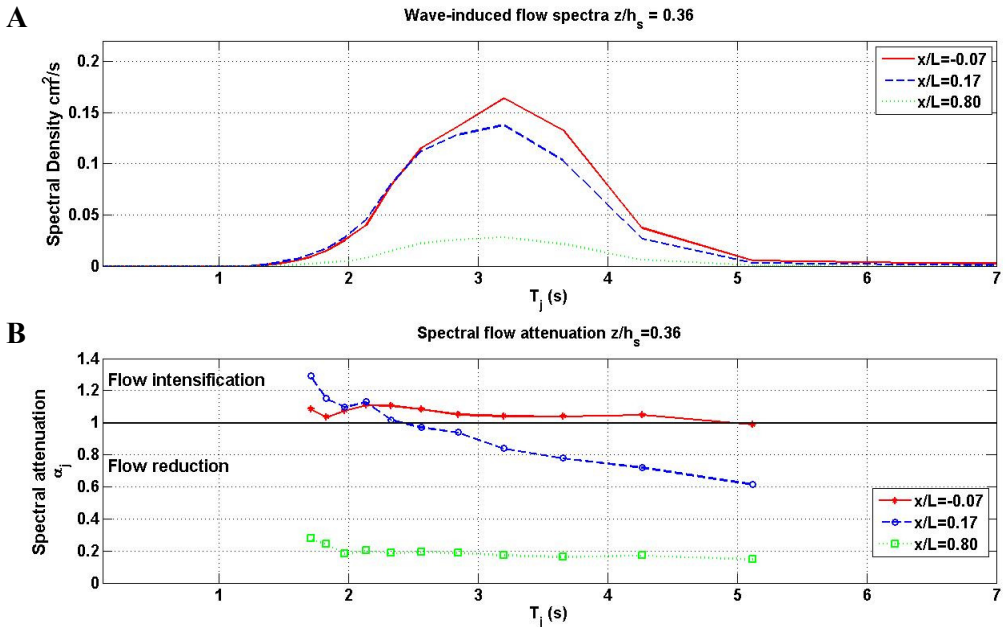

Figure 6.12 A) Spectra of the wave-induced flows measured in the lower canopy at the 3 locations along the flume; and B) the spectral attenuation parameter α_j (attenuation of flow at each frequency of the spectral component). The curves represent different locations along the flume. Test 26 (T_p=3.2 s, H_0=0.32 m, h_s/D=0.42 and 360 stems/m^2)

In all of the tests, the spectral attenuation coefficient (α_j) measured in the lower canopy (z/hs=0.36) increased with increasing frequency of the spectral component, at both locations within the patch and for both meadow densities (Figure 6.13). In front of the patch, at x/L=-0.07, α_j is close to 1, as expected, varying between 1.2 and 0.95, and this is largely independent of the component of the spectrum. At the edge of the patch (x/L=0.17), the flows created by the high-frequency components of the spectrum are

enhanced by the vegetation. At this location, reduction occurs only for the low frequency components, whilst farther inside the patch (x/L=0.80) the wave-induced flow attenuation is significant for all frequencies (ranging between 0.1 and 0.4, depending upon the tests conditions).

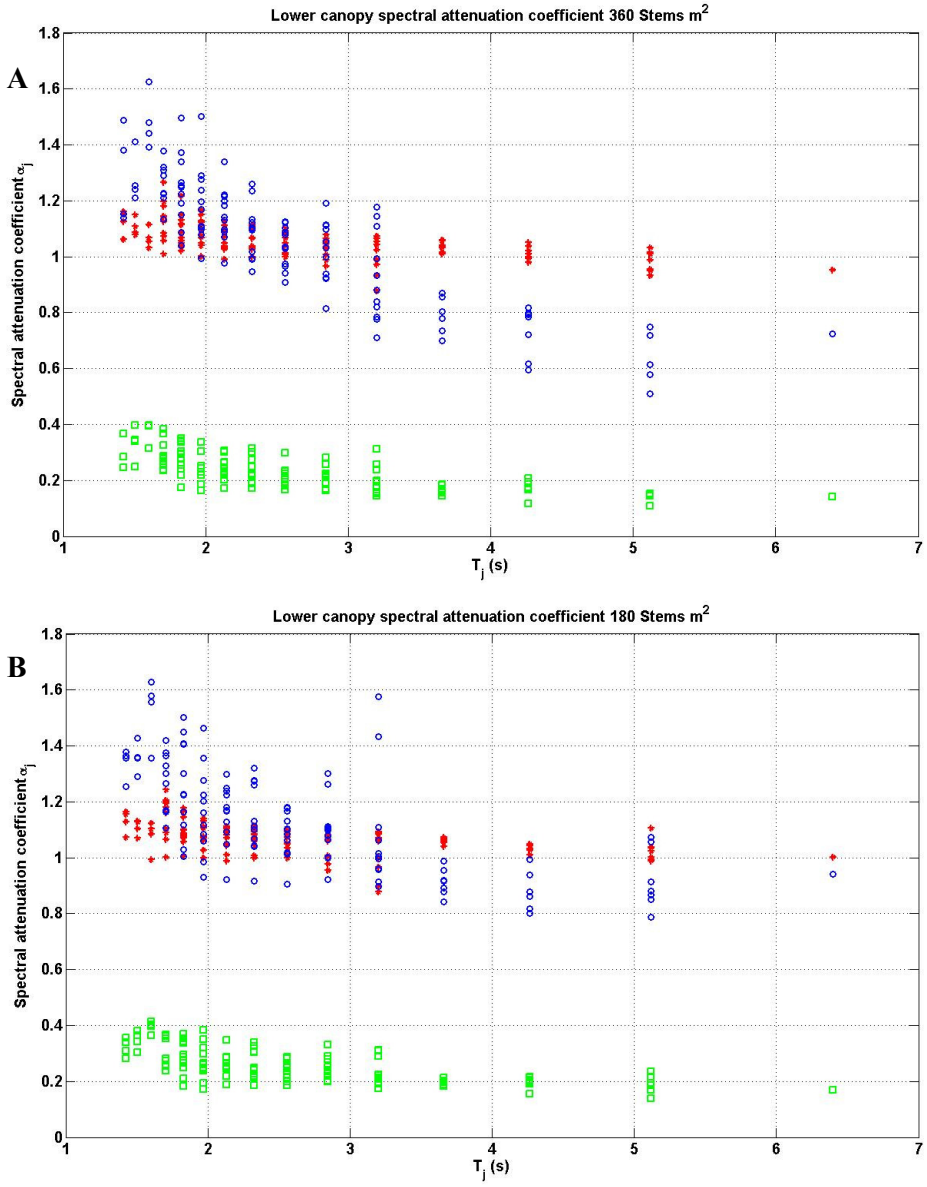

Figure 6.13 The spectral attenuation coefficient α_j in the lower canopy calculated for each wave period (T_j) of the wave-induced velocity spectral component for all 360 stems/m^2 tests (A) and 180 stems/m^2 tests (B). The red asterisks refer to the α_j values obtained at x/L=-0.07; the blue dots refer to the α_j values at x/L=0.17 and the green squares refer to the α_j values at x/L=0.80.

The α_j was significantly less for all components of the spectrum (indicated by the period of the component (T_j), for the tests having the highest submergence ratio (Figure 6.14). The largest α_j values were measured always in the tests of the lower patch

density, when the same wave spectra and depths were compared. The effect of patch density was significant at all water depths and also for the least energetic wave conditions. The divergence was greatest within the longer period components of the spectrum and at the edge of the patch (Figure 6.15).

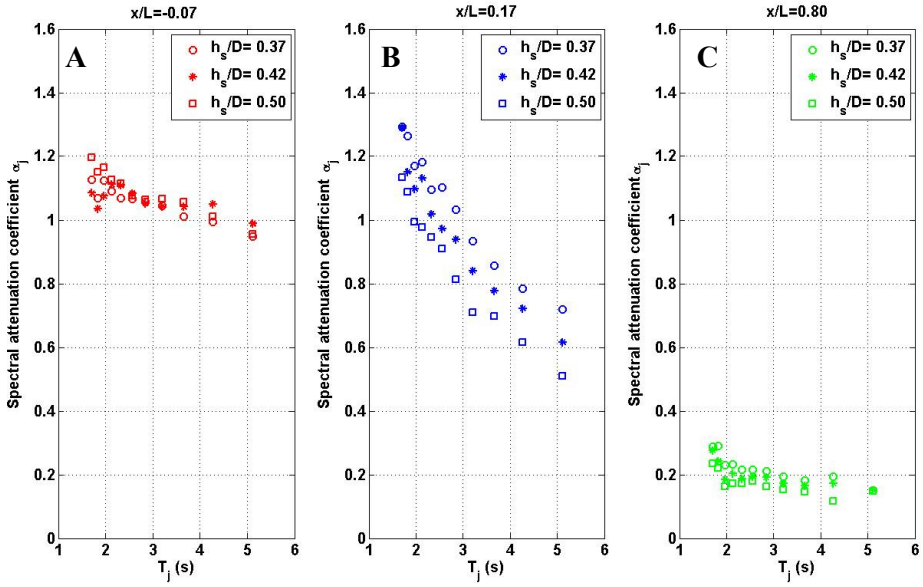

Figure 6.14 Effect of submergence ratio (h_s/D) on the spectral attenuation coefficient (α_j) , calculated for each wave period (T_j) of the wave-induced velocity spectra component. The data at the three locations along the flume are shown in each plot (A-C). Tests 16 (h_s/D=0.37 and H_0 =0.34 m), Test 26 (h_s/D=0.42 and H_0=0.32 m) and Test 43 (h_s/D=0.50 and H_0=0.33 m). All tests were carried out with density of 360 plants/m^2 and T_p=3.2 s.

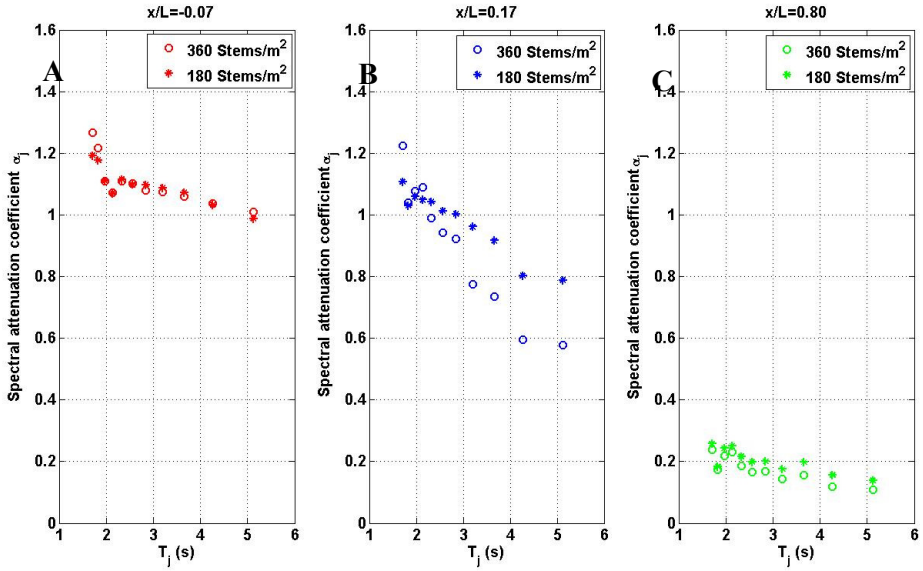

Figure 6.15 Effect of plant density on the spectral attenuation coefficient (α_j), calculated for each wave period (T_j) of the wave-induced velocity spectral component. The data at the three x/L locations are shown in each plot (A-C). Tests 44 and 90 with H_0 =0.30 m and H_0 =0.28 m respectively. Both test were carried out with h_s/D=0.50 and T_p=3.7 s.

The spectral attenuation coefficient at the components of the spectra with periods smaller than 2 s is often significantly larger than 1 at x/L=-0.07 (see, for example, Figure 6.15A). The same phenomenon is observed at very short periods, also inside the patch at x/L=0.17. Why this occurs it is not clear. As this happens in all tests, it might be an artefact of the methods used, due to wave non-linearity, for example. Despite this divergence, the main trend of increasing wave-induced flow reduction (decreasing α_j) with increasing wave period can be considered significant and it is consistent in all tests.

6.4.2 Representative wave-induced velocities and attenuation coefficient

The peak in the vertical distribution of U_r (the representative orbital velocity, corresponding to U_{rms} for regular waves) was found either at the top of the canopy (for large values of A, 0.2 m), or in the upper canopy (for smaller values of A). Some typical results are shown in Figure 6.16, for tests with a submergence ratio h_s/D=0.50. In Figure 6.16, Tests 42 and 88 have similar conditions, only different densities. The same is true for Tests 44 and 90, which had a larger peak wave period and wave heights.

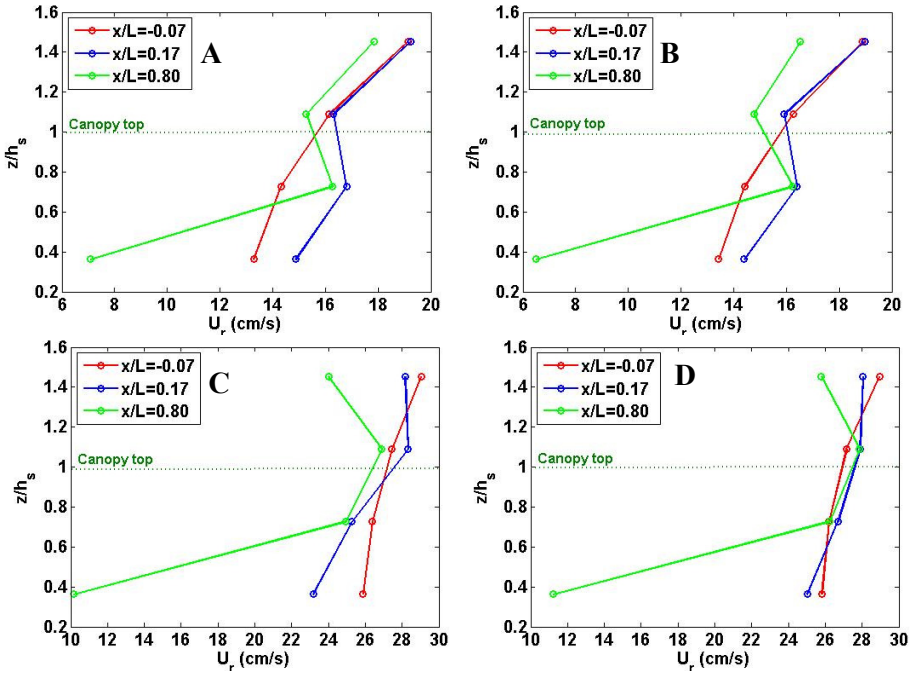

Figure 6.16 Vertical profiles of Ur (representative wave-induced horizontal velocity under spectral waves) for some typical tests with h_s/D=0.50. A) Tests 42 (T_p=1.98 s, H_0=0.22 m and 360 stems/m^2); B) Tests 88 (T_p=1.98 s, H_0=0.21 m and 180 stems/m^2); C) Tests 44 (T_p=3.7 s, H_0=0.30 m and 360 stems/m^2); D) Tests 90 (T_p=3.7 s, H_0=0.28 m and 180 stems/m^2).

The lowest U_r value was always located in the lower canopy and, at x/L=0.80, it was always greatly reduced compared to the value measured at the same elevation in front of the canopy (x/L=-0.07).

At each elevation, U_r was normalised against the corresponding value measured in front of the patch. An attenuation parameter was calculated and defined as:

$$\alpha_r(z) = \frac{U_r(z)}{U_r^0(z)} \qquad \textbf{Eq. 6-17}$$

with U^0_r being the representative wave-induced velocity measured at x/L=-0.07. Data from all tests were analysed and the results are plotted against the wave orbital amplitude in Figure 6.17 for tests with 360 stems/m^2. At both x/L=0.17 and x/L=0.80, at all elevations (except at the canopy top), the normalised velocities decrease with A. In the lower canopy (z/h_s=0.36), a large reduction in velocities (α_r<1) occurred, with α_r decreasing with increasing A and distance from the leading edge of the patch. However, some flow intensification (α_r>1) in the lower canopy was observed, near the edge of the patch (x/L=0.17) for A<0.07 m.

In the upper canopy (z/h_s=0.73) velocities were reduced compared with the un-vegetated area, but only for tests having A larger than about 0.20 m. For less energetic tests, the velocities in the upper canopy were intensified. Furthermore, wave-induced velocities in the upper canopy seem to be further intensified with distance inside the patch, not further reduced as occurred below in the lower canopy. At the canopy top (z/h_s=1.09), the flow was not significantly reduced and flow intensification occurred only for the largest A. Above the canopy (z/h_s=1.45), flow was not significantly affected by the canopy near the patch edge, whilst a significant reduction was observed further inside the patch (x/L=0.80) for the largest A. The same phenomena were observed for tests with 180 stems/m^2. The results of these series of tests are shown in Figure 6.18.

From the comparison of the two data-sets with the different mimic densities it is clear that for similar A the values of α_r in the lower canopy are less than for tests with 360 stems/m^2, at both locations. This pattern is consistent with observations on the effect of density at each component of the velocity spectra (see Figure 6.15 in previous Section). In addition, when A>0.15 m in the upper canopy (z/h_s=0.73) the orbital velocities are even greater for the less dense than fo the more dense patch.

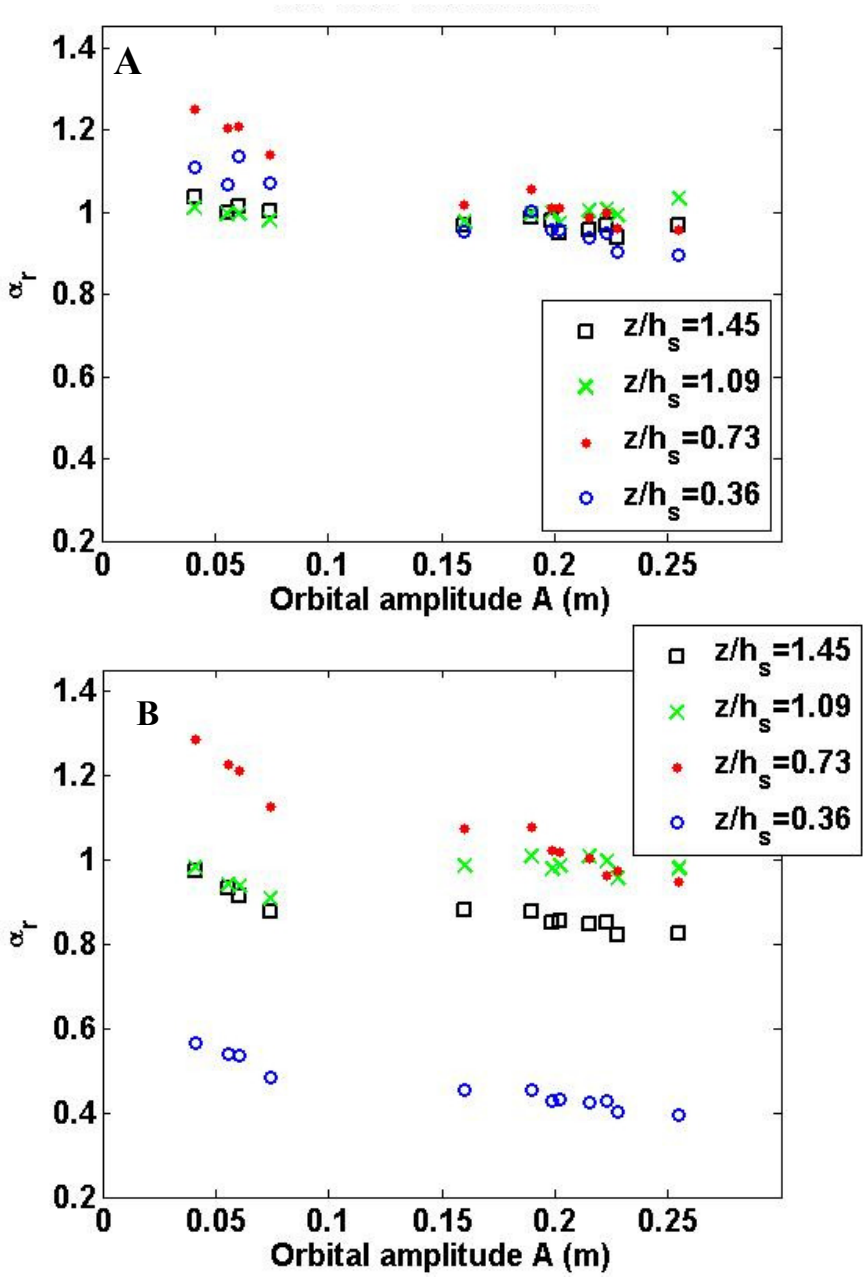

Figure 6.17 Attenuation parameter of representative velocities (α_r) plotted against the wave orbital amplitude for all tests with stem density 360 stems/m2. A) Data measured at x/L=0.17; and B) data measured at x/L=0.80.

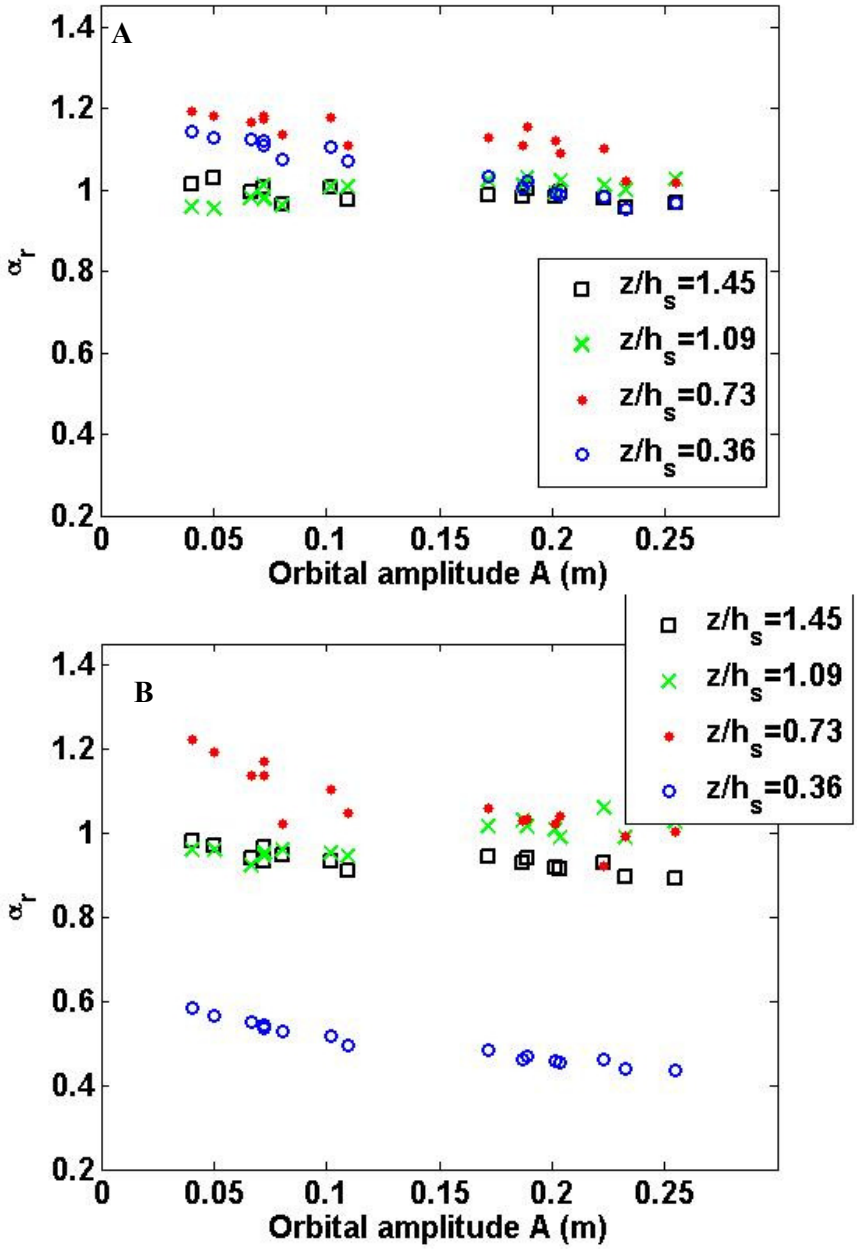

Figure 6.18 Attenuation parameter of representative velocities (α_r) plotted against the wave orbital amplitude for all tests with stem density 180 stems/m^2. A) Data measured at x/L=0.17 (inside the canopy near the edge); and B) data measured at x/L=0.80 (further inside the canopy)

These results are similar to those found for regular waves (Figure 5.21, Chapter 5), and the trends are clearer. Overall, the effect of the canopy on orbital velocities was largest for the largest values of A, both under regular and spectral waves. In the lower canopy, wave-induced flow reduction increased exponentially with A. Table 6-5 contains the coefficients and correlation coefficient of the fit (R^2) to the an exponential decay function (Eq. 5.25), for irregular wave tests; they are compared to those from

regular waves tests (already, in Table 5-4, Chapter 5). The data and the fit to an exponential function are shown in Figure 6.19 and Figure 6.20. An increase in stem density produced greater flow reduction and a steeper increase of flow reduction with A (the coefficient b is more negative for tests with 360 stems/m^2); this has been observed also for regular waves.

Intensification of flows, for smaller values of A took place mostly in the upper canopy, not at the canopy top as it has been observed in some studies on seagrass under long waves [*Verduin and Backhaus*, 2000; *Wallace and Cox*, 2000]. These observations support those obtained from the regular wave experiments and the evidence that for smaller values of orbital amplitude (A<0.20 m), flow intensification occurs inside the canopy. Also, there is evidence that near the canopy edge, for very small values of A (A<0.07 m or A<0.1 m, for the less dense patch), intensification might occur even in the lower canopy. In addition, flow reduction in the lower canopy increased with distance inside the canopy at all spectral components, as observed already under monochromatic waves.

Table 6-5 Flow reduction as a function of A in the lower canopy (z/hs=0.36) for both irregular and regular waves. The *a* and *b* coefficients of the fits to Eq. 5-25 (exponential decay curve) are indicated, as well as their confidence limits (calculated as twice the standard error, with 95% level of confidence) and the correlation coefficient (R^2).

		x/L=0.17			x/L=0.80		
Wave type	**Density (stems/m^2)**	**a**	**b**	**R^2**	**a**	**b**	**R^2**
Irregular	360	1.16 ±0.04	-0.97 ±0.22	0.90	0.58 ±0.02	-1.50 ±0.27	0.94
	180	1.18 ±0.18	-0.83 ±0.10	0.95	0.59 ±0.01	-1.28 ±0.15	0.96
Regular	360	1.16 ±0.09	-1.05 ±0.30	0.83	0.54 ±0.08	-0.98 ±0.29	0.81
	180	1.12 ±0.08	-0.64 ±0.30	0.52	0.54 ±0.05	-0.80 ±0.35	0.50

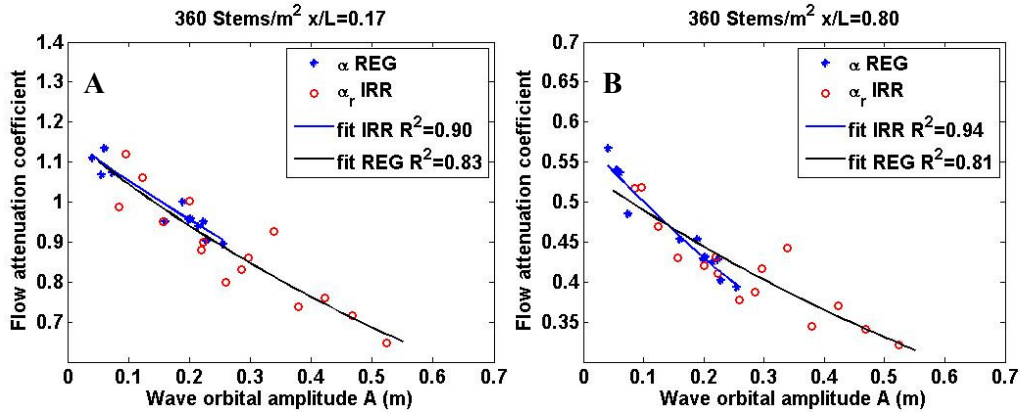

Figure 6.19 Lower canopy flow attenuation coefficient poltted with wave obital amplitude (A). Tests with 360 stems/m^2 at x/L=0.17 (A) and at x/L=0.80 (B). The fit to an exponential decay function is shown, for both irregular and regular waves (see Chapter 5).

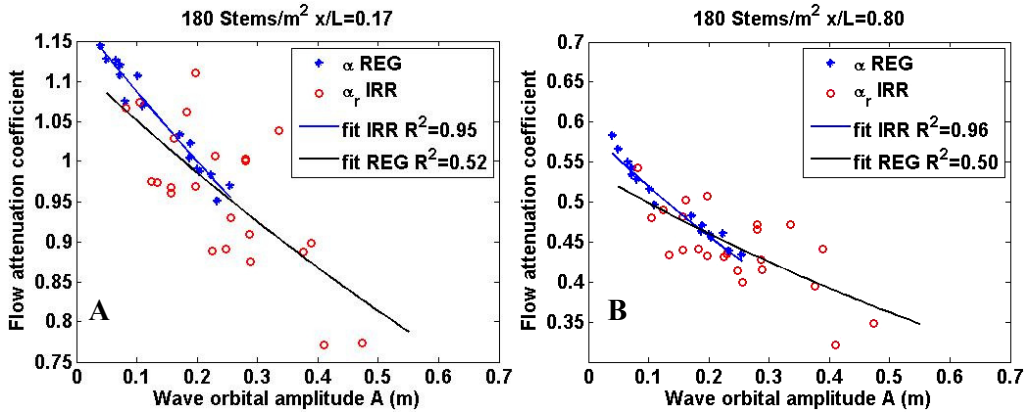

Figure 6.20 Lower canopy flow attenuation coefficient poltted with wave obital amplitude (A). Tests with 180 stems/m^2 at x/L=0.17 (A) and at x/L=0.80 (B). The fit to an exponential decay function is shown, for both irregular and regular waves (see Chapter 5).

6.5 Concluding remarks

Frequency-dependent wave dissipation was greatest at the peak spectral frequencies, consistent with what has been observed elsewhere in natural seagrass beds, under less turbulent flows [*Bradley and Houser*, 2009]. Furthermore, more energy reduction results from the least energetic tests, a denser patch and for the largest submergence ratios. Moreover, wave dissipation factors ($f_{e,r}$) tend to decrease with A, varying between 0.365 and 0.929 for tests with a density of 360 stems/m^2; between 0.246 and 0.333 for tests with a density of 180 stems/m^2. The values of $f_{e,r}$ were close to the f_e values obtained from the model, based upon the Nielsen (1992) formula, with the roughness values found from the regular waves data-set. However, the model was only

valid for the more turbulent tests. Low energy tests, with Re_w values less than 1.8×10^4, were characterised by a friction factor larger than that observed for the more energetic tests, but not as high as predicted by the model. It was concluded that the model could not be applied to all flow regimes, and the dissipation factor might not increase as rapidily at less turbulent regimes.

Under very low energy conditions the system seemed to behave different to higher energy conditions. Indeed, even on sandy beds, *fe,* depends not only on r/A but also on the flow regime (indicated by the Reynolds wave number, Re_w) [*Nielsen*, 1992; *Soulsby*, 1997]. These findings show the importance of large-scale flume experiments in understanding processes in vegetated beds: small-scale tests are unable to generate sufficiently large Reynolds numbers, to demonstrate the patterns of behaviour observed here.

For $Re_v >$ of 3000, the drag coefficients were close to those observed for regular waves, whilst $C_{d,r}$ decreased with Re_v. Values of $C_{d,r}$ found in the present study (between 0.45 and 1.34), are larger than values found in the literature, derived from tests on artificial kelp beds [*Kobayashi et al.*, 1993; *Mendez et al.*, 1999]. However, they are lower than modelled values obtained considering the relative motion of flexible vegetation elements [*Mendez and Losada*, 2004]. Interestingly, for smaller values of $Re_{v,}$ the canopy drag was smaller than expected from the regular wave results and, although still larger, they were closer to values obtained in the field on natural seagrass beds under very low energy conditions ($200<Re_v<800$). Despite wave period being included in its expression, no relationship was found between the Keulegan-Carpenter number (KC) and the drag.

Flow reduction increased with distance inside the canopy at all spectral components and for all conditions tested, as already observed under monochromatic waves.

Inside the canopy, the velocity reduction induced by the seagrass varied across the spectrum: attenuation was largest for the longest wave periods (ranging between 1.4 to 6.4 s), which can be considered typical of wind wave conditions in the coastal Mediterranean Sea [*Franco et al.*, 2004]. It emerged also that wave-induced flow attenuation was largest for the largest values of wave orbital amplitude A. This effect has also been observed for wave-induced flow spectra within rigid canopies by Lowe (2007), for waves between 2 and 25 s.

Interestingly, the peak orbital velocity was not always located at the top of the canopy, as previously observed; rather, for small wave orbital amplitudes, it was located at a lower level inside the canopy, as found for regular waves. This observation might indicate that thickness of the boundary layer was increasing with A.

It was clear also that the dampening of the longest period component of the wave-induced flows was greatest inside the denser patch and under highest submergence ratios, confirming trends from the regular wave tests. In particular, the effect of meadow density was more significant amongst the long period components of the flow spectrum.

7 Chapter 7: General Discussion and Conclusions

7.1 General discussion

This study was divided into a field study (in the Gulf of Oristano, Sardinia, Italy) and laboratory experiments (in the CIEM flume, UPC-Barcelona). This thesis is an examination of the effects of the seagrass *Posidonia oceanica,* on wave-induced flows and wave dissipation in the nearshore.

Findings from Chapters 3-6 are summarised, compared and discussed in Sections 7.1.1 (flows and turbulence) and 7.1.2 (wave dissipation). A conceptual model on processes and structure of the boundary layer in a *Posidonia* canopy is proposed (Section 7.1.3). The effects of the distance into the seagrass, mimic density and submergence ratios on wave dissipation induced by the seagrass, are also presented (Sections 7.1.4 to 7.1.6). Similarly those effects on oscillatory flow and turbulence variations are considered in these Sections. Limitations produced by the use of plastic mimics are evaluated in Section 7.1.7. This Chapter contains also some comments on the implications for nearshore sediment transport from the presence of seagrass (Section 7.1.8). Finally, a summary of the main findings of this study are reported in Section 7.2 and the recommendations for future work are suggested in Section 7.3.

7.1.1 Effects of *Posidonia oceanica* canopies on flows

Unidirectional currents were reduced by natural *Posidonia* plants during both breezy and windy conditions, confirming previous findings [e.g. *Granata et al.*, 2001] from a deep (15 m) *Posidonia* meadow. Unidirectional flows in the upper canopy of the meadow were halved, compared with the velocity at the shoreward edge of the seagrass bed and reduced by one third compared to the site in shallow water. Conditions within the meadows were almost unaffected by variations in the general hydrodynamic conditions whilst, at stations outside the meadow, even breezes affected current magnitude and direction. In contrast, wave orbital velocities (U_{max}) in the upper canopy at the *Posidonia* site seemed unchanged compared to oscillatory flows elsewhere.

Nevertheless, there was some evidence that attenuation of oscillatory flows at the edge of the patch took place for the largest waves (characterized by a large wave orbital amplitude, A).

In the laboratory, both under regular and spectral waves, it was clear that oscillatory flow in the upper canopy was not reduced for small wave amplitudes; the oscillatory flow dissipation increased with increasing values of orbital amplitude. Inside the canopy, the velocity reduction, induced by the seagrass, varied across the wave spectrum; attenuation was largest for the longest wave periods (ranging between 1.4 to 6.4 s), which are typical of wind waves in the coastal Mediterranean Sea [*Franco et al.*, 2004]. Also, in the lower canopy, orbital velocities associated with small amplitude regular waves were able to pass through the canopy, whilst the flows from long period waves were greatly attenuated. This phenomenon has been previously observed in rigid canopies [*Lowe et al.*, 2005b], but never, to the author's knowledge, in seagrass canopies. A layer of flow intensification was observed above the canopy as in previous field studies on seagrass species under waves [*Verduin and Backhaus*, 2000; *Wallace and Cox*, 2000; *Backhaus and Verduin*, 2008]. However, interestingly, for small wave amplitudes the flow intensification layer was located inside the canopy, both under regular and irregular waves.

A peak in turbulent kinetic energy was located at the top of the canopy, in all cases. This pattern is consistent also with previous studies on seagrass [*Wallace and Cox*, 2000; *Koch et al.*, 2006a] and rigid canopies exposed to waves [*Reidenbach et al.*, 2007; *Lowe et al.*, 2008]. Findings on the structure of turbulence within and above the canopy are summarised and discussed in relation with wave dissipation in the next section (Section 7.1.3).

Evidence from the field shows that the presence of a *Posidonia* meadow increases oscillatory flow asymmetry compared to bare sand (at z/h_s between 0.75 to 1.35, corresponding to the upper/canopy top, see Chapter 3). This asymmetry was defined in the laboratory tests by the Stokes asymmetry parameter R, for regular waves (see average values in Table 7-1, for 360 stems/m^2 tests, together with Chapter 5). Generally, all waves tested were slightly asymmetric with the peak oscillatory velocity under the crest larger than under the trough ($R>0.5$). At the canopy top ($z/h_s=1.09$), the rate of increase of R with increasing Ursell number was much more rapid than in front of the seagrass patch. This pattern is consistent with observations obtained from previous flume experiments, with artificial vegetation under waves [*Price et al.*, 1968].

This orbital asymmetry creates a shoreward drift above the canopy, especially for the largest waves. This enhanced drift above the canopy could have an effect on the coastal circulation (i.e. crossshore/longshore currents). However, laboratory results also indicate that inside the canopy orbital velocities are more symmetrical than over bare sand at the same depth. This suggests that a shoreward drift does not exist within the canopy.

7.1.2 Effects of *Posidonia oceanica* canopies on wave dissipation and seabed roughness

The artificial *Posidonia oceanica* meadow affected significantly the propagation of both regular and irregular waves and there is evidence, from field measurements, that natural *Posidonia* meadows also have an effect on wave height decay across the canopy. As low energy waves travelled above the *Posidonia* bed (in the field, for 132m), a 5% reduction of wave height was measured. A larger reduction was measured in flume experiments (of up to 35% over a 10 m patch, for regular waves), but there were several significant differences in the experimental conditions. The *Posidonia oceanica* meadow in the study area had a patchy distribution and a 24 cm average canopy height (reaching up to 48 cm, in places). The natural meadow had a density 251±51 stems/m^2 , which was comparable to that in the laboratory (180 and 360 stem/m^2). These densities are at the low end of typical *Posidonia oceanica* meadow densities; so can be classified as "very sparse" following *Giraud*'s [1977] classification. It is also important to note that the submergence ratio (h_s/D) in the field was significantly lower than in the flume (about 0.06 in the field and between 0.32 and 0.5 in the flume). Furthermore, other processes such as wind shear stress at the water surface, changes in wave direction or wave reflection might have affected the wave height decay in the field. Submergence ratio and wave conditions affect significantly wave height decay over the submerged canopy, both for regular and irregular waves.

Wave dissipation factors in the field were estimated to be 0.26 on average. However, the data were characterised by high scatter, due to the variation in wave characteristics and the varying experimental conditions. Nonetheless, it was found that wave height decay was significant only in low energy conditions whilst, during a moderate Mistral storm event, wave height reduction was not detected. The laboratory results confirm this trend and indicate that the largest wave height reduction induced by the meadow takes place under large submergence ratios and for shorter waves, under

both irregular [*Manca et al.*, 2010; Chapter 5 and Chapter 6] and regular waves [*Stratigaki et al.*, accepted; Chapter 5] The average wave dissipation factor found in the field was similar to the more rigid coral canopies [*Lowe et al.*, 2005a] and saltmarshes [*Möller et al.*, 1999] (see Table 2-2 of Chapter 2, which are expected to be stiffer and to have a higher value than seagrass), probably because the flow regime in which they were measured was different. Interestingly, under regular waves, the dissipation factors varied predictably as a function of wave amplitude, for the range of wave Reynolds numbers (Re_w) tested; they follow the classical Nielsen (1992) empirical model, that is valid for sandy and rippled beds:

$$f_w = \exp\left[5.2\left(\frac{r}{A}\right)^{0.2} - 6.3\right] \qquad \textbf{Eq. 7-1}$$

The best correlation coefficient of Eq. 7-1 (R^2=0.91) was produced when the hydraulic roughness (r) was 0.23 m for a canopy density of 360 stems/m^2, it was 0.15 m (R^2=0.95) when the density of the canopy was 180 stems/m^2 (see Section 5.3.3 Chapter 5). Therefore, hydraulic roughness was, therefore, a fraction of the canopy height; it is likely to be dependent upon the canopy density, as observed in other vegetation exposed to currents [*Neumeier*, 2007].

The observed decrease in the wave friction factor with wave orbital amplitude agrees with previous studies of wave dissipation over rough seabeds ([coral, sandy and rippled beds; *Sleath*, 1984; *Nielsen*, 1992; *Lowe et al.*, 2005a; *Soulsby and Clarke*, 2005].

Irregular wave tests were performed to examine wave attenuation at different parts of the wave spectra and to express wave dissipation as a frequency-dependent wave dissipation factor ($f_{e,j}$). Spectral wave dissipation ($f_{e,\,j}$) was highest for the least energetic wave spectra and was greatest at the peak frequency confirming observations over seagrass beds of other species [*Bradley and Houser*, 2009]. Representative wave dissipation factors ($f_{e,r}$, measured under spectral waves at the peak frequency), were close to those expected from the Nielsen's model (derived from regular wave measurements). However, under spectral waves, low energy tests ($Re_w < 1.8 \times 10^4$) were characterised by a friction factors larger than those observed for more energetic tests, but not as high as predicted by the Nielsen's model. It was concluded that the Nielsen model could not be applied to all flow regimes, and the dissipation factor might not increase as rapidily with decreasing Re_w. This indicates that wave dissipation factors

depend on wave orbital amplitude and on the flow regime (indicated by the Reynolds wave number, Re_w), as for sandy beds [*Nielsen*, 1992; *Soulsby*, 1997].

Wave energy dissipation was evaluated also as drag coefficients and the results confirm that the capacity of seagrass, to reduced waves, dependent strongly upon the flow regime. Drag coefficients, calculated using the *Dalrymple* rigid model [1984], were largely dependent on Re_v (the vegetation Reynolds number). The Dalrymple model assumes the canopy to be rigid, but it has been applied successfully to studies of wave dissipation over vegetated beds [*Kobayashi et al.*, 1993; *Mendez et al.*, 1999]; it appeared to define drag over seagrass beds well [*Bradley and Houser*, 2009]. The drag caused by *Posidonia* is larger than found for artificial kelp beds [*Kobayashi et al.*, 1993; *Mendez et al.*, 1999]; however, it is smaller than that for kelp beds, considering the relative motion of flexible kelp elements [*Mendez and Losada*, 2004]. Seagrass beds in the field, under low energy conditions [*Bradley and Houser*, 2009], were characterised by smaller drag coefficients than found in this study, especially for the more turbulent tests.

The Keulegan-Carpenter number (KC) did not provide an improved explanation of the variation of C_d with flow and wave conditions, despite including the effect of wave period. This observation is in contrast with the findings of drag over kelp beds [*Mendez and Losada*, 2004], but is in line with observations of drag over natural seagrass beds [*Bradley and Houser*, 2009].

The results from this study are summarised in Figure 7.1, compared to those of other flume studies on wave dissipation over sandy flat or rippled beds. The relative roughness (r/A) created by the artificial canopy is consistently higher than over rippled sands and flat sands under the same wave conditions (in laboratory experiments). The relative roughness is larger for the denser canopy, than for the less dense canopy. The relative roughness for irregular waves is similar to that of regular waves, for Re_w larger than about 4×10^4. However, in low energy conditions the relative roughness is less under random waves, than under regular waves. The rate of decrease of relative roughness with increasing wave Reynolds number, is similar to that found over sandy beds (except at the lowest Re_w tested). These findings fit with previous studies undertaken on the interaction between submerged vegetation and waves, i.e. that seagrass increases bed roughness under waves [*Koch et al.*, 2006a; *Bradley and Houser*, 2009]. *Posidonia oceanica* in particular, increases bed roughness under unidirectional flows in deep meadows [*Gacia and Duarte*, 2001]. This work shows that they also

reduce wave energy and increase relative bed roughness compared to sandy beds in similar flow regimes, particularly under small amplitude waves.

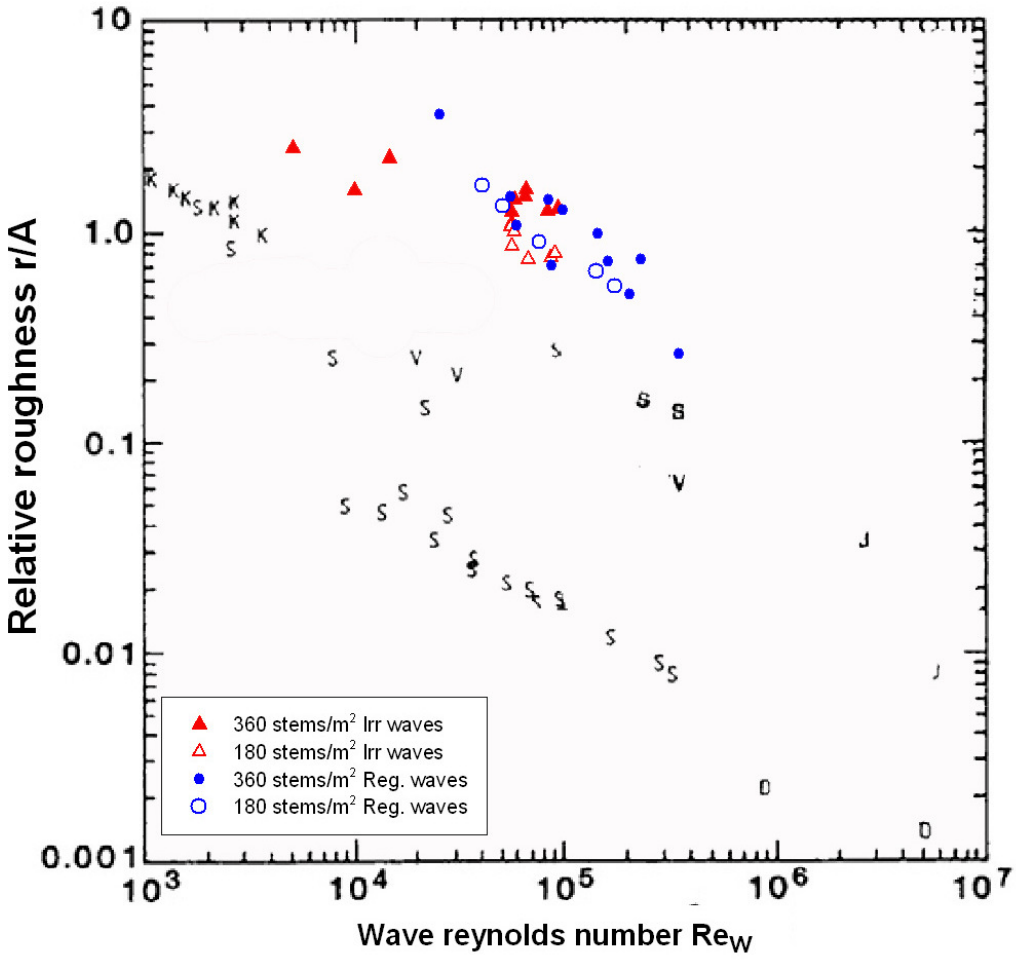

Figure 7.1 Relative bed roughness of an artificial *Posidonia* canopy compared to sandy beds under various wave conditions. Results from this study under the 2 tested plant densities and wave types (regular and irregular) are shown by the coloured symbols. The letters refer to different studies carried out in flumes with rippled or flat sandy beds (see Nielsen, 1992 and references therein). The range of r/A<0.08 corresponds to flat sandy beds with little sand movement; r/A>0.2 corresponds to rippled sandy beds (Nielsen, 1992).

Wave energy dissipation rates used in the calculation of drag and wave dissipation coefficients are a result, not only of the drag exerted by the canopy, but also of the shear stress contribution in the benthic boundary layer. Shear stress was evaluated at the canopy top, from the analysis of the turbulent Reynolds shear stresses under regular waves. The shear stress coefficient (C_f) was mostly an order of magnitude lower than C_d and f_e (except under very low submergence ratios, h_s/D, with h_s canopy height and D water depth). This might indicate that shear stresses forming at the canopy top

were not main drivers of flow into the canopy, especially under small amplitude waves; this is the same as has been suggested for coral canopies [*Lowe et al.*, 2008].

7.1.3 Processes and boundary layer structure in *Posidonia oceanica* canopies

A conceptual model of the processes and the structure of the boundary layer in the presence of a *Posidonia*-like submerged canopy under waves is proposed, based on the findings of this study (Figure 7.2). The observed turbulence and flow structure in the lower water column are related to wave energy dissipation. Table 7-1 summarises the main parameters obtained for tests with 360 stems/m^2 (under regular and irregular waves). The conceptual model defined based upon general observations of the dense canopy tests. The main trends were also observed under the sparse canopy and in the field.

Two states were distinguished which are likely to occur in *Posidonia* canopies:

- conditions of low orbital amplitude waves (A ranging between 0.1-0.2 m), with the plants remaining fairly stationary and;
- conditions of large orbital amplitude waves (A ranging between 0.21 m-0.5 m), with the plants moving vigorously through an S shape (whip-like motion).

The 0.2 m wave orbital amplitude threshold between the two states corresponds to Ursell numbers of 10-15. Ursell numbers less than 15 are typical of linear waves [*Myrhaug et al.*, 2009]. The wave orbital amplitude threshold was slightly higher (about 0.3 m) for the tests with the less dense canopy (180 stems/m^2), which suggests a dependency on canopy characteristics.

Table 7-1 A summary of the main parameters obtained from tests with large and small orbital amplitude waves (tests with 360 stems/m^2 , under regular and irregular waves.) The reported parameters related to orbital velocity and turbulence, correspond to measurements made at x/L=0.80 (8 m shoreward of the leading edge of the canopy). A positive value of the phase shift indicates that U_{max} occurs before the passage of the wave crests. A negative value of orbital velocity reduction indicates flow increase

Parameter –Regular wave tests		Small amplitude waves	Large amplitude waves
Wave orbital amplitude A (m)		0.10-0.20	0.21-0.50
Ursell number		3-15	16-40
Reynolds vegetation number Re_v		3.0×10^3-3.8×10^3	4.6×10^3-9.3×10^3
Reynolds wave number Re_w		3.3×10^4 -8.0×10^4	1.16×10^5-5.3×10^5
Drag coefficient C_d		0.47-1.0	0.25-0.52
Wave dissipation factor f_e		0.36-1.47	0.10-0.48
Shear stress coefficient c_f		0.01-0.08	0.03-0.12
Turbulent kinetic energy peak- relative elevation (z/h_s)		1.09 (canopy top)	1.09 (canopy top)
Peak of U_{max}/U_∞- relative elevation (z/h_s)		0.73 (upper canopy)	1.09 (canopy top)
Average phase shift between U_{max} and the passage of the wave crest (degrees)	Above canopy	3±9.4	1±8.4
	Canopy top	-10±13.1	2±5.9
	Upper canopy	8±8.5	32±8.0
	Lower canopy	4±10.7	21±9.3
Average reduction of rms orbital velocity (vertical component) W_{rms} (%)	Above canopy	20±8.3	27±11.2
	Canopy top	27±12.6	37±11.6
	Upper canopy	39±24.6	24±22.5
	Lower canopy	77±6.2	82±6.0
Average reduction of rms orbital velocity (horizontal component) U_{rms} (%)	Above canopy	12±7.2	13±5.5
	Canopy top	4±7.7	-12±15.2
	Upper canopy	-10±12.4	17±11.3
	Lower canopy	54±4.5	62±4.0
Stokes asymmetry R	Above canopy	0.5-0.55	0.57-07
	Canopy top	0.5-0.58	0.58-0.67
	Upper canopy	0.5-0.55	0.50-0.56
	Lower canopy	0.5-0.55	0.5-0.6

Parameter –Irregular wave tests	Small amplitude waves	Large amplitude waves
Reynolds vegetation number Re_v	1.3×10^3-3.9×10^3	3.3×10^3-4.5×10^3
Reynolds wave number Re_w	5.9×10^3-8.8×10^4	7.6×10^4-1.3×10^5
Representative drag coefficient $C_{d,r}$	0.49-0.82	0.45-1.06
Representative wave dissipation factor f_{er}	0.36-0.93	0.42-0.54

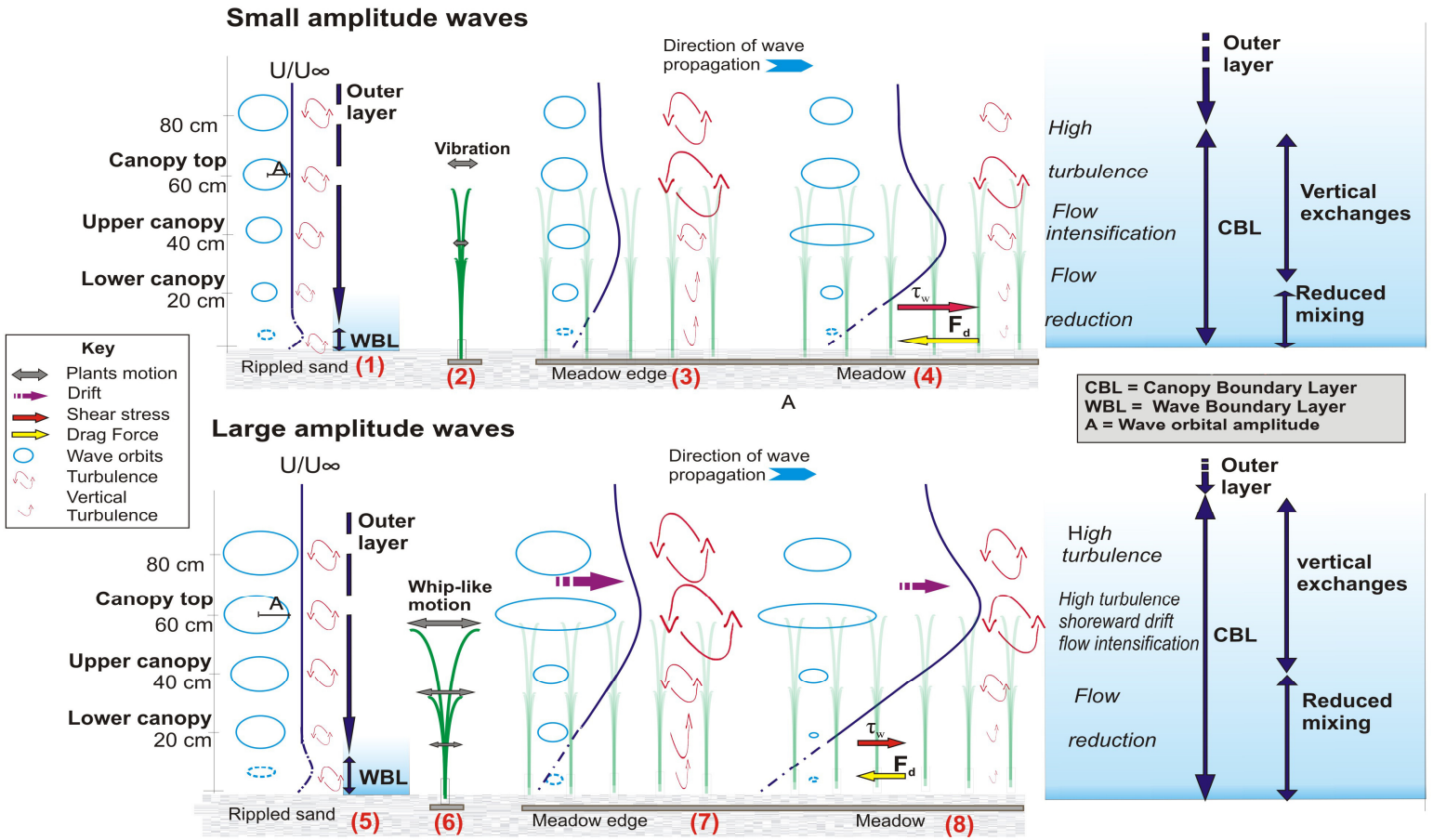

Figure 7.2 Conceptual model of the effect of an artificial *Posidonia oceanica* canopy on the benthic boundary layer under waves. See description in the text.

Small orbital amplitude wave conditions:

- In front of the leading edge of the canopy (indicated with (1), in Figure 7.2), on rippled sand, the wave boundary layer is expected to lie very close to the bed, a few cm thick according to classic WBL (wave boundary layer) theory [*Sleath*, 1984; *Nielsen*, 1992; *Soulsby*, 1997]. Threrefore, most of the water column is unaffected by the bed (outer layer). Turbulence is low and orbital velocities are reduced from the water surface to the seabed. At the depth tested, waves are practically symmetric, thus flow asymmetry (R) is also small.
- Plants oscillation (2) is limited, as a result of the small orbital velocity produced by the waves, and very little motion is expected in the lower part of the canopy, where the flows acting on the blades are even less.
- At the edge of the patch (3), the horizontal orbital velocities are slightly reduced in the lower canopy compared to orbital velocities at (1); they are accelerated in the upper part, where the canopy biomass decreases. The "overshoot" (the peak in the vertical distribution of the horizontal orbital velocities) is also located in the upper canopy. Vertical orbital velocities are also attenuated, particularly in the upper canopy. Turbulence is greater than at all elevations. The peak in turbulence is formed at the canopy top. Flows at the canopy top are slightly more asymmetric, than over sandy beds.
- Further shoreward within the meadow (4) the velocity gradient between the upper and lower parts of the canopy is high and the vertical orbital velocity is dampened. The height of the "overshoot", the flow intensification layer and the maximum turbulence are similar to those near the edge of the patch ((2) in Figure 7.2). Turbulence is reduced, compared to turbulence levels at (2) and levels of turbulence in front of the canopy are comparable to those outside the patch (1). Near-bed turbulence is very low.

This structure of turbulence and velocity within the meadow ((4) where conditions are more stable) suggests that the region indicated as "above canopy" (z/hs=1.45 and above) is not affected by the presence of the canopy. The canopy boundary layer extends below this region. Findings on the vertical distribution of the phase shift seem to support this interpretation: in-canopy velocities are characterised by a positive phase shift. Generally, a positive shift (with orbital velocities peaking

before the passage of the wave crest) is characteristic of the wave boundary layer [*Nielsen,* 1992, see Section 5.4.4, Chapter 5].

The canopy top and upper canopy are areas of high turbulence and vertical mixing. The lower canopy and near-bed layers are relatively sheltered, dominated by drag. Vertical mixing may occur from interaction with the turbulent vortices, created by wave passage above the canopy, but turbulence is not advected from the sides.

Large orbital amplitude wave conditions:

- The stronger orbital velocities induce a more pronounced oscillation of the plants (indicated by (6), in Figure 7.2). Even the stiffer central and lower plants move in the flow. In these conditions plants are S-shaped when moving, which reflects as a bowing back and then rushing forward of the leaves with each wave passage (whip-like oscillation; see also Figure 4.5, Chapter 4)
- At the canopy edge, (7), orbital velocities (horizontal and vertical components) are reduced in the canopy and enhanced at the canopy top. The peak of turbulent energy and the "overshoot" occur at the canopy top. Turbulence, particularly the vertical component, is greater than formed at the front of the canopy; it is greater also in the canopy. Flow asymmetry is increased significantly at the canopy top suggesting an enhanced shoreward drift.
- The orbital velocity gradient in the vertical increases farther shoreward (8), as flow in the canopy is attenuated and enhanced at the canopy top. The "overshoot", peak in turbulence and the flow-intensification region are, as in (7), at the canopy top. Flow asymmetries (hence the potential drift) is reduced (compared to (7)), probably as a consequence of the attenuated wave height downstream. The in-canopy phase lag is large (wave orbital velocity peaks before the passage of the wave crest). Turbulence is decreased compared to (7), at all elevations; it is reduced significantly in the lower canopy. Turbulence in the "above canopy" area is higher than at the same level in front of the canopy.

Regular wave results indicate that in-canopy and above canopy phase shifts become larger with increasing values of orbital amplitude ($A<0.5$m). In addition, the distribution of turbulence described above (associated with points 6-8, in Figure 7.2) suggest that the top of the CBL is located above the "above canopy area". The lower vertical

gradient in orbital velocity under large amplitude waves also suggests that the CBL is thicker than under small amplitude waves. The layer of in-canopy flow reduction is thicker (extending to the upper canopy) for large values of A, than for smaller values. The CBL might also be characterised by a shoreward drift at the canopy top.

Generally, when the WBL thickness is large, shear stresses are distributed across a greater depth and the wave dissipation is less [*Sleath*, 1984; *Nielsen*, 1992; *Soulsby*, 1997]. Lower wave dissipation was associated with the large amplitude waves, a finding which is clear from both field and laboratory evidence.

The regular and irregular wave results demonstrate that flow decreased exponentially with increasing A and with increasing wave periods (α_j for spectral waves, Chapter 6). It is likely, that oscillatory flows characterised by small orbits can penetrate into the canopy deeper than those with larger orbits, and therefore the latter are reduced more. Because flow speed under large orbital amplitude waves is less the drag (which is proportional to the flow speed) is also reduced (Figure 7.2). This is manifested as a thicker boundary layer. This phenomenon is proposed to be responsible for wave energy reduction in coral canopies [*Lowe et al.*, 2007]; it is likely that the same applies to flexible *Posidonia*-like canopies.

7.1.4 The edge effect

Most of wave height decay over a flat artificial seagrass bed occurred within the first few metres of the patch, falling away exponentially with distance from the edge in most of the tests performed with both regular and spectral waves. This is similar to most studies [*Kobayashi et al.*, 1993; *Augustin et al.*, 2009; *Bradley and Houser*, 2009]. In a few tests, wave height increased in the first metres of the patch, but then decayed due to frictional dissipation. This has been recorded in natural shallow seagrass beds (and it could be explained by local wave interaction, by reflection or diffraction) caused by the sudden change in bottom topography encountered by the waves. Under all conditions, oscillatory flow velocity at the edge of the patch was greater than downstream, resulting in higher drag at the edge of the patch and explaining the largest wave height reduction rates near the leading edge.

Turbulence, in particular the vertical component, was in many tests larger at the edge of the patch than in the upstream sandy area. Increased turbulence took place under the largest wave orbital amplitude and the largest flow magnitudes at the edge of the patch. It is probably the result of greater mimic oscillations, which produces higher

turbulent exchanges. Turbulent kinetic energy was largest at the edge of the patch than farther downstream. This suggests that the size of the patch is important in determining the hydrodynamic conditions and, thus, sediment and particle motion.

7.1.5 The effect of stem density on waves and flow changes

Stem density has a clear effect on wave dissipation, oscillatory flows and turbulence in an artificial *Posidonia* canopy. Wave dissipation (expressed as wave height decay coefficients or friction factors) and oscillatory flow reduction in the lower canopy were larger for the denser canopy, than the less dense canopy; this was true for both regular and irregular waves. The effect of density on relative roughness is shown in Figure 7.1. A higher meadow density causes a larger relative seabed roughness at all values of Re_w tested. The difference in r/A, obtained by doubling the canopy density, is not as large as the difference in roughness between the vegetated and the non-vegetated beds.

The denser seagrass patch produced also a greater oscillatory flow reduction in the lower canopy, at all the wave amplitudes tested. Seagrass density influenced also flow attenuation, as a function of A: flows attenuated more rapidily with increasing A, inside a 360 stems/m^2 canopy, than a 180 stems/m^2, under both regular and irregular waves.

If wave particle orbits are small enough and can penetrate the canopy, flows are faster (because they are not reduced by the canopy) and drag increases. By decreasing the canopy density (hence, increasing the canopy element spacing) orbital velocities are able to penetrate further into the canopy. A larger flow was observed indeed through the less dense canopy, however this did not correspond to increased wave dissipation. This is probably a result of "sheltering": as more plants are present, their capacity to move with the flow is reduced and the canopy, as a whole, becomes more rigid, thus creating a larger resistance to the flow.

7.1.6 The effect of submergence ratio on waves and flow changes

High submergence ratios (h_s/D) produced a larger attenuation of oscillatory flows in the lower canopy, both under regular and irregular waves. According to the conceptual model, these reduced in-canopy velocities should result in less drag. The highest submergence ratios produced the greatest wave height decay along the patch under both regular and irregular waves. However, the changes in the submergence ratio

(for a constant canopy height), on dissipation rates and drag coefficients were probably not significant compared to the effect of wave period (and A) for the range of submergence ratios tested here (between 0.32 and 0.5).

The effect of submergence ratios on wave–canopy interaction is complicated, by the different waving motion of the plants under varying submergence ratios.

Posidonia oceanica is found only in the Mediterranean Sea, where the tidal range is small (often less than 0.2 m), therefore, for a meadow located at a certain depth the variation in submergence ratio it to which it is exposed to, will be small, so that its effect on wave dissipation can be considered constant during a tidal cycle.

Furthermore, submergence ratio has a clear effect on turbulence. Turbulent kinetic energy (measured at all elevations) and shear stresses at the canopy top (C_f, from the Reynolds shear stress) increased with decreasing submergence ratio. This indicates that shear at the canopy top is greater for shorter canopies or deeper water (submerged conditions), as has been found for seagrass under unidirectional flow.

7.1.7 Limitations of seagrass mimics

The stiffness of the plants will affect wave dissipation [*Bouma et al.*, 2005]. Scaling formulae involving the modulus of elasticity of the leaf materials (such as λ_1 and λ_2, Section 4.2.3 of Chapter 4) are useful to compare leaf stiffness and, as a first indication in the selection of the plastic material for the construction of the plants. The mimics used in this study were within the accepted range for $\lambda 1$ in seagrass beds [*Ghisalberti and Nepf*, 2002], but the parameter, λ_2 (the ratio between drag forces and inertial forces) depends upon the flow magnitude applied and the natural canopy height (which varies greatly and it is not the same for all leaves). The parameter λ_2 was calculated considering a natural leaf length of 27 cm (as measured by divers in the field). To obtain the same bending and response of the mimic underwater (under the conditions typical of the field experiments) and to account for the different elasticity modulus (E) of *Posidonia* leaves compared to the plastic blades, the velocity in the flume had to be about 5 times larger than in the field (according to these scaling laws). This suggests that the leaves were too stiff, but this might not apply to the whole plant. The overall stiffness of the mimics is given, not only by the bending of 1 blade, but also by the structure of the whole plant and by the number of leaves and the height of the rhizome. Furthermore the scaling factor assumes a cantilever movement of the plant

(see Chapter 4), which might not always be appropriate for seagrass (characterised by a whip-like oscillation, [*Ghisalberti and Nepf*, 2002]). Nevertheless, this information was taken into account and a smaller number of leaves (4, compare to the average 6 in *Posidonia oceanica*, *[Buia et al., 2004]*) was used in the construction of the mimics.

In order to evaluate the bending and the overall response of the *Posidonia* mimics to waves, prior to the flume experiments, videos of the mimic in the CIEM flume were compared with videos of a similar size of natural *Posidonia* patch under similar wave conditions to the field. The typical whip-like oscillation was achieved during the full-scale experiments. Despite this similarity, the resulting value for wave dissipation found in this study may not be universal for all *Posidonia* meadows and flow conditions. Moreover, the exact threshold of wave amplitudes (between the two condition in Figure 7.2) might be expected to change, depending upon the detailed structure and density of plants, although a threshold between the two states would still exist.

The mimics were characterised by a variable leaf length, to recreate the vertical variation of "biomass" and the increased stiffness towards the root of the plants, found in natural *Posidonia oceanica* meadows. Some preliminary flume experiments (see Appendix B) showed that this structure was best at mimicking the plant "whip-like motion" observed in the field. However, the exact elevation of the peak in horizontal oscillatory velocity and the structure of the CBL might be affected by the details of the structure of the mimics (such as the number of leaves and length) as well as other characteristics of the meadow, such as density and plant distribution. For example, in this study, a regular distribution of the mimics was adopted, whilst in natural beds it is often random.

7.1.8 Implications for sediment transport

Posidonia oceanica is capable of modifying its hydrodynamic environment creating a rough surface and causing wave energy reduction, particularly for short-period waves and at low Reynolds numbers. Unidirectional flows were largely reduced and orbital velocities were also greatly affected, especially for the long-period waves tested. These findings confirm that *Posidonia* is able to shelter the seabed and protect beaches from wave erosion.

Waves play a much more important role in sediment transport (and hydrodynamics) in the study area than the extensively studied near-bed steady currents.

During storm conditions characterised by longer waves and largest wave heights (large A), the capability of the plants to absorb wave energy is reduced (possibly these plants have evolved their structure as a strategy to avoid damage from storm waves). However, under these large waves, the plants are still capable of producing locally-sheltered conditions, as they proved to be very efficient at reducing the orbital velocities very close to the bed; therefore, reducing also shear stresses and local sediment transport.

In the study region, an area of medium well-sorted sand was indentified in a narrow strip parallel to the shore, confined between the shoreface and the edge of the seagrass patch. The lack of this type of (highly-mobile) sand within the meadow amongst the plants might indicate that the plants prevent offshore sediment transport. Indeed, there is evidence of a positive (shoreward) asymmetry of wave-induced flows at the canopy top, from both the laboratory and field results, which would favour a shoreward drift (of water and probably of sand), especially for the largest waves (under storm conditions); this would provide a mechanism in beach protection.

However, the laboratory results also indicate that inside the canopy velocities become more symmetric than those over sand at the same water depth. It is therefore not clear from this study if this enhanced Stokes drift will have an effect near the seabed. Also, if the sand is transported in suspension over the seagrass it could be trapped by the plants, though turbulent exchange processes. These exchange processes should be investigated further.

The trapping effects of *Posidonia* meadows are expected to be reduced at the edge of the patches, because the vertical component of turbulence may be higher than outside the patch. Increased sediment resuspension, instead of deposition, could take place at the edge of the meadows under waves, as takes place around saltmarshes [*Feagin et al.*, 2009].

The large turbulent vertical exchanges observed are crucial for many ecological processes [*Koch et al.*, 2006a]; also, depending on the flow conditions, it may impact sediment motion in the canopy. Unfortunately, the OBS data collected in this study were not available, but observation of the sediment accumulations created after the tests indicated that there was considerable sediment movement; this probably took place in suspension. At the canopy edges (mainly seaward but, to a lesser extent, also shoreward) sand was progressively removed to the middle of the patch, where accretion occurred. However, in a natural *Posidonia* meadows the rough surface created by the rhizome, roots and associated organisms will help to trap sediment. Small, local scour

holes around the base of the mimics, about 1.5 cm deep, were observed throughout the patch, even in the central parts. These observations might not be applicable for established *Posidonia* beds on rough matte surfaces, but might occur when the plants are growing on sand in the first stages on new colonisation of the plant.

7.2 Conclusions

A number of conclusions can be drawn from this research:

1. The ability of shallow *Posidonia* meadows to reduce steady currents has been confirmed from field measurements. Current speed is reduced significantly and the current direction is more uniform than outside the seagrass meadow.
2. Field results indicate that shallow *Posidonia* meadows are effective at reducing wave energy, especially under low wave energy conditions and small wave amplitudes. Experiments under controlled conditions, with an artificial *Posidonia* canopy confirm this trend under both regular and irregular waves. Drag coefficients decrease in increasingly turbulent regimes (and Reynolds vegetation numbers), as in other submerged vegetation.
3. Friction factors produced by submerged canopies under higher wave Reynolds number decay with wave amplitude and may be predicted by empirical formulae, such as the Nielsen (1992) model. For a certain wave Reynolds number regime, canopy roughness (r) is only a function of the canopy characteristics, such as plant density and height. However, more work is required in low energy environment and field conditions, to examine the range of validity of this model.
4. Wave attenuation under irregular wave conditions (Jonswap spectra) by the artificial *Posidonia* canopy occurs at all frequencies, but mostly at the peak spectral frequency; thus confirming field results from other seagrass species in low energy environments.
5. *Posidonia* canopies in both natural conditions and the flume appear to enhance flow asymmetry above the canopy, especially under waves with the largest wave amplitudes. This is considered to have a significant effect on littoral drift, and that the shorewards component of the drift would be enhanced.
6. In the lower canopy wave-induced flows are reduced in all conditions but especially under the largest waves.

7. Both field and flume experiments show that, in the upper part of the canopy, oscillatory flows are not always reduced. Flume experiments confirmed this trend under both regular and irregular waves, indicating that in the upper part of the canopy flow reduction is likely to occur under waves with large orbital amplitudes.
8. Under regular waves the peak of turbulent kinetic energy is located at the top of the canopy; this was observed for other seagrass canopies under waves and unidirectional flows, in the field.
9. The structure of the benthic boundary layer is believed to be affected significantly by the wave orbital amplitude. The thickness of the canopy boundary layer is increased under waves characterised by large wave orbital amplitudes.
10. Increases in plant density, in the conditions tested, induce: greater wave attenuation; enhanced oscillatory flow deceleration; enhanced turbulent kinetic energy, at the top of the canopy.
11. High submergence ratios (h_s/D) in the flume experiments, produced larger wave height reduction and flow reduction within the lower part of the canopy. Vertical turbulent exchanges were lower at high submergence ratios, than lower submergence ratios.
12. The flume results show that conditions at the edge of the canopy are more turbulent and oscillatory flows are less reduced, than further inside the meadow, where more uniform and stable hydrodynamic conditions prevail.
13. Under large waves, *Posidonia oceanica* is less efficient at reducing wave energy; however, it is very efficient at reducing oscillatory flows, therby locally reducing sediment transport. There is also evidence that above *Posidonia* canopie flow asymmetries are increased and a preferential shoreward drift might develop. This would reduce sand dispersal offshore.

7.3 Future work

This study focuses mainly upon the hydraulic roughness of canopies under waves. The next step would be to examine how this modified roughness influences sediment transport, with direct measurements.

Research on wave-submerged canopy interaction is still limited, especially for the Mediterranean *Posidonia oceanica,* an important habitat-forming species located in

a microtidal, wave-dominated regime. The field survey revealed that the complexity of the topography, in the nearshore areas, is determined by *Posidonia oceanica* distribution. This complex topography may contribute to the seabed roughness, which would act in addition to the canopy hydraulic roughness (quantified in the laboratory for *Posidonia* mimics over a flat sandy bed). Quantification and description of the physical roughness of seagrass meadows may lead to better predictions of the hydraulic drag. Also more detailed numerical modelling (such as boundary layer processes models), based on this large dataset, would improve the understanding of the processes involved in submerged flexible canopy-wave interactions. This will also benefit research on sediment transport in vegetated canopies, having implications for ecological studies.

The data on water turbidity (hence, suspended sediment concentration) from the CIEM flume experiments have not been analysed yet, partly because: (a) sediment movement was larger than expected; and (b) during most of the tests the OBSs were buried by sand or sediment starved. However, the available data will be analysed in the future and compared with the hydrodynamic conditions found in this study. This will give direct evidence of the effect of *Posidonia* mimics on sediment motion at the edge of the patch and in the surrounding area. Similar work should be carried out in the field (away from any lagoons), where the presence of root structures and the complex sediment composition will probably have a large effect on the sediment transport in *Posidonia* canopies, in wave-dominated environments.

A hydrodynamic model should be calibrated with the data collected in this study and validated with the data obtained in the field (bathymetry, canopy height and distribution, hydrodynamics), in order to examine beach stability in Sardinia. It could also be used to predict wave propagation in the presence of a *Posidonia* meadow, and then used for coastal management of many Mediterranean shorelines.

Further work is required on the structure of the orbital velocities in natural *Posidonia* beds, to validate the conceptual model presented earlier in this Chapter under different wave conditions. Also the range of conditions and the applicability of the wave dissipation model, based upon Nielsen's (1992) formula needs verification in a natural system.

Other important aspects to explore are the interaction of large storm waves and the combination of waves and steady currents within submerged canopies. If a steady current is superimposed on a wave boundary layer, it could be expected to affect the height of the canopy, the amount of plant motion; hence, the structure of the canopy

boundary layer. This would be important in tidal areas, but also for those growing in shallow areas, where waves are likely to be asymmetric and where significant drift results.

Few studies have considered how wave conditions might affect the distribution of *Posidonia oceanica*. Furthermore, these studies might be affected by local factors (i.e. they might be affected by, presence of currents, water turbidity levels, sediment characteristics). Manca (2006) has suggested that high sediment mobility might be a limiting factor for *Posidonia* growth, in an exposed beach in the west Sardinia. Others have also suggested, from investigations undertaken in the Ligurian Sea, that the depth of closure could be an indication of the location of the upper limit of the meadow [*Vacchi et al.*, 2010]. Understanding the levels of wave energy (and sediment transport) that this species of seagrass can tolerate could thus, be valuable in coastal and ecological modelling. This information, together with further research undertaken on *Posidonia*'s effects on waves, will be valuable for improving numerical morphodynamic modelling in vegetated coastal areas, for a more accurate evaluation of the economic value of the *Posidonia* ecosystem and the protection of this valuable habitat.

APPENDIX A : Field data

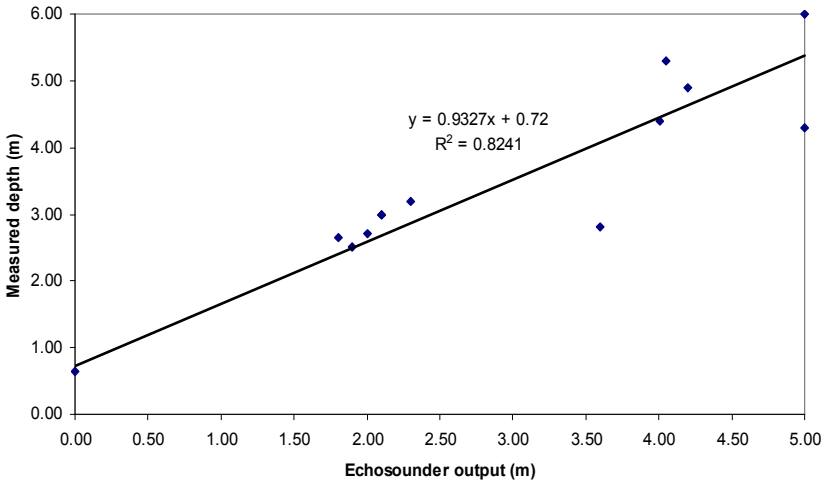

Figure A. 1 Calibration curve of the echosounder for the bathymetry survey (Significance level P=0.05).

Table A. 1 Descriptions of *Posidonia oceanica* shoots and location of the samples in UTM coordinates (WGS 84 datum) and distance from the shoreline.

ID	Eastings	Northings	Distance from shore (m)	Average shoot length (cm)	Std dev. shoot length	Average width (cm)	Average base length (cm)	Number of leaves	Max density (shoots/m^2)	Mean density (shoots./m^2)	St.dev. mean density
V3	461338	4408713	405	36.1	4.5	1.0	3.4	6	312	212	87
V2	461463	4408670	275	0	0	0	0	0	0	0	0
V2.edge	461463	4408670	280	21.0	8.0	0.8	2.6	5	232	187	40
V1	461527	4408662	218	0.0	0.0	0.0	0.0	0.0	0	0	0
Stn1	461118	4408784	634	22.3	3.9	0.8	1.7	5	448	365	73
Stn2	461118	4408784	634	21.2	6.9	0.8	2.4	5	288	256	49
Stn3	461423	4408649	300	37.2	2.8	0.9	3.8	5	320	296	21
Stn5	461513	4408642	218	0	0	0	0	0	0	0	0
Stn7	461569	4408607	152	0	0	0	0	0	0	0	0
Stn8	461609	4408578	102	0	0	0	0	0	0	0	0
Stn9	461624	4408568	84	0	0	0	0	0	0	0	0
Stn10	461431	4408680	308	20.8	0.6	0.9	2.4	6	340	235	96
Stn11	461388	4408697	353	33.5	4.7	1.1	3.4	4	244	227	21
Stn12	461334	4408697	401	26.2	5.0	0.8	2.5	5	252	228	22
Average values excluding un-vegetated stations				**27.3**	**4.6**	**0.9**	**2.8**	**5.2**	**304.5**	**250.7**	**51.1**

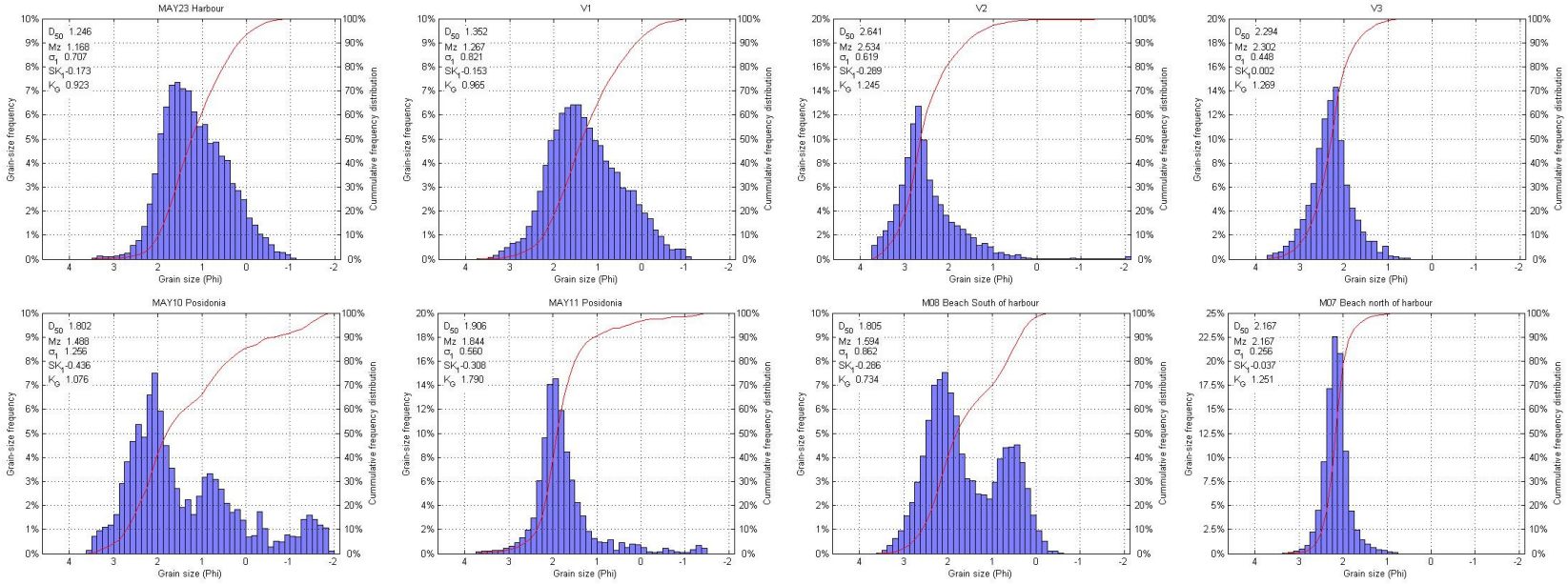

Figure A. 2 Sand grainsize distribution curves at some representative locations in the field study site. Red curves are the cumulative distribution of grain-size

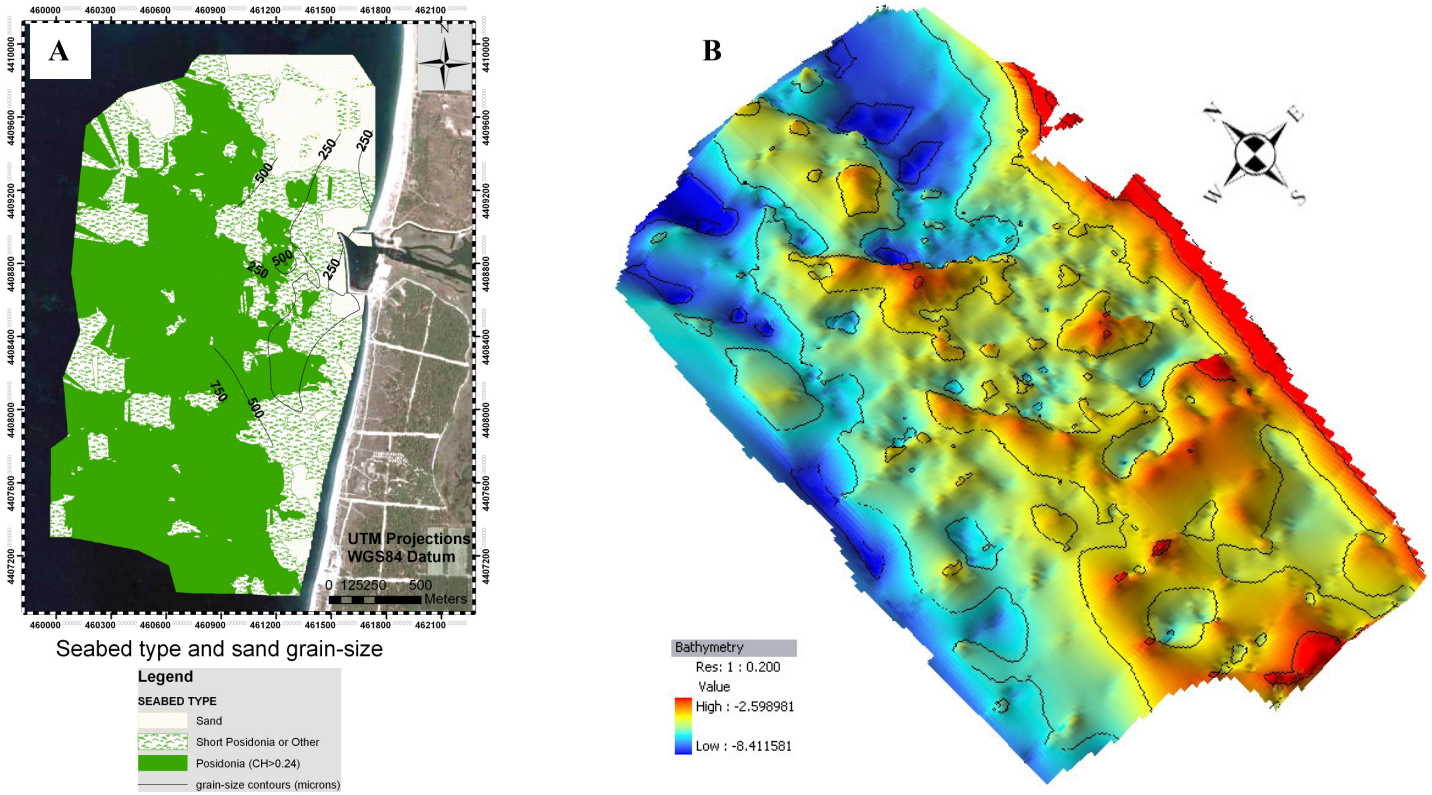

Figure A. 3 A) Seabed type and grain size distribution in the study area. B) 4 3D maps of the seabed morphology and bathymetry contours in the study region

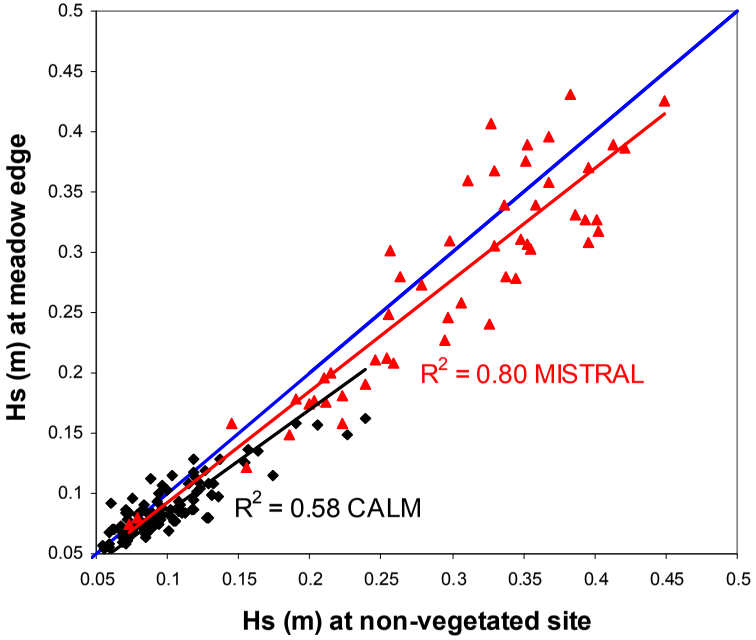

Figure A. 5 Wave height variation between the site at the edge of the seagrass meadow (V2) and the un vegetated site (V1). Regression lines are plotted with their corresponding correlation coefficients for both Mistral and low energy periods.

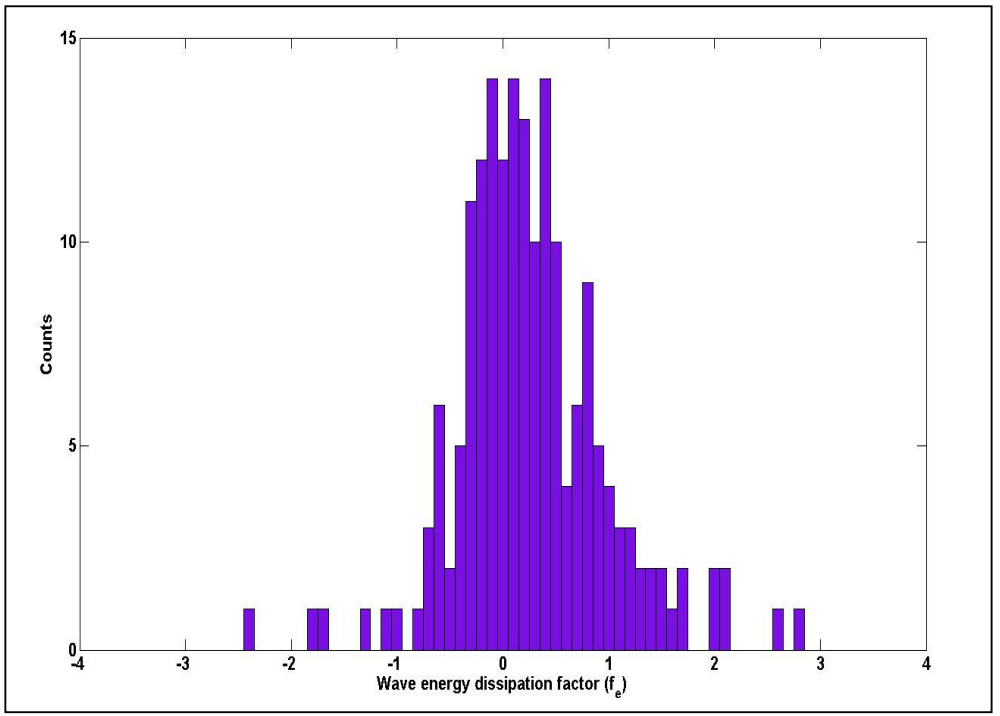

Figure A. 6 Histogram of wave energy dissipation factor between stations V3 and V2.

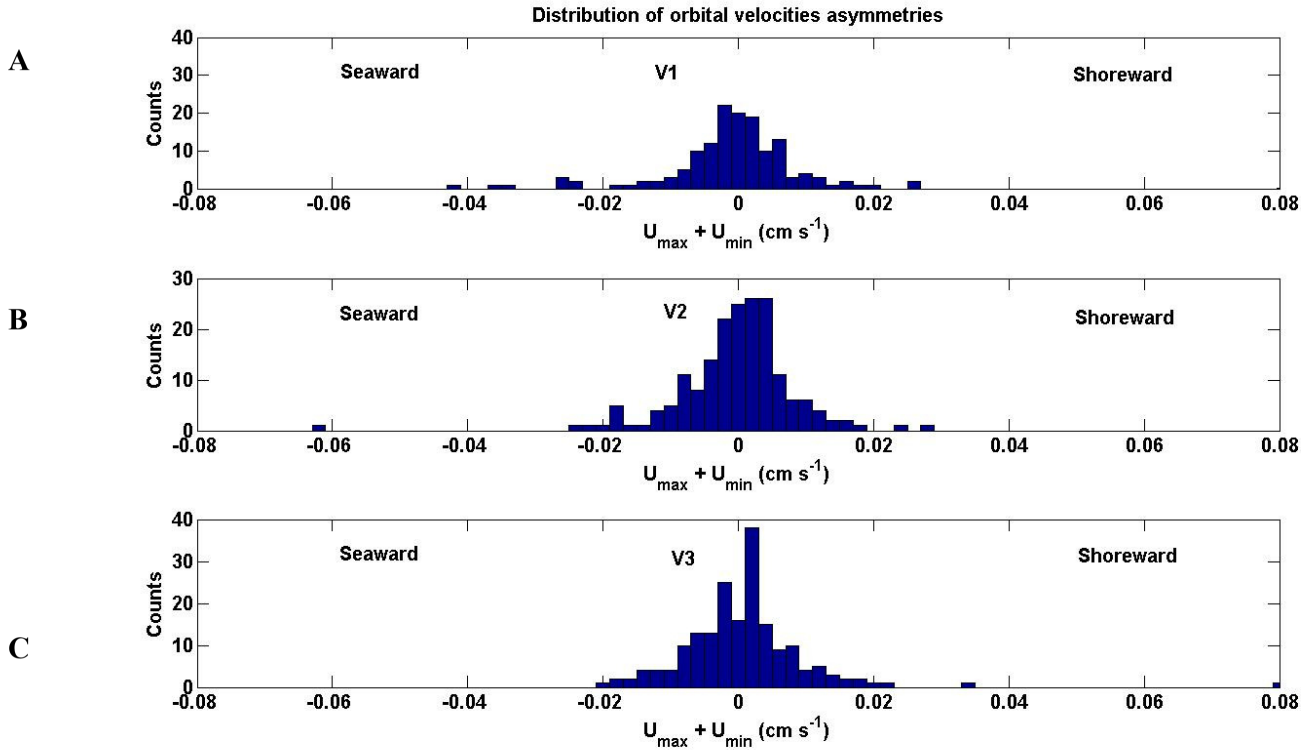

Figure A. 7 A) Histogram of orbital velocity asymmetries (U_c+U_t) at V1; B) Histogram of orbital velocity asymmetries (U_c+U_t) at V2; C)Histogram of orbital velocity asymmetries (U_c+U_t) at V3. A positive asymmetry indicates a potential net shoreward drift.

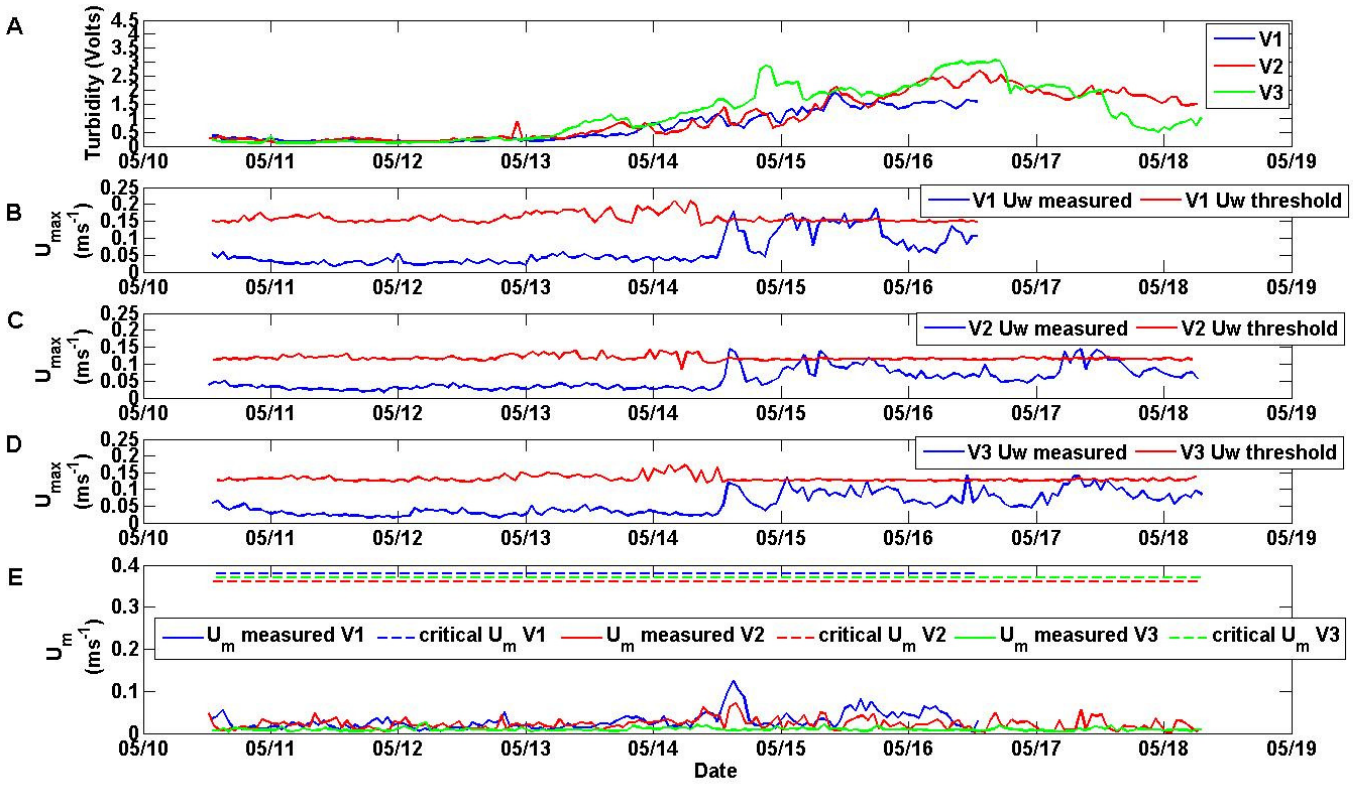

Figure A. 8 A) Measured turbidity at V1, V2 and V3. B) Measured maximum orbital velocity (U_{max}) and critical orbital velocity for sediment motion at V1 C) Measured maximum orbital velocity (U_{max}) and critical orbital velocity for sediment motion at V2 D) Measured maximum orbital velocity (U_{max}) and critical orbital velocity for sediment motion at V3. E) Measured mean current and threshold current for sediment motion at V1, V2 and V3.

APPENDIX B: Design of *Posidonia oceanica* mimics

B.1 Introduction

This section briefly describes an investigation, undertaken at the National Oceanography Centre, for the design of a suitable full scale *Posidonia oceanica* mimic. A plastic mimic of natural shoots of *Posidonia oceanica* was required for use in a wave flume for two main reasons: *Posidonia oceanica* is a protected species [*Buia et al.*, 2004] and hence cannot be harvested; and the full scale flume uses only freshwater while *Posidonia oceanica* is a marine species. Furthermore the ratio between the plant blade density and water density differs between saltwater and freshwater. No information or guidelines were found in literature on how to design a plastic mimics that simulate the behaviour of a marine mimic in water. Hence the reason for this research.

The experiences on mimic design are presented here. In Section B.2, the morphology of the plants and the relevant characteristics of a *Posidonia oceanica* meadow are described. The first part of Section B.3 deals with preliminary observations on the behaviour of natural *Posidonia oceanica* shoots under unidirectional currents and the comparison with several plastic materials. The second part examines the four mimic options selected after the preliminary tests. In Section B.3.3 velocity profile experiments are presented comparing these mimic options with results from a patch constructed from real *Posidonia* shoots. Finally in Section B.3.4 the mimic design proposed for the full scale tests is described.

B.2 Characteristics of *Posidonia oceanica* meadows

Posidonia oceanica plants are made of several shoots growing up from vertical rhizomes. The shoots (Figure A.1) have ribbon-like leaves, 1 cm wide and up to 75 cm long [*Buia et al.*, 2004]. The base, attached to a vertical rhizome, is stiff and is characterised by scales, which can be several years old, made of old bases of leaves that have become senescent and detached. External leaves are older and generally stiffer and longer. They are characterised by a thicker less flexible base with two “little wings”

(stipule) (Figure B. 1). Intermediate leaves are shorter and thinner. *Posidonia* shoots are therefore thicker and more rigid at their bases and thinner and more flexible at their tips. Typical *Posidonia oceanica* canopy characteristics, relevant to the design of the mimics, are reported in Table B. 1. The height, determined from the leaf length, is variable and changes with the season, with the longest leaves occurring in summer (Gobert et al., 2006).

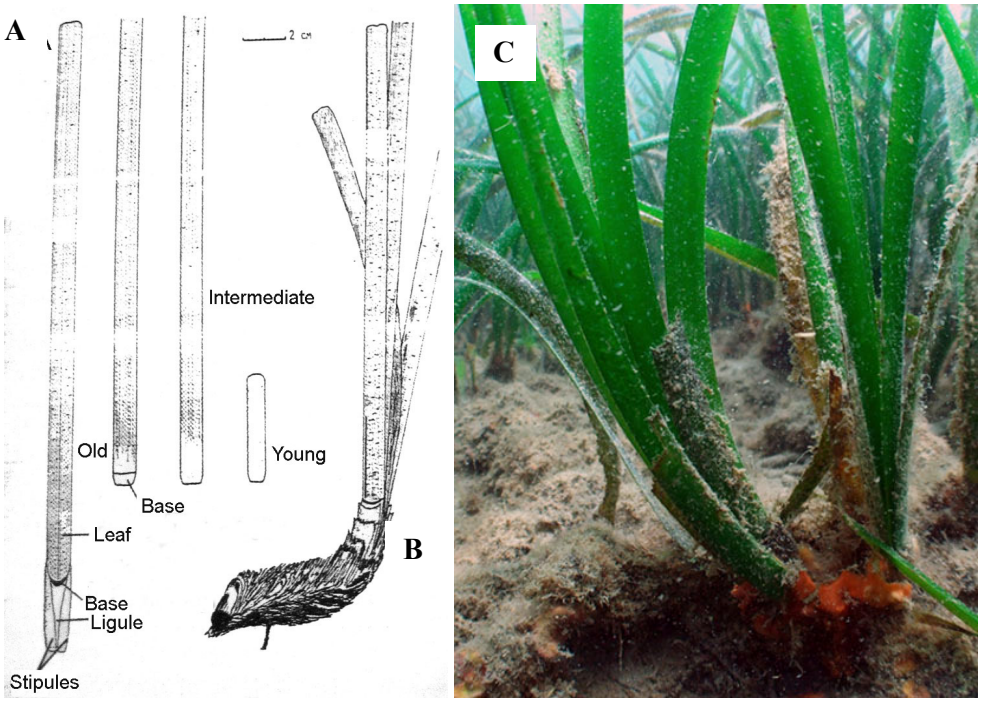

Figure B. 1 A) *Posidonia oceanica* leaf morphology and classification: Old leaves have a stiff base: Intermediate leaves don't have a base and are longer than 5 cm: juvenile leaves are shorter than 5 cm Rhizome with scales (old sheaths) and leaf shoot (modified from Buia et al., 2003). B) *Posidonia* oceanica shoots. C) *Posidonia* oceanica plants.

In general, shoots are arranged in small groups (within one plant) and groups have a random distribution. In some cases, when the flow is in a constant direction (whether unidirectional or oscillatory), seagrass shoots align in rows perpendicular to the flow, giving the maximum drag (Fonseca and Koehl, 2006). The density of the plants (see Table B_1) generally decreases with depth [*Gobert et al.*, 2006], and does not significantly change throughout the year [*Pergentmartini and Pergent*, 1994; *Gacia and Duarte*, 2001].

Table B. 1 Shallow *Posidonia oceanica* plants and meadow characteristics. The measured data refer to samples collected during the field campaign in May 2007 described in Chapter 3.

Average parameter	*Posidonia oceanica* (shallow)	Reference
Stem density (stems/m^2)	700	[*Buia et al.*, 2004]
	230 (between 3 and 5 m depth)	Measured (herein)
Number of leaves per shoot	7/8 (all types of leaves)	[*Buia et al.*, 2004]
	4 (adults leaves only)	Measured (herein)
	6.2 ± 1.85 (all types of leaves)	Measured (herein)
Average leaf width (mm)	10	[*Buia et al.*, 2004]
	9.0±0.9	Measured (herein)
Maximum leaf length (cm)	75	[*Buia et al.*, 2004]
	58.6	Measured (herein)
Base height (cm)	2.7 ±0.5	Measured (herein)
Leaf Thickness (mm)	0.2	[*Folkard*, 2005]
Modulus of elasticity of leaves (Nm^{-2})	4.7±0.6 X 10^8	[*Folkard*, 2005]
Density of leaf material (kg m^{-3})	910±110	[*Folkard*, 2005]

B.3 Mimic selection

B.3.1 Preliminary tests

Several cheap plastic materials were considered as possible *Posidonia* mimics and compared to real plant shoots. The shoots used in this study came from rock pools in Sardinia (Italy), where a recent large storm had conveniently deposited entire plants shoots

The plants were kept refrigerated in bags with saltwater and flown to the National Oceanography Centre (NOC) were they were immediately placed in a saltwater aquarium exposed to sunlight. The plants remained in very good condition in the aquarium. During the experiments, the plants were moved to a freshwater unidirectional flume for only a few hours each day. The bending and buoyancy of some readily available plastic materials were compared to the natural shoots of similar maximum length.

Preliminary visual comparison tests of the mimics with the natural seagrass plants, under a unidirectional flow, were used to select materials that showed similar

bending to the natural seagrass. A photo taken during one of these experiments is shown in Figure B. 2. The numbers 1-6 in the image are codes for the type of plastic used, described in Table B. 2 Furthermore later comparisons in the flume were made with another material Polypropylene (PP) (Figure B. 7).

Table B. 2 Plastic materials used in preliminary tests.

Code Number in Figure B. 2	Abbreviation	Material	Thickness (mm)
1	PVC	PVC film (common plastic folders)	0.25
2	LDPE 3	Low Density Poly-ethylene foam	3.0
3	LDPE FILM	Low Density Poly-ethylene film	0.1
4	BB	Bubble wrap	0.5-7.0
5	LDPE 1.5	Low Density Poly-ethylene foam	1.5
6	LDPE	Low Density Poly-ethylene foam	1.0
Not included See Figure B.2	PP	Poly –propylene	1.0

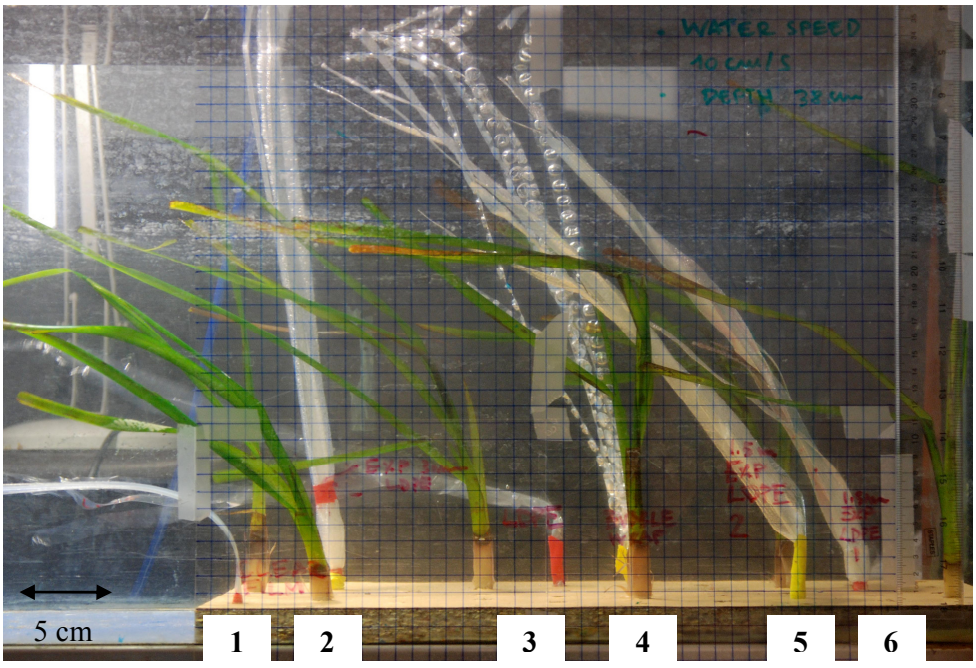

Figure B. 2 Preliminary tests for the selection of the mimic plastic material. Plastic mimics and *Posidonia oceanica* seagrass shoots in the NOC flume. All mimics were made of 6 leaves and a common structure. The test shown was for a flow depth of 38cm and flow speed of 10 cm s^{-1}.

All mimic plants were created in the same way: by aligning three 110 cm long strips, folded in half to create 6 “leaves” with a length of 50 cm. The stiff base was

simulated by folding and stapling the lower 10 cm of the "leaves" (example for LDPE Figure B. 3, 6 staples 1cm long). Part of the base was wrapped with tape and inserted into a 1cm diameter hole in a plywood plate.

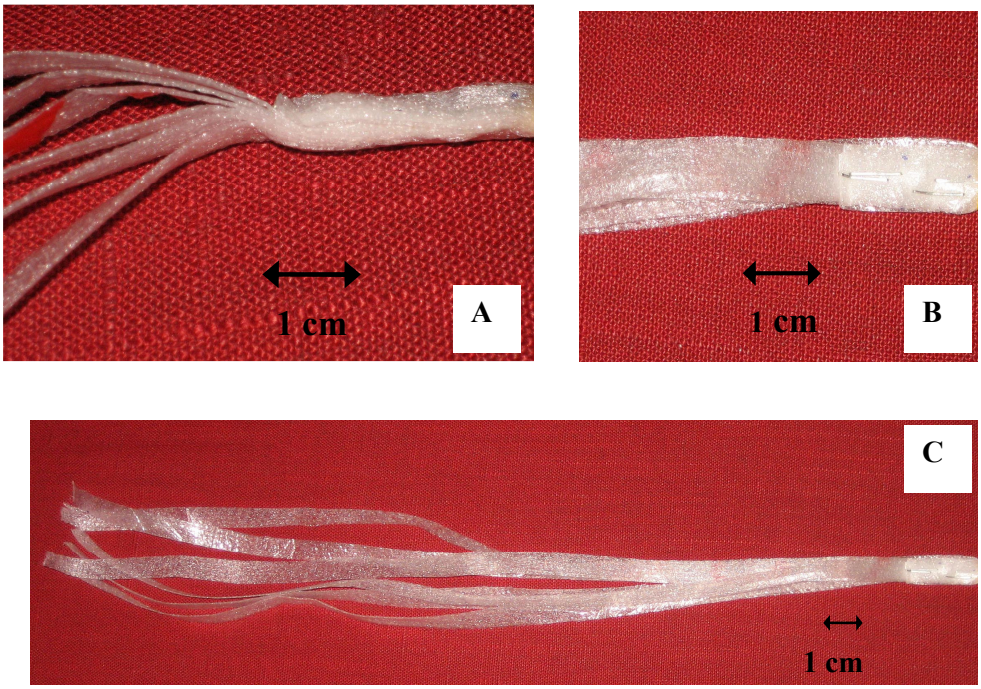

Figure B. 3 LDPE mimics. A: detail of the base, side view. B: Detail of the base, top view. C: Full size mimic

The tests showed that LDPE 1 mm thick foam had the closest hydraulic behaviour to natural plants, and it was selected for more detailed tests. The LDPE FILM (0.1 mm) that was used in previous studies in small unidirectional flumes by Folkard (2005) and Maltese (2007), was very flexible and bent more than real seagrass, and was thus rejected from full scale experiments. Further tests were then carried out with stiffer Polypropylene strips (PP). This material has the advantage that it is cheap and available pre-cut in 1 cm wide strips, commonly used at parcel strapping.

B.3.2 Mimic options

The following 4 options, summarised in Table B. 3, were considered as possible mimics for *Posidonia oceanica* and more detailed tests were carried out. Plants were made either with the same leaf length (Options 1 and 2, in Table B. 3) or with variable leaf length as proposed by Folkard (2005) and Maltese (2007), giving a more realistic canopy structure (Option 3 in Table B. 3). The shoot arrangement and geometry are the

same as for Option 1 and 2, but with leaves pairs having lengths: 50cm, 25 cm, and 15 cm. The leaves were arranged with the shortest ones innermost and the longest outermost.

B.3.3 Velocity profile experiments.

In order to select a suitable shape and material for *Posidonia oceanica* tests were performed in a NOC flume. The vertical velocity profiles produced downstream of the trailing edge of a patch of natural seagrass were compared with profiles by a patch of mimics. The 4 options of Table B. 3 were tested.

The flume at the NOC is 5 m long, 0.3 m wide and has a maximum water level of 0.45 m [*Neumeier*, 2007]. The experiments were performed under a constant unidirectional current of around 8 cm s^{-1} (SLOW) and 10 cm s^{-1} (FAST). Forty-three real shoots were "planted" in a wooden board 0.28 m wide and 0.45 m long with 0.01 m holes, and were distributed in a regular pattern with a density of 350 shoots m^{-2}. Pre- and post-patch vertical velocity profiles were measured and recorded under "SLOW" and "FAST" flow conditions with a high resolution velocimeter (Acoustic Doppler Velocimeter, Vectrino, Nortek Ltd) sampling at 25 Hz.

Table B. 3 Mimic design options and characteristics of the options further tested

	Option 1	Option 2	Option 3	Option4
Name	LDPE	PP	LDPE mod	PP var
Material	LDPE	PP	LDPE	PP
Number leaves/shoot	6	6	6	6
Width strip (mm)	10	10	1.2	1.2
Length strips (cm)	50	50	Variable 40,25, 10	Variable 40,25, 10
Base height (cm)	5	5	5	
Thickness strips (mm)	0.8	1	0.8	1
Modulus of elasticity of leaves (N/m^2)	unknown	0.85×10^8	unknown	0.85×10^8
Density of leaves (kg/m^3)	450	880 (Butyl Products Ltd.)	450	880 (Butyl Products Ltd.)

The profile post-patch was located at X=0.65 m (X=0 is the upstream edge of the board, positive values downstream), and the one pre-patch at X=-0.2 m. In the first tests ("SEAGRASS") real *Posidonia* shoots were fixed to the board. Natural shoots had a variable leaf length with a maximum value of 56 cm, most of the leaves were about 40 cm long. The heights of the base of the plants were between 1.5 and 3.5 cm high. The

canopies (real plants and mimics) were submerged at all times. Control tests, with the board only, were also performed.

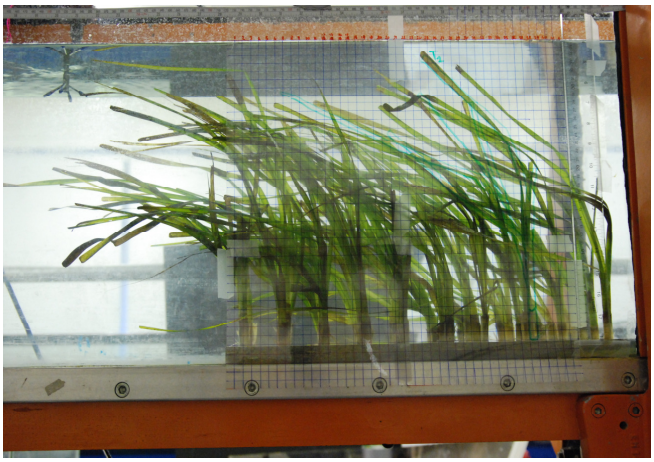

Figure B. 4 *Posidonia oceanica* patch in the NOC flume under a 10 cm/s unidirectional flow.

An example of the results from the natural canopy is presented in Figure B. 6 (FAST flow case). An increase of flow velocity compared to the control profile (board only profile) was observed above the canopy. At mid depth, flow reduction was measured, peaking at an elevation roughly corresponding to the maximum leaf biomass. These results agree qualitatively with those found in previous studies on *Posidonia oceanica* mimics under currents performed in small flumes [*Folkard*, 2005; *Maltese et al.*, 2007].

LDPE foam mimics were prepared, according to Option 1 (LDPE) and Option 3 (LDPE mod) of Table B. 3 as shown in Figure B. 1. Images of the tests relative to Option 1/LDPE are shown in Figure B. 5 plot A, and tests relative to Option 3/LDPE mod are shown in Figure B. 5 plot B. An example of the resulting profiles, for these two options, is shown in Figure B. 6.

From the tests, it emerged that variable length LDPE mimics (Option 3/LDPE mod) were able to better reproduce the skimming flow at the canopy top and the reduction in flow below, than mimics with constant blade length (Option 1/LDPE). However the structure of the profile at the canopy level differed greatly from real seagrass measurements. Moreover, the velocity reduction with the LDPE mimics was smaller. This was probably due to the fact the plastic leaves were seen to be “flapping” and undulating much more than real ones, therefore they were too buoyant and flexible.

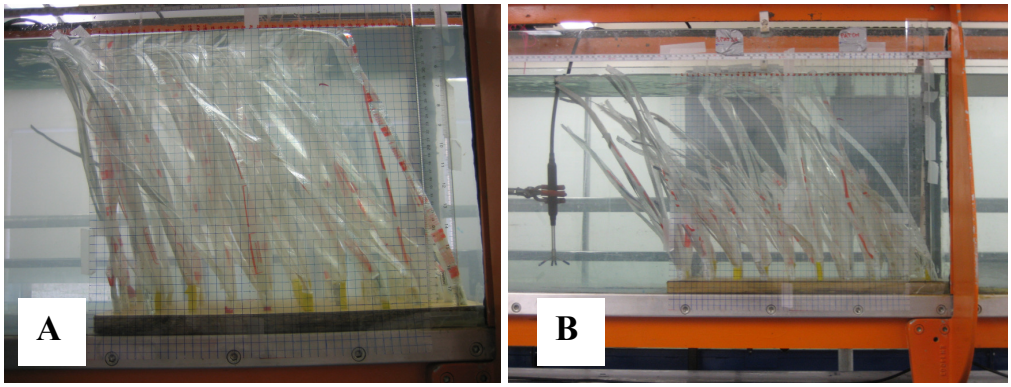

Figure B. 5 A) LDPE mimics (Option 1/LDPE), with uniform leaf length patch under a 10cm/s unidirectional flow. B) LDPE Modified mimics (Option 3/LDPE mod), with variable leaf length patch

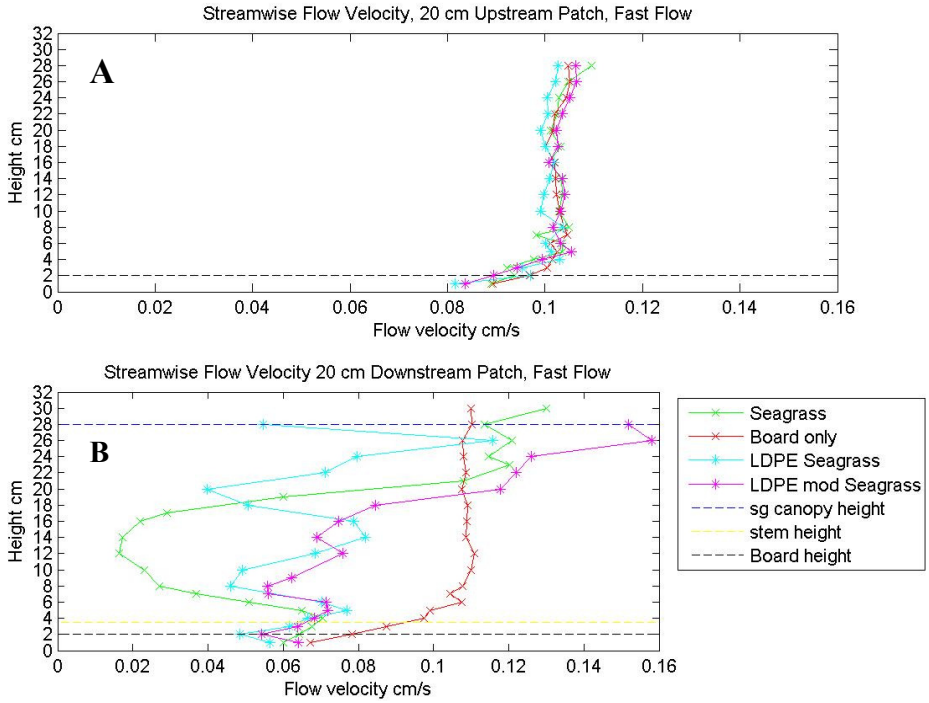

Figure B. 6 Options 1 and 3, "FAST" flow conditions Plots of vertical velocity profiles obtained upstream (A) and downstream (B) of a real *Posidonia* patch (Seagrass), a mimic patch (LDPE =Option1 and LDPE mod =Option 3) and the board only (Board only). The yellow line refers to the maximum height of the leaf base, the blue line is the top level of the bent canopy and the black line indicates the height of the board that was holding the shoots in place.

The PP strapping was then tested in the flume (Option 2/PP and Option 4/PP var) under the same flow conditions as the previous tests with real seagrass (Figure B. 7A and B). Mimics were assembled using the same method as described for LDPE in Figure B. 3. The observed bending and movement in the water of the PP mimics was very similar to that of the real plant at several flow

speeds. However, in the case with uniform leaf length (Option 2/PP) most of the canopy mass was restricted to a narrow range between 29 and 20 cm above the flume bed, therefore the peak attenuation was recorded in that region. It is clear from the graph (Figure B. 8) that the total attenuation of flow is considerably less than both the real seagrass and the variable length mimics (Option 4/PP var).

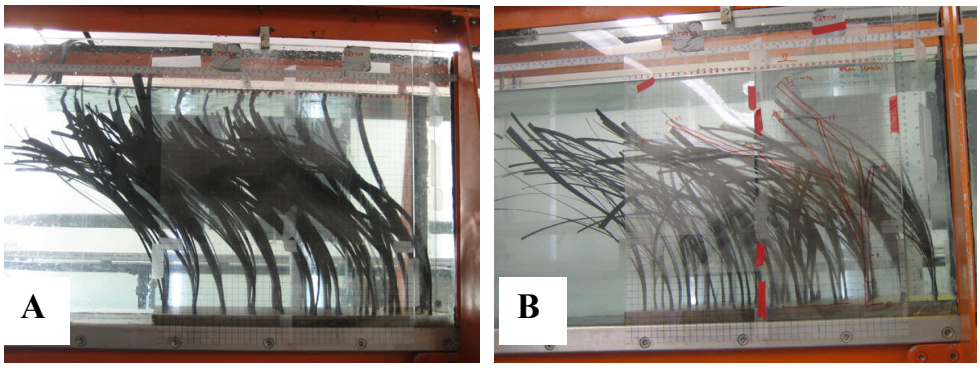

Figure B. 7 A) PP regular length (Option 2/PP) under a 10 cm/s flow. B) PP variable length (Option 4/PP var) under a 10cm/s flow.

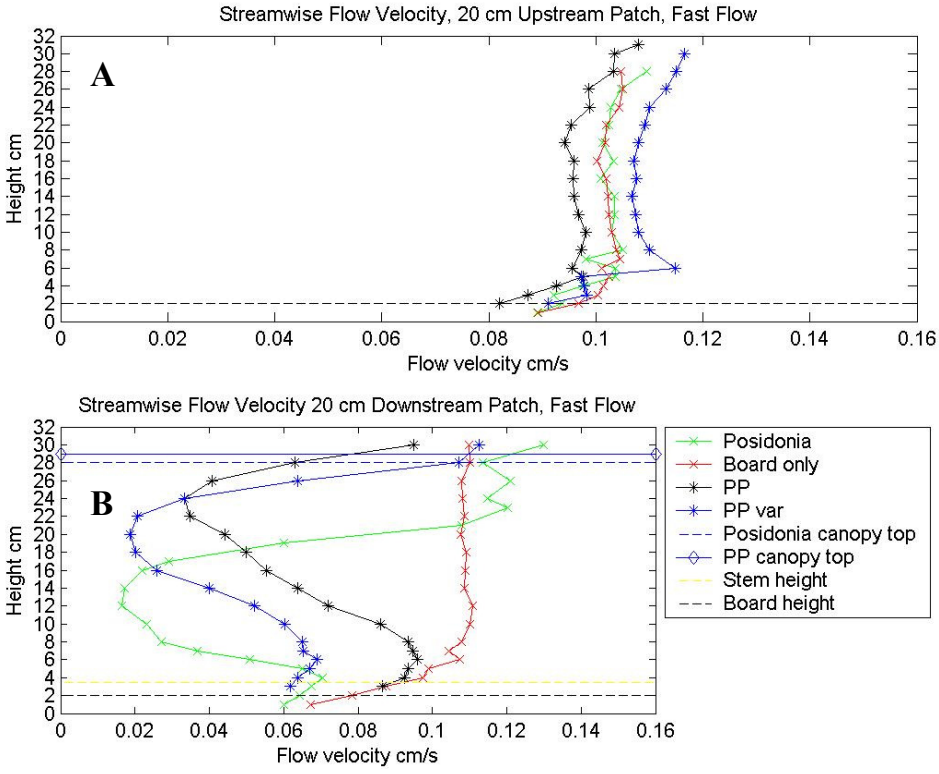

Figure B. 8 Options 2 and Option 4 for "FAST" flow conditions. Plots of vertical velocity profiles obtained upstream (A) and downstream (B) of a real *Posidonia* patch (Posidonia), a PP mimic patch (PP corresponding to Option 2), a variable length PP patch (PP var, corresponding to Option 4) and the board only (Board only). The yellow line refers to the maximum height of the leaf base, the

black line indicates the height of the board, the blue solid line is the top level of the bent canopy and the blue dashed line is the top of the bent PP canopy.

In addition, the uniform mimics produce little attenuation compared to the real seagrass (and also the variable length mimics) closer to the seabed. The structure of the flow was best reproduced by the Option 4 mimic.

B.3.4 Final mimic canopy design

Posidonia meadows could be simulated with randomly distributed shoots as in previous flume studies involving *Posidonia* (Folkard 2005, Maltese et al., 2007). A density of about 325 shoots/m^2 is proposed. The patch length should at least be equal to the wave length, which in the flume will vary between around 5 and 13 m (for the tests in program, see Chapter 4). According to Fonseca and Koehl (2006) a uniform seagrass bed is better mimicked when the bed width equals the flume width (3 m), however the movement of the mimics at the edges will be affected by the flume's sidewalls. If a patchy seagrass distribution instead of a uniform meadow, is to be simulated, than a patch width smaller than the flume width could be adopted.

Option 4, with six 1.2 mm wide polypropylene plastic leaves and variable leaf length (15, 25 and 40 cm length), was found to be best suited for the design of the mimic. The advantage of this material is that it is cheap, it is not water absorbent; it is available from the packing industry in Barcelona and readily available in strips of 1cm or 0.9 cm width.

Ultimately this material was not adopted in the final design of the mimic because when the material was supplied in commercial quantities as coils, even when cut, it retained a "memory" of the bending from storage in the coils. The fact that this material has a "memory", could have caused problems after several runs in the flume. Therefore it was not used and a similar material (PVC foam) was tested and selected, available as flat sheets and easy to cut (as presented in Chapter 4). The plant mimics still incorporated the structure and the variable leaf length design, which was better at reproducing the structure of the canopy under flow and produced a similar velocity profile to real plants.

APPENDIX C: Laboratory data

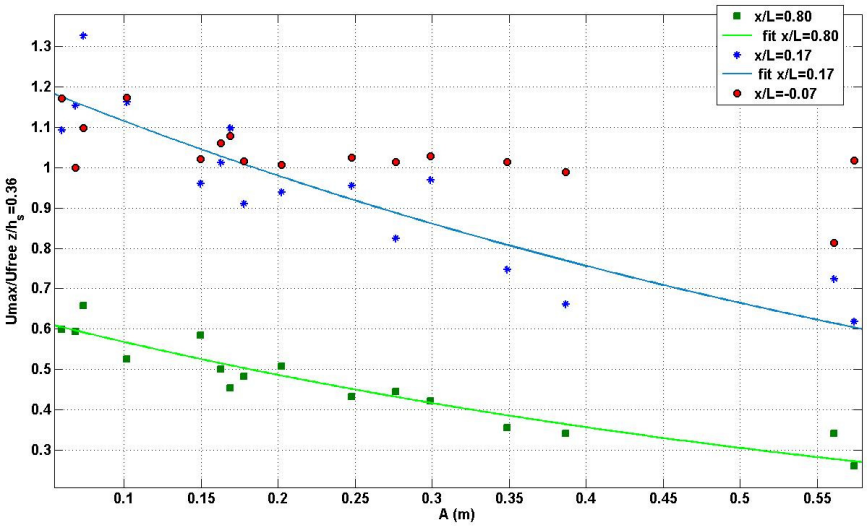

Figure C. 1 Normalised horizontal orbital velocities ($U_{max}/U_{free,}$) in the lower canopy (z/h_S=0.36) plotted with wave orbital amplitude. Tests with 260 stems/m^2. Different colours correspond to different locations: in front of the patch (x/L=-0.07); within the patch near the leading edge (x/L=0.17) and further into the patch (x/L=0.80). The solid lines are the fit to an exponential decay function $\frac{U_{\max}}{U_{free}} = a\exp(bA)$, with the coefficients a and b reported in Table C. 1

Table C. 1 Fit of the normalised velocities (U_{max}/U_{free}) to an exponential decay function. U_{max} is the maximum orbital velocity, U_{free} is the free stream velocity, A is the wave orbital amplitude, R^2 is the correlation coefficient of the fit, RMSE is the root mean square error of the fit, a and be are the coefficients of the function. The functions are plotted in Figure C. 1.

z/h_s	x/L	R^2	RMSE	*a*	*b*
0.36 (lower canopy)	0.17	0.81	0.088	1.27	-1.29
	0.80	0.89	0.038	0.66	-1.55

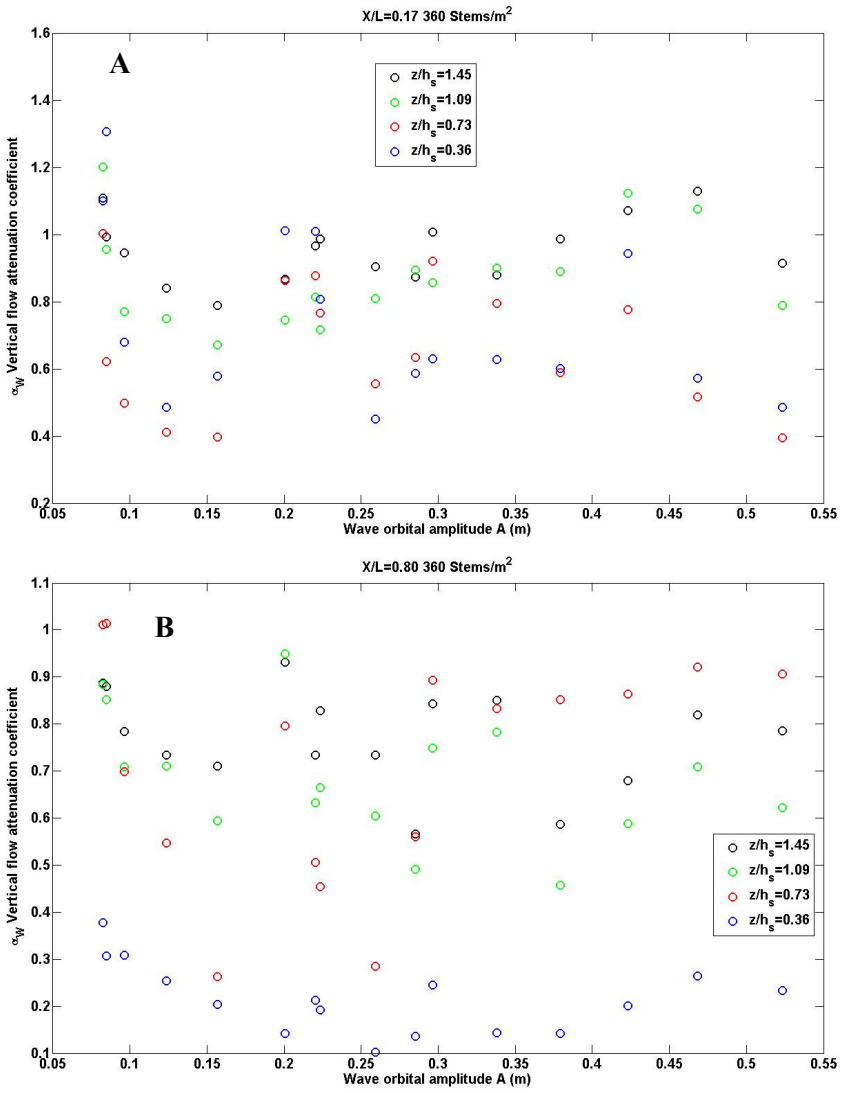

Figure C. 2 Vertical component of the oscillatory flow. Variation of the vertical flow attenuation coefficient (α_W) with wave orbital amplitude (A) at 4 elevations above the bed for the tests with 360 stems/m^2 at x/L=0.17(plot A) and at x/L=0.80 (plot B).

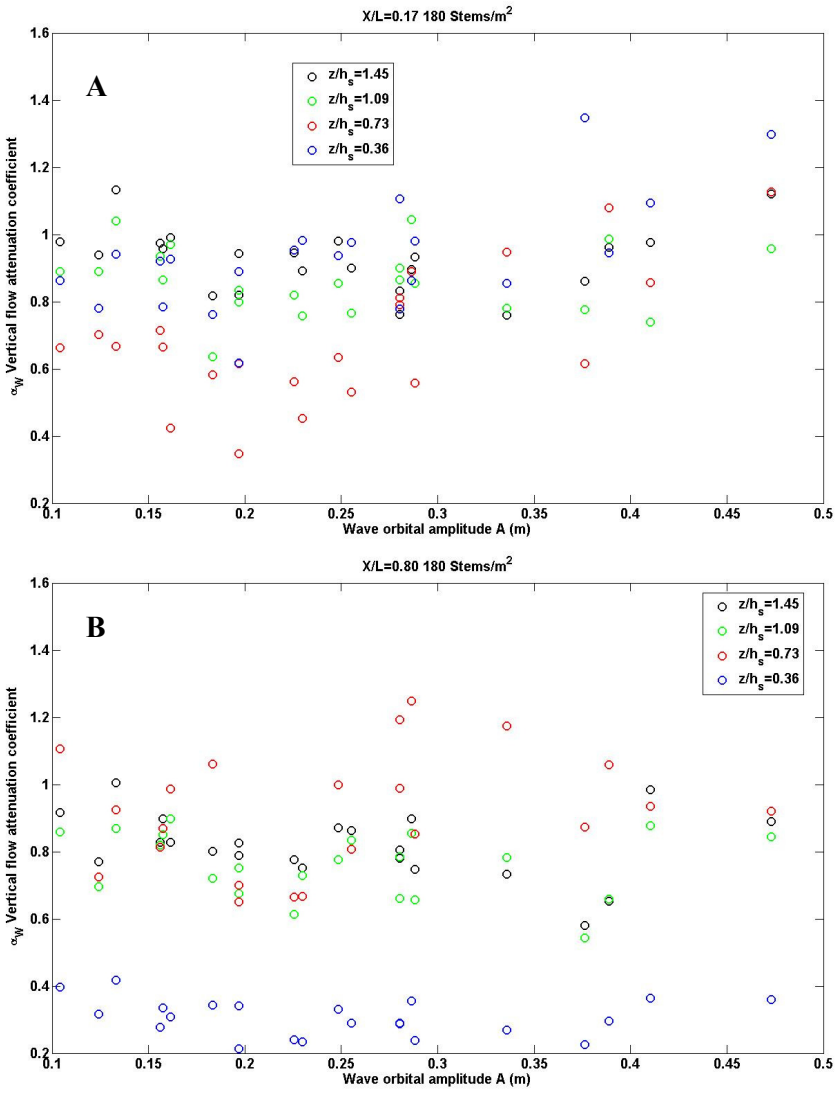

Figure C. 3 Vertical component of the oscillatory flow. Variation of the vertical flow attenuation coefficient (α_W) with wave orbital amplitude (A) at 4 elevations above the bed for the tests with 180 stems/m^2 at x/L=0.17(plot A) and at x/L=0.80 (plot B).

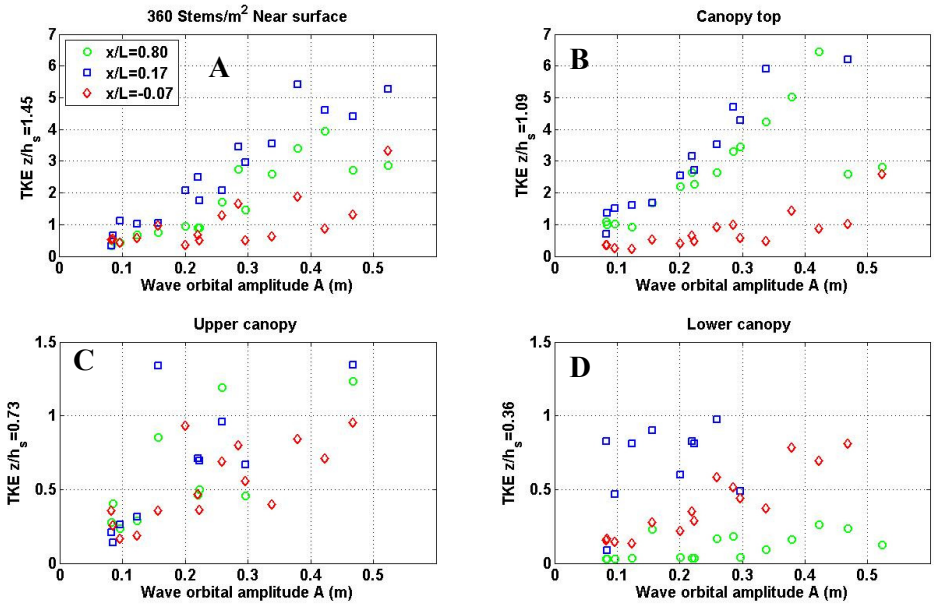

Figure C. 4 Turbulent kinetic energy (TKE) at different elevations from the bed plotted against wave orbital amplitude (A-D). Symbols in each plot indicate different locations along the flume, (tests with 360 stems/m^2).

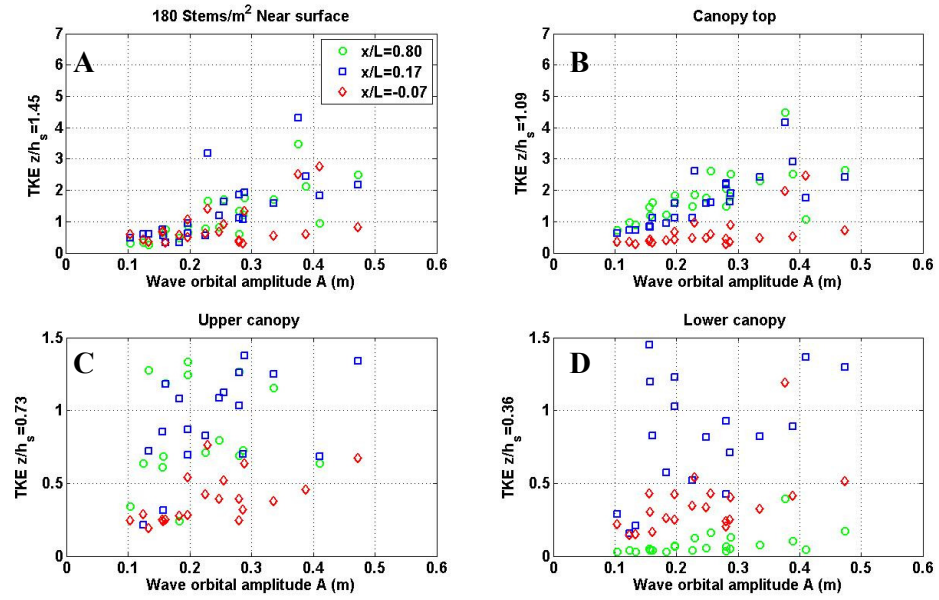

Figure C. 5 Turbulent kinetic energy (TKE) at different elevations from the bed plotted against wave orbital amplitude (A-D). Symbols in each plot indicate different locations along the flume, (tests with 180 stems/m^2).

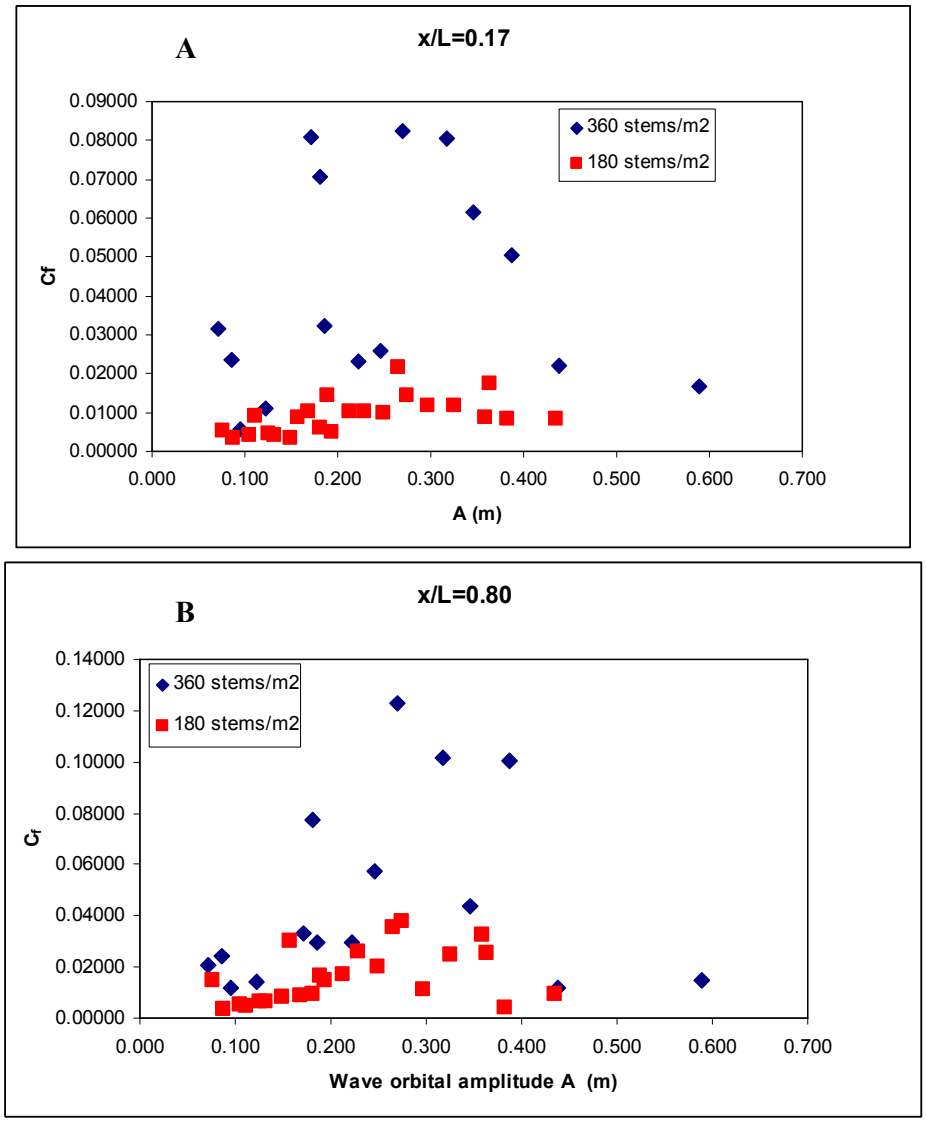

Figure C. 6Shear stress coefficients (C_f) plotted with wave orbital amplitude (A) for both canopy densities tested. A) near the leading edge of the patch at x/L=0.17 B) and further into the patch at x/L=0.80.

APPENDIX D : Publications and Reports

Literature cited

Almela, E. D., N. Marba, E. Alvarez, R. Santiago, R. Martinez, and C. M. Duarte (2008), Patch dynamics of the Mediterranean seagrass Posidonia oceanica: Implications for recolonisation process, *Aquatic Botany*, *89*(4), 397-403.

APAT (2006), Atlante delle Coste Italiane http://www.apat.gov.it/site/it/Servizi_per_l'Ambiente/Stato_delle_coste/Atlante_delle_coste/, Agenzia Protezione Ambiente e Territorio

ARPA-Sardegna (2005), Dipartimento Specialistico Regionale Idrometeoclimatico http://www.sar.sardegna.it.

Asano, T., S. Tsutsui, and T. Sakai (1988), Wave damping characteristics due to seaweed, 35th Coastal Engineering Conference in Japan, 138-142, ASCE Task Committee on Sea Level Rise.

Asano, T., H. Deguchi, and K. N. (1992), Interaction between water waves and vegetation, 23rd International Conference On Coastal Engineering 2710-2723, ASCE, Venice, Italy

Atzeni, A. (2003), Effetti idrodinamici sulle spiagge della costa occidentale della Sardegna, *Studi Costieri*, *7*, 61-80.

Augustin, L. N., J. L. Irish, and P. Lynett (2009), Laboratory and numerical studies of wave damping by emergent and near-emergent wetland vegetation, *Coastal Engineering*, *56*(3), 332-340.

Backhaus, J. O., and J. J. Verduin (2008), Simulating the interaction of seagrasses with their ambient flow, *Estuarine, Coastal and Shelf Science*, *80*(4), 563-572.

Ballesta, L., G. Pergent, V. Pasqualini, and C. Pergent-Martini (2000), Distribution and dynamics of Posidonia oceanica beds along the Alberes coastline, *Comptes Rendus De L Academie Des Sciences Serie Iii-Sciences De La Vie-Life Sciences*, *323*(4), 407-414.

Baptist, M. J. (2003), A flume experiment on sediment transport with flexible, submerged vegetation, International workshop on RIParian FORest vegetated channels: hydraulic, morphological and ecological aspects, Trento, Italy, 20–22 February.

Baroli, M., G. De Falco, and G. Piergallini (2003), Le praterie di Posidonia oceanica del Golfo di Oristano e della Penisola del Sinis. Distribuzione e stato di salute, in *Mare,*

Golfo, Lagune. Studi e Ricerche, G. De Falco and G. Piergallini (Ed.), 82-101, Editrice S'alvure, Oristano.

Benilov, A. Y., and B. N. Filyushkin (1970), An Application of Linear Filtration Technique for Analysis of Fluctuations in Sea Surface Layer, *Izvestiya Akademii Nauk Sssr Fizika Atmosfery I Okeana*, *6*(8), 810-819.

Borum, J., C. M. Duarte, D. Krause-Jensen, and T. M. Greve (2004), European seagrasses: an introduction to monitoring and management. A publication by the EU project Monitoring and Managing of European Seagrasses (M&MS)

Boudouresque, C. F., and A. Jeudi de Grissac (1983), L'Herbier à *Posidonia Oceanica* en Méditeranée: Les interactions entre la plant et le sédiment, *Journal de Recherche Océanographique*, *8*(2), 99-122.

Boudouresque, C. F., G. Bernard, P. Bonhomme, E. Charbonnel, G. Diviacco, A. Meinesz, G. Pergent, C. Pergent-Martini, S. Ruitton, and L. Tunesi (2006), Préservation et conservation des herbiers à Posidonia oceanica, 200 pp, Monaco.

Bouma, T. J., M. B. De Vries, E. Low, G. Peralta, C. Tanczos, J. Van de Koppel, and P. M. J. Herman (2005), Trade-offs related to ecosystem engineering: A case study on stiffness of emerging macrophytes, *Ecology*, *86*(8), 2187-2199.

Bouma, T. J., L. A. van Duren, S. Temmerman, T. Claverie, A. Blanco-Garcia, T. Ysebaert, and P. M. J. Herman (2007), Spatial flow and sedimentation patterns within patches of epibenthic structures: Combining field, flume and modelling experiments, *Continental Shelf Research*, *27*(8), 1020-1045.

Bradley, K., and C. Houser (2009), Relative velocity of seagrass blades: Implications for wave attenuation in low-energy environments, *Journal of Geophysical Research, 114*, 10.1029/2007jf000951: 10.1029/2007jf000951.

Brampton, A. H. (1992), Engineering significance of British saltmarshes, in *Saltmarshes: Morphodynamics, Conservation and Engineering Significance*, J. R. L. Allen and K. Pye (Ed.), 115–122, Cambridge University Press, Cambridge, UK.

Bryan, K. R., H. W. Tay, P. C. A., C. J. Lundquist, and H. L. Hunt (2007), The effects of Seagrass (*Zostera muelleri*) on boundary-layer hydrodynamics in Whangapoua Estuary, New Zealand., *Journal of Coastal Research*(SI 50 (Proceedings of the 9th International Coastal Symposium)), 668-672.

Buia, M. C., M. C. Gambi, and M. Dappiano (2004), Seagrass Systems, in *Mediterannean marine benthos: a manual of methods for its sampling and study* M. C. Gambi and M. Dappiano (Ed.), 604, Societa' italiana di biologia marina, Genova.

Butt, T., J. Miles, P. Ganderton, and P. Russell (2002), A simple method for calibrating optical backscatter sensors in high concentrations of non-cohesive sediments, *Marine Geology*, *192*, 419-424.

Cabaco, S., R. Santos, and C. M. Duarte (2008), The impact of sediment burial and erosion on seagrasses: A review, *Estuarine Coastal and Shelf Science*, *79*(3), 354-366.

Cáceres, I., J. Grüne, L. V. Rijn, A. Sánchez-Arcilla, A. Ahmari, and J. Ribberink (2008), Mobile-bed tests: The sand project, International Conference on Coastal Engineering 2622-2632, World Scientific, Hamburg.

Cancemi, G., M. Baroli, G. De Falco, S. Agostini, G. Piergallini, and I. Guala (2000), Cartografia integrata delle praterie superficiali come indicatore dell'impatto antropico sulla fascia costiera, *Biologia Marina Mediterranea*, *7*(2), 509-516.

Carboni, S., F. Di Gregorio, C. Ferrara, L. E. Cipriani, and E. Pranzini (1990), Fogli 216-217, Capo San Marco-Oristano, SELCA, Florence (Italy).

Cavazza, W., F. Immordino, L. Moretti, A. Peirano, A. Pironi, and F. Ruggiero (2000), Sedimentological parameters and seagrasses distributions as indicators of anthropogenic coastal degradation at Monterosso Bay (Ligurian Sea, NW Italy), *Journal of Coastal Research*, *16*(2), 295-305.

Collar, P., and G. Griffiths (2001), Single point current meters, in *Encyclopedia of ocean Sciences*, 2796-2803, Academic Press, San Diego, USA.

Costanza, R., R. d'Arge, R. de Groot, S. Farber, M. Grasso, B. Hannon, K. Limburg, S. Naeem, R. V. O'Neill, J. Paruelo, R. G. Raskin, P. Sutton, and M. van den Belt (1997), The value of the world's ecosystem services and natural capital, *Nature*, *387*(6630), 253-260.

Cucco, A., A. Perilli, G. De Falco, M. Ghezzo, and G. Umgiesser (2006), Water circulation and transport timescales in the Gulf of Oristano, *Chemistry and Ecology*, *22*, 307-331.

Cuomo, G., W. Allsop, T. Bruce, and J. Pearson (2010), Breaking wave loads at vertical seawalls and breakwaters, *Coastal Engineering*, *57*(4), 424-439.

D&A-Instruments-and-engineering (1988), Optical Backscatter Turbidity Monitor-Instruction manual-Revision 8/88, 32 pp.

Dalrymple, R. A., J. T. Kirby, and P. A. Hwang (1984), Wave diffraction due to areas of energy-dissipation, *Journal of Waterway Port Coastal and Ocean Engineering*, *110*(1), 67-79.

De Falco, G., S. Ferrari, G. Cancemi, and M. Baroli (2000), Relationship between sediment distribution and Posidonia oceanica seagrass, *Geo-Marine Letters*, *20*(1), 50-57.

De Falco, G., E. Molinaroli, M. Baroli, and S. Bellacicco (2003), Grain size and compositional trends of sediments from Posidonia oceanica meadows to beach shore, Sardinia, western Mediterranean, *Estuarine, Coastal and Shelf Science*, *58*(2), 299-309.

De Falco, G., and G. Piergallini (2003), *Mare Golfo Lagune Studi e Ricerche* S'alvure Ed, Oristano.

De Falco, G., M. Baroli, E. Murru, G. Piergallini, and G. Cancemi (2006), Sediment analysis evidences two different depositional phenomena influencing seagrass distribution in the Gulf of Oristano (Sardinia, western Mediterranean), *Journal of Coastal Research*, *22*(5), 1043-1050.

De Falco, G., M. Baroli, A. Cucco, and S. Simeone (2008), Intrabasinal conditions promoting the development of a biogenic carbonate sedimentary facies associated with the seagrass Posidonia oceanica, *Continental Shelf Research*, *28*(6), 797-812.

Dean, R. G., and R. A. Dalrymple (1991), *Water wave mechanics for engineers and scientists*, 353 pp., World Scientific.

Dean, R. G., and C. J. Bender (2006), Static wave setup with emphasis on damping effects by vegetation and bottom friction, *Coastal Engineering*, *53*(2-3), 149-156.

Di Carlo, G., F. Badalamenti, A. C. Jensen, E. W. Koch, and S. Riggio (2005), Colonisation process of vegetative fragments of Posidonia oceanica (L.) Delile on rubble mounds, *Marine Biology*, *147*(6), 1261-1270.

Duarte, C., and J. Cebrian (1996), The fate of marine autotrophic production, *Limnology and Oceanography*, *41*(8), 1758-1766.

Duarte, C. M., and K. Sandjensen (1990), Seagrass colonization - biomass development and shoot demography in Cymodocea nodosa patches, *Marine Ecology-Progress Series*, *67*(1), 97-103.

Duarte, C. M., and C. L. Chiscano (1999), Seagrass biomass and production: a reassessment, *Aquatic Botany*, *65*(1-4), 159-174.

Duarte, C. M., H. Kirkman, T. S. Frederick, A. S. Catherine, and G. C. Robert (2001), Methods for the measurement of seagrass abundance and depth distribution, in *Global Seagrass Research Methods*, F. T. Short and R. G. Coles (Ed.), 141-153, Elsevier Science, Amsterdam.

Duarte, C. M. (2002), The future of seagrass meadows, *Environmental Conservation*, *29*(2), 192-206.

Duarte, C. M., N. Marba, D. Krause-Jensen, and M. Sanchez-Camacho (2007), Testing the predictive power of seagrass depth limit models, *Estuaries and Coasts*, *30*(4), 652-656.

Dubi, A. M., and A. Tørum (1994), Wave damping by kelp vegetation., 24th International Conference on Coastal Engineering, 142-156, ASCE, Kobe, Japan.

Dubi, A. M. (1995), Damping of water waves by submerged vegetation—a case study on Laminaria hyperborea, Dr. Ing. thesis, 108 pp, University of Trondheim, Trondheim Norway.

Elwany, M. H. S., W. C. Oreilly, R. T. Guza, and R. E. Flick (1995), Effects of Southern California Kelp Beds on Waves, *Journal of Waterway Port Coastal and Ocean Engineering-Asce*, *121*(2), 143-150.

ETC/BD (2009), Habitats Directive Article 17 report, European Topic Centre on Biological Diversity, Paris.

Eurosion (2004), Living with coastal erosion in Europe: Sediment and Space for Sustainability PART I - Major findings and Policy Recommendations of the EUROSION project, Directorate General Environment European Commission, Brussels.

Feagin, R. A., S. M. Lozada-Bernard, T. M. Ravens, I. Moller, K. M. Yeager, and A. H. Baird (2009), Does vegetation prevent wave erosion of salt marsh edges?, *Proceedings of the National Academy of Sciences of the United States of America*, *106*(25), 10109-10113.

Ferrarin, C., and G. Umgiesser (2005), Hydrodynamic modeling of a coastal lagoon: The Cabras lagoon in Sardinia, Italy, *Ecological Modelling*, *188*(2-4), 340-357.

Folk, R. L., and W. C. Ward (1957), Brazos River bar: a study in the significance of grain size parameters, *Journal of Sedimentary Petrology*, *27*(1), 3-26.

Folk, R. L. (1974), *Petrology of sedimentary rocks*, Hemphills, Austin, Texas, USA.

Folkard, A. M. (2005), Hydrodynamics of model Posidonia oceanica patches in shallow water, *Limnology and Oceanography*, *50*(5), 1592-1600.

Fonseca, M. S., J. S. Fisher, J. C. Zieman, and G. W. Thayer (1982), Influence of the seagrass, *Zostera marina* on current flow, *Estuarine Coastal and Shelf Science*, *15*(4), 351-364.

Fonseca, M. S. (1983), Comparisons of current flow and wave dynamics through 4 seagrass species, *Estuaries*, *6*(3), 257-258.

Fonseca, M. S., and J. S. Fisher (1986), A comparison of canopy friction and sediment movement between 4 species of seagrass with reference to their ecology and restoration, *Marine Ecology-Progress Series*, *29*(1), 15-22.

Fonseca, M. S., and J. A. Cahalan (1992), A preliminary evaluation of wave attenuation by 4 species of seagrass, *Estuarine Coastal and Shelf Science*, *35*(6), 565-576.

Fonseca, M. S., S. S. Bell, and B. D. Robbins (2006), Foreword, *Estuarine, Coastal and Shelf Science*, *68*(3-4), 380-382.

Fonseca, M. S., and M. A. R. Koehl (2006), Flow in seagrass canopies: The influence of patch width, *Estuarine Coastal and Shelf Science*, *67*(1-2), 1-9.

Fonseca, M. S., M. A. R. Koehl, and B. S. Kopp (2007), Biomechanical factors contributing to self-organization in seagrass landscapes, *Journal of Experimental Marine Biology and Ecology*, *340*(2), 227-246.

Franco, L., R. Piscopia, S. Corsini, and R. Inghilesi (2004), L'Atlante delle onde nei mari italiani - Italian Wave Atlas, APAT-University of Roma Tre.

Gacia, E., T. C. Granata, and C. M. Duarte (1999), An approach to measurement of particle flux and sediment retention within seagrass (Posidonia oceanica) meadows, *Aquatic Botany*, *65*(1-4), 255-268.

Gacia, E., and C. M. Duarte (2001), Sediment retention by a mediterranean Posidonia oceanica meadow: The balance between deposition and resuspension, *Estuarine Coastal and Shelf Science*, *52*(4), 505-514.

Gambi, M. C., A. R. M. Nowell, and P. A. Jumars (1990), Flume observations on flow dynamics in Zostera marina (eelgrass) beds, *Marine Ecology-Progress Series*, *61*(1-2), 159-169.

Gaylord, B., M. W. Denny, and M. A. R. Koehl (2003), Modulation of wave forces on kelp canopies by alongshore currents, *Limnology and Oceanography*, *48*(2), 860-871.

Ghisalberti, M., and H. M. Nepf (2002), Mixing layers and coherent structures in vegetated aquatic flows, *Journal of Geophysical Research-Oceans*, *107*(C2), 1-11.

Ghisalberti, M., and H. Nepf (2006), The structure of the shear layer in flows over rigid and flexible canopies, *Environmental Fluid Mechanics*, *6*(3), 277-301.

Giraud, G. (1977), Contribution à la description et à la phènologie quantitative des herbiers à Posidonia oceanica (L.) Delile 150 pp, Université Aix-Marseille II, Marseille.

Gobert, S., M. L. Cambridge, B. Velimirov, G. Pergent, G. Lepoint, J. M. Bouquegneau, P. Dauby, C. Pergent-Martini, and D. I. Walker (2006), Seagrasses: Biology, Ecology and Conservation, A. W. D. Larkum*, et al.* (Ed.), 387-408, Springer.

Goring, D. G., and V. I. Nikora (2002), Despiking acoustic Doppler velocimeter data, *Journal of Hydraulic Engineering*, *128*(1), 117-126.

Graham, G. W., and A. J. Manning (2007), Floc size and settling velocity within a Spartina anglica canopy, *Continental Shelf Research*, *27*(8), 1060-1079.

Granata, T. C., T. Serra, J. Colomer, X. Casamitjana, C. M. Duarte, and E. Gacia (2001), Flow and particle distributions in a nearshore seagrass meadow before and after a storm, *Marine Ecology-Progress Series*, *218*, 95-106.

Hendriks, I. E., T. Sintes, T. J. Bouma, and C. M. Duarte (2008), Experimental assessment and modeling evaluation of the effects of the seagrass Posidonia oceanica on flow and particle trapping, *Marine Ecology-Progress Series*, *356*, 163-173.

Holmedal, L. E., and D. Myrhaug (2009), Wave-induced steady streaming, mass transport and net sediment transport in rough turbulent ocean bottom boundary layers, *Continental Shelf Research*, *29*(7), 911-926.

Hughes, A. R., S. L. Williams, C. M. Duarte, K. L. Heck, and M. Waycott (2009), Associations of concern: declining seagrasses and threatened dependent species, *Frontiers in Ecology and the Environment*, *7*(5), 242-246.

Hughes, S. A. (1993), *Physical models and laboratory techniques in coastal engineering*, 588 pp., World Scientific, Singapore.

Hunt, J. N. (1979), Direct solution of wave dispersion equation, *Journal of the Waterway Port Coastal and Ocean Division*, *105*(4), 457-459.

IPCC (2007), Climate Change 2007: The Physical Science Basis. Contribution of Working Group I to the Fourth Assessment Report of the Intergovernmental Panel on Climate Change, 996 pp, Intergovernmental Panel on Climate Change, Cambridge, United Kingdom and New York, NY, USA, .

Istituto-Idrografico-della-Marina (1985), Carta Nautica scala 1:40.000, Foglio 293, Golfo di Oristano, Istituto Idrografico della Marina, Genova (Italy).

Jensen, B. L., B. M. Sumer, and J. Fredsøe (1989), Turbulent oscillatory boundary layers at high Reynolds numbers, *Journal of Fluid Mechanics*, *206*, 265–297.

Jeudi de Grissac, A., and C. F. Boudouresque (1985), Rhôle des herbiers a phanérogames marines dans les mouvements des sediments côtiers: les herbiers à Posidonia Oceanica, Collection Franco-Japonais Oceanographie 143-151, Marseille, France, 16-21 Sept 1985.

Jonsson, I. G. (1966), Wave boundary layers and friction factors, 10th International Conference Coastal Engineering, 127-148, Tokyo.

Kamphuis, J. W. (1991), Physical Modelling, in *Handbook of coastal and Ocean Engineering*, J. B. Herbich (Ed.), Gulf publishing Company, Houston.

Kamphuis, J. W. (2002), *Introduction to coastal engineering and managament*, 437 pp., World Scientific, Singapore.

Kendrick, G. A., M. Marba, and C. M. Duarte (2005), Modelling formation of complex topography by the seagrass Posidonia oceanica, *Estuarine Coastal and Shelf Science*, *65*(4), 717-725.

Kobayashi, N., A. W. Raichle, and T. Asano (1993), Wave attenuation by vegetation, *Journal of Waterway Port Coastal and Ocean Engineering*, *119*(1), 30-48.

Koch, E. M. (2001), Beyond light: Physical, geological, and geochemical parameters as possible submersed aquatic vegetation habitat requirements, *Estuaries*, *24*(1), 1-17.

Koch, E. W. (1999), Sediment resuspension in a shallow Thalassia testudinum banks ex Konig bed, *Aquatic Botany*, *65*(1-4), 269-280.

Koch, E. W., and G. Gust (1999), Water flow in tide- and wave-dominated beds of the seagrass Thalassia testudinum, *Marine Ecology-Progress Series*, *184*, 63-72.

Koch, E. W., J. D. Ackerman, J. J. Verduin, and M. van Keulen (2006a), Fluid dynamics in seagrass ecology: from molecules to ecosystems., in *Seagrasses: biology, ecology and their conservation.*, A. Larkum*, et al.* (Ed.), 691, Springer-Verlag, Berlin, Germany.

Koch, E. W., L. P. Sanford, S.-N. Chen, D. J. Shafer, and J. M. Smith (2006b), Waves in seagrass systems: Review and technical recommendations, Report, 82 pp, U.S. Army Corps of Engineers.

Koch, E. W., E. B. Barbier, B. R. Silliman, D. J. Reed, G. M. E. Perillo, S. D. Hacker, E. F. Granek, J. H. Primavera, N. Muthiga, S. Polasky, B. S. Halpern, C. J. Kennedy, C. V. Kappel, and E. Wolanski (2009), Non-linearity in ecosystem services: temporal and spatial variability in coastal protection, *Frontiers in Ecology and the Environment*, *7*(1), 29-37.

Komar, P. D., and M. C. Miller (1974), Sediment threshold under oscillatory waves, 14th International Conference on Coastal Engineering, 756–775, American Society of Civil Engineers

Le Hir, P., Y. Monbet, and F. Orvain (2007), Sediment erodability in sediment transport modelling: Can we account for biota effects?, *Continental Shelf Research*, *27*(8), 1116-1142.

Lefebvre, A. (2009), Bed roughness over vegetated beds: sonar imaging techniques and effect on unidirectional currents, Ph.D. thesis, 212 pp, University of Southampton, Southampton.

Lefebvre, A., C. E. L. Thompson, K. J. Collins, and C. L. Amos (2009), Use of a high-resolution profiling sonar and a towed video camera to map a Zostera marina bed, Solent, UK, *Estuarine Coastal and Shelf Science*, *82*, 323-334.

Leonard, L. A., and M. E. Luther (1995), Flow hydrodynamics in tidal marsh canopies, *Limnology and Oceanography*, *40*(8), 1474-1484.

Leonard, L. A., and A. L. Croft (2006), The effect of standing biomass on flow velocity and turbulence in Spartina alterniflora canopies, *Estuarine Coastal and Shelf Science*, *69*(3-4), 325-336.

Li, C. W., and K. Yan (2007), Numerical investigation of wave-current-vegetation interaction, *Journal of Hydraulic Engineering-Asce*, *133*(7), 794-803.

LIM/UPC (2010), CIEM LAB Instrumentation Report, 15 pp, Universitat Politecnica de Catalunya, Barcelona (Spain).

Longuet-Higgins, M. S. (1953), Mass transport in water waves, *Philosophical Transactions of the Royal Society of London*, *A 345*, 535-381.

Lovas, S. M. (2000), Hydro-physical conditions in kelp forests and the effect of wave damping on dune erosion: A case study on *Laminaria Hyperaborea*, PhD thesis, University of Trondheim, Trondheim, Norway

Løvås, S. M., and A. Tørum (2001), Effect of the kelp Laminaria hyperborea upon sand dune erosion and water particle velocities, *Coastal Engineering*, *44*(1), 37-63.

Lowe, R. J., J. L. Falter, M. D. Bandet, G. Pawlak, M. J. Atkinson, S. G. Monismith, and J. R. Koseff (2005a), Spectral wave dissipation over a barrier reef, *Journal of Geophysical Research-Oceans, 110*(C4), 10.1029/2004jc002711: 10.1029/2004jc002711.

Lowe, R. J., J. R. Koseff, and S. G. Monismith (2005b), Oscillatory flow through submerged canopies: 1. Velocity structure, *Journal of Geophysical Research, 110*, 10.1029/2004jc002788: 10.1029/2004jc002788.

Lowe, R. J., J. L. Falter, J. R. Koseff, S. G. Monismith, and M. J. Atkinson (2007), Spectral wave flow attenuation within submerged canopies: Implications for wave energy dissipation, *Journal of Geophysical Research-Oceans*, *112*.

Lowe, R. J., U. Shavit, J. L. Falter, J. R. Koseff, and S. G. Monismith (2008), Modeling flow in coral communities with and without waves: A synthesis of porous media and canopy flow approaches, *Limnology and Oceanography*, *53*(6), 2668-2680.

Madsen, J. D., P. A. Chambers, W. F. James, E. W. Koch, and D. F. Westlake (2001), The interaction between water movement, sediment dynamics and submersed macrophytes, *Hydrobiologia*, *444*(1-3), 71-84.

Madsen, O. S., P. Y.-K., and G. H.C. (1988), Spectral wave attenuation by bottom friction: Theory, 21st International Conference on Coastal Engineering, 492-504, ASCE, Torremolinos.

Maltese, A., E. Cox, A. M. Folkard, G. Ciraolo, G. La Loggia, and G. Lombardo (2007), Laboratory measurements of flow and turbulence in discontinuous distributions of ligulate seagrass, *Journal of Hydraulic Engineering-Asce*, *133*(7), 750-760.

Manca, E. (2006), An evaluation of seagrass distribution in relation to shoreface stability, MSc thesis, 94 pp, University of Southampton, Southampton, UK.

Manca, E., V. Stratigaki, I. Caceres, and P. Prinos (2009), Wave Propagation Over Posidonia Oceanica: Report on the experiments, 17 pp, Universitat politecnica de Catalunya, Barcelona (Spain).

Manca, E., V. Stratigaki, and P. Prinos (2010), Large scale experiments on spectral wave propagation over *Posidonia oceanica* seagrass 6th International Symposium on Environmental Hydraulics 463-468, Taylor & Francis Group, Athens, Greece, 23–25 JUNE 2010.

Mangos, A., J.-P. Bassino, and D. Sauzade (2010), Valeur économique des bénéfices soutenables provenant des écosystèmes marins méditerranéens (Blue Plan Papers 8), 78 pp, Plan Bleu, Valbonne.

Mansard, E. P. D., and E. R. Funke (1980), The measurement of incident and reflected spectra using a least squares method, 17th Costal Engineering Conference, 154-172, ASCE, Sidney, Australia.

Marchand, M. (2008), The CONSCIENCE project: bridging the knowledge gap for sustainable coastline management Littoral, IAHR/Corila, Venice , Italy, 1st-6th july

Massel, S. R. (1999), *Fluid Mechanics for Marine Ecologists*, 566 pp., Springer-Verlag, Berlin.

Massel, S. R., K. Furukawa, and R. M. Brinkman (1999), Surface wave propagation in mangrove forests, *Fluid Dynamics Research*, *24*(4), 219-249.

Mateo, M. A., J. L. Sanchez-Lizaso, and J. Romero (2003), Posidonia oceanica 'banquettes': a preliminary assessment of the relevance for meadow carbon and nutrients budget, *Estuarine Coastal and Shelf Science*, *56*(1), 85-90.

Meijer, M. C. (2005), Wave attenuation over salt marsh vegetation, a numerical implementation of vegetation in SWAN, MSc thesis, Delft University of Technology, Delft

Mellors, J., H. Marsh, T. J. B. Carruthers, and M. Waycott (2002), Testing the sediment-trapping paradigm of seagrass: Do seagrasses influence nutrient status and sediment structure in tropical intertidal environments? , *Bulletin of Marine Science*, *71*(3), 1215-1226.

Mendez, F. J., I. J. Losada, and M. A. Losada (1999), Hydrodynamics induced by wind waves in a vegetation field, *Journal of Geophysical Research-Oceans*, *104*(C8), 18383-18396.

Mendez, F. J., and I. J. Losada (2004), An empirical model to estimate the propagation of random breaking and nonbreaking waves over vegetation fields, *Coastal Engineering*, *51*(2), 103-118.

Möller, I., T. Spencer, J. R. French, D. J. Leggett, and M. Dixon (1999), Wave transformation over salt marshes: A field and numerical modelling study from north Norfolk, England, *Estuarine Coastal and Shelf Science*, *49*(3), 411-426.

Möller, I. (2006), Quantifying saltmarsh vegetation and its effect on wave height dissipation: Results from a UK East coast saltmarsh, *Estuarine Coastal and Shelf Science*, *69*(3-4), 337-351.

Möller, R. I., T. Spencer, and J. Rawson (2002), Spatial and temporal variability of wave attenuation over a UK East-coast saltmarsh, 28th International Conference on Coastal Engineering, Cardiff, UK, July 2002.

Mori, N., T. Suzuki, and S. Kakuno (2007), Experimental study of air bubbles and turbulence characteristics in the surf zone, *J. Geophys. Res.*, *112*.

Mork, M. (1996), The effect of kelp in wave damping, *Sarsia*, *80*(4), 323-327.

Myrhaug, D., L. E. Holmedal, and M. C. Ong (2009), Nonlinear random wave-induced drag force on a vegetation field, *Coastal Engineering*, *56*(3), 371-376.

Nepf, H., and M. Ghisalberti (2008), Flow and transport in channels with submerged vegetation, *Acta Geophysica*, *56*(3), 753-777.

Nepf, H. M. (1999), Drag, turbulence, and diffusion in flow through emergent vegetation, *Water Resources Research*, *35*(2), 479-489.

Nepf, H. M., and E. R. Vivoni (2000), Flow structure in depth-limited, vegetated flow, *Journal of Geophysical Research-Oceans*, *105*(C12), 28547-28557.

Neumeier, U., and P. Ciavola (2004), Flow resistance and associated sedimentary processes in a Spartina maritima salt-marsh, *Journal of Coastal Research*, *20*(2), 435-447.

Neumeier, U., and C. L. Amos (2006a), Turbulence reduction by the canopy of coastal Spartina salt-marshes, *Journal of Coastal Research*, *1*, 433-439.

Neumeier, U., and C. L. Amos (2006b), The influence of vegetation on turbulence and flow velocities in European salt-marshes, *Sedimentology*, *53*(2), 259-277.

Neumeier, U. (2007), Velocity and turbulence variations at the edge of saltmarshes, *Continental Shelf Research*, *27*(8), 1046-1059.

Nielsen, P. (1985), On the structure of oscillatory boundary layers, *Coastal Engineering*, *9*(3), 261-276.

Nielsen, P. (1992), *Coastal boundary layers and sediment transport* 324 pp., World Scientific.

Nielsen, P., and P. A. Guard (2010), Vertical scales and shear stresses in wave boundary layers on movable beds, 32nd International Conference on Coastal Engineering, Shanghai, China 30 june- 5 july.

Nortek, L. (2005), Vectrino Acousti Doppler Velocimeter User Manual.

NRC, N. R. C. (2005), Valuing ecosystem services, Washington, DC.

Oliveira, T. C. A., F. X. Gironella, A. Sanchez-Arcilla, J. P. Sierra, and M. A. Celigueta (2009), Nonlinear regular wave generation in numerical and physical flumes., *Journal of Coastal Research*(Special Issue 56 - Proceedings of the 2009 International Coastal Symposium, Portugal), 1025-1029.

Orth, R. J., T. J. B. Carruthers, W. C. Dennison, C. M. Duarte, J. W. Fourqurean, K. L. Heck, A. R. Hughes, G. A. Kendrick, W. J. Kenworthy, S. Olyarnik, F. T. Short, M. Waycott, and S. L. Williams (2006), A global crisis for seagrass ecosystems, *Bioscience*, *56*(12), 987-996.

Pasqualini, V., C. Pergent-Martini, P. Clabaut, and G. Pergent (1998), Mapping of Posidonia oceanica using aerial photographs and side scan sonar: Application off the Island of Corsica (France), *Estuarine Coastal and Shelf Science*, *47*(3), 359-367.

Pedersen, C., R. Deigaard, and J. Sutherland (1998), Measurements of the vertical correlation in turbulence under broken waves, *Coastal Engineering*, *35*(4), 231-249.

Penning, W. E., R. Raghuraj, and A. E. Mynett (2009), The effects of macrophyte morphology and patch density on wave attenuation., 7th ISE and 8th HIC Chile.

Peralta, G., L. A. van Duren, E. P. Morris, and T. J. Bouma (2008), Consequences of shoot density and stiffness for ecosystem engineering by benthic macrophytes in flow dominated areas: a hydrodynamic flume study, *Marine Ecology-Progress Series*, *368*, 103-115.

Pergentmartini, C., and G. Pergent (1994), Lepidochronological Analysis in the Mediterranean Seagrass Posidonia-Oceanica State-of-the-Art and Future-Developments, *Oceanologica Acta*, *17*(6), 673-681.

Peterson, C. H., R. Luettich, A. Jr., F. Micheli, and G. A. Skilleter (2004), Attenuation of water flow inside seagrass canopies of differing structure, *Marine Ecology Progress Series*, *268*, 81-92.

Plomaritis, T. (2006), Sediment dynamic processes in the vicinity of offshore breakwaters, Doctoral thesis, 243 pp, University of Southampton.

Plomaritis, T. A., D. Paphitis, and M. Collins (2008), The use of grain size trend analysis in macrotidal areas with breakwaters: Implications of settling velocity and spatial sampling density, *Marine Geology*, *253*(3-4), 132-148.

Pope, N. D., J. Widdows, and M. D. Brinsley (2006), Estimation of bed shear stress using the turbulent kinetic energy approach-A comparison of annular flume and field data, *Continental Shelf Research*, *26*(8), 959-970.

Prager, E. J., and R. B. Halley (1999), The influence of seagrass on shell layers and Florida Bay mudbanks, *Journal of Coastal Research*, *15*(4), 1151-1162.

Price, W. A., K. W. Tomlinson, and J. N. Hunt (1968), The effect of artificial seaweed in promoting the build-up of beaches, 11th International Conference on Coastal Engineering, 570–578, ASCE London.

Prinos, P., V. Stratigaki, E. Manca, I. Losada, J. Lara, M. Sclavo, I. Caceres, and A. Sanchez-Arcilla (2010), Wave propagation over *Posidonia oceanica*: Large scale experiments, HYDRALAB 3 Joint User Meeting, 57-60, FZK Coastal Research Centre, University Hannover & Technical University Braunschweig Hannover, Germany.

Raupach, M. R., R. A. Antonia, and S. Rajagopalan (1991), Rough-wall turbulent boundary layers, *Applied Mechanics Reviews*, *44*(1), 1-25.

Reidenbach, M. A., J. R. Koseff, and S. G. Monismith (2007), Laboratory experiments of fine-scale mixing and mass transport within a coral canopy, *Physics of Fluids, 19*(7), 10.1063/1.2752189: 10.1063/1.2752189.

Ribberink, J. S., and A. A. Al-Salem (1995), Sheet flow and suspension of sand in oscillatory boundary layers, *Coastal Engineering*, *25*(3-4), 205-225.

Rigler, J. K., M. B. Collins, and S. J. Williams (1981), A high precision, digital-recording sedimentation tower for sands, *JOURNAL OF SEDIMENTARY RESEARCH*, *51*(2), 642-644.

Riviere, A. (1977), *Methodes granulometriques; Techniques et interpretations.*, 170 pp., Masson, Paris.

RON (2010), Rete Ondametrica Nazionale www.idromare.it.

Sabol, B., R. Eddie Melton, R. Chamberlain, P. Doering, and K. Haunert (2002), Evaluation of a digital echo sounder system for detection of submersed aquatic vegetation, *Estuaries and Coasts*, *25*(1), 133-141.

Sana, A., and H. Tanaka (2007), Full-range equation for wave boundary layer thickness, *Coastal Engineering*, *54*(8), 639-642.

Sarpkaya, T., and M. Isaacson (1981), *Mechanics of wave forces on offshore structures* 651 pp., Van Nostrand Reinhold Co., New York.

Scandura, P. (2007), Steady streaming in a turbulent oscillating boundary layer, *Journal of Fluid Mechanics*, *571*(-1), 265-280.

SDGM, and ECMWF (1993), *The Wave Forecasting System in the Mediterranean Sea*, Stamperia di Venezia, Venice, Italy.

Shi, Z., and J. M. R. Hughes (2002), Laboratory flume studies of microflow environments of aquatic plants, *Hydrological Processes*, *16*(16), 3279-3289.

Sleath, J. F. A. (1984), *Sea Bed Mechanics*, Wiley Interscience.

Sleath, J. F. A. (1987), Turbulent Oscillatory Flow over Rough Beds, *Journal of Fluid Mechanics*, *182*, 369-409.

Soulsby, R. (1997), *Dynamics of marine sands: a manual for practical applications*, 249 pp., Thomas Teldford, London.

Soulsby, R., and S. Clarke (2005), Bed shear-stress under combined waves and currents on smooth and rough beds, 22 pp, HR Wallingford Ltd.

Stapleton, K. R., and D. A. Huntley (1995), Seabed stress determinations using the inertial dissipation method and the turbulent kinetic energy method, *Earth Surface Processes and Landforms*, *20*(9), 807-815.

Stratigaki, V., E. Manca, and P. Prinos (2009a), Efffects of Posidonia oceanica meadow on wave propagation: Large scale experiments, 4th SCACR International Short Conference on Applied Coastal Research, Barcelona, Spain.

Stratigaki, V., E. Manca, P. Prinos, I. Losada, J. Lara, M. Sclavo, I. Caceres, and A. Sanchez-Arcilla (2009b), Large scale experiments on wave propagation over *Posidonia oceanica*, 33rd IAHR Congress: Water Engineering for a Sustainable Environment, 2878-2885, International Association of Hydraulic Engineering & Research Vancouver, Canada.

Stratigaki, V., E. Manca, P. Prinos, I. Losada, J. Lara, M. Sclavo, C. L. Amos, I. Caceres, and A. Sanchez-Arcilla (accepted), Large scale experiments on wave propagation over *Posidonia oceanica*, *Journal of Hydraulic Research*.

Stratigaki, V., E. Manca, P. Prinos, I. Losada, J. Lara, M. Sclavo, I. Caceres, and A. Sanchez-Arcilla (Submitted), Large scale experiments on wave propagation over *Posidonia oceanica*, *Journal of Hydraulic Research*.

Svendsen, I. A. (1987), Analysis of Surf Zone Turbulence, *Journal of Geophysical Research-Oceans*, *92*(C5), 5115-5124.

Teeter, A. M., B. H. Johnson, C. Berger, G. Stelling, N. W. Scheffner, M. H. Garcia, and T. M. Parchure (2001), Hydrodynamic and sediment transport modeling with emphasis on shallow-water, vegetated areas (lakes, reservoirs, estuaries and lagoons), *Hydrobiologia*, *444*(1-3), 1-24.

Terrados, J., and C. M. Duarte (2000), Experimental evidence of reduced particle resuspension within a seagrass (Posidonia oceanica L.) meadow, *Journal of Experimental Marine Biology and Ecology*, *243*(1), 45-53.

Thompson, C. E. L., C. L. Amos, T. E. R. Jones, and J. Chaplin (2003), The manifestation of fluid-transmitted bed shear stress in a smooth annular flume - A comparison of methods, *Journal of Coastal Research*, *19*(4), 1094-1103.

Thompson, C. E. L., C. L. Amos, and G. Umgiesser (2004), A comparison between fluid shear stress reduction by halophytic plants in Venice Lagoon, Italy and Rustico Bay, Canada - analyses of in situ measurements, *Journal of Marine Systems*, *51*(1-4), 293-308.

Tigny, V., A. Ozer, G. De Falco, M. Baroli, and S. Djenidi (2007), Relationship between the evolution of the shoreline and the Posidonia oceanica meadow limit in a Sardinian coastal zone, *Journal of Coastal Research*, *23*(3), 787-793.

Ting, F. C. K., and J. T. Kirby (1996), Dynamics of surf-zone turbulence in a spilling breaker, *Coastal Engineering*, *27*(3-4), 131-160.

Tucker, M. J., and E. G. Pitt (2001), *Waves in ocean engineering*, 521 pp., Elsevier, Amsterdam.

Vacchi, M., Montefalcone M., C. N. Bianchi, C. Morri, and M. Ferrari (2010), The influence of coastal dynamics on the upper limit of the *Posidonia oceanica* meadow, *Marine Ecology*, *1*(9).

van Katwijk, M. M., A. R. Bos, D. C. R. Hermus, and W. Suykerbuyk (2010), Sediment modification by seagrass beds: Muddification and sandification induced by plant cover and environmental conditions, *Estuarine, Coastal and Shelf Science*, *89*(2), 175-181.

Van Keulen, M., and M. A. Borowitzka (2003), Seasonal variability in sediment distribution along an exposure gradient in a seagrass meadow in Shoalwater Bay, Western Australia, *Estuarine, Coastal and Shelf Science*, *57*(4), 587-592.

Van Rijn, L. C. (2007), *Manual of sediment transport measurements in rivers,estuaries and coastal seas*, 500 pp., Aquapublications, The Netherlands.

Verduin, J. J., and J. O. Backhaus (2000), Dynamics of plant-flow interactions for the seagrass Amphibolis antarctica: Field observations and model simulations, *Estuarine Coastal and Shelf Science*, *50*(2), 185-204.

Vermaat, J., W. Salomons, L. Bouwer, K. Turner, R. Nicholls, and R. Klein (2005), Climate change and coastal management on Europe's coast, in *Managing European Coasts*, R. Allan*, et al.* (Ed.), 199-226, Springer Berlin Heidelberg.

Wahl, T. L. (2003), Discussion of ``Despiking acoustic doppler velocimeter data'' by Derek G. Goring and Vladimir I. Nikora, *Journal of Hydraulic Engineering*, *129*(6), 484-487.

Wallace, S., and R. Cox (2000), Effects of seagrass on nearshore current and wave dynamics, 27th International Conference on Coastal Engineering, 978-890, ASCE, Sydney, Australia.

Warren, J. D., and B. J. Peterson (2007), Use of a 600-kHz Acoustic Doppler Current Profiler to measure estuarine bottom type, relative abundance of submerged aquatic vegetation, and eelgrass canopy height, *Estuarine Coastal and Shelf Science*, *72*(1-2), 53-62.

Waycott, M., C. M. Duarte, T. J. B. Carruthers, R. J. Orth, W. C. Dennison, S. Olyarnik, A. Calladine, J. W. Fourqurean, K. L. Heck, A. R. Hughes, G. A. Kendrick, W. J. Kenworthy, F. T. Short, and S. L. Williams (2009), Accelerating loss of seagrasses across the globe threatens coastal ecosystems, *Proceedings of the National Academy of Sciences*, *106*(30), 12377-12381.

Welch, P. D. (1967), The use of Fast Fourier Transform for the estimation of Power Spectra: A method based on time averaging over short, modified periodograms, *IEEE Trans. Audio Electroacoustics*, *AU-15*, 70-73.

Wentworth, C. K. (1922), A scale of grade and class terms for clastic sediments *Journal of Geology*, *30*, 377–392.

Wiberg, P. L., and C. R. Sherwood (2008), Calculating wave-generated bottom orbital velocities from surface-wave parameters, *Computers & Geosciences*, *34*(10), 1243-1262.

WOC (2009), Manado Ocean Declaration, World Ocean Conference, Manado, 11th-15th May.

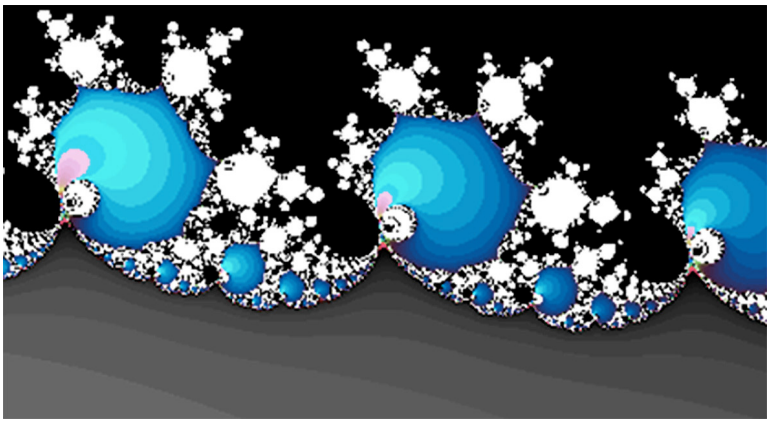

“Nobody will deny that there is at least some roughness everywhere”

Benoit Mandelbrot (1924-2010)